



Characterisation and Understanding of Rail Steel Behaviour for In-Service Life Prediction

Adam Wilby

8th September 2023

Department of Mechanical Engineering

Thesis Submitted for the Degree of Doctor of Engineering

Abstract

Rail steels commonly accumulate large amounts of subsurface plastic deformation due to repeated rail-wheel contacts. The accumulation of this plastic damage is known to be responsible for the generation of RCF (rolling contact fatigue) and significant instances of wear damage while in-service. An improved quantification of this plastic deformation development is important to allow better decisions regarding rail maintenance programmes and the selection of the most suitable rail steel grade, helping to support the installation of premium rail steel metallurgies. In addition, to providing potential cost savings through possibly helping to optimise maintenance programmes and the prevention of rail failures. Therefore, the focus of this thesis is to expand the knowledge and understanding of how plastic damage develops in rail steels due to repeated rail-wheel contacts.

The plastic deformation response of rail steels subjected to cyclic shear-compression loading conditions was characterised from experimental twin-disc samples for different rail steel metallurgies and contact conditions. This information collected provided the data necessary for deriving the rail steel shear stress-strain curve, ratcheting load conversion factor (conversion factor between ratcheting load and increment shear strain), and the shear strain at failure (limit of accumulative shear strain that can occur before the nucleation of voids and microcracks). The shear stress-strain curve, ratcheting load conversion factor, and the shear yield point were found to be insufficient information by themselves for understanding the wear performance of a rail grade. The comparison of results generated under different contact pressures showed that the shear stress-strain curve was insensitive to the normal contact pressure it was derived under and so would be classed as ‘material property’ data. The ratcheting load conversion factor, however, was found to exhibit some dependence with the normal contact pressure the data was derived under, which would class it as ‘machine behavioural’ information. The derivation of the rail steel shear strain at failure was also investigated via a new value optimisation process using an implementation of the brick-based plastic ratcheting simulation model. This value optimisation process looked at varying the material shear strain at failure until the simulation cyclic wear depth loss results matched up with the experimental twin-disc data. The results generated from this approach was successful for the conditions it was believed to be best suited for, however, it was less successful for the conditions believed at the time to be challenging to apply this approach to.

The development of a novel optical monitoring system for application to twin-disc testing was also explored in this thesis. The intention of this system was to photograph in-detail the surface evolution of a twin-disc sample’s running track during standard twin-disc experiments without the need to

interrupt tests. The images collected using this system were able to clearly observe the development of wear flakes via the shadows they cast onto the sample's running surface for dry twin-disc tests. The visualisation of the development of RCF cracks from water-lubricated experiments was not as clear due to interference caused by the water film present on the specimen's running track. A comparison of the wear flake shadow pixel count and the wear data showed a good correlation between the two datasets, showing the potential of understanding the wear behaviour of rail steels using this equipment. Investigating the wear flake morphological change using this equipment revealed a correlation between wear flake size and the undeformed hardness of the rail steel, with harder rail steels generating smaller wear flakes. A delayed initiation of the wear flakes was observed on the heat-treated rail steel grade R350HT compared to the air-cooled grades R260 and HP335, which is believed to be caused by the refined pearlitic microstructure of R350HT. The effect of the elongated MnS inclusions orientation on wear flake behaviour could also be seen, with elongated MnS inclusions orientated perpendicular to the running surface causing earlier initiation and faster development of wear flakes compared to elongated MnS inclusions orientated parallel. Tracking the development of individual wear flakes showed them occasionally growing and shrinking over time, but not completely disappearing, which points to material only being removed as wear debris from the tips of wear flakes. A comparison of the surface plastic flow measured using the optical monitoring system correlated well with the surface plastic flow predicted by the plastic ratcheting simulation model during the early stages of the experiment. This correlation between simulation and experimental results did break down later into the experiment, which is possibly caused by the 2D nature of the simulation model used and the fact that wear and plastic deformation counteract each other's influence on the movement of wear flakes.

Acknowledgements

I would like to express my sincerest gratitude to my supervisors: Prof. David Fletcher and Prof. Roger Lewis from the University of Sheffield, and Dr. Jacob Corteen from British Steel R&D. Their support, guidance, and advice throughout my EngD study has been key to the success of this work.

I would also like to extend my thanks to the many technical staff and academics at the University of Sheffield from the AMSCDT (Advanced Metallic Systems Centre for Doctoral Training), Material Science and Engineering Department, and Mechanical Engineering Department for their technical advice. I am deeply grateful to the technician David Butcher at the University of Sheffield, for his expertise and help in designing, developing, and commissioning the various experimental equipment that have been critical to undertaking the research in this thesis. I am also deeply appreciative of my dyslexia tutor Victoria Mann for her guidance during the write up of this thesis. I would also like to express thanks to my fellow colleagues from the MERail research group and Advanced Metallic Systems CDT for their encouragement and friendship.

My gratitude also goes to the many people I have met from the rail R&D team at British Steel for their helpful advice and technical knowledge. Notable people I would like to say thank you include Dr Andy Trowsdale, Dr Stephen Lewis, Dr Gari Harris (now at Teesside University), Stephen Danks, and Scott Dyball. I am also grateful to Gary Claxton for helping collect the SEM (scanning electron microscope) micrographs for me to measure the interlamellar spacing and pearlite colony size for the rail steel samples tested in this thesis.

I am thankfully for the funding provided to undertake this research from my industrial sponsor British Steel Ltd. and the EPSRC (Engineering Physical Science Research Council) through the AMSCDT (EPSRC grant ref. EP/L016273/1). I would also like to thank British Steel Ltd. and Dr. Samuel Hawksbee from the University of Huddersfield for the supply of rail steel, and Wabtec Rail Ltd. for the supply of wheel steel material used to manufacture the twin-disc samples tested in this thesis.

Finally, I would like to thank my family for providing their unceasing support and encouragement they have given over the past few years.

Declaration

I, Adam Wilby, confirm that the Thesis is my own work. I am aware of the University's guidance on the use of unfair means (www.sheffield.ac.uk/ssid/unfair-means). This work has not been previously presented for an award at this, or any other, university.

Contents

| | |
|--|-------------|
| Acronyms | vii |
| Nomenclature | viii |
| Chapter 1: Introduction | 1 |
| 1.1 Research Problem Background | 1 |
| 1.2 Research Aim and Areas of Focus | 5 |
| 1.3 Structure of Thesis..... | 6 |
| 1.4 Contribution..... | 7 |
| Chapter 2: Literature Review | 9 |
| 2.1 Introduction | 9 |
| 2.2 Rail-Wheel Contact Geometry, Forces and Vehicle Dynamics | 9 |
| 2.3 Rail Steel Metallurgy..... | 20 |
| 2.4 Rail Steel Loading Response..... | 22 |
| 2.5 Shakedown Theory..... | 25 |
| 2.6 Rolling Contact Fatigue (RCF) Cracks | 31 |
| 2.7 Wear | 35 |
| 2.8 Rail Steel Grade Selection..... | 38 |
| 2.9 Rail-Wheel Contact Experimental methods | 40 |
| 2.10 Summary of Research Gaps Identified..... | 44 |
| Chapter 3: Characterisation of the Asperity and Bulk Contact Driven Plastic Deformation Behaviour of Rail Steel | 47 |
| 3.1 Introduction | 47 |
| 3.2 Experimental Methodology | 51 |
| 3.3 Experimental Results..... | 56 |
| 3.4 Shear Stress-Strain Curve Relationship | 75 |
| 3.5 Ratcheting Load Conversion Factor | 82 |
| 3.6 Discussion | 95 |
| 3.7 Conclusions | 100 |
| Chapter 4: Determining the Shear Strain at Failure of Rail Steels | 102 |
| 4.1 Introduction | 102 |
| 4.2 Evaluating Pre-Existing Methods..... | 103 |
| 4.3 Value Optimisation Methodology | 106 |
| 4.4 Results | 114 |

| | | |
|---|--|------------|
| 4.5 | Discussion | 119 |
| 4.6 | Conclusions | 122 |
| Chapter 5: Development and Testing of a Novel Optical Monitoring System for Twin-Disc Testing..... | | 125 |
| 5.1 | Introduction | 125 |
| 5.2 | Equipment Description..... | 126 |
| 5.3 | Methodology | 129 |
| 5.4 | Results and Discussion..... | 131 |
| 5.5 | Conclusions | 138 |
| Chapter 6: Rail Steel Damage Development Observed in Real Time | | 139 |
| 6.1 | Introduction | 139 |
| 6.2 | Methodology | 141 |
| 6.3 | Results | 142 |
| 6.4 | Plastic Ratcheting Theory Correlation with Real Time Experimental Data | 152 |
| 6.5 | Discussion | 154 |
| 6.6 | Conclusions | 161 |
| Chapter 7: Conclusions and Further Work | | 164 |
| 7.1 | Introduction | 164 |
| 7.2 | Project Conclusions..... | 165 |
| 7.3 | Recommendation for Further Work | 169 |
| References | | 172 |
| Appendix A1: Supplementary Information for Chapter 3 | | 187 |
| Appendix A2: Indentation Size Error Effect for R260 Rail Steel Study | | 211 |
| Appendix A3: Supplementary Information for Chapter 4 | | 214 |
| Appendix A4: MATLAB Code for the SUROS2 Optical Monitoring System Wear Flake Shadow Pixel Analysis | | 219 |

Acronyms

| | |
|--------|---|
| ACFM | Alternating Current Field Measurement |
| BCC | Body Centred Cubic |
| BOF | Basic Oxygen Furnace |
| EAF | Electric Arc Furnace |
| FOV | Field Of View |
| HAGB | High Angle Grain Boundaries |
| HS2 | High Speed 2 |
| ISE | Indentation Size Effect |
| LAGB | Low Angle Grain Boundaries |
| LED | Light Emitting Diode |
| RAMS | Reliability Availability Maintainability Safety |
| RCF | Rolling Contact Fatigue |
| RPM | Revolutions Per Minute |
| RSSB | Rail Safety Standards Board |
| SEM | Scanning Electron Microscope |
| UKRRIN | UK Rail Research Innovation Network |

Nomenclature

| | | |
|---------------|---|-----|
| b | Contact Half Width Dimension | mm |
| b_a | Asperity Contact Half Width Dimension | mm |
| B_{lost} | Total Number of Brick Elements Lost | |
| B_x | Horizontal Number of Brick Elements | |
| B_z | Vertical Number of Brick Elements | |
| c | Ratcheting Load Conversion Factor | |
| C | Circle of Confusion | mm |
| d | Twin-Disc Sample Diameter | mm |
| dz | Vertical Thickness of Bricks | mm |
| E_r, E_w | Rail and Wheel Young's Modulus | MPa |
| f | Relative Aperture | |
| H | Hardness | HV |
| H_0 | Undeformed Hardness | HV |
| k | Shear Yield Stress | MPa |
| k_0 | Initial Shear Yield Strength | MPa |
| K | Wear Coefficient | |
| L | Contact Length | mm |
| M | Optical Magnification | |
| n | Contact Cycle Number | |
| N | Total Number of Contact Cycles | |
| p_0 | Maximum Contact Pressure | MPa |
| p_a | Asperity Maximum Contact Pressure | MPa |
| P_{size} | Optical Camera Sensor Pixel Size | mm |
| R | Reduced Radius of Curvature | mm |
| S | Spatial Resolution | |
| t | Time | s |
| $T_{ratchet}$ | Nondimensionalised Severity of Ratcheting Load Above the Shear Yield Strength | |
| P | Contact Load | N |
| x | Longitudinal Distance | mm |
| z | Depth Below Running Surface | mm |

| | | |
|------------------|--------------------------------------|--------------------|
| θ | Angle of the Deformed Microstructure | $^{\circ}$ |
| λ_a | Asperity Separation | mm |
| μ | Coefficient of Friction | |
| γ | Shear Strain | |
| γ_c | Shear Strain at Failure | |
| ν_r, ν_w | Rail and Wheel Poisson Ratio | |
| $\tau_{ratchet}$ | Ratcheting Load | MPa |
| τ_{xz} | Shear Stress | MPa |
| ρ | Density | g mm^{-3} |
| ρ_a | Asperity Tip Radius | mm |
| σ_y | Tensile Yield Strength | MPa |
| ω | Rotational Speed | RPM |

Chapter 1: Introduction

1.1 Research Problem Background

This thesis focuses on characterising the plastic deformation response of both conventional and premium rail steel grades in-service under cyclic shear-compression loading conditions, in addition to developing a novel optical monitoring system to understand rail steel damage behaviour in real time. These are important because the information generated in this thesis will help provide rail steel manufacturers and rail networks operators a better understanding of how damage accumulates in service. This will contribute to allowing better decisions regarding rail maintenance programmes and the selection of most suitable rail steel grade, helping to support the installation of premium rail steel metallurgies.

Looking at a higher level, this is of importance because the movement of people and freight between two places via rail is one of the safest and fastest forms of land-based methods of transportation available. An average of 0.3 fatalities per billion passenger/vehicle mile occurred with rail transport in the UK in 2018/19 compared to 3.0 for cars and 3.5 for bus transportation [1]. Equally, rail transportation is relatively more energy-efficient and environmentally friendlier compared to road and aviation transport. This is because an average of 0.024 million tons carbon dioxide equivalent emission per billion passenger kilometres were produced by rail in the UK during 2019 compared to 0.124 for cars and motorcycles, 0.094 for buses and coaches, and 0.156 for aviation [2], [3]. Furthermore, the 2016 UK rail freight strategy report [4] highlights that rail freight produces 76% fewer carbon emissions compared to road-hauled freight for the equivalent journey. Consequently, this sustainability benefit has renewed interest in rail transportation from governments and the wider public. The UK strategy for decreasing greenhouse gas emissions emphasises that there needs to be a modal transport shift towards rail for the UK to meet its 2050 emission targets [5]. The growing importance of a rail as a mode of transport can also be observed from the current construction of new rail projects, such as High Speed 2 (HS2) – as increasing rail capacity and reducing carbon emissions in the UK are two of the core reasons for why HS2 is being constructed [6]. Furthermore, the growing importance can also be seen from the recent growth in total UK passenger journeys prior to the Covid-19 pandemic, where UK passenger journeys increased 135.6% between 1995-2020 to 1738.7 million [7], as illustrated in Figure 1.1. Even though the UK rail passenger numbers took a severe hit during the Covid-19 pandemic, data from the Department for Transport [8] shows that national rail passenger numbers have already recovered to pre-Covid levels, as shown in Figure 1.2.

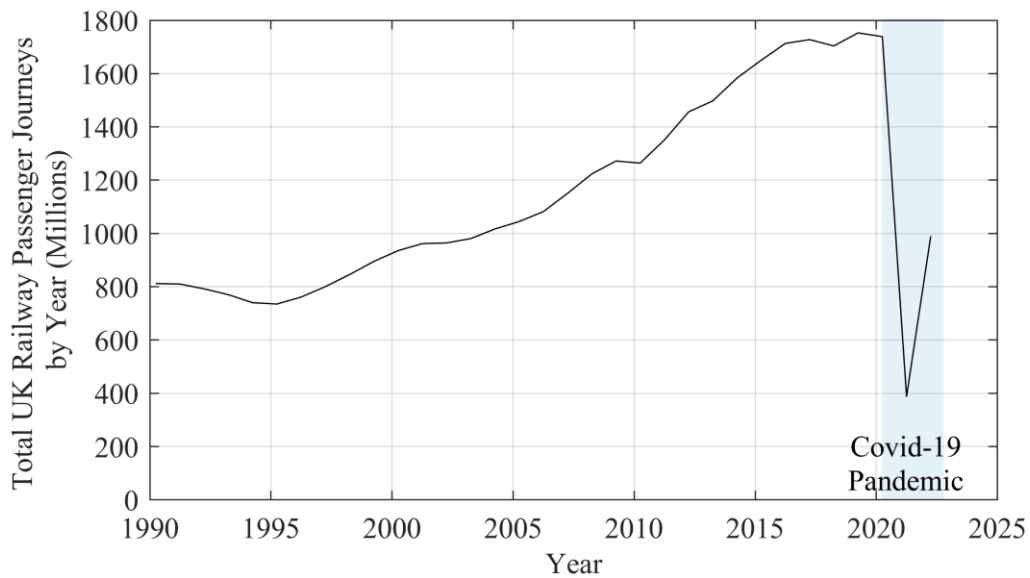


Figure 1.1: Total number of UK passenger journeys observed between 1990-2022 for the UK railway industry using data collected in the reference [7].

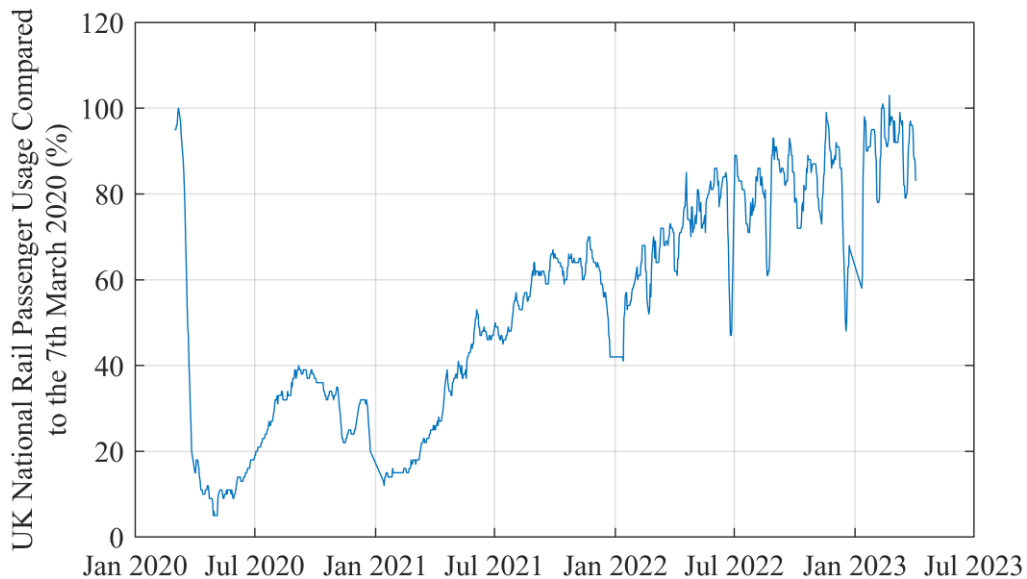


Figure 1.2: UK national rail passenger Usage compared to the 7th March 2020 figures between 1st March 2020 and 3rd April 2023 using data collected in the reference [8].

This desire to expand the utilisation of rail transportation has contributed to the current trend in the industry for higher speeds, greater axle loads and more frequent track usage [9]. This results in a higher propensity for wear and rolling contact fatigue (RCF) damage accumulating in a rail section. Examples of this damage observed on used rail steels removed from track is presented in Figure 1.3.

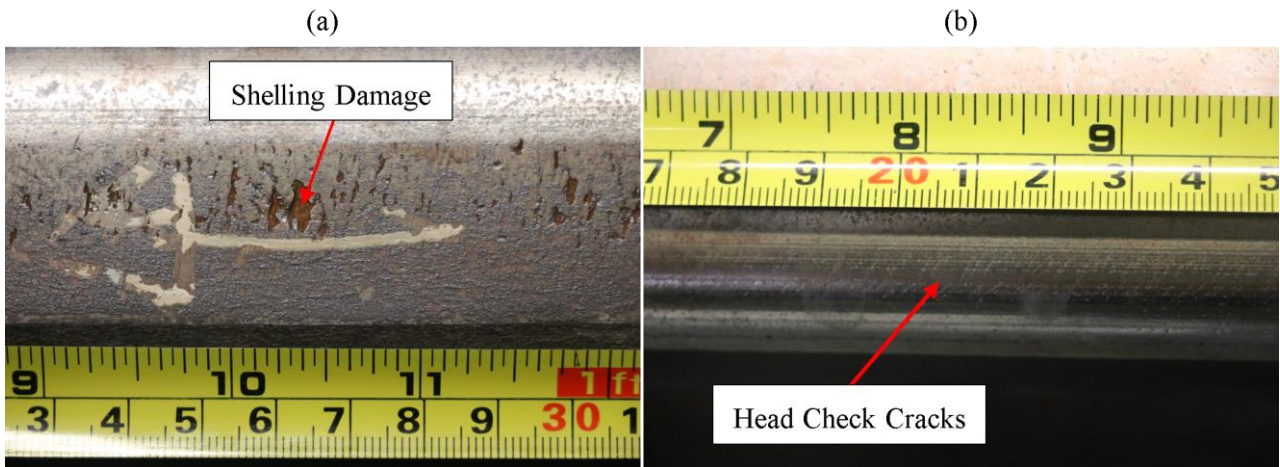


Figure 1.3: Image of (a) shelling and (b) head check crack damage observed on the railhead of a used rail section removed from a metro system.

The accumulation of damage from these mechanisms are undesirable as both can affect the integrity of a rail steel and the safe running of a railway network. Wear damage can change the rail profile and widen the track gauge, potentially leading to dynamic issues; whereas RCF damage left unchecked can cause rail breakages and shelling. To remove these two forms of damage or their effects, expensive track maintenance programmes (grinding/milling/weld repair/replacement) are normally undertaken. For example, during the 2020/21 financial year the cumulative track renewal expenditure by Network Rail in the UK was £1,207m [10]. The presence of wear damage, however, can be beneficial in helping to remove RCF damage from the running surface of a rail steel [11], considering the relatively more difficult nature of RCF damage in terms of monitoring and prediction compared to wear damage. In addition, compared to wear, RCF damage is more likely to cause unpredictable rail breakages.

The combination of high compression and shear stress that rail steels are typically subjected to during rail-wheel contacts can produce large amounts of plastic deformation localised on the surface of the rail head, as shown in Figure 1.4. This plastic deformation is known to be the cause of significant incidences of wear and rolling contact fatigue (RCF) damage mechanisms in rail [12]. A major focus of this thesis is, therefore, to better understand the behaviour of modern rail steel grades under rail-wheel contacts. This was accomplished by examining wear performance, evolution of surface roughness, and the change in plastic deformation from hardness and shear strain measurements subsurface for modern rail steel grades. The data collected about the change in plastic deformation also allowed other material information to be obtained that are suitable input for simulation methods such as the layer-based [13] and brick-based [14] plastic ratcheting simulation models. These include the shear stress-strain curve, shear strain at failure (limit of accumulative shear strain that can occur

before the nucleation of voids and microcracks), and the ratcheting load conversion factor (conversion factor between the ratcheting load and incremental shear strain). This information was collected for the first time to the authors knowledge from harder premium rail steel grades. In addition, verification of conventional rail steel performance was also conducted to provide a baseline for comparison against the information obtained from the premium rail steels

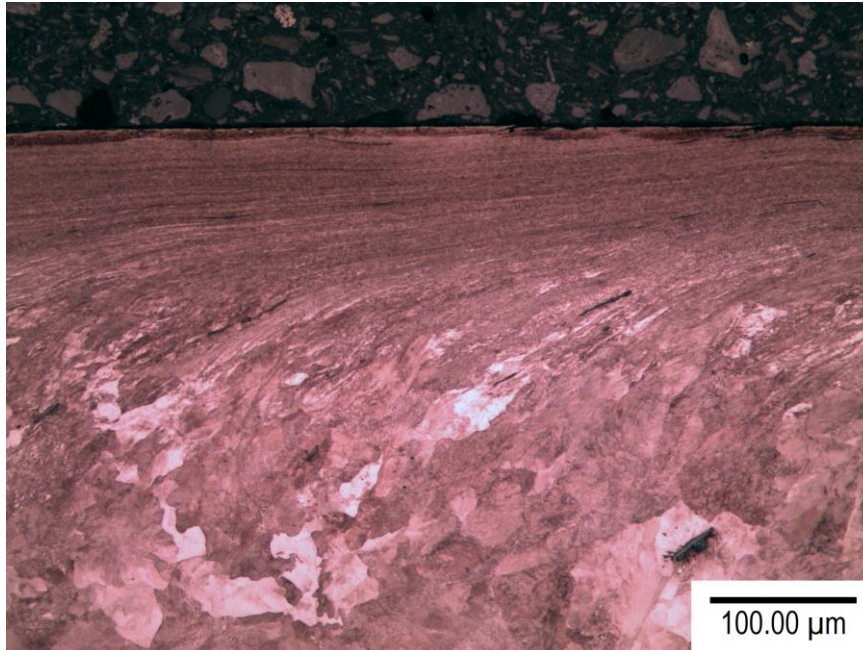


Figure 1.4: Optical micrograph of the near surface plastic deformation observed beneath the running track of an R260 rail steel sample using a small-scale twin-disc machine. The plastic damage shown is typical of what usually found in actual rail removed from track that is produced by the cyclic interaction of rail-wheel contacts.

In terms of experimental testing to understand the performance of rail steels, small-scale twin-disc tests provide a good balance between accurately representing the rail-wheel contact, accessibility, and affordability. The limitation of these small-scale twin-disc tests, however, is that information about the rail steels plastic deformation behaviour, wear and RCF damage development is only obtained after a test is interrupted or has finished. This provides a record of the rail steels material response only intermittently. Moreover, it can be prohibitively expensive to conduct separate tests of different contact cycle durations to fully quantify material behaviour. The in-situ optical monitoring of the twin-disc sample running surface during experiments while rotating at about 400 rpm is an untried technology solution that has been identified, which is also explored in this thesis. The potential for an in-situ optical monitoring system provides the unique opportunity to monitor in real time the surface material plastic flow and the initiation and development of damage, such as wear flakes and RCF cracks.

Overall, an improved quantification of the rail steels response to load can, therefore, allow the selection of rail steel grades to be better targeted to the duty they will experience in track. As for rail network operators, maximising the service life of rail helps to create a rail network with a lower maintenance requirement and carbon footprint linked to the steel's production. However, for rail manufacturers, such as British Steel Ltd, predicting the accumulation of rail steel damage is important to allow them to better serve their customers. In addition, it can support the installation of premium rail steel grades through better understanding their application and eventual failure modes.

1.2 Research Aim and Areas of Focus

The overarching aim of this research project is to expand the knowledge and understanding of how plastic damage develops in rail steels due to the cyclic interaction of rail-wheel contacts. The information collected will help drive and improve simulation models that predict the service life of rail steels. The work presented in this thesis can be broken down into the following two areas of focus based on the gaps identified in the literature.

1. Characterisation of Rail Steel Plasticity:

This part of the thesis explored how new and existing analysis techniques could be developed to enable the better characterisation of the plastic deformation behaviour of modern rail steel grades from twin-disc testing. In addition, this section looked into how this information could be obtained more efficiently so that as few twin-disc tests as possible were required to derive this data. A comparison of the material information collected was then performed to examine the influence of different rail steel metallurgies and maximum Hertzian contact pressures.

2. Visual Observation of the Surface Damage Evolution on Rail Steels:

The development of a novel optical monitoring system for twin-disc testing was explored for this section of work. The system was developed with the aspiration of visualising the surface morphological change of surface defects associated with the accumulation of shear strain in rail and the development of wear flakes and RCF cracks in-situ during twin-disc tests. This equipment was then used to examine what new information could be derived about rail steel plastic damage development. In addition, the evolution of rail steel plastic damage for different rail steel grades was also investigated.

The work presented in this thesis presents some of the collaboration work undertaken between the University of Sheffield and British Steel Ltd under the umbrella of UKRRIN (UK Rail Research Innovation Network). The UKRRIN framework has enable investment into new experimental

equipment for this collaboration, such as the SUROS2 (Sheffield University Rolling Sliding 2) twin-disc machine, Bruker Hysitron TS77 select nanoindenter, and Alicona PortableRF infinite focus microscope. Both this collaboration and investment have been indispensable in allowing the research questions mentioned above to be explored in this thesis.

1.3 Structure of Thesis

The background and justification for conducting this research project has been given in this preliminary chapter. The content of the following chapters in this thesis are as follows:

Chapter 2 – Literature Review

A literature review is presented in chapter 2 exploring the current understanding of rail-wheel contact mechanics, rail steel metallurgy, plastic deformation behaviour, development of wear and RCF damage, and experimental approaches for testing rail steels. Following this literature survey, a summary of the gaps identified in this academic field will be presented to contextualise the areas of focus in this research project.

Chapter 3 – Characterisation of Rail Steel Plastic Deformation Behaviour

In chapter 3, the plastic deformation behaviour of rail steel was characterised from data gathered from experimental twin-disc tests. The information derived in this chapter includes the shear stress-strain curve and the ratcheting load conversion factor, which is the conversion factor between the ratcheting load experienced by a material and the plastic shear strain accumulated. The methodology of determining the ratcheting load conversion factor have been updated in this work to improve efficiency and enable this parameter to be determined for premium rail steel grade which experience little bulk plastic damage. The experiments performed in this investigation allowed this material information to be compared across the three different rail steel grades R260, HP335, and R350HT under the same contact conditions. In addition, a comparison of this material information derived from R260 when loaded under different maximum Hertzian contact pressure was also examined. The intention for these different contact pressure tests was to understand whether the material information derived are ‘material property’ or ‘system behavioural’ information, in which are only valid for specific contact conditions.

Chapter 4 – Derivation of the rail steels shear strain at failure

The derivation of the shear strain at failure of the rail steel twin-disc samples tested in chapter 3 was explored in chapter 4. To determine the shear strain at failure, the development of a new optimisation process was explored based on comparing the wear depth estimated using an implementation of the

brick-based plastic ratcheting simulation model against the experimental observations. Like the work presented in chapter 3, a comparison of the shear strain at failure calculated for the three different rail steel grades R260, HP335, and R350HT under 1500 MPa, dry contact conditions were undertaken. Furthermore, the shear strain at failure determined for R260 loaded under different maximum Hertzian contact pressure was also examined.

Chapter 5 – Development of a novel optical monitoring system for twin-disc testing

A novel optical monitoring system for twin-disc testing was developed in chapter 5. This new system enables observation of the surface morphological development of damage on a twin-disc sample running track in-situ during experiments while rotating at about 400 rpm. After development preliminary tests were conducted to explore the capabilities of this new equipment in allowing wear flakes and RCF cracks to be observed during dry and water lubricated contact experiments. Image analysis was also performed to understand how the information derived from the captured photographs compares to wear rate results collected in chapter 3.

Chapter 6 – Real time observation of plastic damage development in rolling contact of steels

The optical monitoring system developed in chapter 5 was used in chapter 6 to photograph in-situ the evolution of plastic damage during twin-disc testing of the three rail steel grades R260, HP335, and R350HT under identical contact conditions. A comparison of the wear flake morphology and development observed from the three rail steel materials was conducted. Furthermore, the development of individual wear flakes was also monitored to investigate what new information can be gathered about the process involved in wear flake initiation, development, and eventual removal as wear debris. The surface material flow observed during the R260 experiment was also tracked and compared to the simulation results generated using an implementation of a layer-based plastic ratcheting simulation model originally developed by Kapoor et al. [13] that utilised the material data generated in chapter 3.

Chapter 7 – Conclusions and recommendations for further work

A summary of the conclusions derived from the results generated from this work is given in chapter 7. In addition, a recommendations list is provided suggesting areas of further work that could be explored outside of this thesis.

1.4 Contribution

The primary contribution of this research project was the new optical monitoring system developed for twin-disc testing. The images acquired from this equipment have provided to the authors

knowledge the first in-situ visual observation of wear flake and RCF crack development and surface material flow of rail steel loaded under cyclic rolling sliding contact conditions. The quality of results obtained directly by this system and the analysis techniques developed alongside it has opened new ways of understanding experimentally the development of plastic damage on rail steel. In addition, the information already collected about wear flake evolution has also provided a unique insight into how they initiated, develop, and eventually detach as wear debris.

This research project has also provided new and updated approaches for characterising the plastic deformation of the rail steel from twin-disc tests. This helps to minimise the number of samples needed and allow the characterisation of modern premium rail steels that experience little bulk plastic deformation. The results collected have also provided new material information for rail steels grades that have not before been characterised in a way that is suitable for input to plastic ratcheting-based simulation models.

Chapter 2: Literature Review

2.1 Introduction

This literature review will first familiarise the reader with key details involved with rail-wheel contacts and the metallurgy of rail steels produced and used in the UK. The changes observed in the rail steel microstructure due to the accumulation of shear strain in the near surface plastic damage region resulting from repeated rail-wheel contacts is next investigated. The plastic shakedown theory is later explored to establish the theoretical understanding surrounding how shear strain accumulates in rail steels and how simulation models implement this theory. This is followed by an examination of the initiation and development of wear and RCF damage commonly observed in rail steels. The factors influencing the decision of which rail steel to use for a particular track section and the Ty model will then be discussed next. This will be concluded afterwards with a consideration of the different experimental techniques currently undertaken to test rail steels, with a significant emphasis on twin-disc testing.

2.2 Rail-Wheel Contact Geometry, Forces and Vehicle Dynamics

A railway wheelset, as shown in Figure 2.1, consists of two wheels featuring a small cone angle on the tread connected by a common axle. This cone angle coupled with lateral shift of the wheelset help provides the wheelset's steering mechanism when negotiating curves.

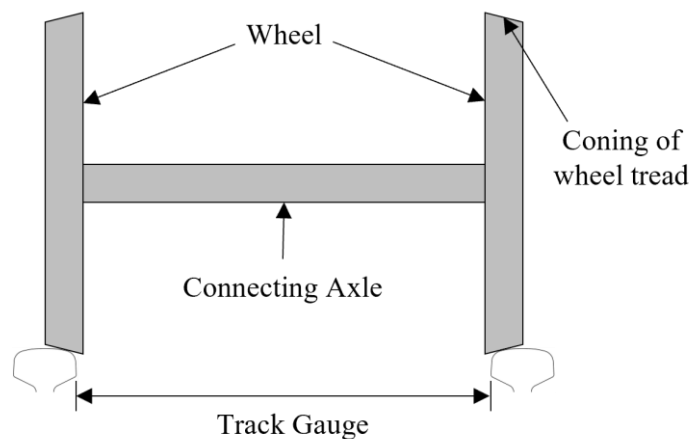


Figure 2.1: Illustration of a railway wheelset.

2.2.1 Normal Contact Pressure

The interaction between a rail and a wheel in-service typically occurs over a small contact area approximately 1cm^2 in size [15]. This small contact area, therefore, leads to the creation of high

normal contact pressures being exerted onto the rail running surface. The magnitude of the maximum contact pressure is dependent on the load transmitted through the contact, the geometry of the rail and wheel, and the rail vehicle system dynamics. For a train travelling on a straight or light curve track section, maximum contact pressures between 600-1500 MPa are commonly observed [16]–[19]. In some cases, however, such as the rail-wheel contact interaction on switch and crossing components or tight curves, it is not unusually for the maximum contact pressures to reach as high as about 3600 MPa [16], [20].

Three types of rail-wheel contacts can be categorised depending upon the location of where this interaction occurs on the railhead, as shown in Figure 2.2. The three categories of rail-wheel contacts are as follows [21]:

- Region A contacts – refers to the rail-wheel interaction on the central portion of the wheel tread and rail head, which is commonly encountered on straight or mild curve track sections. The contact pressures observed are the lowest out of the three categories, with longitudinal creep comparatively more significant than lateral creep.
- Region B contacts – denotes the rail-wheel interaction on the rail gauge corner and wheel flange. These typically occur on tight curve sections, location of poor track alignment, and areas of rail running profile discontinuities (switches, crossings, rail joints). A single point contact in this region is characterised by high contact pressures, spin creep, and high longitudinal creep. A two-point contact in this region is generally attributed with high wear rates and material flow due to the high degree of slip that occurs in one of the contacts. Overall, all region B contacts possess high angles of attack and lateral creep, and compared to region A contacts also possess higher contact pressures.
- Region C contacts – represents the rail-wheel interaction on the field side of the rail and wheel, which rarely happens but can take place due to the development of hollow wheels and improper track separation. Region C contacts compared to region A contacts also possess higher contact pressure and higher longitudinal creep, which unfavourable provide improper steering of the wheelset.

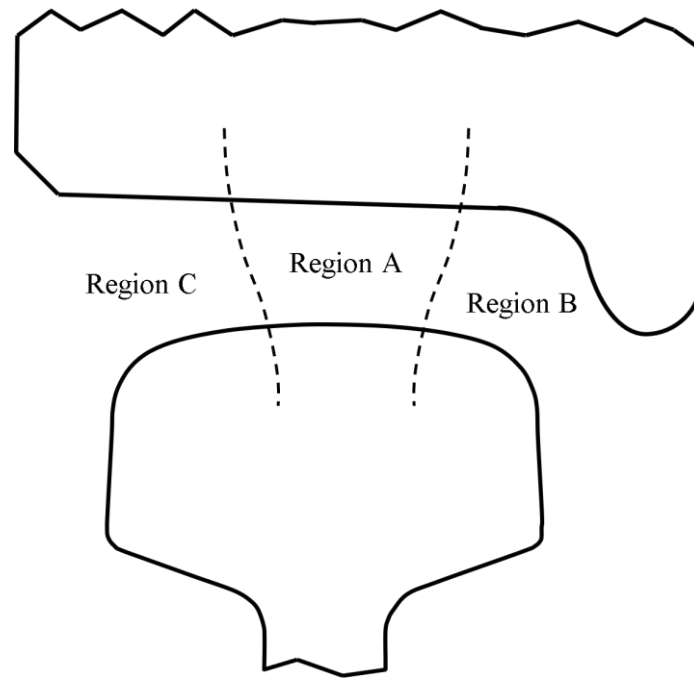


Figure 2.2: Illustration of the three main contact zones in rail-wheel contacts.

Hertzian's contact theory is a regularly utilised contact model used to estimate the contact stresses encountered within the rail-wheel contact. This theory assumes the rail and wheel are perfectly smooth and idealises the finite contact area between two perfectly elastic non-conformal curved bodies touching and being loaded together as an ellipse. The normal contact pressure created also follows a semi-elliptical distribution [22]. For application with rail-wheel contacts this has usually been done by simplifying the complex geometry of these two bodies down to a 2D representation of a roller on a flat surface, as illustrated in Figure 2.3 [23]. This approach treats the rail-wheel interaction as a line contact, whereby the contact half-width dimension, b , and maximum Hertzian contact pressure, p_0 , can be evaluated using Equations 2.1 and 2.2, respectively.

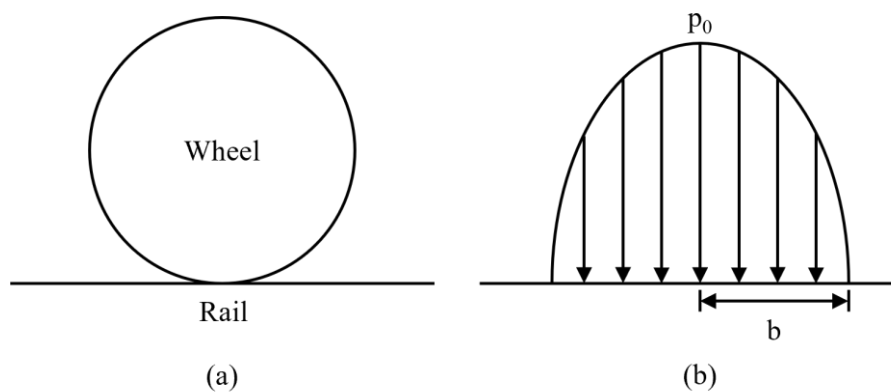


Figure 2.3: (a) Simplified 2D representation of the rail-wheel contact as a roller on a flat surface and (b) contact pressure distribution derived for a Hertzian line contact.

$$b = \sqrt{\frac{4PR}{L\pi} \left(\frac{1 - \nu_r^2}{E_r} + \frac{1 - \nu_w^2}{E_w} \right)} \quad \text{Equation 2.1}$$

$$p_0 = \frac{2P}{L\pi b} \quad \text{Equation 2.2}$$

where P is the contact load, R is the reduced radius of curvature, L is the contact length, E_r and E_w is the rail and wheel young's modulus, and ν_r and ν_w are the rail and wheel Poisson ratio. The shape of the pressure distribution and contact area created in actual rail-wheel contacts, however, is more complicated than the ideal solution generated by Hertzian's contact theory. Alternatively, a range of numerical methods have been developed by Kalker, such as the simplified and exact theorem, to provide a better estimate to the rail-wheel contact problem. In addition, the dedicated programs FASTIM and CONTACT have been created based around these theories [24]. However, despite providing a more accurate solution, the work presented in this thesis has primarily use the Hertzian contact model. This was due to providing a more generalised representation of rail-wheel contact not heavily influenced by rail and wheel condition and the wheelset lateral position. On top of the high computational cost associated with Kalker's theories, which makes them impractical to use when simulating many rail-wheel contact passes.

2.2.2 Friction and Tangential Contact Stresses

During actions of acceleration, deceleration, or maintaining speed on a gradient, the driving wheels on a rail vehicle rotate faster or slower relative to the train's translational velocity. This is characterised by the parameter 'longitudinal creep' or 'slip', which is defined as the ratio of the sliding velocity (difference between train and rolling velocity) over the train's translational velocity. The presence of longitudinal creep induces tangential forces within the rail-wheel contact, in which the magnitude is related to the normal contact force via the traction coefficient [15]. The traction coefficient is related to the longitudinal creep by Carter's creep force law [25], in which states that the traction coefficient is zero for pure rolling contact while limited by the friction coefficient for full sliding contacts. An illustration of the idealised longitudinal creep against traction coefficient relationship described by Carter's creep force law is shown in figure 2.4. Experimental studies [26]–[29], however, have shown that the traction coefficient does not always plateau with increasing longitudinal creep after the onset of full-sliding conditions within the rail-wheel contact. Instead, the traction coefficient has been observed in some cases to continue increasing or start to decrease with increasing longitudinal creep known as positive or negative friction behaviour, respectively.

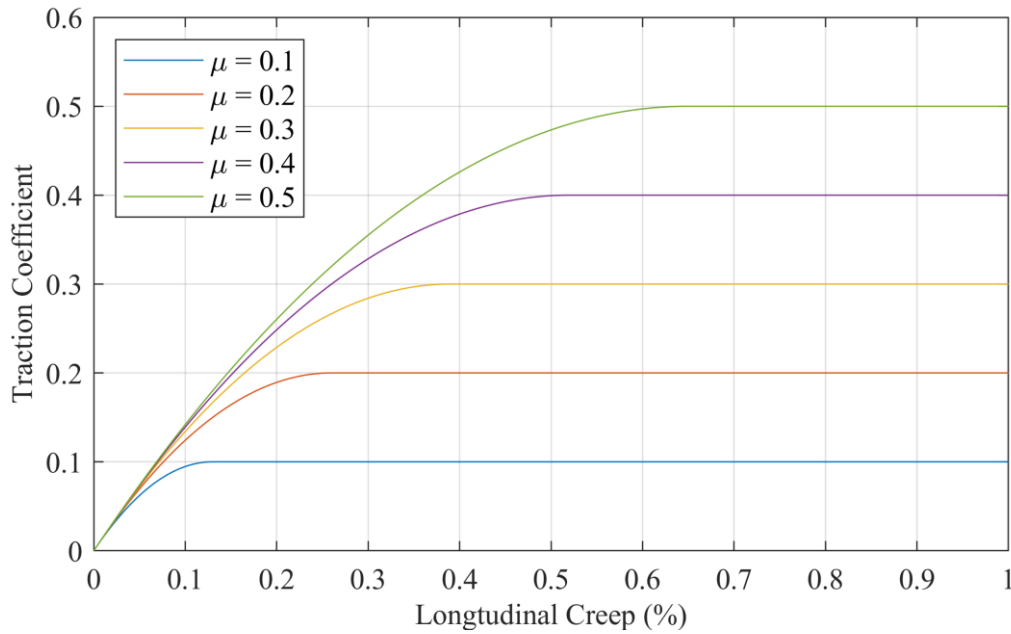


Figure 2.4: Idealised longitudinal creep against traction coefficient curve described using Carter’s creep force law for a rail-wheel contact.

The open tribological nature of rail-wheel contact means that the interfacial interaction between a rail and wheel is influenced by the presence of contaminants and environmental conditions. This includes water, oil, grease, relative humidity, leaf mulch, top of rail friction modifiers, and sand, which can all reduce or increase the limiting friction coefficient by differing amounts. For dry rail-wheel contact conditions the friction coefficient has typically been found to range between 0.4-0.6 [30]–[32]. The product of the tangential tractive force T and the creep γ in the longitudinal and lateral direction of a rail-wheel contact known as T-gamma, is a commonly used parameter utilised to understand the severity of damage induced by a rail-wheel contact, which will be revisited later on in Section 2.8. This parameter represents the energy expended through a contact by creepage [33].

2.2.3 Subsurface Orthogonal Shear Stress

Beneath the rail running surface, the interaction of rail-wheel contacts exposes material to orthogonal shear stresses. For pure rolling contacts, both the positive and negative peak of the orthogonal shear stress distribution are located subsurface. The magnitude, horizontal and vertical location relative to the contacts centre at the surface is given by $0.25p_0$, $\pm 0.87b$ and $0.5b$, respectively [34] as shown in Figure 2.5. The presence of friction within the rail-wheel contact influences the magnitude and location of these orthogonal shear stress peaks. As one peak would move towards the running surface and intensify in magnitude while the other peak would migrate deeper beneath the surface and diminish in magnitude with increasing friction. When the friction coefficient exceeds roughly 0.3, one of the orthogonal shear stress peaks would then become located at the surface of the rail [22].

Expressions of the subsurface orthogonal shear stress distribution based on Hertzian contact model accounting for friction have been created by M'Ewen [35], given as Equations 2.3-2.5.

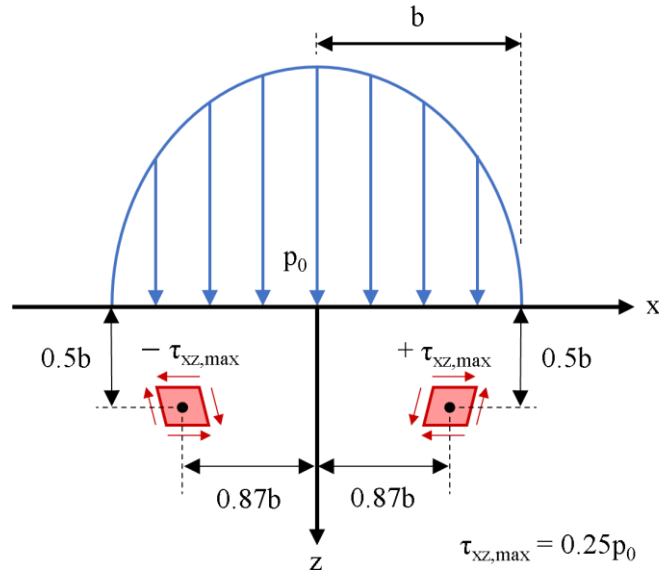


Figure 2.5: Illustration showing the magnitude and location of the maximum orthogonal shear stress for a pure rolling line contact

$$\tau_{xz} = \frac{p_o}{b} \left[n \left(\frac{G^2 - z^2}{G^2 + F^2} \right) + \mu \left(G \left(1 + \frac{z^2 + F^2}{G^2 + F^2} \right) - 2z \right) \right] \quad \text{Equation 2.3}$$

$$G^2 = \frac{1}{2} \left[\sqrt{(b^2 - x^2 + z^2)^2 + 4x^2z^2} + (b^2 - x^2 + z^2) \right] \quad \text{Equation 2.4}$$

$$F^2 = \frac{1}{2} \left[\sqrt{(b^2 - x^2 + z^2)^2 + 4x^2z^2} - (b^2 - x^2 + z^2) \right] \quad \text{Equation 2.5}$$

where z is the depth below the running surface, x is longitudinal distance from the centre of the contact, and μ is the coefficient of friction within the contact.

2.2.4 Influence of Surface Roughness

Like all engineering components, the running track of the rail and wheel are never perfectly smooth and always exhibit some degree of surface roughness. The implication of this surface roughness is that the bulk rail-wheel contact is made up of multiple micro contacts due to the interaction happening between asperities. The relatively smaller contact area of these individual asperity contacts creates normal contact pressure spikes, which in turn produces significantly higher orthogonal shear stresses localised near the surface of a rail. This has the effect of increasing the rate of strain accumulation in a shallow surface layer of rail steel material compared to if the rail-wheel contact is perfectly smooth.

In addition, to causing surface plastic damage to still occur even when the stresses of a smooth rail-wheel contact are insufficient to generate plastic deformation [36], [37].

A variety of different numerical approaches have been developed to estimate the stresses generated within a rough contact. These different approaches can be categorised into the following two groups: i) uniform asperity morphology rough contact models and ii) fractal rough contact models.

2.2.4.1 Uniform Asperity Morphology Rough Contact Models

The Greenwood-Williamson model [38] is one of the earliest and commonly used stochastically methods that applies to the contact between one smooth and one rough flat elastic plane. The model considers the uniform asperity tip radius, asperity height gaussian distribution, and asperity area density to derive the real contact area fraction and average real contact pressure between the two planes. Extensions of the Greenwood-Williamson model have been made to introduce an asperity tip radius gaussian distribution on top of the asperity height gaussian distribution already existing in the original method [39]. In addition, to expanding the application of this method to two flat rough planes with their own distinct asperity height gaussian distributions [40]. The inclusion of the principle of volume conservation of plastically deformed asperities has also investigated in the Chang-Etsion-Bogy model [41] in an attempt to improve the estimate during low contact loads. However, issues with the Chang-Etsion-Bogy model have been raised about the inaccurate results it generates for certain conditions [42]. The addition of the effect of asperity interaction into the Greenwood-Williamson models has also been explored in the ref. [43]–[46] to also help improve the model output under low and intermediate contact loads. The application of the Greenwood-Williamson model to a cylinder on plate contact has also been explored in the Greenwood-Tripp model [47]. The results generated provides the average statistical normal contact pressure distribution for a rough line contact. In comparison to Hertzian solution, the normal contact pressure distribution generated by the Greenwood-Tripp model is bell shaped rather than semi-elliptical, as shown in Figure 2.6. This bell-shaped normal contact pressure distribution does approach the semi-elliptical Hertzian pressure distribution at higher normal contact loads. One issue with the Greenwood-Tripp model is that this method is only applicable when a high number of asperity interactions occurs with the bulk contact. This would be problematic for simulating small contacts, such as a twin-disc contact, where the discs are expected to interact via a small number of asperity contacts. In additions, the results generated by all these stochastically methods only give a statistical estimate of the normal contact pressure distribution. They do not look at the subsurface orthogonal shear stress distribution, which is crucial for understanding the subsurface plastic deformation behaviour of rail steels.

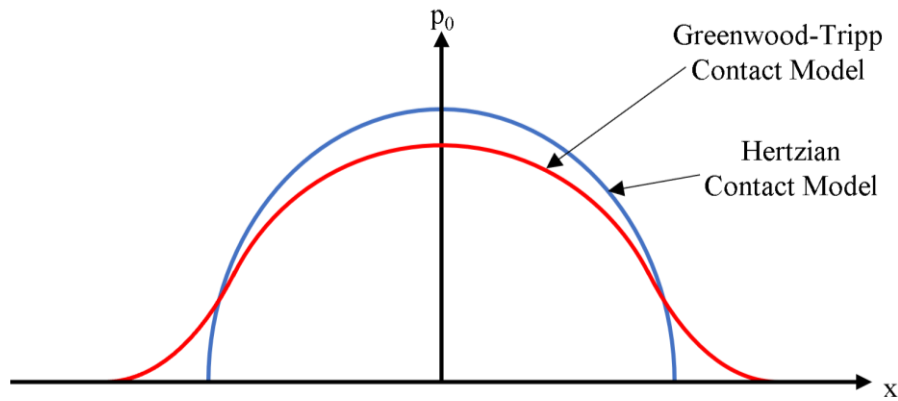


Figure 2.6: Illustration showing the general comparison of the bell-shaped normal contact pressure distribution estimated by the Greenwood-Tripp model in comparison to the semi-elliptical contact pressure distribution derived from the Hertzian contact model for the same contact conditions.

The Nowell-Hills roughness model [48], [49] is an alternative analytical method developed to simulate the rough contact of a 2D smooth cylinder on a rough flat plane. In this method, the random geometry of the roughness profiles is simplified by regular periodic asperities with the same asperity tip radius ρ and separation λ , as illustrated in Figure 2.7. The results generated is an array of the contact half-width b_a and maximum Hertzian contact pressure p_a for each asperity contact that occurs within the bulk contact, as shown in Figure 2.8. The maximum Hertzian contact pressure and contact half-width dimensions determined can then be placed into the Equations 2.3-2.5 to obtain the orthogonal shear stress distribution contribution for each asperity contact. An orthogonal shear stress distribution for the entire rough contact can then be generated by summing the contributions from each asperity, see Figure 2.9. In comparison to the statistical Greenwood-Tripp model, the Nowell-Hills model is applicable to simulating rough contacts with relatively few asperity interactions, such as a twin-disc contact. A limitation of this approach, however, is that the location of the asperities needs to be symmetrical and does not allow the asperities to simulated with an offset.

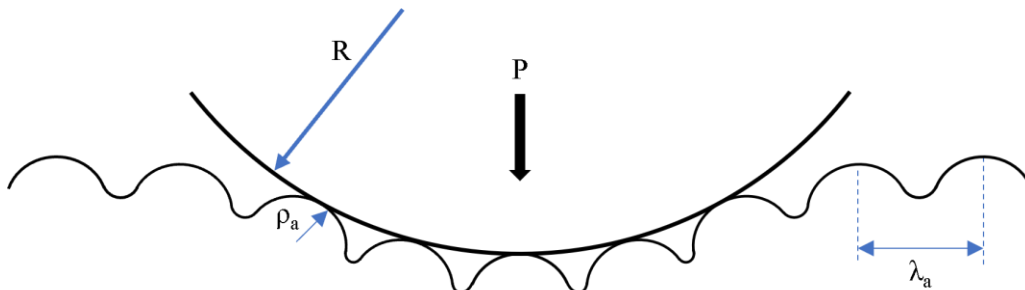


Figure 2.7: Illustration of a 2D smooth cylinder on an idealised rough flat plane with regular periodic asperities with the same asperity tip radius ρ and separation λ as represented in the Nowell-Hills roughness model.

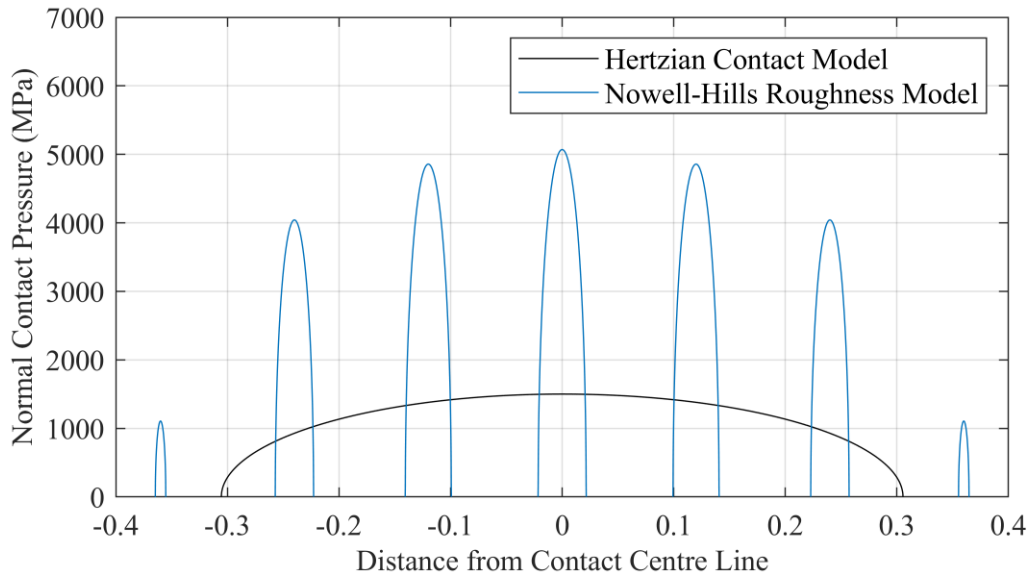


Figure 2.8: Plot comparing the normal contact pressure distribution estimated for a rough contact using the Nowell-Hills Roughness Model and the smooth contact pressure distribution given by Hertzian contact model. The distributions shown are for a pair of 47 mm diameter twin-disc samples loaded under a nominal maximum Hertzian contact pressure of 1500 MPa with a rough surface with an asperity separation and tip radius of 120 μm and 250 μm , respectively.

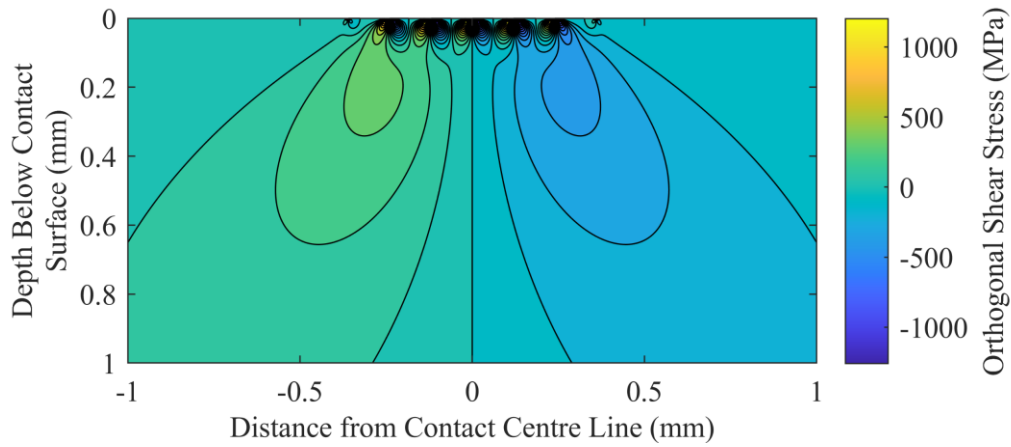


Figure 2.9: Plot of the subsurface orthogonal shear stress distribution calculated for a pair of 47mm diameter twin-disc samples loaded with a nominal maximum Hertzian contact pressure of 1500 MPa with no traction using the Nowell-Hills model with an asperity separation and tip radius of 120 μm and 250 μm , respectively.

2.2.4.2 Fractal Rough Contact Models

Fractal-based rough contact models differ from the uniform asperity morphology rough contact models mentioned in the previous subsection by accounting for the different scales of surface roughness simultaneously. One of the earliest iterations of a fractal rough contact model is the

Majumdar-Bhushan model [50]. In this model, the rough surface topography is characterised using the Weierstrass-Mandelbrot fractal function based on power spectral density data of a rough surface. The contact area of each interaction is then determined by truncating the rough profile at a constant height. The load on each contact patch is subsequently derived using either Hertzian's contact model or by assuming the pressure is equal to the conventional hardness for the purely elastic or elastic-plastic deformation behaviour, respectively. A controversial output from this approach is that due to the assumption asperities completely deform and the critical contact area is only scale dependent, the model predicts plastic deformation to precede elastic deformation of asperities with increasing contact load. A revised model by Morag and Etsion [51] fixes this counterintuitive aspect for the case of a single fractal asperity by making the critical interference, contact area, and contact load all scale dependent. This has been further expanded upon by Miao and Huang [52] to consider the entire rough contact based on this model. The universal power law relationship used in the original model was replaced with a size distribution function valid for elastic, elastoplastic, and fully plastic deformation individually developed for surfaces with elliptic asperities by Chung and Lin [53] to better predict the number of interaction in the rough contact. The Majumdar-Bhushan model was originally developed as a 2D model, however, other studies [54] have expanded upon this to predict a 3D rough contact using a 2D version of the Weierstrass-Mandelbrot fractal function.

Persson diffusion contact model [55], [56] is another fractal-based method that uses diffusion theory to estimate the rough contact output based on the overall idea that contact pressure diffuses through the different scale of surface roughness. In this approach, the interfacial contact pressure is described using a parabolic partial differential equation with the diffusivity term approximating that the power spectral density of the elastically deformed surface is equal to the undeformed surface. The assumption that the power spectral density of the deformed surface is equal to the product of the undeformed surface power spectral density and contact area fraction is then used to calculate the stored elastic energy. A common issue raised about Persson diffusion contact model is that it is difficult to follow and implement. There are simplified forms of this rough contact models, however, that have been formulated by Hyun et al. [57] and Carbone and Bottiglione [58]. Persson [55], [56] has stated that their rough contact model is exact for the case of full-contact conditions, however, a comparison of different analytical and numerical rough contact models by Xu and Jackson [59] has made this debatable.

The stacked multi-scale model is a rough contact method based on the concept by Archard and Allibone [60] of progressively stacking smaller spherical asperities to model the fractal nature. In the model developed by Ciavarella et al. [61], the rough surface are represented by the superposition of sinusoid, known as a Weierstrass function, and is solved elastically using a Westergaard solution.

Gao and Bower [62] has expanded upon Ciavarella et al. [61] 2D stack multi-scale model through adding elastic-plastic deformation behaviour into this approach. The model proposed by Jackson and Streater [42] also used the same idea by Archard and Allibone [60], however, characterises the fractal nature of the rough contact using a Fourier series.

Out of the rough contact models mentioned, the effect of surface roughness on the stresses generated within the rail-wheel contact would be considered in the work presented later on in this thesis by using the Nowell-Hill rough contact model [48]. This rough contact model was chosen based on the desirability criteria that the selected model needed to allow the calculation of the rough contact subsurface orthogonal shear stress with low computing load, so that it can be utilised over many contact cycles. In terms of suitable pre-existing surface data available in the literature for the running surface of rail steels, the asperity tip radius and separation was measured by Kapoor et al. [37] on both the running surface of a turned and a ground and polished JIS E1101 rail steel twin-disc sample. Their measurements recorded an average asperity tip radius of 130 μm and an asperity separation of 20 μm for the ground and polished specimen. The turned sample, however, had an average asperity tip radius of 92 μm and asperity separation of 12 μm . The cyclic variation of the asperity tip radius and separation has also been measured by Tomlinson [63] for the running surface of an R260 twin-disc sample subject to 1500 MPa, 1% slip, dry contact conditions. Their results presented in Figure 2.10 showed that both the asperity tip radius and separation generally increased overall compared to the unused sample, however, there is a lot of variation in the data.

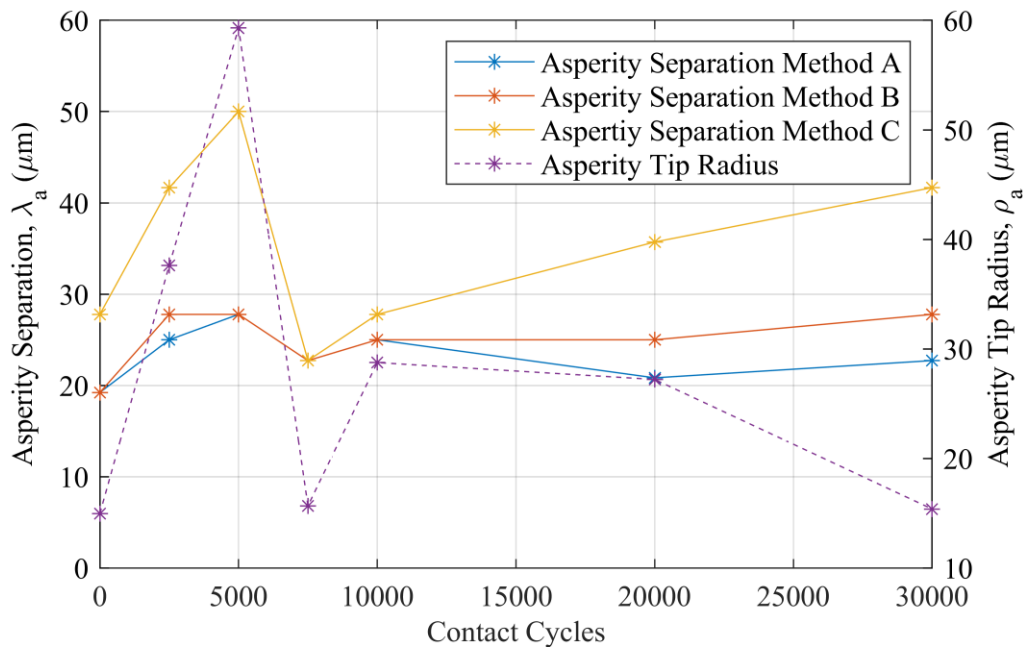


Figure 2.10: Cyclic variation of the asperity tip radius and separation results measured from R260 rail steel samples subject to 1500 MPa, dry contact conditions recorded by Tomlinson [63].

2.3 Rail Steel Metallurgy

The introduction of the Bessemer process in 1856, helped drive the first adoption of steel rail and the significant transition from wrought iron to steel during the 1870s [64], [65]. The steelmaking of rail steels used today is carried out using either the basic oxygen furnace (BOF) or electric arc furnace (EAF) process. The liquid steel produced by either process is subsequently turned into blooms via continuous casting. After the blooms have cooled, they are reheated, rolled to the correct profile, air-cooled at a controlled rate, and then straightened [66], [67].

In the UK, most of the rail steels used are as rolled with a medium/high carbon composition. This produces a rail steel that consists of entirely pearlite or pearlite with proeutectoid ferrite along the prior austenite grain boundaries. The volume fraction of proeutectoid ferrite present decreases with increasing carbon content and becomes non-existent at the eutectoid composition (≈ 0.77 wt% C). The pearlite is a lamellar morphology of soft, ductile ferrite (α -Fe) and hard, brittle cementite (Fe_3C). This pearlite morphology is favourable for rail steels due to its relatively low manufacturing cost, adequate strength and wear properties, and high work hardening capacity [68]. Furthermore, soft, ductile MnS inclusions are also present as elongated ‘stringers’ orientated along the rails longitudinal direction [69].

The three main microstructural features that affect the mechanical properties of rail steels are the interlamellar spacing, prior austenite grain size, and pearlite colony size; in which are all influenced by the rail steels thermomechanical processing and chemical composition. Refining the interlamellar spacing has been observed to increase the rail steels yield strength, ultimate tensile strength, ductility, and cleavage fracture stress [70]–[73]. A smaller pearlite colony has been found to increase the rail steels yield strength, ultimate tensile strength, ductility, fracture toughness and cavitation erosion resistance [73]–[75]. The reduction of the prior austenite grain size has tended to increase the ductility and fracture toughness of rail steels [72], [75], [76]. Experiments conducted by Li et al. [77] found that rail steel wear resistance was most heavily influenced by the pearlite colony size, followed by the pearlite interlamellar spacing, and then the prior austenite grain size. The order of greatest influence for rolling contact fatigue damage was the pearlite interlamellar spacing, followed by the pearlite colony size, and then the prior austenite grain size.

The chemical composition and mechanical properties of rail steel grades used in the UK, according to rail technical standards are present in Tables 2.1 and 2.2, respectively. As with other steels, the most important alloying element of rail steel is carbon. This element has been shown to help improve hardness and tensile strength but detrimentally reduces ductility and toughness of steels with increasing concentrations [78]. Other alloying elements include silicon that has been found to help

strengthen ferrite by solid solution strengthening [79] and inhibit the formation of grain boundary cementite in hypereutectoid steels [80], [81]. Manganese has been observed to aid solid solution strengthening of ferrite, refine the pearlite interlamellar spacing and prior austenite grain size [79] and combines with sulphur to create MnS inclusion and eliminate sulphurs embrittling effect [82]. Chromium has been demonstrated to assist in refining the pearlite interlamellar spacing and decrease the eutectoid transformation temperature [83], [84]. The addition of aluminium has been found in small quantities to facilitate as a deoxidation agent to control oxygen and hydrogen levels in steel [85]. The addition of vanadium has been shown to help increase the hardness and tensile strength of steel; however, there are conflicting statements of whether this was due to the precipitation of vanadium carbonitrides in ferrite [86], [87] or enrichment of the cementite lamellae [88]. Finally, both sulphur and phosphorus have been found to be impurity elements present in all steels that originate from the steelmaking process and detrimentally embrittling the steel [85].

Table 2.1: Chemical composition requirements for as-rolled, heat-treated and bainitic rail steel grades used on the UK rail networks, according to the rail steel specifications [66], [89].

| Rail Grade | C | Si | Mn | P | S | Cr | Al | V | H ₂ (ppm) |
|-------------------|----------------|----------------|----------------|---------|-----------------|----------------|---------|----------------|-------------------------|
| As-Rolled Rail | | | | | | | | | |
| R200 | 0.40 / 0.60 | 0.15 / 0.58 | 0.70 / 1.20 | ≤ 0.035 | ≤ 0.035 | ≤ 0.15 | ≤ 0.004 | ≤ 0.03 | ≤ 3.0 |
| R260 | 0.62 / 0.80 | 0.15 / 0.58 | 0.70 / 1.20 | ≤ 0.025 | ≤ 0.025 | ≤ 0.15 | ≤ 0.004 | ≤ 0.03 | ≤ 2.5 |
| HP335 | 0.87 / 0.97 | 0.75 / 1.00 | 0.75 / 1.00 | ≤ 0.020 | 0.008 / 0.02 | ≤ 0.10 | ≤ 0.004 | 0.09 / 0.13 | ≤ 2.0 |
| Heat-Treated Rail | | | | | | | | | |
| R350HT | 0.70 / 0.82 | 0.13 / 0.60 | 0.65 / 1.25 | ≤ 0.025 | ≤ 0.030 | ≤ 0.15 | ≤ 0.004 | ≤ 0.03 | ≤ 2.5 |
| MHH | 0.72 / 0.82 | 0.40 / 0.80 | 0.80 / 1.10 | ≤ 0.020 | ≤ 0.020 | 0.40 / 0.60 | ≤ 0.004 | ≤ 0.03 | ≤ 2.0 |
| R400HT | 0.90 / 1.05 | 0.20 / 0.60 | 1.00 / 1.30 | ≤ 0.020 | ≤ 0.020 | ≤ 0.30 | ≤ 0.004 | ≤ 0.03 | ≤ 1.5 |
| Bainitic Rail | | | | | | | | | |
| B320 | 0.10 / 0.30 | 0.80 / 1.80 | 1.20 / 1.80 | ≤ 0.025 | ≤ 0.025 | 0.30 / 0.80 | ≤ 0.004 | - | 0.10 / 0.20 |
| B360 | 0.20 / 0.40 | 0.80 / 1.80 | 1.20 / 1.80 | ≤ 0.025 | ≤ 0.025 | 0.30 / 0.80 | ≤ 0.004 | - | 0.10 / 0.20 |

Table 2.2: Mechanical property requirements for as-rolled, heat-treated, and bainitic rail steel grades used on the UK rail network, according to the rail steel specifications [66], [89].

| Rail Grade | Tensile Strength Rm (MPa) | Elongation min. (%) | Hardness of the Rail Running Surface (BHN) |
|-------------------|------------------------------|------------------------|---|
| As-Rolled Rail | | | |
| R200 | ≥ 680 | ≥ 14 | 200 / 240 |
| R260 | ≥ 880 | ≥ 10 | 260 / 300 |
| HP335 | ≥ 1175 | ≥ 7 | 335 / 375 |
| Heat-Treated Rail | | | |
| R350HT | ≥ 1175 | ≥ 9 | 350 / 390 |
| MHH | ≥ 1280 | ≥ 12 | 381 / 408 |
| R400HT | ≥ 1280 | ≥ 8 | 400 / 440 |
| Bainitic Rail | | | |
| B320 | ≥ 950 | ≥ 12 | 340 / 380 |
| B360 | ≥ 1200 | ≥ 13 | 350 / 390 |

On top of the as-rolled pearlitic rail grades, there are also heat-treated pearlitic and as-rolled and heat-treated bainitic rail steel grades available. The heat-treated grades involve taking rail either directly after rolling or reheated and accelerate cool the railhead material to reduce the isothermal transformation temperature. This, therefore, creates a region of refined pearlite on the railhead that provides improved hardness and tensile strength without detrimentally affecting ductility [67]. The bainitic rail steels, in contrast, are alloyed and heat-treated in design to either have a lower bainitic or carbide-free bainitic microstructure. This overall provides for the equivalent hardness to pearlitic rail steels improved RCF crack resistance [90], [91].

2.4 Rail Steel Loading Response

The high hydrostatic compressive stresses produced by rail-wheel contacts commonly results in the accumulation of plastic deformation near the surface of a railhead. This plastic deformation results in strain-flattening and elongation of the different microstructural phases, coupled with reorientation in the direction of strain, which increases in severity at shallower depths [92], as exemplified in Figure 1.4. The accumulation of this plastic damage is a crucial driver in the creation and development of RCF damage and significant instance of wear in rail steels. This is because the plastic deformation undesirable promotes void and microcrack nucleation, that can eventually coalesce to form wear flakes and RCF cracks [12].

2.4.1 Strain Partitioning and Modification of the Microstructure

Microstructural studies [92]–[94] that have examined the plastic deformation in hypoeutectoid rail steels have all showed strain partitioning occurring between proeutectoid ferrite and pearlite. The accumulation of this plastic flow was preferentially in the proeutectoid ferrite, due to the lower hardness and higher ductility, leading to the faster strain accumulation and earlier ductility exhaustion compared to pearlite. Garnham and Davis [94] noted that the higher the hardness difference between the two phases, the more shear that accumulates in proeutectoid ferrite prior to any plastic flow happening in the pearlite.

For hypoeutectoid rail steel grades, the volume fraction of proeutectoid ferrite has been shown to be a critical factor influencing plastic deformation behaviour with a higher volume fraction of proeutectoid ferrite causing faster shear strain accumulation [94]. As rail steels with a low volume fraction generally possess a thinner initial matrix of proeutectoid ferrite along the prior austenite grain boundaries that would be more constrained by neighbouring pearlite nodules [95], [96]. In addition, a lower volume fraction of proeutectoid ferrite also creates more sites of proeutectoid ferrite discontinuities along the prior austenite grain boundaries; producing more pearlite-pearlite boundaries which are stronger compared to their pearlite-proeutectoid ferrite counterparts. The result was the slower accumulation of shear strain in the proeutectoid ferrite, due to the pearlite-pearlite boundaries shielding the proeutectoid ferrite from the applied stress field [94], [95].

Inside the pearlite colonies, strain accumulation has also been found to be preferential in the lamellar ferrite compared to the lamellar cementite due to the lower hardness [97] and the higher ductility caused by the greater number of slip systems available [98]. This preferential strain accumulation causes a thinning of the lamellae ferrite that reduces the interlamellar spacing [97]. The cementite lamellae, however, bends and fractures, leading to the breakup of the initial pearlite structure [96], [99] that produces a fibrous microstructure in the most severely deformed region closest to the surface. In the transition zone between the severe deformed region and rail steel matrix, Zhou et al. [100] observed that the morphology of the cementite lathes was dependent on the initial pearlite colony orientation relative to the rolling direction. For pearlite lamellar orientated parallel to the rolling direction the pearlite decomposition was found to be dominated by shortening of the interlamellar spacing and the cementite lathe curling. For Pearlite lamellar orientated perpendicular or at a large angle to the rolling direction, however, the pearlite decomposition was dominated by cementite twisting and breaking.

The energy introduced from plastic deformation has also been revealed to result in the nucleation and migration of dislocations in both proeutectoid and lamellae ferrite [92], [99], [101]. These

dislocations tend to group into dislocation cells due to the inherently lower energy state compared to a random distribution of dislocations. The boundary of these dislocation cells become more defined, as the dislocation density increases. This eventually allows localised rotation of the crystal lattice inside the cell to create sub-grains and eventually grains as the lattice misorientation increases [102], raising the proportion of LAGB (Low Angled Grain Boundary) to HAGB (High Angle Grain Boundaries) [100], [103]. This produces grain refinement via dynamic recrystallisation that increases the yield strength of the proeutectoid and lamellae ferrite due to the Hall-Petch relationship. Wen et al. [103] observed that the smaller initial interlamellar spacing coupled with the smaller pearlite colony and nodule size of R370CrHT led to the formation of strong dislocation cells that were more resistant to plastic deformation compared to R260. Zhou et al. [100] has also showed that a hypereutectoid rail developed a more severe LAGB's-to-HAGB's transition and dynamic recrystallisation process compared to a eutectoid rail steel.

2.4.2 Crystallographic Texture Evolution with Shear Strain

In the undeformed matrix of a rail steel, the grains are normally randomly orientated without a preferential crystallographic texture. The accumulation of shear strain, however, rotates and realigns this microstructure leading to the creation of a strong (111) crystallographic texture in the rolling direction [99], [100], [103], [104]. This crystallographic texture arises because of the prevalence of the $\langle 111 \rangle$ slip direction in all three slip system families for BCC (Body Centred Cubic) materials, such as ferrite, as illustrated in Figure 2.11. The process of dynamic recrystallisation induced by the plastic deformation in the heavily deformed material reintroduces the random orientation of the grains in the microstructure, which diminishes the strength of the (111) crystallographic texture [100].

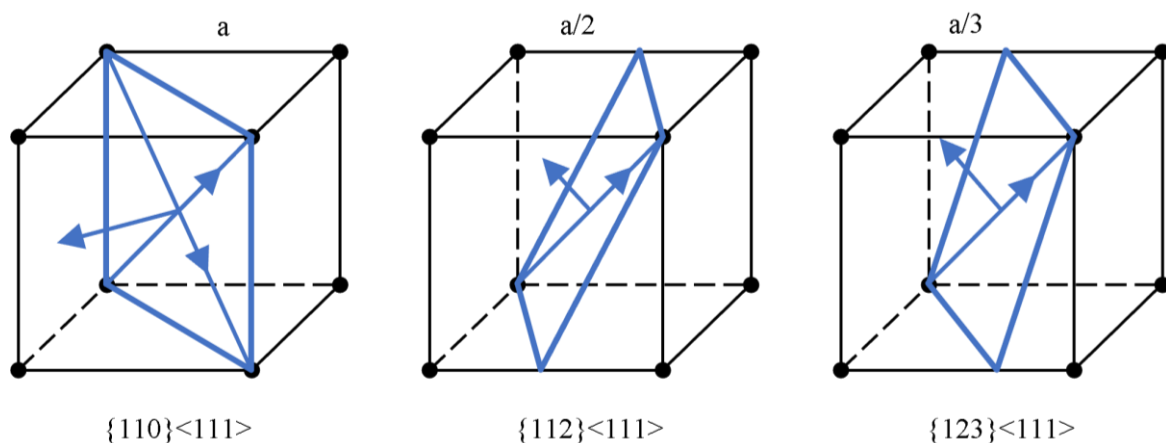


Figure 2.11: The three family of slip system observed in a BCC unit cell.

2.4.3 Cementite Lathe Dissolution

There are several studies [83], [105], [106] that have also noted observations of dissolution of the cementite lathes because of the surface plastic deformation created by rail-wheel contacts. This decomposition of the cementite in turn enriches the nearby ferrite to create supersaturated ferrite. The driving force for this cementite dissolution is still under debate with two current hypotheses. Gridnev et al. [107] theorises that for dislocations on the interface between ferrite and cementite carbon would be pulled out of the cementite due to the higher binding energy of carbon with dislocation than carbon with iron. Languillaume et al. [108], however, states that cementite dissolution happens due to the increased interfacial contribution to the cementite's Gibbs free energy because of its fragmentation caused by plastic deformation. This is because when cementite particles become too small their interfacial free energy exceeds the driving force for nucleation and, therefore, become thermodynamically unstable and dissolve into the nearby ferrite.

2.4.4 Work Hardening and Depth of Plastic Damage

The accumulation of shear strain in a rail steel work hardens the plastically deformation surface material, which considerably increases the hardness and shear yield strength compared to the undeformed matrix. The depth of the surface material affected by plastic deformation has been observed to be different depending on what data is analysed, as a shallower depth of plastic damage has been commonly observed from optical visible appearance compared to microhardness results. This is because optical microscopy only observes the macroscopic changes that happen in the material [109]. Hua et al. [110] noted that for low values of shear strain below any optically visible plastic deformation the rail steel was hardened by dislocation strengthening. As plastic deformation increases in severity and becomes more observable, the hardness of the material was affected by both dislocation and microstructural refinement strengthening. Near the surface where the plastic damage was most severe, the hardness was affected by a combination of dislocation, microstructural refinement, and solid solution strengthening by the dissolution of carbon into the interlamellar ferrite.

2.5 Shakedown Theory

The shakedown theories state that an elastic-plastic material subjected to cyclic compressive loads, such as rail-wheel contacts, can respond in four ways depending upon the magnitude of the contact loads [36], as illustrated in Figure 2.12. These four material response regimes are: i) elastic, where materials subjected to contact loads below the elastic limit experience only purely elastic and reversible deformation. ii) Elastic shakedown, where contact loads between the elastic limit and the elastic shakedown limit causes a material to experience some initial yielding but returns to being

elastic due to the development of residual stresses and material strain hardening. iii) Plastic shakedown, where contact loads between the elastic and plastic shakedown limit causes material to experience plastic deformation and create a closed plastic shear strain loop with no net strain accumulation. iv) Plastic ratcheting, where contact loads above the plastic shakedown limit causes material to plastically deform and create an open plastic shear strain loop resulting in the cyclic accumulation of shear strain. Overall, the service life of a component would be detrimentally reduced for materials experiencing either the plastic shakedown and plastic ratcheting load responses.

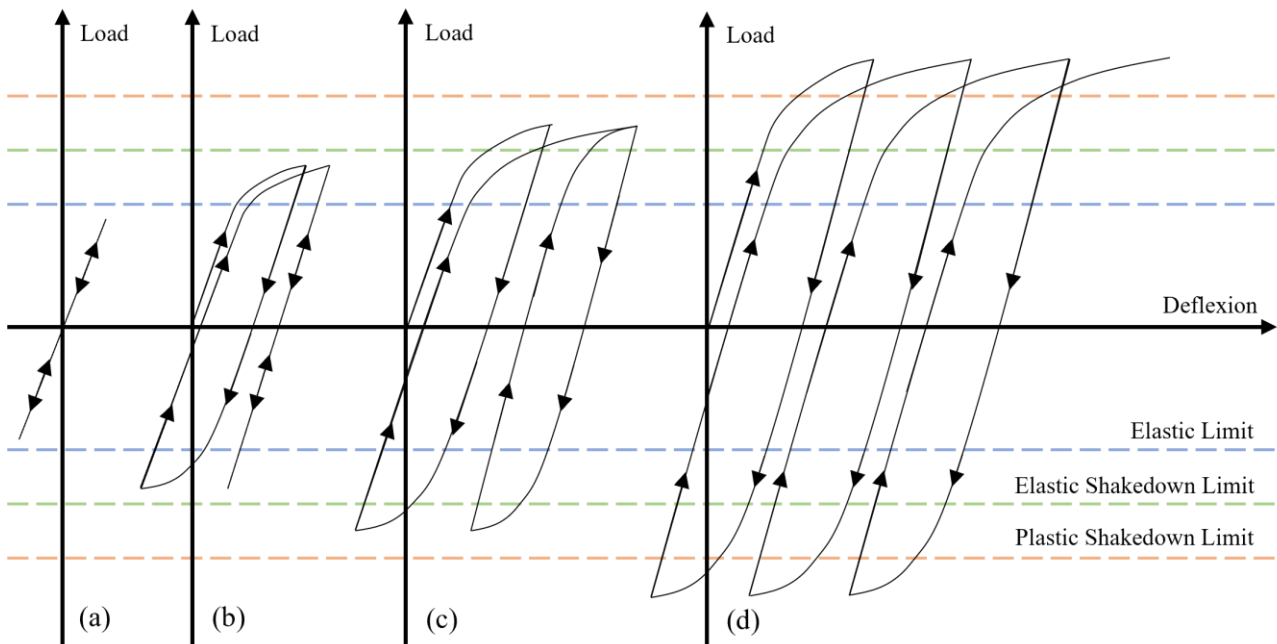


Figure 2.12: Illustration of the four ways (elastic, elastic shakedown, plastic shakedown, plastic ratcheting) that elastic-plastic materials can respond when subjected to cyclic compressive-shear contact loads.

To understand whether the contact loads generated would be enough to cause plastic ratcheting the two theories, Melan’s statical theorem and Koiter’s kinematical theorem, have both been established to derive analytically the materials plastic shakedown limit. According to Melan’s statical theory, elastic shakedown would only occur when the residual stress field, together with the elastic stresses created by the contact load were within the materials elastic limit. Koiter’s kinematical theory, however, states that elastic shakedown would not occur when the work done by an external load was greater than the materials internal plastic work during any kinematically admissible cycle of plastic strain. The problem is that Melan and Koiter’s theorem, respectively, only provide the lower and upper bound estimate to the true plastic shakedown limit, with an exact solution only found when both theories agree [111]. This, therefore, creates regions of uncertainty for deriving analytically the true shakedown limit when both theorems do not agree.

In simulation models, the rail-wheel contact is commonly simplified using either a line or point contact representation. For line contacts, the only kinematically acceptable mechanism of incremental strain is where the surface layers of a rail are sheared parallel in the direction of travel. Furthermore, only two direct components of the residual stress field exist due to the requirement of symmetry and equilibrium. Point contacts, however, have two kinematically acceptable mechanisms of incremental strain. The first mechanism is the process of a wheel ploughing into the rail, creating a groove where the material is displaced laterally and deposited on the groove's rim. The second mechanism, like the case for line contacts, is where plastic deformation of material directly below the contact is sheared parallel to the motion of the contact load. Additionally, all six components of the residual shear stress field are possible due to the existence of undeformed material on either side of the deformation track [111]. The comparison of the shakedown plots between line (refer to Figure 2.6 in ref. [15]) and point (refer to Figure 4 in ref. [112]) contact shows that points contact are able to handle a higher contact load factor before experiencing plastic shakedown compared to line contacts. In addition, the critical friction coefficient for when plastic flow transitions from subsurface to surface is slightly higher in the case for point contacts compared to line contacts.

Jones et al. [113] investigated the influence of material strain hardening on the shakedown limits for R220 rail steel. Their finding showed that once material strain hardening reached steady state conditions, the shakedown limits load factor for a pure rolling line contact increases from 4 to 7.4, due to the material's higher shear yield stress. Furthermore, the critical coefficient of friction also increases from 0.367 to 0.55. This was because as the plastic deformation in rail was localised at the surface with increasing severity at shallower depths, the materials shear yield strength was higher at the surface compared to the subsurface bulk material. Therefore, necessitating a higher coefficient of friction to overcome the materials higher shear yield strength at the surface. This type of analysis, however, has only currently been conducted for R220 rail steel and so it remains unknown how they change with other rail steel grades and contact conditions.

2.5.1 Plastic Ratcheting-Based Simulation Models

The 'layer' model [13] is a simulation approach developed to predict the subsurface plastic deformation behaviour of materials subjected to cyclic shear-compression loading conditions. The accumulation of shear strain is calculated in this model using the numerical method devised by Kapoor and Franklin [114] based on the concept of plastic ratcheting. The 'Layer' model treats the rail-wheel contact as a two-dimensional portrayal of a roller on a flat surface with the rail discretised into numerous layers and the rail-wheel contact represented by a Hertzian pressure profile. The 'brick' model [14], [115], expands upon this by discretising each layer into numerous rectangular elements.

This approach enables variation of the strain accumulation both longitudinally and with depth to be considered for the purposes of investigating the development of wear and RCF crack initiation. Furthermore, the ‘brick’ approach also allows material properties of different phases (proeutectoid ferrite, pearlite) to be implemented to dual-phase rail steel microstructure [116]. To drive these plastic ratcheting-based simulation models, material information in the form of the shear stress-strain curve, ratcheting load conversion factor (conversion factor between incremental shear strain and ratcheting load), and shear strain at failure (limit of accumulative shear strain that can occur before the nucleation of voids and microcracks) are needed as data inputs.

2.5.1.1 *Shear Stress-Strain Curve*

Kapoor et al. [13] has derived the shear stress-strain curve relationship for BS11 rail steel under high compression, high shear loading conditions utilising the twin-disc data generated by Tyfour et al. [117]. In their approach, shear strain and shear stress data were characterised from the observed plastic deformation at a fixed depth of 200 μm below the running surface from samples tested to varying contact cycle durations. The shear strain data was obtained by measuring the angle of the deformed microstructure, whereas the shear stress data was acquired from the hardness results. The combination of both datasets provided data points to the material’s shear stress-strain curve, in which a modified Voce equation in the form of Equation 2.6 was then fitted to the data to provide a numerical expression.

$$k = m(1 - e^{-n\gamma})^p \quad \text{Equation 2.6}$$

Where k is shear yield stress, γ is shear strain, and m , n , and p are coefficients found by fitting the relationship to the experimental data. This method has been simultaneously improved by Tomlinson et al. [118] and Alwahdi et al. [119] by removing the requirement to examine multiple samples and instead derive this relationship by analysing only a single sample. Both works accomplished this through measuring the shear stress and strain at a range of different depths taking advantage of the strain gradient typically observed below the running surface of twin-disc samples or actual rail removed from track. In comparison to the original methodology, this improved approach eliminates the issue regarding what depth the data was collected at from becoming an artifact of the results. A summary of the modified Voce equation coefficients that have already been derived in literature for different rail steel materials and contact conditions investigated is presented in Table 2.3.

Table 2.3: Summary of the modified Voce equation coefficients already derived for different combinations of rail steel metallurgy and contact conditions investigated.

| Rail Steel | Contact Conditions | Modified Voce Equation Coefficients | | | Ref. |
|------------|------------------------|-------------------------------------|---------|--------|-------|
| | | M | n | p | |
| BS11 | 1500 MPa, 1% slip, dry | 446 | 0.47 | 0.80 | [13] |
| R260 | 1500 MPa, 1% slip, dry | 834.8 | 0.09177 | 0.2219 | [118] |

2.5.1.2 “Ratcheting load” conversion factor

The “ratcheting load” conversion factor (actually a non-dimensional quantity but conventionally referred by this name¹) is a parameter devised by Tyfour et al. [120], in which describes the conversion between the normalised ratcheting load experienced by a material during a loading cycle and the incremental shear strain. The higher this value, the faster the accumulation of shear strain for the same given contact condition. This parameter is determined from the linear constant of proportionality between data comparing the total ratcheting load experienced above the plastic shakedown limit and the total accumulated shear strain. A summary of the ratcheting load conversion factors that has already been derived in literature for different rail steel materials and contact conditions investigated is tabulated in Table 2.4. From the current two studies [63], [120] that have derived the ratcheting load conversion factor for rail steels, both have accomplished this inefficiently by collecting only one data point per sample tested. There is, therefore, scope to improve this methodology to enhance the efficiency of data collection so more data can be obtained from each individual specimen tested.

Table 2.4: Summary of the ratcheting load conversion factors already derived for different combinations of rail steel and contact conditions investigated.

| Rail Steel | Contact Conditions | Ratcheting Load Conversion Factor | Ref. |
|------------|------------------------|-----------------------------------|-------|
| BS11 | 1500 MPa, 1% slip, dry | 0.00231 | [120] |
| R260 | 1500 MPa, 1% slip, dry | 0.0009853 | [63] |

2.5.1.3 Shear Strain to Failure

The shear strain to failure of rail/wheel steels under cyclic compression-shear loading conditions has previously been estimated using a variety of different methodologies. The first method identified derives this parameter from the asymptotic value of shear strain from measuring the angle of the

¹ This parameter is deriving by dividing contact pressure over shear stress which are both stress terms and overall gives a nondimensional parameter. This nondimensional parameter, however, is referred to in the original publication [120] as the conversion factor of net ratcheting load. To retain continuity with previous publications, this parameter will continue to be called the “ratcheting load” conversion factor.

deformed microstructure at a fixed depth below the running surface observed over different contact cycle durations [13], [121]. The results presented by Kapoor et al. [13] use a fixed depth of 200 μm ; whereas Akama and Kimata [121] use a depth of 30 μm to derive their respective results. Alternative approaches have used the presence of RCF cracks on the rail running surface to determine the shear strain at failure. This takes advantage of the understanding that RCF cracks initiate when the accumulation of shear strain in rail steels reaches the shear strain at failure. There are, however, two different ways in how the RCF cracks can be used to derive this parameter. Tomlinson et al. [118] and Namura et al. [122] determines this parameter based on the mean entrance angle of RCF cracks on the rail running surface. Donzella et al. [123], Mazzù [124], and Halama et al. [125], conversely, have all determined the shear strain to failure by measuring the mean angle of the deformed microstructure local at the tip of RCF cracks observed in their samples. Table 2.5 summarises the current estimates for the shear strain to failure of different rail and wheel steels from experimental results in literature. The different approaches mentioned, while suited to the studies they feature, do involve compromises that will limit their wider applicability. For examples, the measurement of the angle of different specific parts of the rail steels microstructure will make the method highly sensitive to error when dealing with angles approaching 90 degrees - as experienced very near the surface of rail steels. In addition to some featuring assumptions of suitable depths at which to take the shear strain measurements that are tied to the depth of plastic damage for those materials. Overall, the number of different approaches and the compromises involved with them implies that a definitive approach of deriving the shear strain to failure of rail steels subject to cyclic shear-compression loading conditions has yet to be found and will need further investigation.

Table 2.5: Summary of the shear strain to failure results derived for rail/wheel steel materials subjected to cyclic combined compression-shear loading condition in literature.

| Rail/Wheel Steel | Contact Conditions | Shear Strain to Failure, γ_c | Ref. |
|----------------------------------|--|-------------------------------------|-------|
| BS11 rail steel | 1500 MPa, 1% slip, dry | 11.5 | [13] |
| Unspecified pearlitic rail steel | 1100 MPa, 1% slip, lubricated with water containing 5% cutting oil | 11 | [121] |
| R260 rail steel | 1500 MPa, 1% slip, dry | 11.7 | [118] |
| Unspecified pearlitic rail steel | Rail removed from track | 2.89 | [122] |
| 900 A rail steel | 1100 MPa, 0.06% slip, dry | 10.4 | [123] |
| R7T wheel steel | 1100 MPa, 0.06% slip, dry | 9.3 | [123] |
| 900 A rail steel | 1100 MPa, 0.065% slip, dry | 12.8 | [124] |
| R7T wheel steel | 1200 MPa, 0.75% slip, dry | 9.1 | [125] |

2.6 Rolling Contact Fatigue (RCF) Cracks

Rolling contact fatigue (RCF) cracks are one of the two main damage mechanisms that can initiate and develop on the running surface of rail originating from the accumulation of plastic deformation. These defects are undesirable because of their natural tendency to cause railhead shelling and transverse rail breakages. Furthermore, from a maintenance point of view, the subsurface nature of this type of damage makes them difficult to monitor and predict in-service. Relative to the length of the RCF crack, the initiation and growth cycle of RCF damage can be categorised by three stages [126], as shown in Figure 2.13.

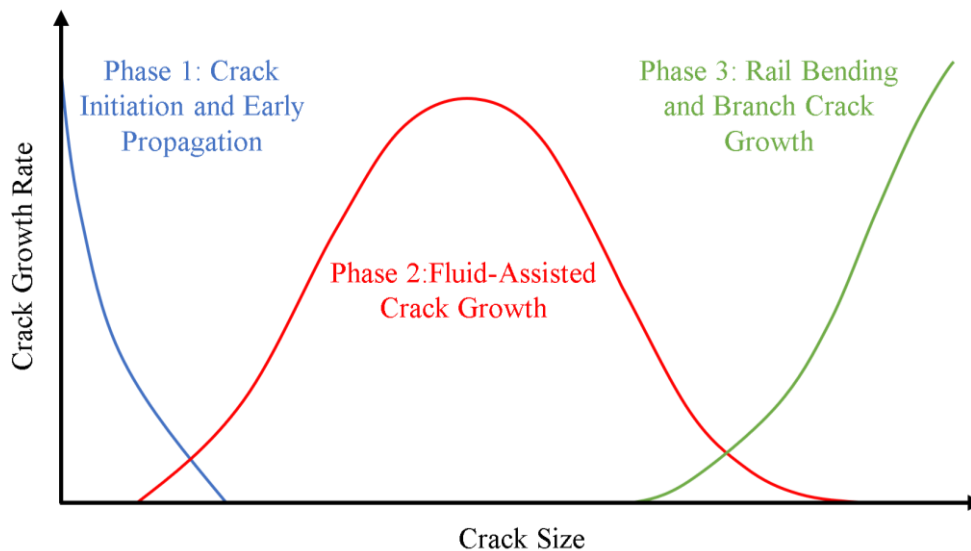


Figure 2.13: Stages of the initiation and propagation of RCF cracks in rail steel.

2.6.1 Phase One – RCF Crack Initiation and Early Propagation

The first stage of this development cycle of RCF cracks is the initiation and early propagation, in which during this phase the evolution of RCF cracks are highly influenced by the rail steel microstructure. In hypoeutectoid rail steels, the strain partitioning that happens between proeutectoid ferrite and pearlite creates planes of weakness along their boundary that facilitates the initiation and propagation of RCF cracks. Once initiated, these premature RCF cracks propagate until they reach the limit of the proeutectoid ferrite in the favourable strain direction, with further propagation inhibited by them having to go through pearlite [94], [96]. The accumulation of plastic deformation causes these premature RCF cracks along with the prior austenite grain boundaries to become more stress driven. Alongside which, the thinning of the pearlite allows these RCF cracks to jump the pearlite phase onto adjacent prior austenite grain boundaries to continue propagating [93]. The influence of the proeutectoid ferrite volume fraction during this stage has been explored by Garnham et al. [96], in which observed that rail steels with a higher volume fraction of proeutectoid ferrite

displayed faster crack initiation and earlier propagation. This result arises because of the faster strain accumulation and ductility exhaustion of the proeutectoid ferrite phase.

In fully pearlitic rail steels, Masoumi et al. [105] found that the portions of the rail steel microstructure containing high Taylor factor grains (grains that are not able to rotate and meet the slip requirement) and high kernel average misorientation were highly prone to RCF crack initiation. This was because the lack of enough slip systems in these parts of the microstructure restrict the movement of dislocations, leading to the development of stress concentrations. These stress concentrations facilitate the development of the asymmetric lattice disclination and enlarges pre-existing regions of crystallographic defects and lattice distortions. The dynamic recrystallisation of the interlamellar ferrite has also been suggested to create weak spots in the rail steel microstructure that assists the initiation and propagation of RCF cracks in the pearlite phase [127]. This idea has been potentially supported by the finding generated by Zhou et al. [100], in which observed a lower RCF resistance for the rail steel that displayed a higher degree of dynamic recrystallisation.

The strain-flattening of MnS inclusions, which are commonly present as elongated stringers in the microstructure of all modern rail steels grades, are another potential source of weak spots that can facilitate the initiation and propagation of RCF cracks. The influence of this microstructural feature to facilitate the initiation and propagation of RCF cracks is understood to be more significant for rail steels containing a smaller volume fraction of proeutectoid ferrite along the prior austenite grain boundaries [69], [94]. There has also been results published recently that have also found that the orientation of these elongated MnS inclusions relative to the rolling direction also influences the initiation and propagation behaviour of RCF cracks facilitated by this microstructural feature [128], [129]. There is conflicting evidence, however, of which elongated MnS inclusion orientation is more detrimental in encouraging RCF crack behaviour. This is because Nakai et al. [128], observed from experimental results a higher RCF life associated with MnS inclusions in steels orientated parallel to the rolling direction compared to their perpendicular or transverse counterpart. On the other hand, the simulation results reported by Madhavi et al. [129] suggests parallel MnS inclusions are more damaging with stress concentrations predicted to be 87.8% higher compared to a perpendicularly orientation MnS inclusion.

From the point-of-view of track operators and researchers, the definition of RCF crack initiation in rail steels has got a different meaning. For track operators, they regard crack initiation as when RCF cracks are large to be detected during rail inspection (≈ 4 mm for ultrasonic testing). However, researchers view crack initiation on a microscopic scale as the initial movement of dislocations that coalesce to form a crack [130].

2.6.2 Phase Two – Fluid Assisted RCF Crack Growth

The second phase consists of RCF crack growth governed by the contact forces and fluid-assisted mechanisms. During this phase, the presence of fluids, such as water or oil is known to be a key driver of the propagation of RCF cracks with observations of higher crack growth rates when fluids are present on rail with pre-existing cracks [120]. A definitive answer of how fluids accelerate the propagation of RCF cracks is not fully understood with four theoretical mechanisms hypothesised, as illustrated in Figure 2.14. These four mechanisms are:

- **Shear crack growth** – The orthogonal shear stresses created by rail-wheel contacts can cause RCF cracks to propagate via shear. The presence of fluid in the contact reduces the COF between the crack faces, thus amplifying mode II crack propagation [131].
- **Hydraulic crack growth** – The fluid forced into the RCF crack by rail-wheel contacts can act as a wedge pulling the crack faces apart, therefore, generating a mixture of mode I and II crack growth [131].
- **Fluid Entrapment** – The rail-wheel contacts could close the crack mouths, preventing any fluid inside the crack from escaping. Any fluid present inside the crack become pressurised and, therefore, produces mode I and II crack propagation [131].
- **Squeeze film crack growth** – The rapid compression of fluid present inside RCF cracks due to rail-wheel contacts can result in pressure peaks in the fluid without the need of the crack mouth closing causing a mixture of mode I and II crack propagation [132].

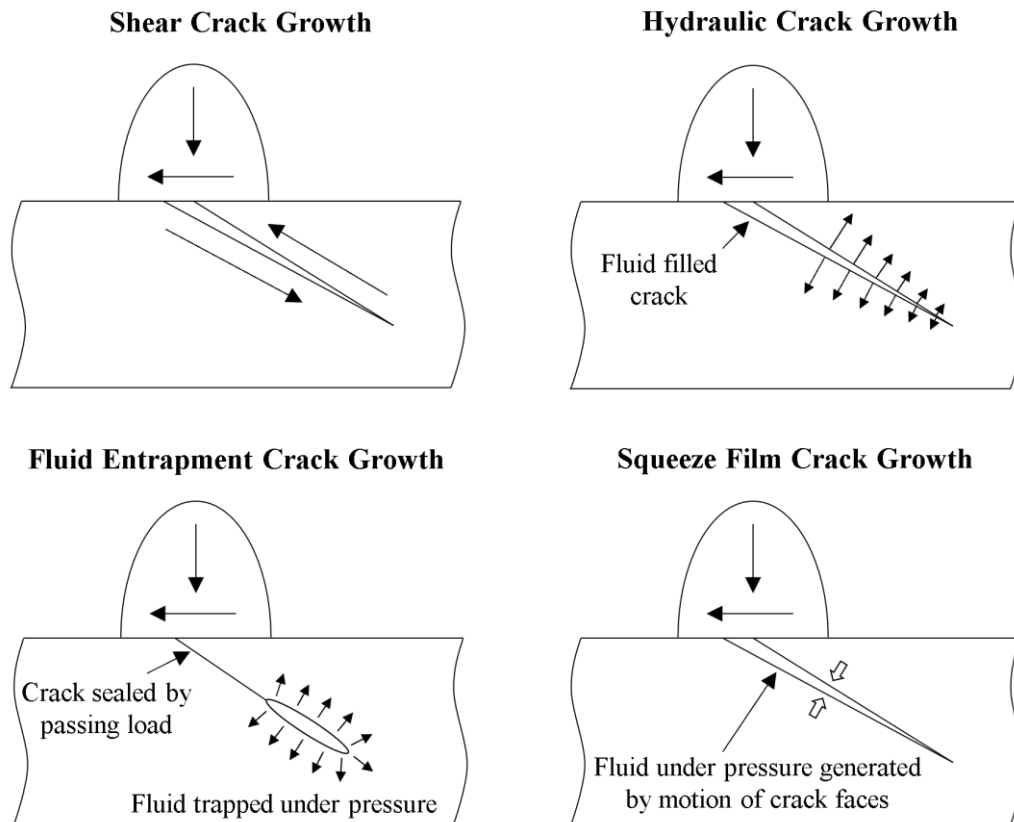


Figure 2.14: Illustration of the four fluid-assist mechanism theorised for the RCF crack propagation during phase two.

Overall, one or a combination of these mechanisms are potentially responsible for RCF crack propagation during this stage. Wang et al. [133] noticed that higher viscosity fluids produced RCF cracks with higher growth angles, slower growth rates and the development of more branch cracks. Suggesting that lower viscosity fluids can enter and lubricate the cracks faces more easily, therefore, enhancing mode II propagation. The higher viscosity fluids, however, are thought to not enter the cracks as well and thus, a hydraulic crack growth mechanism is more probable.

These mechanisms work well from an idealised two-dimensional viewpoint, but not for real three-dimensional RCF cracks. This is because real cracks can in some cases grow large enough three-dimensionally not to become completely covered by a rail-wheel contact. Coupled with the interconnecting of cracks, this prevents mechanisms relying on sealing and pressurisation of the fluid. Additionally, crack face roughness, branching and curvature can complicate RCF cracks propagating via shear [130].

Larijani et al. [134] found that the way RCF cracks propagate during this phase is also dependent on material anisotropy. Their simulation results showing RCF cracks having a higher tendency to propagate down into a rail for rail steels exhibiting highly anisotropic surface material. While weakly

anisotropic and isotropic surface material tended to propagate RCF cracks towards the surface. In addition, a critical crack length exists where, regardless of the surface material anisotropy, RCF cracks always tended to propagate down into a rail. Masoumi et al. [105] also showed that grains with a {110} orientation relative to the rolling direction enhanced the growth rate of RCF cracks; grains with an {111} orientation were found to inhibited the growth rate of RCF cracks.

2.6.3 Phase Three – Rail Bending and Branching Crack Growth

As the tip of RCF cracks move further away from the rail surface they become less influenced by the localised surface stresses produced by rail-wheel contacts and instead become more affected by the rail bending stresses. During this phase, the crack propagation rate increases rapidly with longer cracks length until a critical length is reached where the stresses are enough to fracture the rail. Overall, rail sections with RCF cracks operating during this phase are dangerous and, therefore, would need to be replaced urgently [126].

2.7 Wear

Wear is the second main damage mechanism that can be associated to the accumulation of plastic deformation in rail steel during significant cases. The wear of a rail section is undesirable as the consequence of this damage mechanism is the widening of the track gauge and the loss of the rail profile, which can create unfavourable rail-wheel contact forces and dynamic interaction. In addition, to detrimentally reducing the integrity of a rail section by decreasing the cross-sectional area available to support the axle loads [126]. Compared to RCF cracks, however, wear is generally less of a concern to rail network operators because of its more predictable and monitorable nature as a surface damage mechanism.

The Archard wear model [135] is a classical wear theory frequently applied in rail and wheel wear investigations to describe the relation between rail-wheel contact conditions and wear volume. In this model, the wear volume is related to the normal contact load P , sliding distance l , and hardness of the wearing surface H by a wear coefficient K , as given by Equation 2.7.

$$V = K \frac{Pl}{H} \quad \text{Equation 2.7}$$

Like other tribological systems, however, a single wear coefficient is insufficient to describe the wear behaviour within rail-wheel contacts over all possible contact conditions, which will be explored in the following sub-sections.

2.7.1 Wear Regime Categories

The wear behaviour of rail and wheel steels subjected to cyclic rail-wheel contacts can be categorised into three wear regimes (mild, severe, catastrophic) based on the wear rate experienced [136], as illustrated in Figure 2.15. The mild wear regime is associated with an oxidation wear mechanism, with wear surfaces exhibiting a smooth and rusty brown appearance and debris containing both oxide and metal particles [136]. The mechanisms associated with the severe and catastrophic wear regimes, however, are dependent on which one of the contact bodies are being examined. This is because for a driving contacting body, material is removed as wear via tribochemical and spalling wear mechanisms. A driven contacting body, however, mainly encounters fatigue wear mechanism dominated by flake generation but can also experience some abrasion as well [137], [138]. The transition from a mild to severe wear regime has been noted by Lewis and Dwyer-Joyce [139] to be potentially linked to the when rail-wheel contact conditions switch from partial to full slip. The reduction in the yield strength and other material properties due to the heat-induced by the high amount of energy generated within the rail-wheel contact was postulated to be responsible for the transition from a severe to catastrophic wear regime. This is supported by analytical and thermal imaging studies [139], [140] that showed rail and wheel material reaching around 200-250°C at the transition point. This corresponded well for when the reduction in the yield strength of carbon-manganese steels (like rail steels) is expected to occur between 200-300 °C [141].

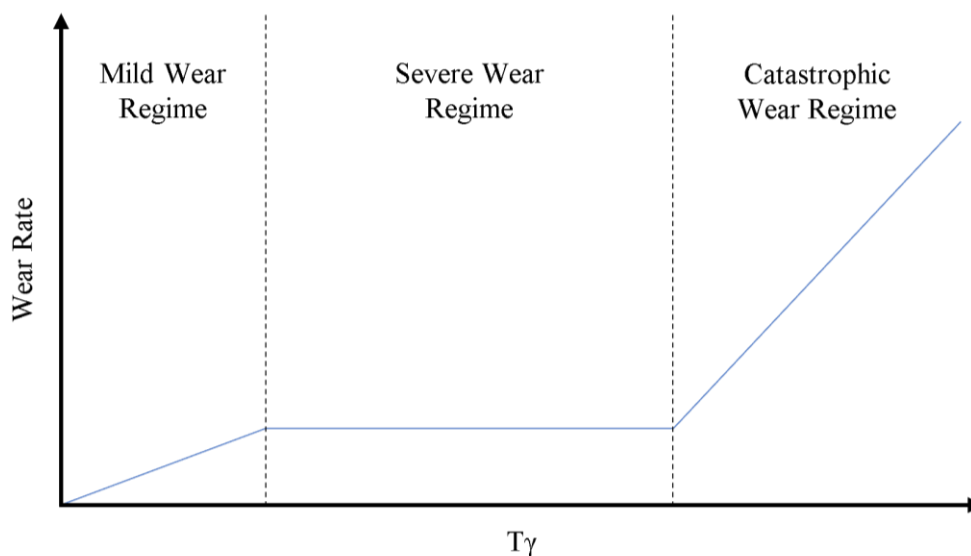


Figure 2.15: Typical example of wear rate against $T\gamma$ for a rail/wheel steel.

There are currently two hypotheses for the generation of flake-like wear debris within the rail-wheel contact. The first hypothesis is delamination wear theory [12], in which describes a process whereby the accumulation of plastic deformation leads to the initiation of fatigue cracks. These fatigue cracks

propagation along the deformation lines of the deformed microstructure, running roughly parallel with the running surface to create a flake-like structure on the running surface of a rail. The tangential shear stresses and the adhesion created within the rail-wheel contact causes them to detach from the running surface to become flake-like wear debris [142]. The second hypothesis is the junction failure and transfer particles theory [143], [144], in which states that the interaction of asperity contacts under sliding causes junction failures to occur, which deposits chunks of material onto the opposite contact surface. These chunks of material adhere to the running surface occasionally transferring back and forth between the rail and the wheel, increasing in size through agglomeration. The compression stresses within the rail-wheel contact compacts these chunks of material into flake-like particles. This process continues until the adhesion forces are no longer able to support these flake-like particles resulting in their eventual detachment as flake-like wear debris. It has also been suggested a combination of both processes could be happening at the same time within the rail-wheel contact [145]. The influence of contact pressure on the wear flake debris generated has been examined by Al-Malaki et al. [142] and Tosangthum et al. [146], showing that the number and size of the wear debris increases with normal contact pressure.

2.7.2 Effect of Contaminants and Environmental Conditions

The open tribological nature of rail-wheel contacts means that the wear of rail and wheel steels are influenced by the presence of contaminants and environmental conditions. The application of water, oil, and greases to rail-wheel contacts has been found to generally decrease the wear rate of rail and wheel steels [147]. In addition, different types of lubricating fluid create their own wear maps, each with different slip ranges for the three wear regimes compared to dry contact, due to the different way energy dissipates between the different lubricated and dry contacts [147]. Wang et al. [148] has also observed that the application order of lubricants is also important, with higher rail steel wear rates recorded for when water is applied before oil/grease compared to vice versa. Additionally, the mixture of two lubricants leads to higher rail wear rates compared to their individual application. The practice of applying sand to the rail-wheel contact for the purpose of improving adhesion in rail-wheel contacts has the opposite of increasing rail wear rates. Lewis and Dwyer-Joyce [149] showed that the application of sand to dry and wet rail conditions increased rail wear rates by a factor of two and four, respectively. The application of sand to wet rails was observed to lead to higher wear rates due to more sand entering the rail-wheel contact because of the water surface tension sticking sand particles together onto the rail and wheel running surface. Arias-Cuevas et al. [32] showed that the size of the sand influences the wear rates of rail; however, is dependent on the rail-wheel contact slip conditions on which size of sand particles causes the highest wear rates. Lyu et al. [150] witnessed rail steel wear rates decrease with increasing relative humidity of the surrounding environment, with an already

oxidised rail surface experiencing a steeper reduction in wear rates with relative humidity compared to a clear rail surface.

2.8 Rail Steel Grade Selection

From the range of different rail steel metallurgies available, there are different grades in which perform better than others against the generation of wear and RCF damage. This choice on which rail steel grade to use for a specific track section is a complicated decision-making process needing to account for a range of different aspects. This involves factoring the track parameters that affect the rail-wheel contact conditions and thus stresses experienced by a rail. These track parameters include: the curve radius, cant (banking angle of curve track sections), gradient, accumulated tonnage, driving dynamics, line speed, type of rolling stock commonly used, and access to lubricants and friction modifiers. In addition, this decision procedure also needs to look at minimising the rail life cycle cost and RAMS (Reliability Availability Maintainability Safety) issues and potential welding requirements [151]. To help simplify and standardised this process, rail network operators commonly use either a radius or rail deterioration based set of guidelines to instruct on what rail grade to use [152].

One rail deterioration based method developed by RSSB (Rail Safety Standards Board) in the UK is the $T\gamma$ model [33]. In this model, experimental tests and field measurements derive a wear and RCF damage function that when combined, create a $T\gamma$ index damage curve for a rail grade, as exemplified in Figure 2.16. The damage produced by wear counteracts the RCF damage, based on the principle that wear truncates and shortens RCF cracks present in a rail steel [11]. When used in conjunction with vehicle dynamics software, such as VAMPIRE, which can derive $T\gamma$ values for a track section, these $T\gamma$ damage index curves help provide an estimate of the type and amount damage expected for that track section.

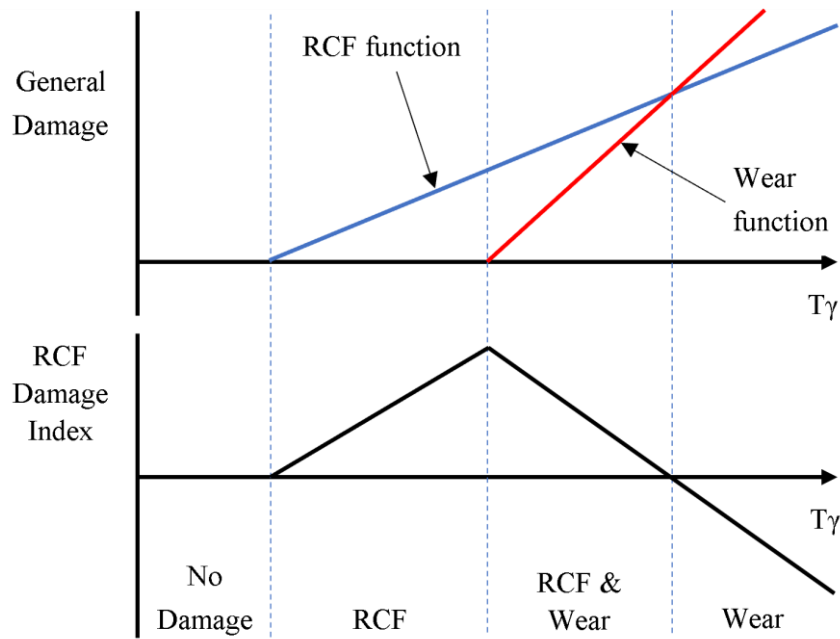


Figure 2.16: $T\gamma$ damage index curve typically found for rail steels [153].

In most of the rail steel grade selection guidelines used by rail networks operators, the common rationale to counteract severe wear and RCF damage prone track sections has been to install harder, premium rail steel grades [152]. The logic behind this reasoning for installing premium rail steel grades was founded on the general trend observed from experimental tests and field observations that higher hardness rail steel grades typically possess higher wear and RCF resistance [137], [154]–[156].

There have been cases, however, where the installation of premium rail steels in some track sections has led to a deterioration in the operation life and ease of management [157], [158]. Their observations in these situations found that the installation of premium rail steels changed the main damage mechanism from a wear to an RCF damage problem. This is an issue as the subsurface nature of RCF damage in comparison to wear damage is a lot more challenging to predict and monitor. A comparison of the $T\gamma$ damage index curves for different rail steel grades, as shown in Figure 2.17 helps to illustrate the change in damage mechanism experienced even though the contact conditions remain the same. This is because some premium rail steel grades can shift the boundaries of the wear and RCF damage domain in the $T\gamma$ damage index curve [153], [159].

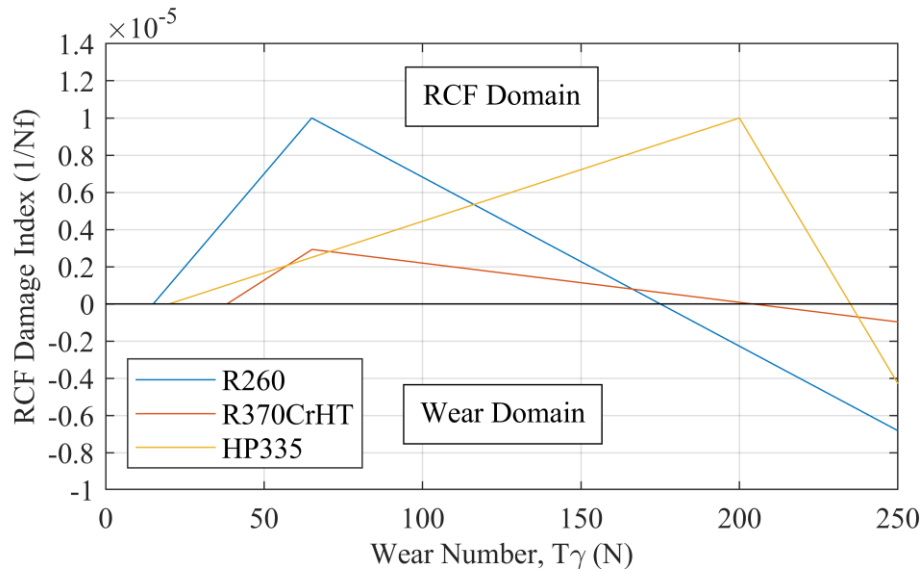


Figure 2.17: Comparison of the $T\gamma$ damage curve for the rail steel grades R260, R370CrHT, HP335 using data collected in the references [153], [159].

In contrast, bainitic rail steels with an equivalent hardness to their pearlitic counterpart usually have inferior wear resistance, but superior RCF crack resistance [90], [91], [160]. The installation of these rail grades, therefore, would be recommend for track sections prone to the most severe RCF crack damage, but where wear would not be much of a problem.

2.9 Rail-Wheel Contact Experimental methods

The understanding of the performance of rail steels due to rail-wheel contacts in research has previously been obtained experimentally via a variety of different approaches that operate on a range of different scales. These include, with increasing scale: pin-on-disc [161]–[163] or ball-on-disc [164]–[166] tribometers, small-scale twin-disc machines [93], [137], [160], [167], full-scale rail-wheel contact laboratory tests [90], [103], [168], and field measurements [90], [105], [164], [169]. The advantage of large-scale experimental techniques compared to small scale approaches is that they provide a more accurate representation of simulating rail-wheel contact or providing real rail-wheel contact geometry for the case of field experiments. This is, however, overshadowed by their associated disadvantageous that includes higher sample preparation and running costs [170] and increasing difficulty to gain access to facilities for conducting these larger scale experiments. These two factors, therefore, limit the number of experiments that can be undertaken with large-scale tests. Another drawback of large-scale experiments is that they provide less precise control of the contact conditions being investigated, which is especially an issue with field measurements due to the open tribological nature of rail-wheel contacts. It can be, therefore, potentially difficult from large-scale

tests alone to draw meaningful conclusions on how specific conditions of the rail-wheel contact can influence the performance of a rail-steel [170].

2.9.1 Small-Scale Twin-Disc Machines

Small-scale twin-disc machines provides a good balance between accurately representing the rail-wheel contact and accessibility and affordability out of the different previous approaches identified. The general principle of small-scale twin-disc machines is that they consist of two discs, one representing the rail and the other portraying the wheel, that are loaded and spun in contact with each other. To simulate longitudinal creepage within the contact, the rotational speeds are usually set so that the running track surface velocity of the rail disc is slower compared to the wheel disc. The encoders on the AC motors enables the disc's revolution count and speed to be monitored and recorded during experiments, while torque transducers can provide information regarding the coefficient of traction within the twin-disc contact [171]. The acquisition of information about rail steel wear and RCF damage development and material performance, however, can only be obtained from standard twin-disc tests after an experiment has finished. This is a limitation of standard twin-disc tests as it provides only a record of the rail steels material response at the end of a test, and it can be prohibitively expensive to conduct separate tests of different contact cycle durations to fully quantify material behaviour.

To increase the amount of data obtained from twin-disc machines about rail steel material behaviour a range of different techniques have been utilised in conjunction with twin-disc experiments. The practice of regularly interrupting a twin-disc test for recording measurements, such as mass loss, or visual observation is one commonly used technique [117], [172], [173]. These test interruptions, however, enable transient effects to be introduced into the experiments due to the delay in re-establishing contact load and traction coefficient after every test resumption. These transient effects are disadvantageous as they can influence the development of wear and RCF damage on a twin-disc sample. Eddy current sensors [174] are a technology that have been used previously monitor the development of RCF cracks, however, these are limited, though, to quantifying surface damage as an electrical signal with no defect morphological details provided. Electromagnetic array sensor [175] and ACFM (alternating current field measurements) [176]–[180] are another non-contact non-destructive-testing technique similar to Eddy current sensor that have previously been used to monitor RCF cracks in rail. This technology has been shown to be capable of estimate of the subsurface shape and angle of an RCF crack [177], [179], [180] and has also been demonstrated to successfully measure from a rotating sample with surface speeds up to 121.5 km/h [176]. A form of this technology has previously been incorporated with twin-disc tests [175], however, this implementation only provided

an electrical signal map of the specimen's running surface with no in-situ analysis of the RCF cracks subsurface morphology. Overall, eddy current sensors, electromagnetic array sensors, and ACFM sensors can only measure the development of RCF cracks and not the wear performance of rail steels.

Optical monitoring systems are another technology previously explored for use with twin-disc machines. These systems have either relied on correlating damage to a speckled pattern based on the reflectivity of the twin-disc samples running surface [181]–[183], photographing a samples running surface by regularly interrupting a test [123], or creating section profiles of the running surface from optical data [184], [185]. Nevertheless, these optical systems have yet to visualise the morphological development of wear flakes or RCF cracks on a twin-disc samples running surface in-situ during a continuous twin-disc test. Additionally, all these current applications of optical monitoring system have only been conducted for twin-disc tests under dry contact conditions. Tests have been conducted with an optical monitoring system during alternating water and dry contact condition twin-disc tests [186]. However, the optical monitoring system during these experiments was only used during the dry contact conditions portions of the experiment. This shows that the surface damage development of rail steels under lubricated contact conditions, such as water or transparent oils, has yet to be visualised in-situ during twin-disc experiments.

The rail and wheel samples used for twin-disc testing are commonly machined out of the railhead and wheels parent material, respectively, as illustrated in Figure 2.18(a-c). This is because of the difficulty of replicating the microstructure and hardness property of the rail and wheel steel for specially made samples [153]. However, for rail twin-disc samples specifically there is a discrepancy on the orientation of how these specimens are extracted out of a railhead across the different studies using small-scale twin-disc samples in literature. The two most common methods of extracting these specimens out of railhead found in literature were either horizontally [32], [169], [187] (see Figure 2.18b) or laterally [93], [172], [188] (see Figure 2.18c). The former of which was preferable due to the significant hardness variation observed for rail twin-disc samples cut laterally out of a railhead [170]. On the other hand, a laterally machined specimen would provide a uniform transverse orientation of elongated MnS inclusions relative to the rolling direction. A horizontally cut sample, however, would have a different relative orientation of the elongated MnS inclusions around the circumference of the sample [69].

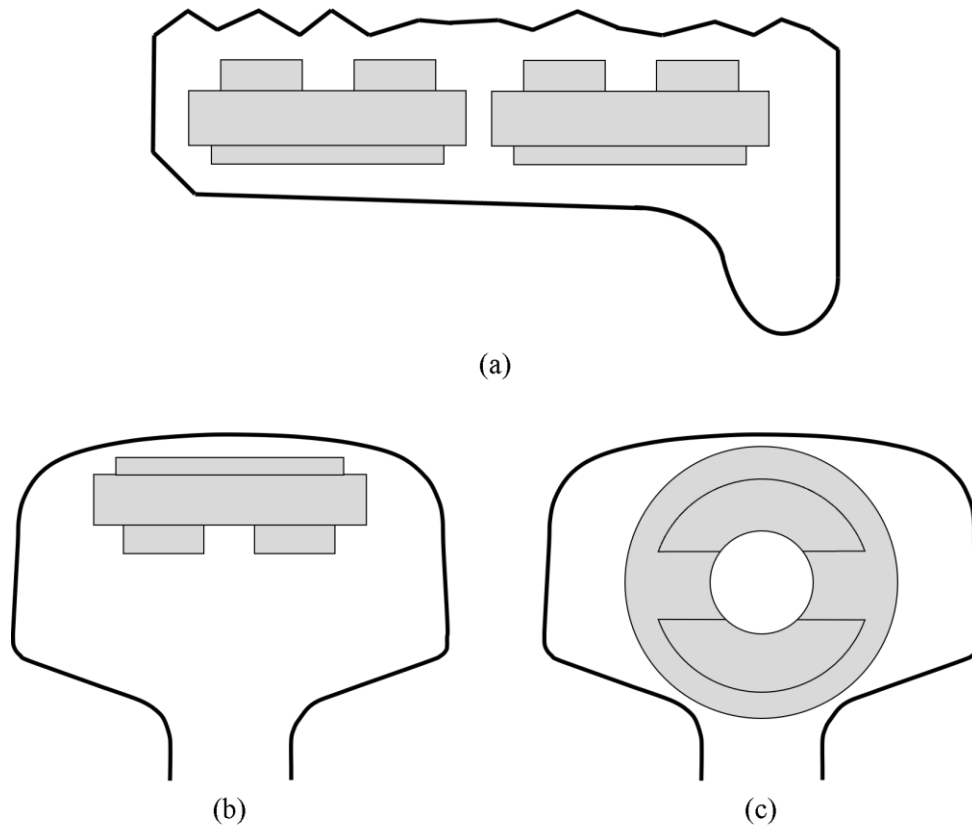


Figure 2.18: Illustration showing how twin-disc samples are extracted out of the (a) wheel tread and the two different common method of sectioning twin-disc sample out of a railhead: (b) horizontally and (c) laterally

2.9.2 Common Issues with Laboratory Approaches

The problem with laboratory techniques, especially for small-scale tests, such as twin-disc test machines, is that intrinsic factors associated with these techniques make it challenging to correlate results to actual rail-wheel contacts. One of these factors is the different contact size represented by these experimental approaches compared to actual rail-wheel contacts. This is because there is a correlation between the depth of maximum orthogonal shear stress and, thus, plastic deformation with contact size. The proportions of the surface roughness, however, does not scale well with the size of the contact simulated with these small-scale experimental approaches. This makes the contact represented by twin-disc machine and other small-scale experimental techniques more sensitive to contact pressure spikes as a results of the natural surface roughness [37]. The effect of the different contact size between twin-disc contact and actual rail-wheel contacts on RCF crack behaviour has previously been investigated by Kráčalík et al. [189]. Their findings showed that to simulate representative size RCF cracks in twin-disc tests with two 50 mm diameter samples, the RCF crack behaviour was more heavily influenced by the surface roughness present compared to actual rail-wheel contacts. The idea of an inverted twin-disc setup, as illustrated in Figure 2.19, has been

explored by Kammerhofer et al. [190]. This was done to increase the size of the contact simulated without significantly increasing the size and manufacturing costs of the specimens tested. However, because of the more enclosed nature of this design it would make it harder to add lubricants and other third-body contaminants into the contact and remove wear debris, which will have an influence on performance. Furthermore, wear and plastic flow of the running surface will make this setup sensitive to longitudinal creep variation.

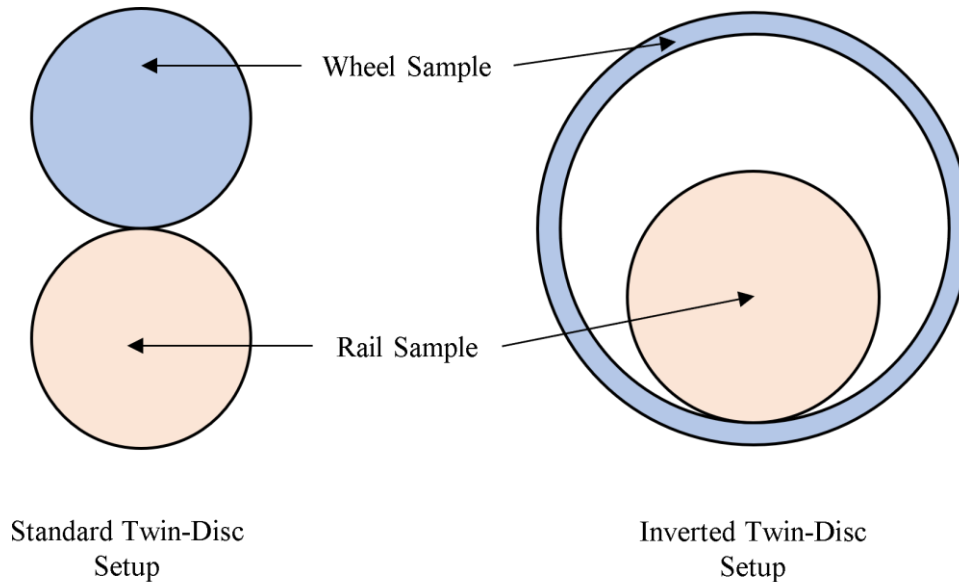


Figure 2.19: Illustration of the inverted twin-disc setup idea compared to a standard twin-disc test machine setup [190].

Another factor is that twin-disc test machines and some full-scale test rigs are only capable of simulating longitudinal creep, whereas longitudinal, lateral and spin creep are all present in real rail-wheel contacts [93]. A final factor is the simplification of the rail-wheel contact geometry. As laboratory techniques, such as twin-disc tests, commonly represent the rail-wheel contact using a line contact rather than a more representative point contact, which brings in issues relating to different shakedown behaviour, see Section 2.5. Curve-on-flat twin-disc tests have been conducted by Olofsson and Telliskivi [169] and Ma et al. [191] rather than the standard flat-on-flat twin-disc test. However, there is scepticism of whether this change fixes the issue, as the lack of lateral movement means that wear and plastic flow will make the discs conform to each other, gradually changing the interaction to a line contact [192].

2.10 Summary of Research Gaps Identified

The survey of the literature presented in this chapter has help identify the research gaps in this academic field to contextualise the areas of focus that will be explored in this thesis, as detailed in

Section 1.2. From this review, it was found that plastic ratcheting-based simulation models have been established to predict the subsurface shear strain accumulation in rail steel due to cyclic rail-wheel contacts. The main material information needed to drive these models are the shear stress-strain curve, ratcheting load conversion factor (conversion factor between ratcheting load and incremental shear strain), and the shear strain at failure (limit of accumulative shear strain that can occur before the nucleation of voids and microcracks). Approaches of deriving this material information from experimental twin-disc data have been created with the methodology of deriving the shear stress-strain curve recently updated to allow this data to be obtained from a single sample. The ratcheting load conversion factor, however, still requires the undertaking of multiple twin-disc tests to derive, which is an area for investigation to understand how this information can be collected from the least number of samples.

For the shear strain at failure, three different methodologies were identified in the literature to determine this parameter under cyclic shear-compression loading conditions. These three methods derive this parameter by either:

- Finding the asymptotic value of shear strain at a fixed depth
- Converting to shear strain the entrance angle of RCF cracks observed on the running surface of a rail.
- Measuring and converting to shear strain the angle of the deformed microstructure at the same depth of the RCF crack tips observed in rail steel samples.

These three methods, while suited to the original studies that they featured in, do involve compromises that will limit their wider applicability. For examples, the measurement of the angle of different specific parts of the rail steels microstructure will make these methods highly sensitive to error when dealing with angles approaching 90 degrees - as experienced very near the surface of rail steels. In addition to some featuring assumptions of suitable depths at which to take the shear strain measurements that are tied to the depth of plastic damage for those materials. Overall, these compromises show that a definitive approach of deriving the shear strain at failure for rail steels subject to cyclic shear-compression loading conditions has yet to be found. An investigation into these current methods and any potential new methodologies will need to be conducted to identify a definitive approach to determining this parameter.

A review into the material information currently collected for rail steels subject to cyclic compression-shear loading conditions showed that this data has mainly derived for 1500 MPa, dry conditions, with limited knowledge outside of this. One of the unknowns, therefore, is whether this material data generated for rail steels under specific contact conditions should be regarded as

‘material property’ or ‘system behavioural’ information, that is only applicable for a certain range of contact conditions. In addition, the material information available in the literature only covers the legacy rail steel BS11 and the standard R260 rail steel. Hence, one area identified for where this research can be expanded upon is the derivation of this material information for the premium rail steel grades, such as R350HT and HP335.

To accurately model the stresses generated within rail-wheel contacts in this work, the effect of rough contacts will need to be implemented. From surveying the different rough contact models that have been developed to estimate the rough contact stresses, it was concluded the Nowell-Hill roughness model was the most suitable for application into this work. This was based on the desirability criteria that the selected model needed to allow the calculation of the rough contact subsurface orthogonal shear stresses with low computing load, so that it can be utilised over many contact cycles. The asperity tip radius and separation are needed as data inputs to drive this model, however, from the literature it has been found that the cyclic variation of this data is only available for R260 rail steel subject to 1500 MPa, dry contact conditions. Therefore, a gap that will need exploring in this thesis is to understand how the asperity tip radius and separation data cyclically varies for rail steels tested under different contact conditions and for different rail grades.

From the different approaches of testing the performance of rail steels in a laboratory environment, twin-disc machines were identified to possess a good balance between accurately representing the rail-wheel contact and accessibility and affordability. The main drawback from standard twin-disc machines is their inability to provide any information about rail steel wear and RCF damage development and material performance while a test is being conducted. This information only becomes available after an experiment has concluded. A range of approaches have been identified in the literature that have been implemented with twin-disc tests previously to expand the amount of information obtained about the initiation and development of these damage mechanisms during experiments. These included regular test interruptions, eddy current sensors, electromagnetic array sensors, and optical camera systems. An unexplored opportunity that has been spotted, however, is for an optical monitoring system that can visualise in real time the morphological initiation and development of wear flakes and RCF cracks on a twin-disc samples running surface while rotating at 400 rpm without needing to interrupt the experiment. In addition, it was also found that the previous optical camera systems detailed in the literature have not yet monitored in-situ a twin-disc sample while the running surface was lubricated with water.

Chapter 3: Characterisation of the Asperity and Bulk Contact Driven Plastic Deformation Behaviour of Rail Steel

Highlights and Novelty

- Quantifying the asperity contact driven near-surface plastic damage via nanoindentation.
- Evaluating the change in rail and wheel steel asperity geometry with contact cycles.
- Updating the methodology of deriving the ratchetting load conversion factor to improve data efficiency and enable characterisation of modern premium rail steels
- Derivation of the shear stress-strain curve relationship and ratcheting load conversion factor for the premium rail steel grades HP335 and R350HT
- Understanding of how contact pressure influences the shear stress-strain curve relationship and ratcheting load conversion factor.

Journal Publication

The work presented in this chapter has been published in the following journal publication:

- A. Wilby, J. Corteen, S. Lewis, R. Lewis, and D. I. Fletcher, “Nano and micro-indentation driven characterisation of asperity and bulk plasticity at the surface of modern premium rail steels,” *Wear*, vol. 530–531, p. 205004, 2023, doi: <https://doi.org/10.1016/j.wear.2023.205004>.

3.1 Introduction

The literature review in chapter 2 showed that subsurface strain accumulation in rail steels due to the cyclic interaction of rail-wheel contacts can be estimated via plastic ratcheting-based simulation methods, such as the Layer [13] and Brick [14] model. To operate these simulation models, though, knowledge of a rail steels plasticity response to contact loads in the form of the shear stress-strain curve, ratcheting load conversion factor (conversion factor between ratcheting load and incremental shear strain), and the shear strain at failure (limit of accumulative shear strain that can occur before the nucleation of voids and microcracks) were needed for these models to function. Due to the combined high compression and high shear loading conditions that rail steels are typically subjected to in-service, methodologies have been developed to derive this data from twin-disc tests [13], [120]. These initial methodologies were generated based around the soft, legacy BS11 rail steel grade which typically accumulates a large amount of plastic damage. The utilisation of these initial methodologies for modern, harder premium rail steel grades, however, does not work as well due to the plastic

damage being more driven by asperity contacts rather than the bulk rail-wheel contact (as explored in section 3.5). Another flaw with these initial methodologies was that they were designed to only collect one data point per twin-disc sample and thus required the undertaking of multiple twin-disc experiments. This is problematic as it is hugely inefficient, costly, and may not always be possible when there are limited supplies of rail metallurgies available. A new optimised approach of deriving the shear stress-strain curve relationship from a single sample has been developed [119], [193]; however, the methodology of deriving the ratcheting load conversion factor has yet to be optimised.

The more efficient generation of this data can enable the opportunity to answer additional questions regarding potential behaviour change of rail steels subjected to different contact conditions. This is because the current rail steel data obtained to characterise their plasticity response has mainly been derived for 1500 MPa, 1% slip, dry contact conditions, with limited data collected outside of these parameters. Therefore, it is currently unknown whether the data generated under these conditions should be regarded as ‘material property’ data or whether it is ‘system behaviour’ data only relevant to a limited range of service conditions.

The aim of this chapter was to examine how data characterising the plastic deformation response of rail steels can be better obtained from twin-disc tests and expand the understanding of rail steel plastic deformation behaviour. The objectives of this chapter are:

- Explore how the methodology of deriving the ratcheting load conversion factor from twin-disc tests can be modified to improve efficiency and be brought up to date to characterise modern premium rail steels grades.
- Characterise and compare the shear stress-strain curve and ratcheting load conversion factor between modern standard and premium rail steels grades and understand how these results relate to rail steel damage data, such as wear rates.
- Investigate how the shear stress-strain curve and ratcheting load conversion factor may potentially change for rail steels subjected to different contact pressures.

3.1.1 Structure of Workflow

A flowchart mapping out the workflow that was undertaken in this first half of the research section of this thesis focusing on characterising the plastic deformation behaviour of rail steels is presented in Figure 3.1. For the three data inputs needed to estimate the accumulation of shear strain in plastic ratcheting simulation models, the shear stress-strain curves were derived in this work using the optimised approach simultaneously developed by Tomlinson et al. [193] and Alwahdi et al. [119]. The ratcheting load conversion factors, which describes the conversion from the ratcheting load to

incremental shear strain, were determined using an updated version of Tyfour et al. [120] methodology. This improved approach avoids the shortcomings that were identified with the original methodology and helps improve efficiency. The determination of the shear strain at failure for the rail steels investigated were determined using a novel value optimisation process. The derivation of the shear stress-strain curve and ratcheting load conversion factor for the rail steels investigated in this work is the focus of this chapter, whereas the calculation of the shear strain at failure is explored in Chapter 4.

For this work, two studies were undertaken to help expand the understanding of rail steel plastic deformation behaviour. The first study compares information derived for the first time to the authors knowledge from the premium rail steel grades HP335 and R350HT against the standard rail grade R260 under 1500 MPa, dry contact conditions. The second study examines information derived from R260 under the four different contact pressures (1500 MPa, 1200 MPa, 900 MPa, 600 MPa) to understand the sensitivity of this data with contact pressure. These contact pressures were chosen to represent the rail-wheel contact conditions for a range of different types of rail vehicles. The 600 MPa contact pressure tests represented the contact conditions from a passenger metro or tram system. The 1500 MPa contact pressure tests, however, characterised the conditions for a typical heavy locomotive engine in the UK and allowed direct comparison of these results with a large body of data in the literature. In addition, restrictions involving the capability of the test equipment used in this research limited the upper range of contact pressures possible to explore to 1600 MPa. All this information derived for these rail steels was based on plastic damage data collected from twin-disc samples due to the ability to precisely control the contact conditions creating the damage during twin-disc tests over a large number of contact cycles. In addition, a record of the contact conditions experienced during the twin-disc experiments was also able to be obtained.

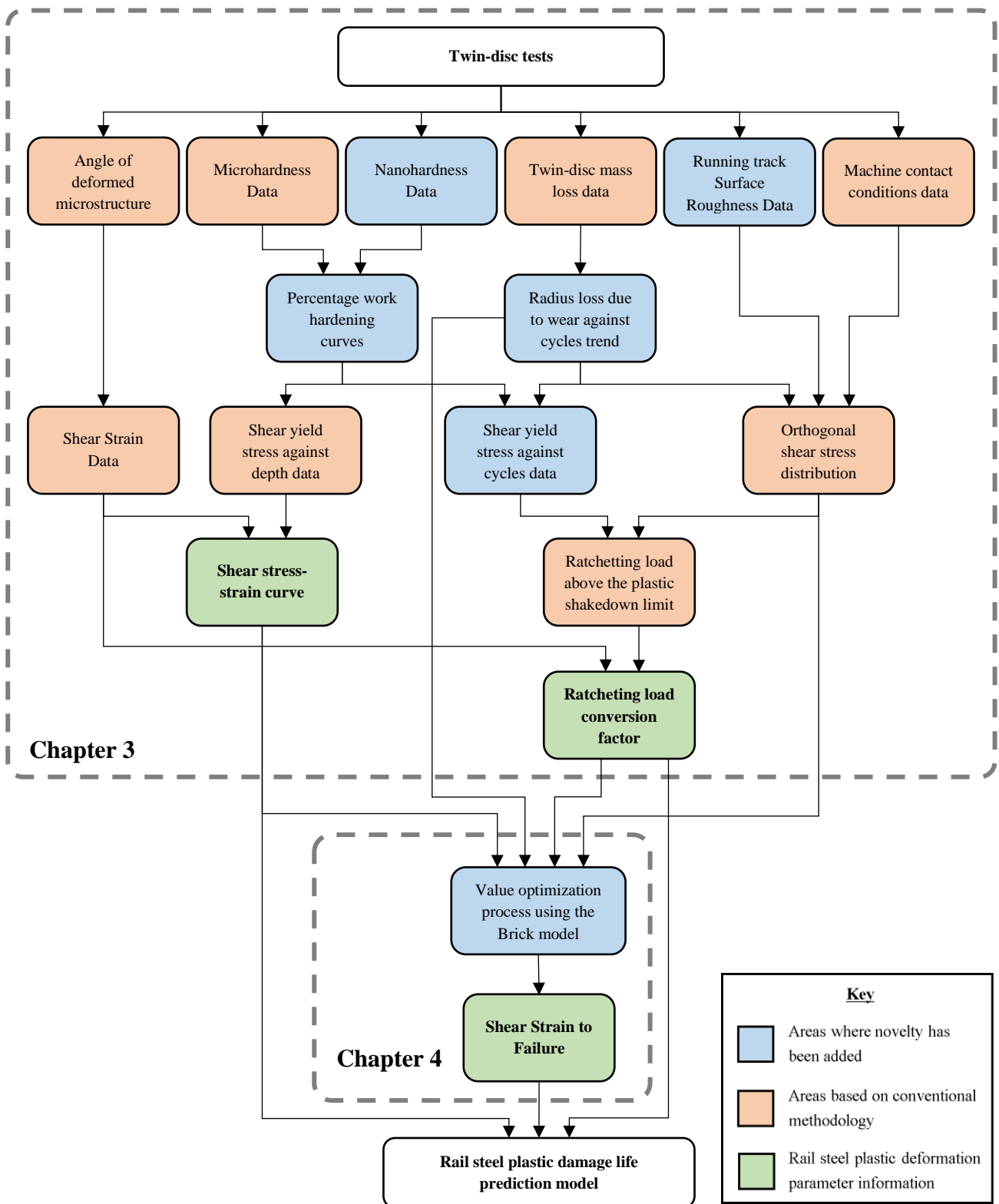


Figure 3.1: Analysis flow chart for calculating the shear stress-strain curve relationship, ratcheting load conversion factor, and shear strain to failure for rail steels.

3.2 Experimental Methodology

3.2.1 SUROS2 Twin-Disc Testing

To replicate in a laboratory environment the plastic damage rail steels experience under high compression and high shear cyclic loading conditions, twin-disc tests were conducted using the SUROS2 (Sheffield University Rolling Sliding) twin-disc machine. SUROS2 is a modified TE72 twin-disc machine designed by Phoenix Tribology that works using the same principles as the original SUROS twin-disc machine and was modified to accept the same 47mm diameter 10mm wide running track sample design [171]. This size of sample was advantageous as it can be machined directly out of the parent material of a full-scale railhead and railway wheel tread, enabling genuine rail and wheel steel to be used during a twin-disc test.

As shown in Figure 3.2, the SUROS2 twin-disc machine comprises of two roller driveshafts assemblies, onto which a pair of twin-disc samples are each fitted to conduct a test. The roller driveshaft used by the wheel sample was fixed whereas the roller driveshaft used by the rail sample was able to traverse across the machine worktable via a linear slider to allow the discs to be brought in and out of contact. The level of the rail roller driveshaft could be adjusted to enable twin-disc samples to be configured with $\pm 1^\circ$ skew misalignment during experiments. The driveshafts were independently rotated by two AC motors with power transferred to the driveshafts via timing belts. The timing belts on the machine could be changed to configure it with different pulley ratio, allowing rotational speeds and torque up to 3000 rpm and approximately 170 Nm, respectively, to be achieved for the roller driveshafts. To obtain creep in the twin-disc contact, the rotation speeds of the roller driveshafts were adjusted so that the running track surface velocity of the wheel sample was greater than that for the rail sample, i.e. simulating a driving wheel. The rotational speed and revolution count of the roller driveshafts were recorded via shaft encoders. In addition, a torque transducer connected to the rail roller driveshaft records the torque for subsequent calculation of traction coefficient at the disc contact. The twin-disc samples were loaded together using a pneumatic air bellows capable of normal contact forces up to 8.2 kN, equivalent to a maximum contact pressure up to 1600 MPa. A load cell mounted between the pneumatic air bellow and the rail roller driveshaft frame records the normal contact force and, consequently, maximum contact pressure within the contact. To cool the twin-disc samples during tests, an electronic fan was mounted and directed towards each of the specimens. The sensing and control equipment communicate with a central computer and were managed using COMPEND software [194].

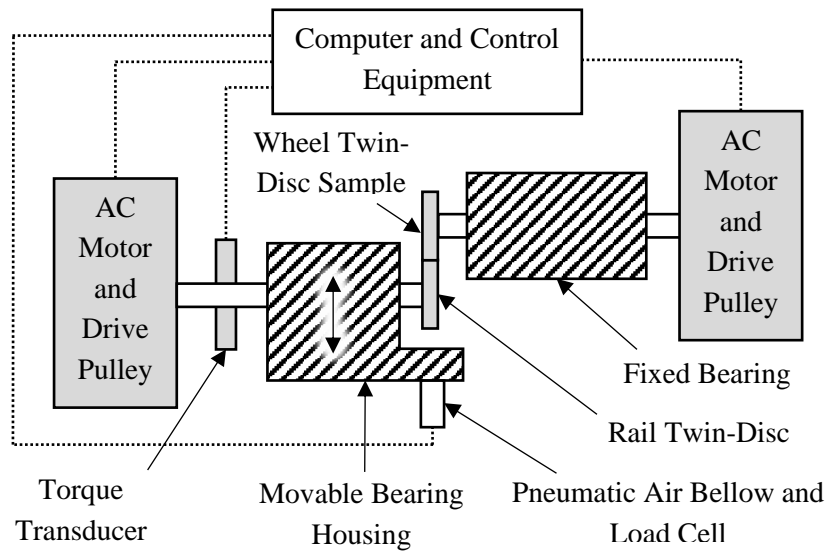


Figure 3.2: Schematic diagram of the SUROS2 twin-disc machine.

A summary of the twin-disc tests conducted in this investigation is tabulated in Table 3.1. For the six different combinations of rail-wheel material pairing and contact conditions investigated, two types of twin-disc tests were conducted. The experiments that were regularly interrupted every 10,000 contact cycles were conducted to understand the rail steel wear behaviour trend for each condition. The uninterrupted tests, however, were performed to collect data characterising the plastic damage observed under different contact cycle durations. The data collected from these uninterrupted tests, was then primarily used to derive information such as the shear stress-strain curve, ratcheting load conversion factor, and the shear strain at failure for each condition. The experiments were performed across closely spaced increments of contact cycle duration for each condition examined, so although no repeat tests under identical conditions were conducted any anomalies in the experiments would have been identified.

Table 3.1: Summary of the different rail-wheel material and contact conditions investigated. The number in brackets indicates any tests that have been repeated.

| Cond. | Rail Steel Grade | Wheel Steel Grade | Contact Type | Maximum Contact Pressure (MPa) | Slip (%) | Nominal Speed (RPM) | Total Number of Contact Cycles for the Rail Sample |
|-------|------------------|-------------------|--------------|--------------------------------|----------|---------------------|---|
| 1 | R260 | R8T | Dry | 1500 | -1 | 400 | 80k in 10k increments (3), 500 (2), 15k (2), 40k (2), 70k (2) |
| 2 | HP335 | R8T | Dry | 1500 | -1 | 400 | 80k in 10k increments (3), 15k, 40k, 70k |
| 3 | R350HT | R8T | Dry | 1500 | -1 | 400 | 80k in 10k increments (3), 15k, 40k, 70k |
| 4 | R260 | R8T | Dry | 1200 | -1 | 400 | 80k in 10k increments, 15k, 40k, 70k |
| 5 | R260 | R8T | Dry | 900 | -1 | 400 | 120k in 10k increments, 15k, 40k, 70k |
| 6 | R260 | R8T | Dry | 600 | -1 | 400 | 120k in 10k increments, 15k, 40k, 70k |

To ensure the sample metallurgies examined were representative of actual rail and wheel steel, the twin-disc samples were respectively machined out of a full-scale railhead and railway wheel tread, as illustrated in Figure 3.3. The running track of these twin-disc samples machined was ground to an average surface roughness R_a of less than $0.5 \mu\text{m}$. Prior to testing these discs, both the rail and wheel samples were cleaned in an ultrasonic bath with acetone to remove any oily residue that could influence the tribological behaviour of the twin-disc contact. In addition, the mass, running track width, and running track diameter of the twin-disc samples was measured at the start, during each interruption, and at the end of each experiment conducted. The mass of the specimens was recorded using an Adam Nimbus 214i analytical balance to a resolution of $\pm 0.001 \text{ g}$, while the specimens running track diameter and width was measured using a pair of Mitutoyo digital callipers to a resolution of $\pm 0.01 \text{ mm}$. A thermometer and hygrometer were used to record the temperature and relative humidity conditions of the SUROS2 laboratory at the start of each experiment, recording an average of 19.4°C and 47% across the experiments. The standard deviation observed with these readings was 2.5°C and 7%, respectively. Traction coefficient data is particularly sensitive to environmental conditions, but no outliers were observed to suggest the tests were significantly influenced by the laboratory environment.

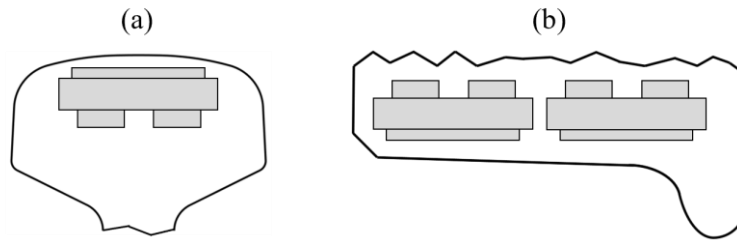


Figure 3.3: Illustration of the orientation the (a) rail and (b) wheel twin-disc samples were machined out of a full-sized rail and railway wheel.

3.2.2 Surface Roughness Measurements

To assess the degree to which asperity contacts helps drive the subsurface plastic deformation observed within the rail twin-disc samples, an understanding of the specimens running track surface roughness evolution was needed. To collect this surface roughness data, 3D scans of the tested rail and wheel twin-disc samples running track was recorded using an Alicona PortableRF infinite focus microscope equipped with a x10 magnification lens. The running track of an unused R260 twin-disc sample was also scanned to provide a baseline measurement of what the specimens surface roughness would be like at the start of the experiments. From these 3D scans, topography and surface roughness parameter data was extracted for 2D line profiles orientated parallel to the specimen's circumferential direction with a cut-off length of 250 μm . As the wear flakes present on heavily plastically deformed samples during dry experiments were typically flattened back down when within the twin-disc contact, the 2D line profiles were purposely drawn in areas exhibiting no wear flakes. This was done to prevent the wear flakes peeling away from the specimens running track from over exaggerating the true surface roughness responsible for driving the subsurface plastic damage.

3.2.3 Metallurgical Sample Preparation and Optical Microscopy

To observe the plastic deformation inside the uninterrupted twin-disc samples, metallurgical samples were sectioned to reveal the circumferential plane halfway across the running track of the tested twin-disc samples, as shown in Figure 3.4. The metallurgical samples were taken from the portion of the discs where the elongated MnS inclusions were orientated parallel to the running track to ensure the data collected was representative of the correct orientation of the rail steel microstructure that is plastically deformed in full-scale rail-wheel contacts. This orientation of these inclusions was present in the microstructure of all three rail steel metallurgies examined providing an indication of the rail sections longitudinal direction resulting from the hot rolled manufacturing process. The sectioned metallurgical samples were then mounted in Bakelite, ground using SiC paper to P1200 grit, followed by polishing using diamond and alumina suspension down to a 0.05 μm surface finished. A 2% Nital

etching solution was used to reveal the rail steels microstructural plastic damage for optical microscopy. Optical micrographs of the plastic damage present in the etched metallurgical samples were captured using a Nikon Eclipse LV150 optical microscope with Buhler Omnimet 9.5 software.

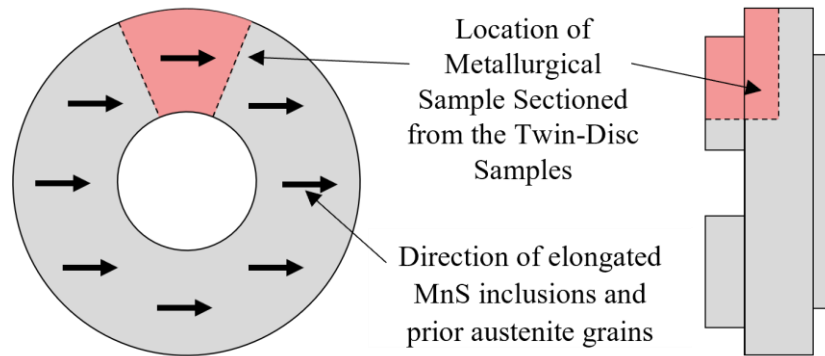


Figure 3.4: Illustration showing how the metallurgical specimens were sectioned from the twin-disc samples in relation to the orientation of the elongated MnS inclusions.

3.2.4 Hardness Testing

Both microhardness and nanohardness testing were conducted on the polished metallurgical samples to characterise the hardness against depth data below the specimens running surface. The microhardness testing was used to measure the hardness against depth data in the bulk of the material, whereas nanohardness testing was conducted to quantify the data near the running track surface. The microhardness data were collected from the polished metallurgical samples using a Struers Duramin-40 microhardness indenter with an array of indents performed at a minimum depth of 60 μm up to 1.5 mm below the running surface in 20 μm increments. These indents were performed using a 50 g indentation load with a 15 s dwell time to allow the indents to be as small as feasibly possible to minimise the indents separation required, while still being large enough to measure. To comply with the spacing requirements in the British Standard BS EN 6507-1:2018 [195], the indent array was staggered into three columns with a column separation of 100 μm .

The nanohardness tests were conducted using a Bruker Hysitron TS 77 Select nanohardness indenter utilising the mechanical property mapping feature. The mechanical property maps consisted of a 10 x 10 grid of nano indents equally separated by 3 μm with each indent taken using a standard Berkovich diamond tip with an indentation load of 2 mN. Nanohardness values were derived from the indenter properties and load against displacement curves using the Oliver and Pharr method [196]. For each metallurgical sample tested, two datasets were collected: i) a plastic deformation region dataset consisting of a 4 x 10 grid of mechanical property maps equally separated by 30 μm , with the long axis of the grid orientated perpendicular to the specimens running surface. ii) An undeformed region dataset consisting of a 5 x 8 grid of mechanical property maps equally separated by 100 μm located

at a minimum depth of 2 mm below the twin-disc samples running surface. The depth of the nano indents relative to the twin-disc samples running surface was measured directly from optical micrographs.

A measure of the average undeformed hardness for the three rail steel grades investigated was also collected during microhardness testing. For this data, ten 10 kg indentation load indents with a 15 s dwell time were performed on each rail steel grade. The location of these indents was in the undeformed substrate far away from any observable plastic damage.

A survey of the hardness variation across the cross-sectional railhead profile of the parent rail that the twin-disc samples tested in this work originated from was also conducted. The purpose of these survey's was to confirm sufficient material was available in the railhead of the parent rail to machine twin-disc samples out of without the specimens having any hardness or microstructural variation. For this data, a grid array of 98 indents were performed using a Durascan 70 hardness tester on slices of the parent railhead material for each of the three rail steels investigated. Each of these indents were conducted using a 10 kg indentation load with a 15 s dwell time.

3.3 Experimental Results

3.3.1 Railhead Cross-Section Hardness Results

Figure 3.5(a-c) shows the cross-sectional hardness variation data collected from a railhead slice of the parent rail for the three rail steels tested. The results obtained from the R260 (Figure 3.5a) and HP335 (Figure 3.5c) samples showed that these two rail steels exhibited a near uniform variation of hardness and microstructure across the railhead. For R350HT (Figure 3.5c), however, a region of elevated hardness was observed beneath the running surface of the railhead, as expected of a heat-treated rail grade. The depth of this elevated hardness region was observed up to a depth of 25-30 mm below the rail's running surface. These results implied that for the orientation chosen to extract the twin-disc samples out of the parent rail, illustrated in Figure 3.3b, there was sufficient material in the parent rail for the twin-disc samples to have uniform hardness and microstructure for all three rail grades examined in this work.

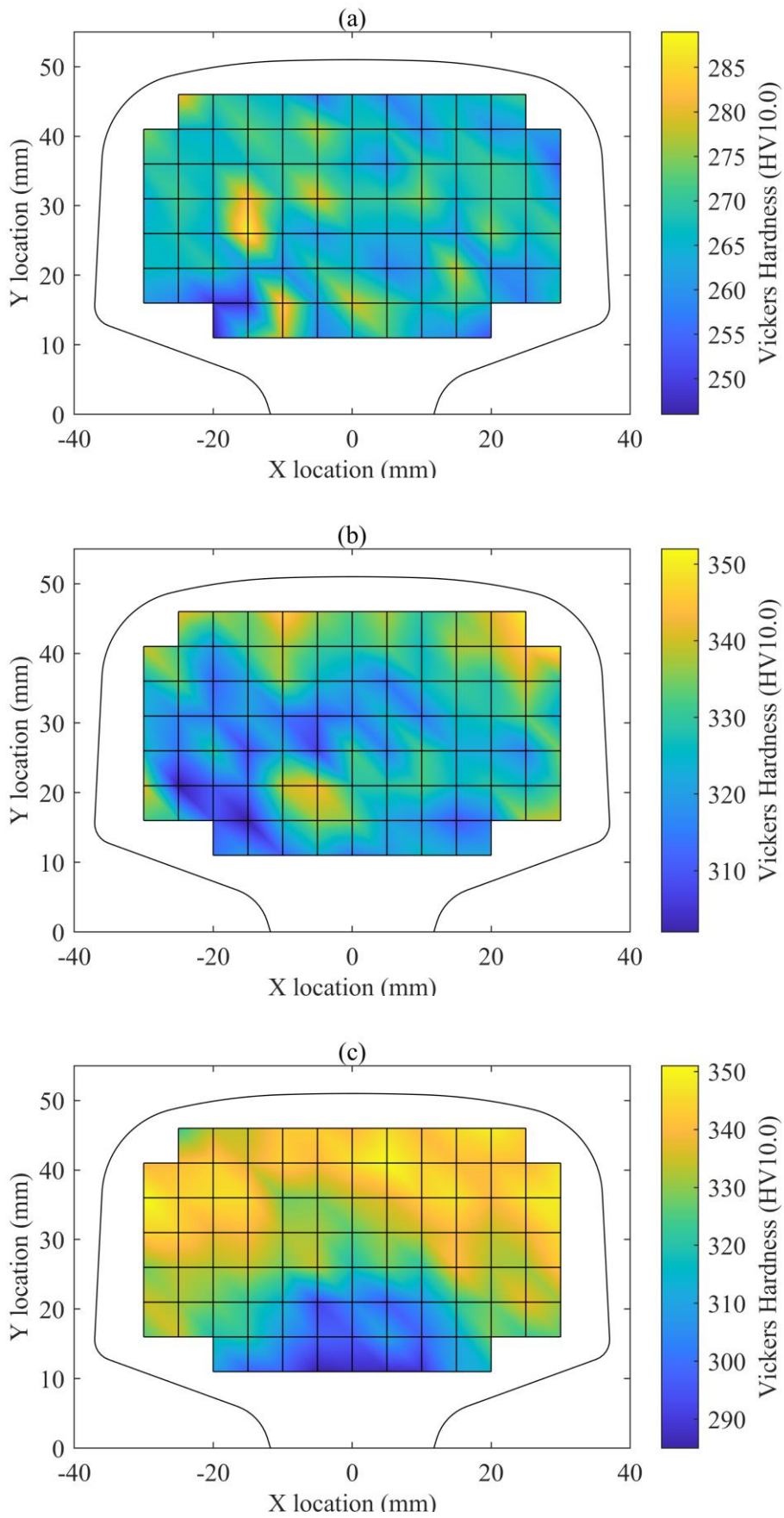


Figure 3.5: Hardness maps showing the variation of hardness for the subsurface railhead material from the parent rail of the (a) R260, (b) HP335, and (c) R350HT twin-disc samples.

3.3.2 Rail Steel Wear Performance Results

The evolution of the rail steels wear rate with contact cycles calculated from interrupted twin-disc test mass change results are shown in Figure 3.6(a-b). In Figure 3.6a comparing the wear rate evolution of the three different rail steel metallurgies (R260, HP335, R350HT) under 1500 MPa, dry contact conditions a clear ranking was observed once steady-state wear conditions were achieved. The results showed HP335 rail steel wearing the least (14.15 $\mu\text{g}/\text{cycle}$), followed by R350HT (17.65 $\mu\text{g}/\text{cycle}$) and then R260 (22.96 $\mu\text{g}/\text{cycle}$). In terms of the onset of steady-state wear conditions, this was achieved by the rail steels R260, HP335, and R350HT at 30,000, 40,000, and 50,000 contact cycles, respectively.

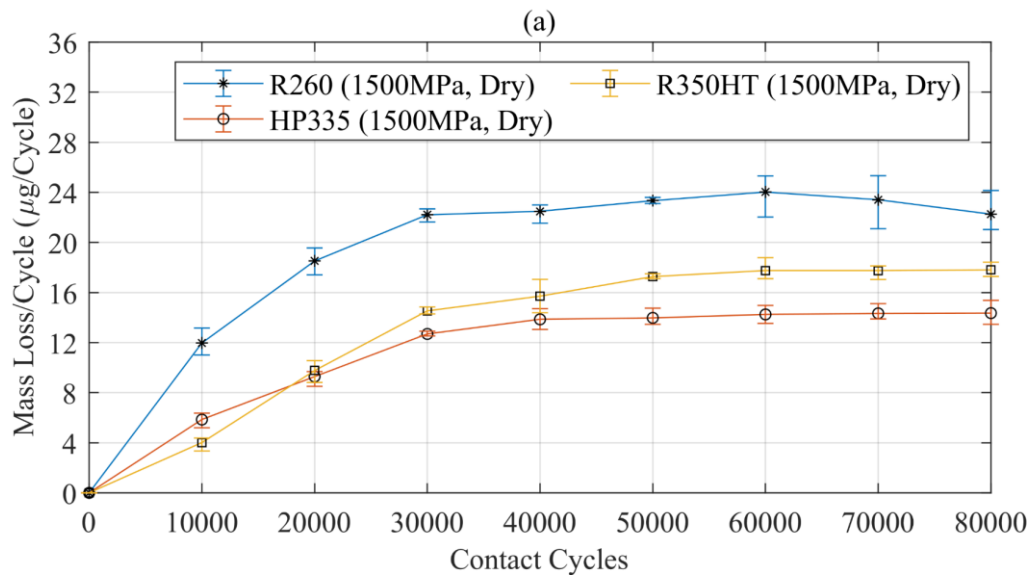


Figure 3.6: Mass loss per cycle against contact cycles results comparing (a) the three different rail steels R260, HP335, and R350HT tested under 1500 MPa, 1% slip, dry contact conditions and (b) R260 rail steel under the four different contact pressures (1500 MPa, 1200 MPa, 900 MPa, 600 MPa) and dry contact conditions.

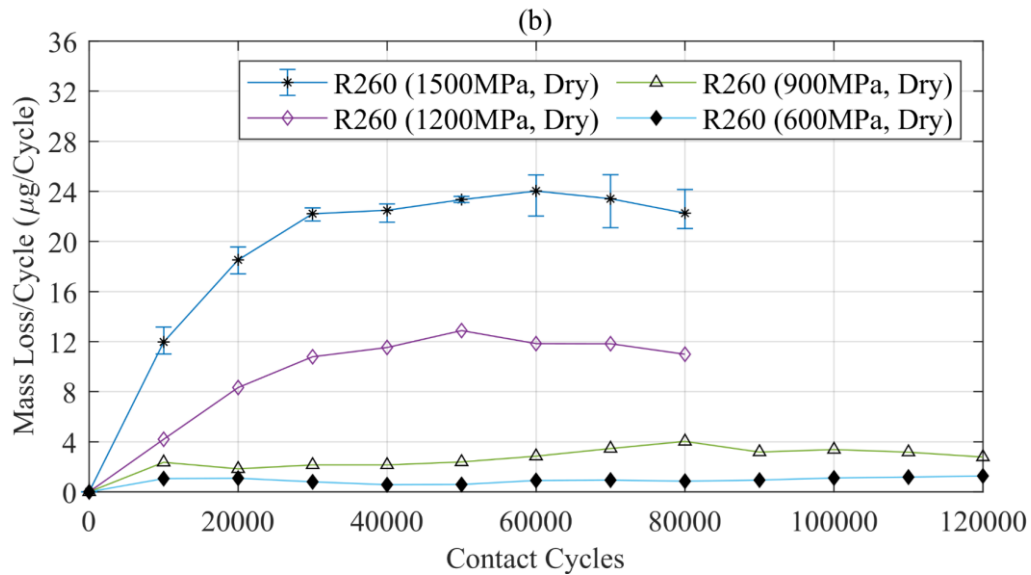


Figure 3.6: Continued.

In Figure 3.6b comparing the wear rates of R260 under the four different maximum Hertzian contact pressures (1500 MPa, 1200 MPa, 900 MPa, 600 MPa), the wear rates decreased with lower contact pressure. The tests conducted with 1500 MPa and 1200 MPa contact pressure showed steady-state wear conditions being achieved by 30,000 and 40,000 contact cycles, respectively. The experiments conducted under 900 MPa and 600 MPa contact pressure, however, showed a different cyclic wear rate behaviour, with wear rates staying relatively constant throughout the tests.

3.3.3 Coefficient of Traction Results

A comparison of the coefficient of traction results recorded from the SUROS2 twin-disc machine during the 70,000 contact cycles uninterrupted experiment for all six conditions investigated is shown in Figure 3.7. The coefficient of traction data obtained for all the uninterrupted twin-disc tests performed are presented in Appendix A1 as Figure A1.1. The results in Figure 3.7 show that after an initial spike at the start of the experiment, the coefficient of traction recorded during the R260 tests under all four contact pressures investigated plateaued in the range of 0.34-0.37 later into the experiment. The HP335 and R350HT tests conducted under 1500 MPa, dry contact conditions, however, showed a continuous decrease in the coefficient of traction with increasing contact cycles. At the end of the 70,000 contact cycles experiment, the coefficient of traction for the HP335 and R350HT tests had decreased to 0.24 and 0.23, respectively.

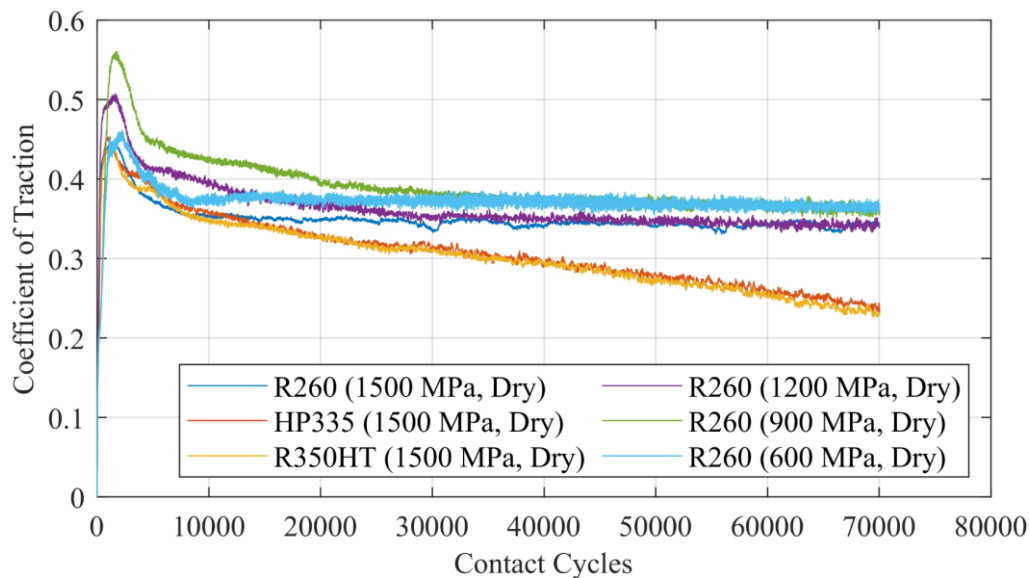


Figure 3.7: Comparison of the coefficient of traction results collected during the uninterrupted 70,000 contact cycles twin-disc test from the SUROS2 twin-disc machine for the R260 (1500 MPa, 1200 MPa, 900 MPa, 600 MPa), HP335 (1500 MPa) and R350HT (1500 MPa) conditions.

This continuous decrease in coefficient of traction observed during the HP335 and R350HT experiments was an artefact caused by the rail steels higher wear resistance compared to the wheel steel grade used in these tests. This was because the wheel steel twin-disc samples were observed to wear more and thus reduce their running track diameter faster compared to the rail steel twin-disc samples. The fact that the wheel sample rotated faster than the rail sample and that the disc speeds were not adjusted to compensate for the wear rate meant the increasing disc diameter dissimilarity resulted in the slippage decreasing within the twin-disc contact. For the HP335 and R350HT uninterrupted tests under 1500 MPa, dry contact conditions, the slippage within the twin-disc contact decreased from -1% to -0.52% and -0.66%, respectively, at the end of the 70,000 contact cycles experiment. The slippage within the twin-disc contact of the uninterrupted R260 test under identical contact conditions, however, only slightly increased after the 70,000 contact cycles experiment from -1% to -1.05%. According to Carter's creep force law [25], as the twin-disc contact slippage decreases past a point and tends towards full rolling conditions, the coefficient of traction decreases and approaches zero as a result. This argument was supported by the coefficient of traction results shown in Figure 3.8 comparing the data obtained from the uninterrupted and interrupted HP335 experiments. The results show that the interrupted HP335 test, which had the disc speeds adjusted to compensate for the changing running track diameter did not observe the continuous decrease in the coefficient of traction in contrast to the uninterrupted test.

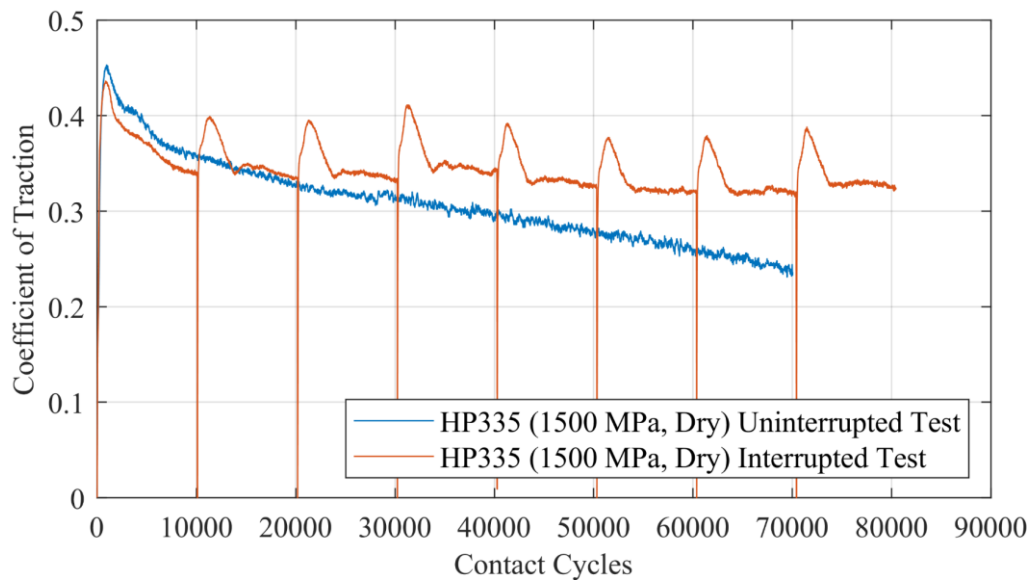


Figure 3.8: Comparison of the traction coefficient curves obtained for the uninterrupted and one of the interrupted twin-disc tests for HP335 against R8T under 1500 MPa, dry contact conditions.

Overall, the implications of this continuous decrease in the coefficient of traction means that the wear rates would be expected to taper off with increasing contact cycles for the HP335 and R350HT uninterrupted tests rather than exhibit steady-state wear behaviour. In hindsight, the experiments should have been designed to avoid this oversight, which will be further discussed in Section 3.7.2. For material information characterising the plastic deformation behaviour of HP335 and R350HT the expected tapering of wear rates during the experiments were account for in the data analysis to compensate. The adjustments made to the calculations are explained later in this chapter.

3.3.4 Asperity Geometry Results

A typical example of the roughness topography data obtained for one of the 2D line profiles drawn on the twin-disc samples running track 3D scans is shown in Figure 3.9.

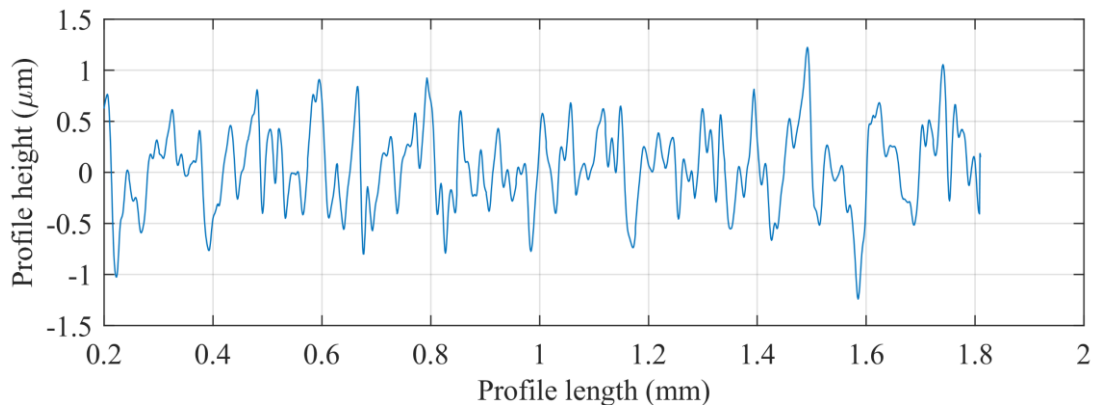


Figure 3.9: 2D roughness profile data obtained from the running track of an unused R260 twin-disc sample using the infinite focus microscope with a 250 µm cut off length.

To utilise the Nowell and Hills roughness model [48], which has been used later on for calculating the ratcheting load conversion factor (explored in section 3.5), the tip radius and separation of significant asperities on the rail and wheel sample running track needed to be measured. To obtain this, a procedure was devised for measuring the necessary data from the roughness topography results. In this procedure, the significant asperities were first identified from the topography data using a height criterion based on a fixed percentage of the roughness profiles Rz roughness parameter (mean roughness profile peak to valley height) relative to the profiles mean line. This height criterion used in this work was similar to the one used to identify significant profile peaks and troughs for measuring the Rsm roughness parameter (mean separation of profile irregularities) in the standard BS EN ISO 4287:1998 [197]. In the standard, a default value of 10% is usually used; however, different values were explored in this work to understand how this choice influences the result calculated later on. For each significant asperity identified a circular relationship was then fitted to the profile data points to measure the asperity's tip radius. The fitting of this circular relationship was pinned at the two nearest points where the profile crosses the mean line with the circles centre located midway between these two points. The maximum height of the circular relationship was also fixed using the maximum profile height of each significant asperity identified. The separation of significant asperities was determined by measuring the profile length between the centres of each fitted circular relationship. An illustration of this procedure to measure the tip radius and separation of significant asperities from the 2D roughness profile data is presented in Figure 3.10.

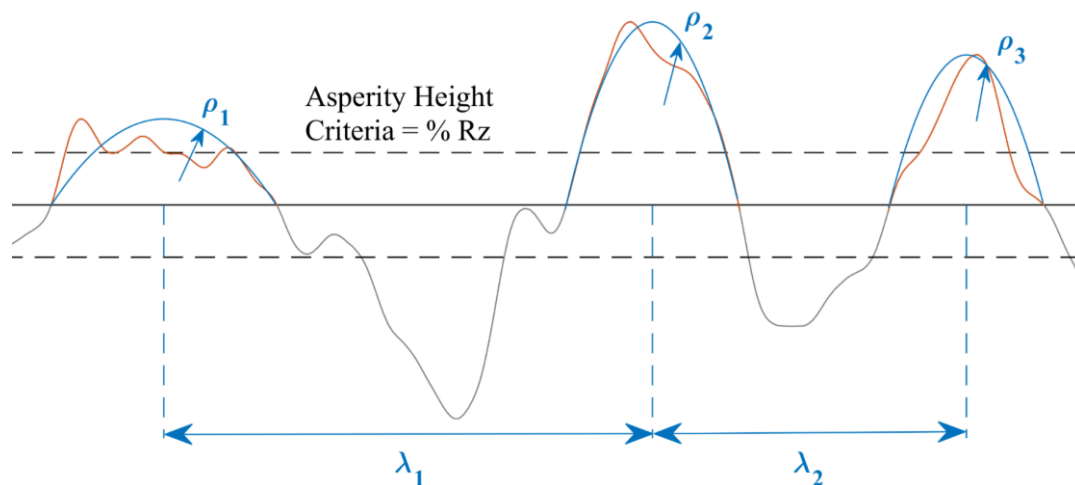


Figure 3.10: Illustration showing how the asperity tip radius, ρ_a , and separation, λ_a , was measured from the 2D roughness profile data.

To describe the natural variation of the asperity tip radius and separation data measured from the twin-disc samples running track a Birnbaum-Saunders probability distribution function [198] was fitted to the results. After fitting to the data, the shape and size of the Birnbaum-Saunders distribution

could be inputted into models using a scale parameter α and a shape parameter β . The reason a Birnbaum-Saunders distribution was fitted to the results was because this type of probability distribution function provided the best fit to describe the observed distribution of the asperity tip radius and separation data. An example of a Birnbaum-Saunders distribution fitted to the asperity tip radius data measured from the new twin-disc sample running track is shown in Figure 3.11.

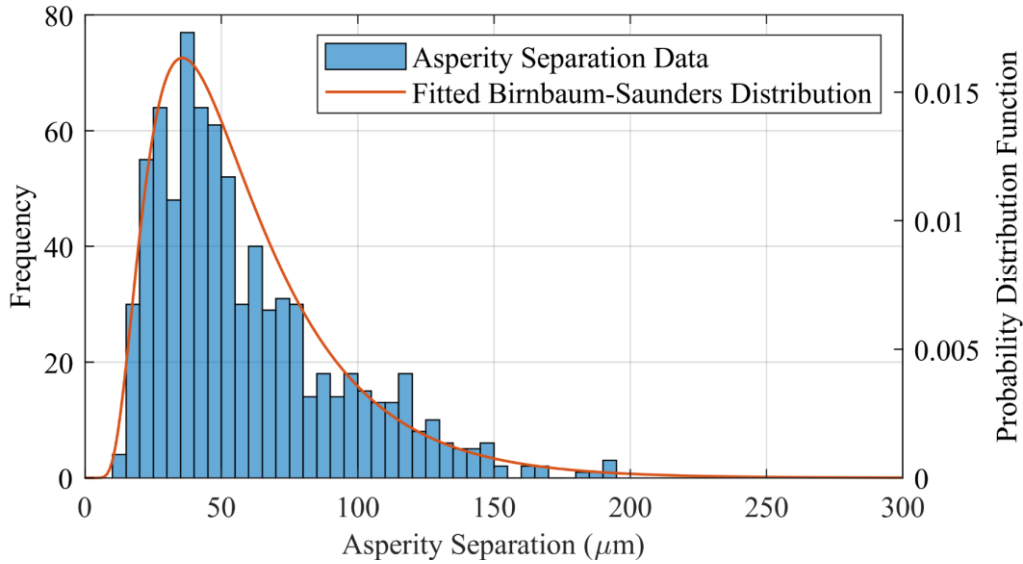


Figure 3.11: Comparison of the histogram of the asperity separation measured from the R260 twin-disc samples running surface tested up to 70,000 contact cycles under 1500 MPa, dry contact conditions and the Birnbaum-Saunders distribution fitted to the results.

Figure 3.12 and 3.13 shows a comparison of the Birnbaum-Saunders distribution curves fitted to the asperity tip radius and separation data collected from the running surface of the rail and wheel specimen, respectively, from the 1500 MPa R260 test using a 10% Rz minimum height criterion. The Birnbaum-Saunders distributions derived for all six conditions investigated are presented in Appendix A1 as Figures A1.2-A1.7. The variation with contact cycles of the asperity tip radius and separation based on the location of the distributions peak and the distributions width in Figure 3.12, showed that the asperity tip radius on the rail sample tended to become sharper later into the experiment compared to as new condition. In addition, the asperities on the rail samples running surface also tended to be situated closer together later into the experiment compared to the as new condition.

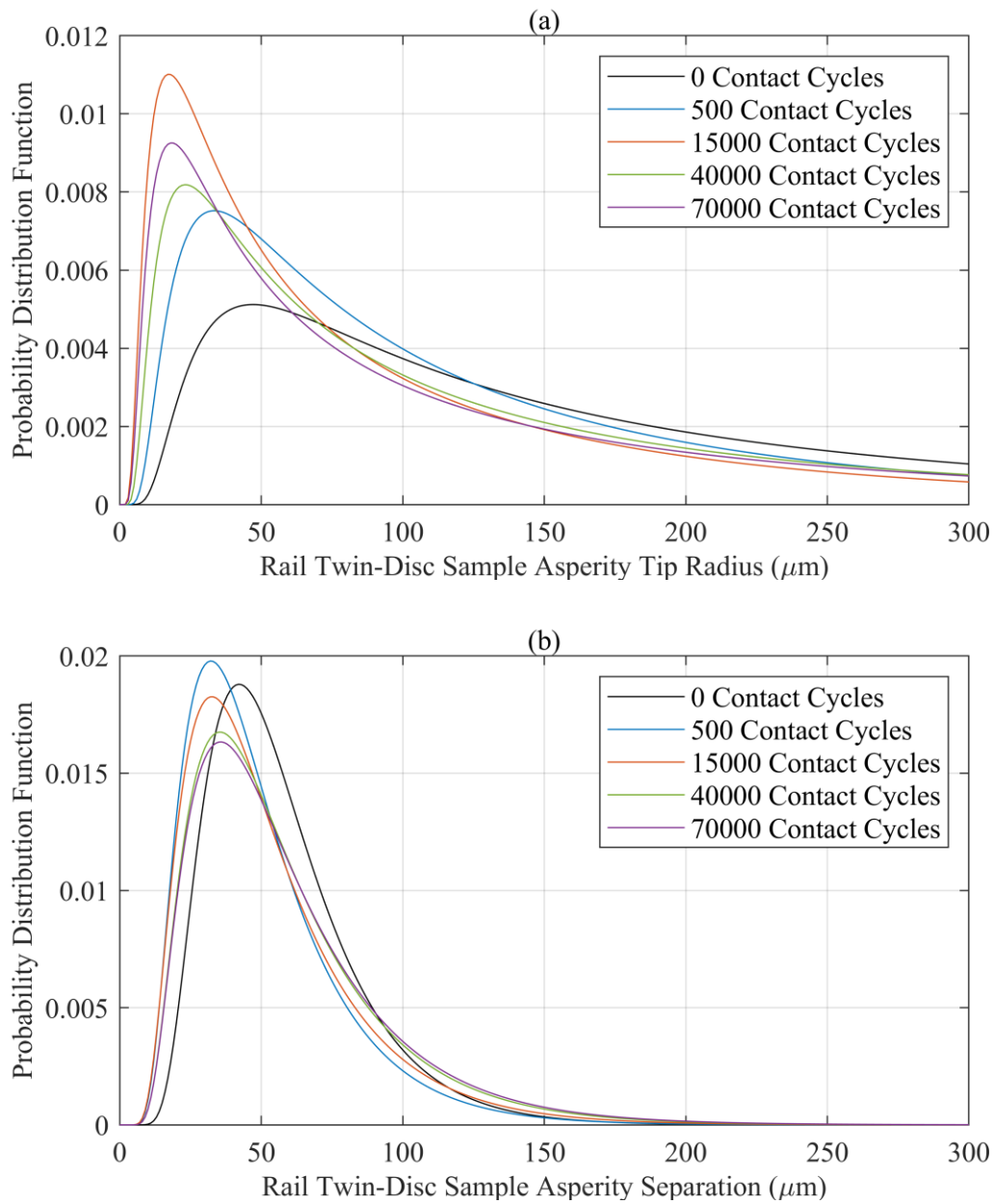


Figure 3.12: Comparison of the Birnbaum-Saunders distributions fitted to the (a) asperity tip radius and (b) asperity separation results from the rail twin-disc sample from the R260 and R8T uninterrupted twin-disc test conducted under 1500 MPa, dry contact conditions.

The Birnbaum-Saunders distribution curves presented in Figure 3.13 derived for the wheel samples tested in the same experiments showed no clear variation with contact cycles behaviour for the asperity tip radius. The variation with contact cycles for wheel sample asperity separation tended to be situated closer together at 500 contact cycles compared with the as new condition. From the longer duration experiments, however, the asperities on the rail samples tended to become more spaced out with a wider distribution.

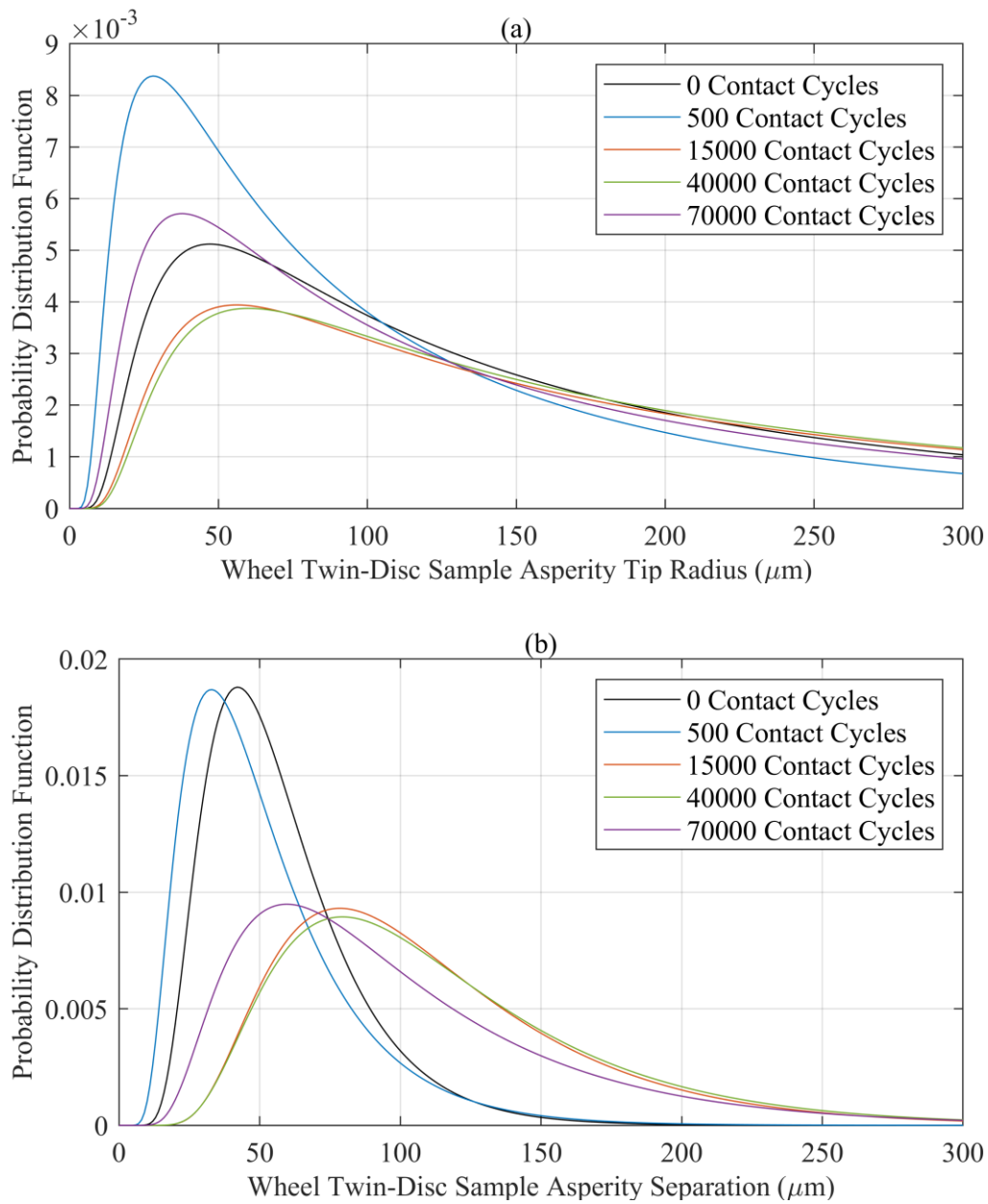


Figure 3.13: Comparison of the Birnbaum-Saunders distributions fitted to the (a) asperity tip radius and (b) asperity separation results measured from the wheel twin-disc sample from the R260 and R8T uninterrupted twin-disc test conducted under 1500 MPa, dry contact conditions.

For the other conditions examined the change of the asperity tip radius and separation probability distributions for the different contact cycles durations tested remained broadly the same. The only difference observed was regarding the asperity separation on the wheel twin-disc sample for the R260 experiments conducted under lower contact pressures. As the separation of asperities on the wheel contact tended to not increase as much compared to the as new condition for the lower contact pressure tests, with the asperity separation remaining constant throughout the test for the 600 MPa condition.

3.3.5 Hardness Results

An example of the microhardness against depth results collected from the uninterrupted R260 twin-disc samples tested under 1500 MPa, dry contact conditions is shown in Figure 3.14. The microhardness against depth data obtained for all six conditions investigated are shown in Appendix A1 as Figure A1.8.

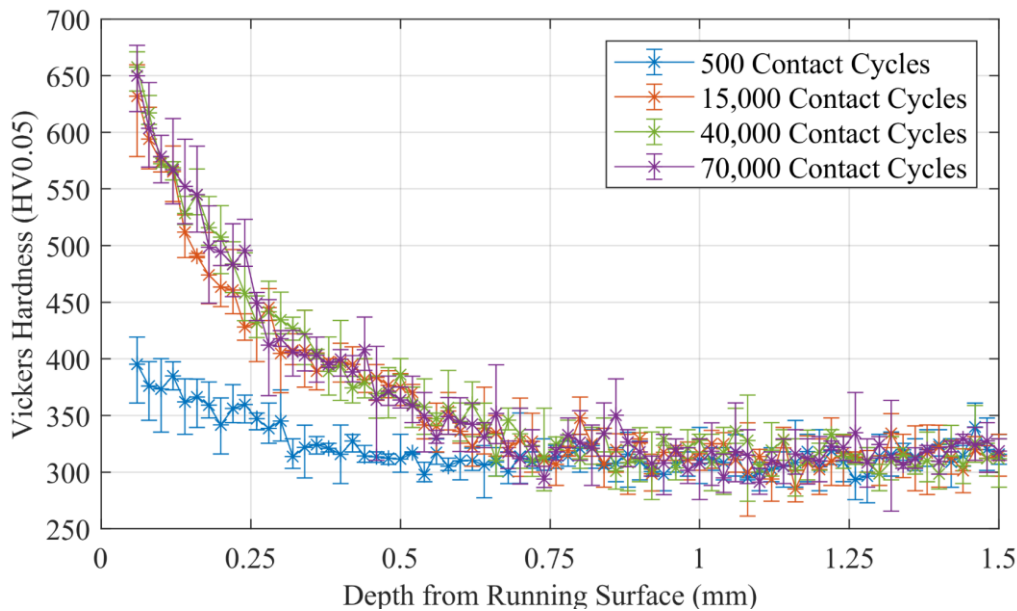


Figure 3.14: Microhardness against depth data collected from the R260 twin-disc samples tested under 1500 MPa, dry contact conditions for 500, 15000, 40000, and 70000 contact cycles.

A comparison of the microhardness against depth results obtained from the twin-disc samples tested up to 70,000 contact cycles for all six conditions examined is shown in Figure 3.15(a-b). In Figure 3.15a comparing the results for the three rail steel metallurgies (R260, HP335, R350HT) tested under 1500 MPa, dry contact conditions, R260 presented the most plastic deformation up to a depth of approximately 700 μm . In contrast, HP335 and R350HT exhibited roughly identical depths of plastic damage up to about 400 μm . For depths between 0-400 μm below the twin-disc samples running surface, the microhardness against depth results for all three rail steel grades were roughly identical and followed the exact same hardness against depth trend, even though the rail steels investigated had different undeformed baseline hardness's.

In Figure 3.15b comparing R260 under different contact pressures for dry conditions, the depth of hardness increase is reduced for the experiments conducted under lower maximum contact pressures. The depth of raised hardness decreased from 700 μm at 1500 MPa, to 500 μm at 1200 MPa, and 250 μm at 900 MPa. There was only a marginal change in the depth of plastic deformation, however,

observed between the R260 twin-disc samples conducted under 900 MPa and 600 MPa contact pressure.

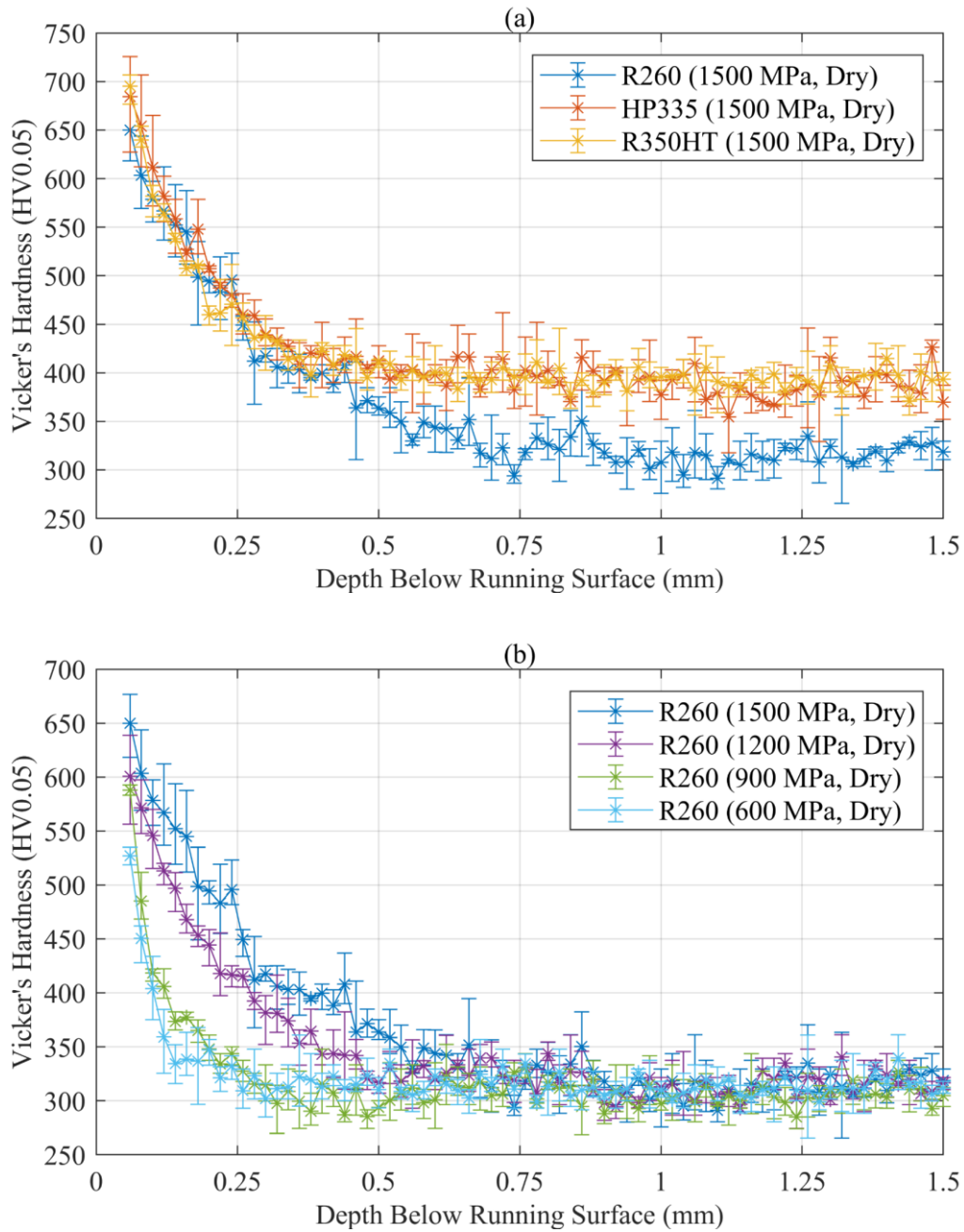


Figure 3.15: Comparison of the microhardness against depth results obtained from the uninterrupted 70,000 contact cycle test for a) R260 (1500 MPa), HP335 (1500 MPa), and R350HT (1500 MPa); and b) R260 (1500 MPa, 1200 MPa, 900 MPa, 600 MPa) under dry contact conditions.

Figure 3.16 shows an example of the nanohardness data measured from the uninterrupted R260 twin-disc samples tested under 1500 MPa, dry contact conditions. The nanohardness data obtained for all six conditions investigated is presented in Appendix A1 as Figure A1.9.

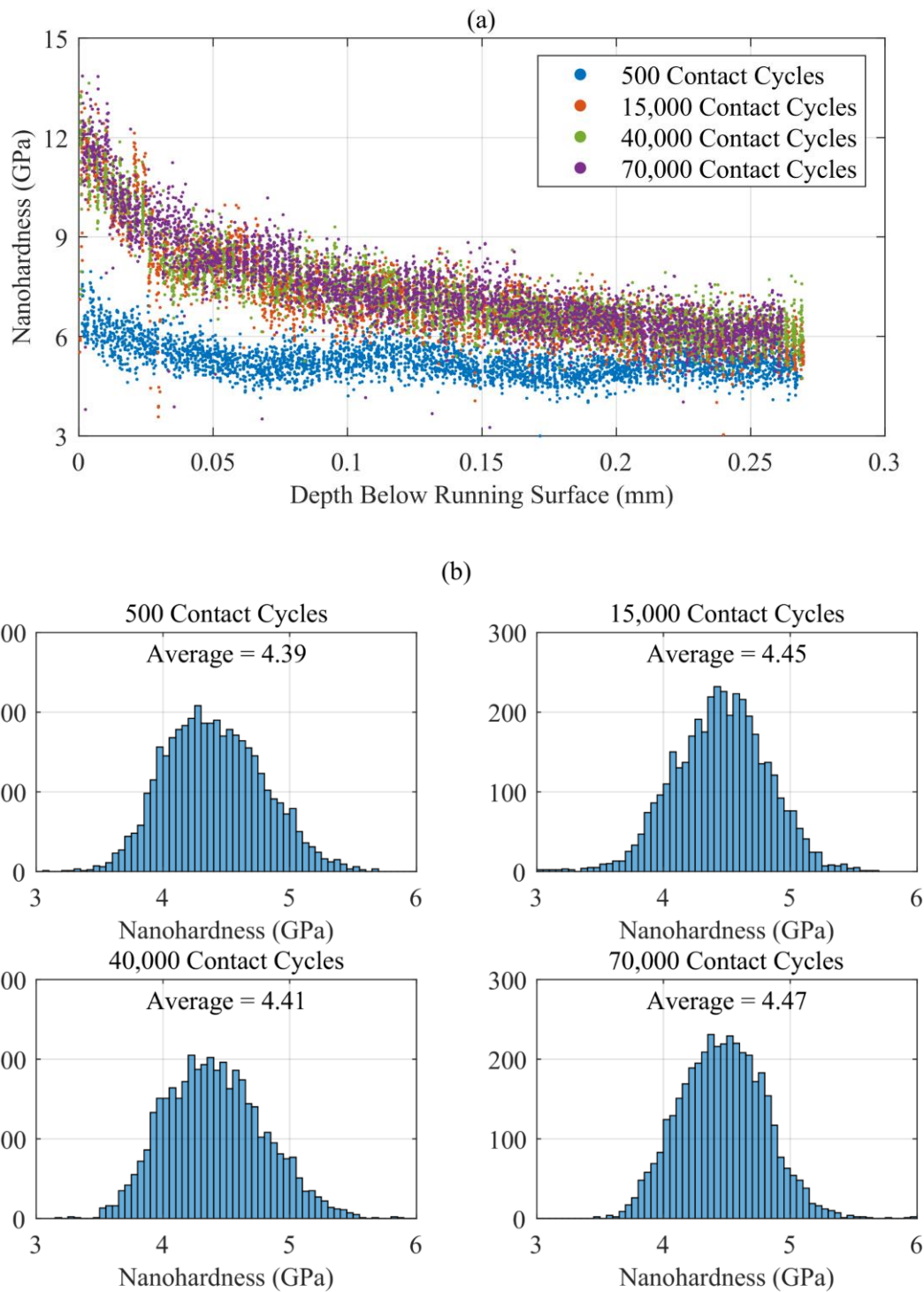


Figure 3.16: a) Nanohardness against depth and b) bulk undeformed nanohardness data collected from the R260 twin-disc samples tested under 1500 MPa, dry contact conditions for 500, 15000, 40000, and 70000 contact cycles.

Figure 3.17(a-b) shows the nanohardness against depth results obtained from the 70,000 contact cycles uninterrupted twin-disc test for all six conditions investigated. For all six conditions examined the rail steels achieved roughly identical values of hardness of about 12 GPa at the running surface.

In addition, for data collected at very shallow depths of less than about 50-100 μm there was a noticeable uptick in the trend of the nanohardness against depth results compared to the data collected at much greater depths below the running surface.

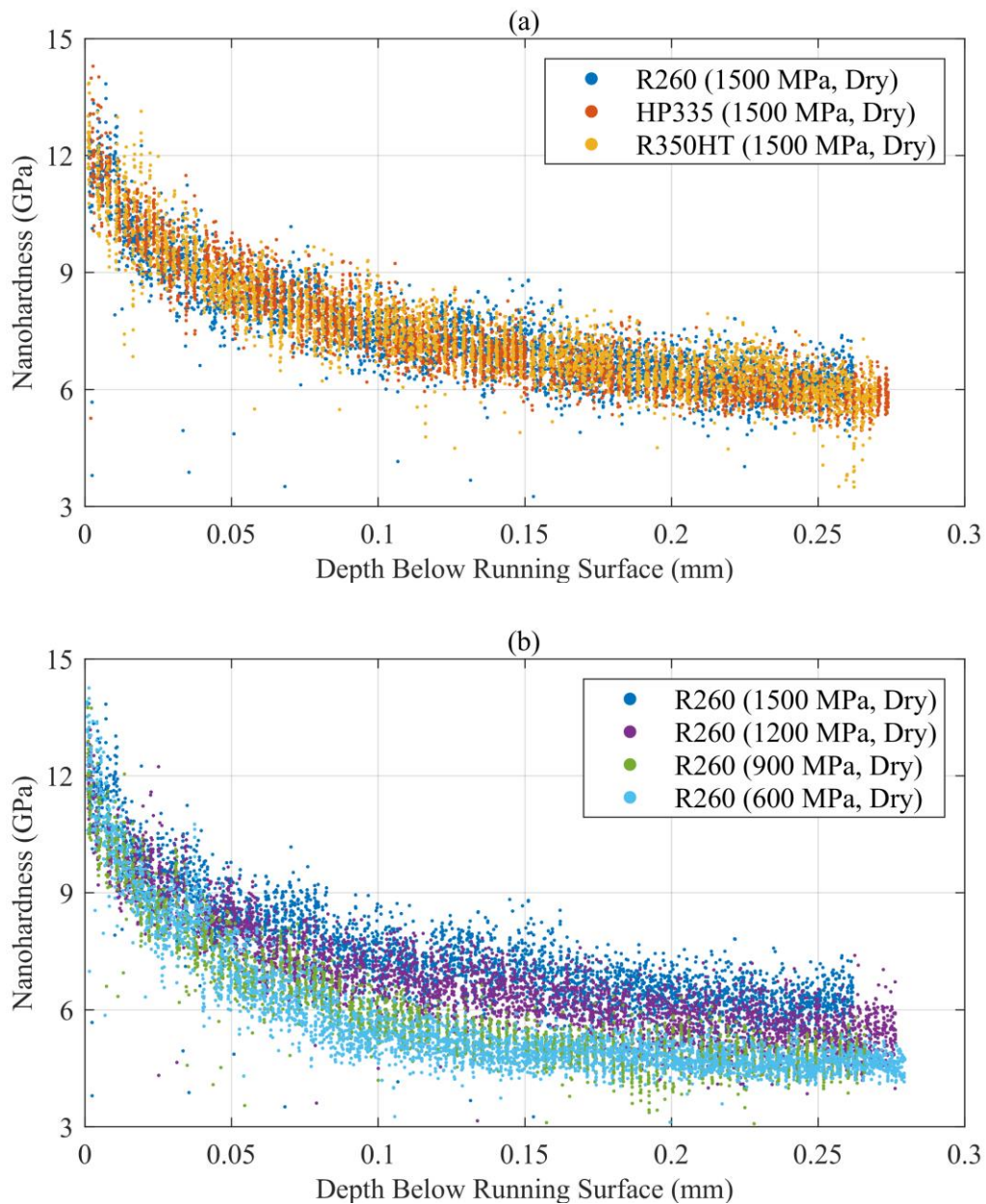


Figure 3.17: Comparison of the nanohardness against depth data obtained from the twin-disc samples tested up to 70,000 contact cycles a) R260 (1500 MPa), HP335 (1500 MPa), and R350HT (1500 MPa); and b) R260 (1500 MPa, 1200 MPa, 900 MPa, 600 MPa) under dry contact conditions.

As different indentation loads were used to collect the microhardness and nanohardness data, the two hardness datasets were combined by normalising the results in terms of percentage work hardening based on their respective hardness measurement of the rail steels undeformed substrate. This

normalisation process avoids issues with the indentation size effect that prevents direct comparison of the magnitude of the hardness measurements using different indentation loads. This manifests itself through an observed increase in hardness with decreasing indentation size, where the increased hardening occurs due to geometrical necessary dislocations being generated from the large strain gradients in small indentations [199]. After normalising the data an expression in the form of Equation 3.1 was then fitted to derive relationships of the percentage work hardening against depth. A weighting was applied to the microhardness results in proportion to the volume of microhardness data compared to the nanohardness data collected.

$$\frac{H}{H_0} = A \exp(Bx) + C \exp(Dx) + 100 \quad \text{Equation 3.1}$$

where A, B, C, D are coefficients found by fitting the expression to the combined data. The two exponential terms in the expression allow fitting to both the bulk and asperity contact driven contributions to the plastic damage. Figure 3.18 shows an example of the percentage work hardening against depth relationships derived from the combined microhardness and nanohardness data. As can be seen, the normalised microhardness data presented the same hardness against depth trend compared to the normalised nanohardness data but offset about 30 μm deeper below the running surface. The reason for this offset was thought to be due to the different indent size between the techniques. The larger size of microhardness indents means that they would have been influenced by a larger strain field and thus affected by the surface plastic deformation at deeper depths compared to the smaller nanohardness indents. For the microhardness indentation, the average diagonal dimension d of the largest indents was about 20 μm and so based on half the British Standard separation requirements of $3d$ between indents [195], the expected radius of the indent strain field would be roughly 30 μm ($1.5d$).

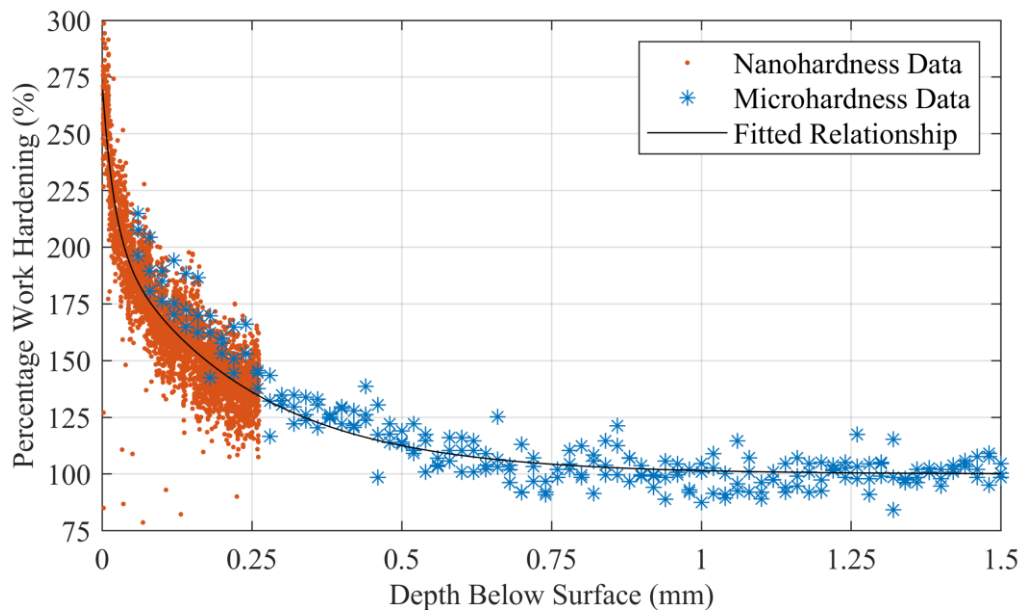


Figure 3.18: An example showing the percentage work hardening against depth relationships derived from the combined microhardness and nanohardness data.

The percentage work hardening against depth relationship derived from the combined microhardness and nanohardness data for all six conditions investigated is provided in Appendix A1 as Figure A1.10. A comparison of the percentage work hardening against depth relationships derived for the twin-disc samples tested up to 70,000 contact cycles for all six conditions is presented in Figure 3.19. The percentage work hardening relationships show that all the R260 samples achieved roughly similar percentage work hardening increases in the range of 260-275 % at the running surface. The HP335 and R350HT steels displayed roughly identical percentage work hardening increases to each other of about 210-225 % at the specimens running surface.

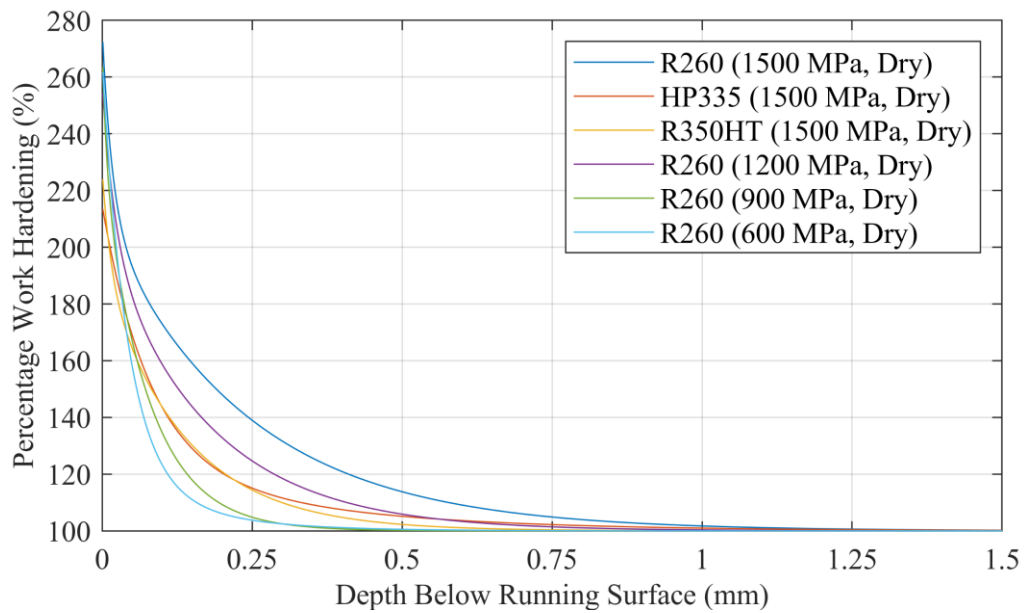


Figure 3.19: Comparison of the percentage work hardening against depth curve derived from 70,000 contact cycles uninterrupted test for R260 (1500 MPa, 1200 MPa, 900 MPa, 600 MPa), HP335 (1500 MPa), and R350HT (1500 MPa) under dry contact conditions.

3.3.6 Shear Strain Results

An example of an optical micrograph captured of the plastic damage observed in the tested samples is shown in Figure 3.20a. The shear strain data were measured from these optical micrographs, by measuring the angle θ of the observed deformed microstructure relative to the normal of the twin-disc samples running surface at different depths z below the twin-disc samples running surface, as shown in Figure 3.20b. These angles were then converted to shear strain using Equation 3.2.

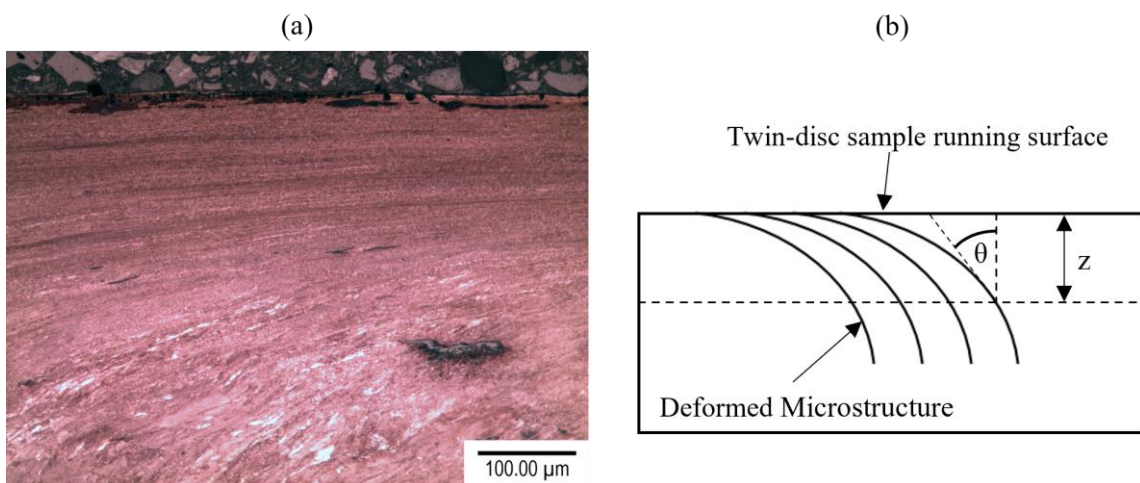


Figure 3.20: (a) Example of an optical micrograph of the plastic damage observed in the uninterrupted R260 sample tested up to 70,000 contact cycles under 1500 MPa, dry contact conditions. (b) Illustration showing how the angle of the deformed microstructure was measured.

$$\gamma = \tan(\theta)$$

Equation 3.2

A comparison of the shear strain data collected from the uninterrupted twin-disc experiments tested up to 70,000 contact cycles for the six conditions investigated is shown in Figure 3.21(a-b). The results showed that the calculated shear strains increased asymptotically with decreasing depth below the running surface. The spread of the shear strain data also increases with decreasing depth due in part to the increased error associated with converting the angles of the deformed microstructure into shear strain with Equation 3.2 as the angle approached 90°. In addition, there was also an observable increase in the amount of variation in the deformed microstructure angles at shallower depths, as exemplified in Figure 3.22.

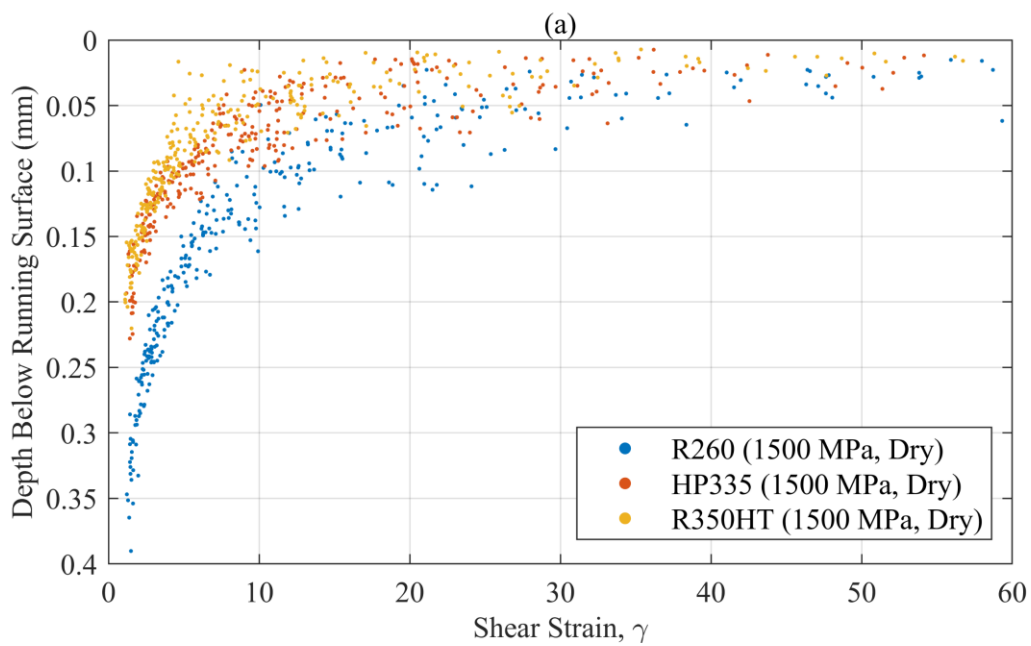


Figure 3.21: Comparison of the shear strain data collected from the uninterrupted tests tested up to 70,000 contact cycles for a) R260 (1500 MPa), HP335 (1500 MPa), and R350HT (1500 MPa); and b) R260 (1500 MPa, 1200 MPa, 900 MPa, 600 MPa) under dry contact conditions.

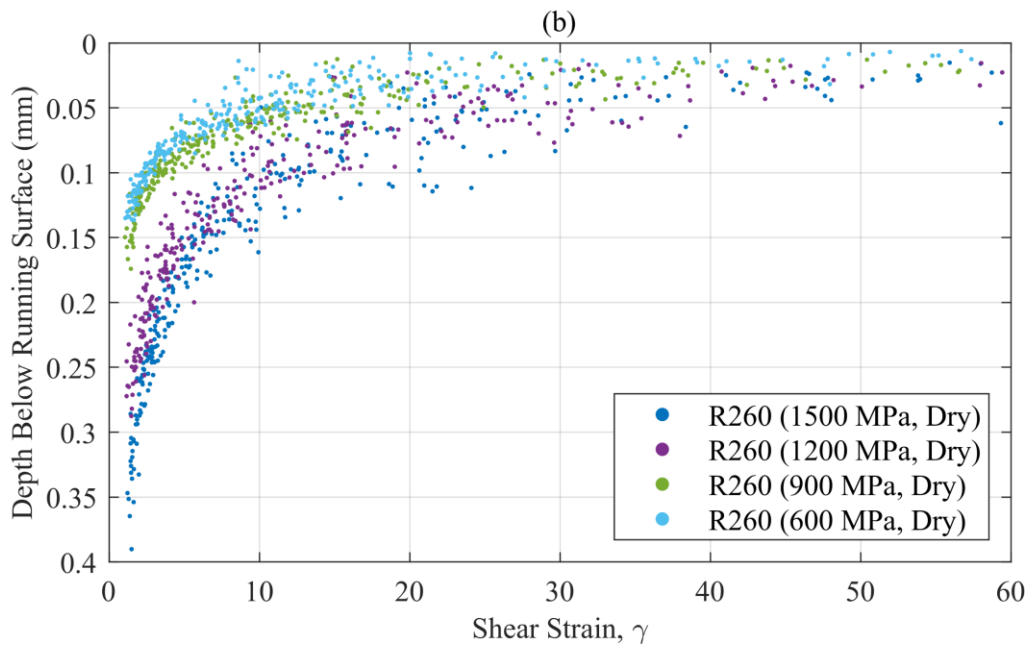


Figure 3.21: Continued.

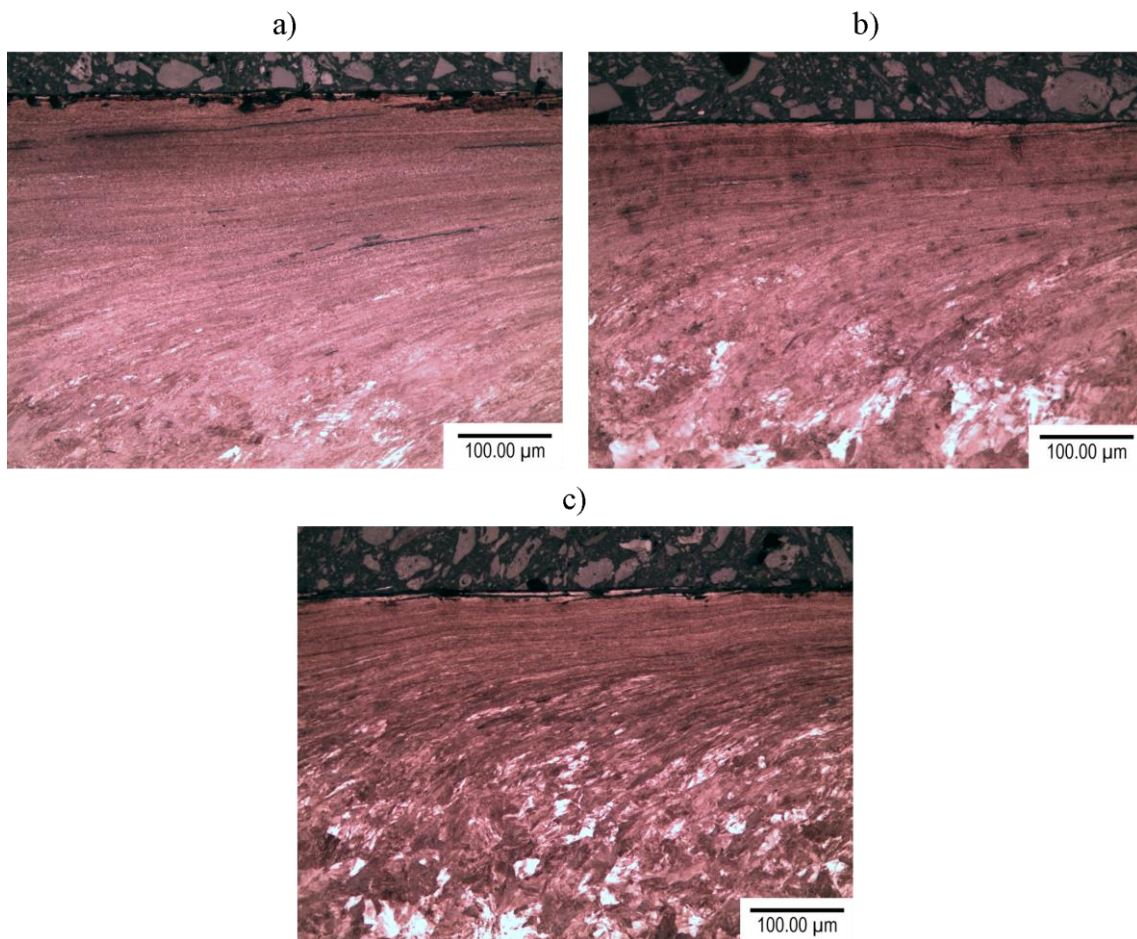


Figure 3.22: Examples of optical micrographs showing the variation in the angle of the deformed microstructure at the depth below the running surface from an a) R260, b) HP335, and c) R350HT twin-disc sample tested under 1500 MPa, dry contact conditions for 70,000 contact cycles.

3.4 Shear Stress-Strain Curve Relationship

3.4.1 Derivation Process

The shear stress-strain curves were derived from the uninterrupted 70,000 contact cycles samples for all six conditions using the same methodology simultaneously developed by Tomlinson et al. [193] and Alwahdi et al. [119]. In this method, shear strain, γ , and shear yield stress, k , data were collected in parallel and then combined to obtain the shear stress-strain curve. A modified Voce equation, given as Equation 3.3, was then fitted to the data to derive an expression for the shear stress-strain curve.

$$k = m(1 - e^{-n(\gamma)})^p \quad \text{Equation 3.3}$$

where m , n , p are coefficients found by fitting the modified Voce equation to the shear stress-strain curve data points. The shear yield stress data was obtained from the percentage work hardening relationships derived from the combined microhardness and nanohardness results, presented in Figure 3.19. These percentage work hardening curves were then converted to shear yield stress using the assumption that the increase in the percentage work hardening was proportional to the percentage increases in the rail steel shear yield stress, as given by Equation 3.4.

$$k = k_0 \left(\frac{H}{H_0} \right) \quad \text{Equation 3.4}$$

where k_0 is the rail steels initial shear yield strength. The rail steels initial shear strength was found by converting the average undeformed bulk hardness measured with a 10 kg indentation load using a hardness against tensile yield strength relationship derived for rail steels, shown in Figure 3.23.

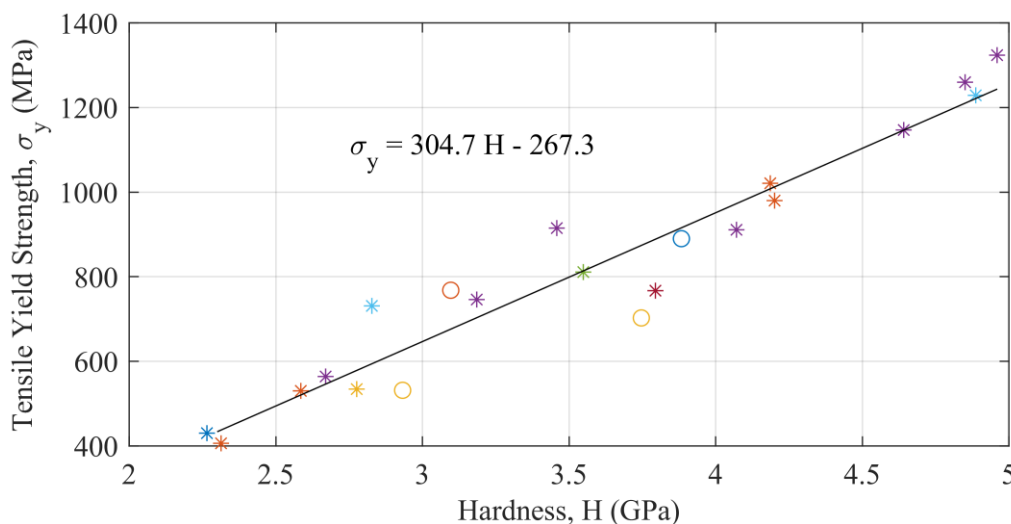


Figure 3.23: Hardness against tensile yield strength relationship derived for various rail steels of different metallurgies and microstructures (pearlite, bainitic, heat-treated). The different colour and style of marker denotes a different source the data was obtained from.

The data used to create the relationship shown in Figure 3.23 was obtained from hardness and tensile test results presented in academic literature and internal tests conducted within British Steel, which is summarised in Table 3.2. Due to the hardness results collected being generated under different indentation loads, the hardness data were normalised to correct the indentation size effect and to become based on a 10 kg indentation load. An understanding of the indentation size effect error with indentation load was characterised by measuring the apparent Vickers hardness reported by the Duramin-40 microhardness indenter for R260 for indentation loads ranging from 0.01 – 10 kg, see Appendix A2. Assuming the same size effect error correction could be applied to hardness results obtained using different hardness testers and rail steels with a different hardness compared to R260.

Table 3.2: Hardness against tensile yield strength relationship data collected from literature and internal tests conducted within British Steels for rail steels. HT denotes rail steel grades usually not heat-treated that were heat-treated. P denotes rail steel grades not specified consisting of a pearlitic microstructure. B denotes rail steel grades not specified consisting of a bainitic microstructure.

| Rail Steel Grade | Hardness | | ISE error (%) | Corrected Hardness (MPa) | Tensile Yield Strength (MPa) | Ref. |
|------------------|----------------|------|---------------|--------------------------|------------------------------|--------------|
| | Reported Value | MPa | | | | |
| R220 | 235 HV0.5 | 2.31 | 1.75 | 2.26 | 430.00 | [200] |
| BS11 | 240 HV0.5 | 2.40 | 1.75 | 2.31 | 406.00 | [117] |
| R260 | 288 HV0.5 | 2.83 | 1.75 | 2.78 | 534.20 | [201], [202] |
| R260 | 277 HV0.5 | 2.72 | 1.75 | 2.67 | 564.00 | [203] |
| R350HT | 350 HV0.1 | 3.43 | 7.24 | 3.19 | 746.00 | [204] |
| B360 | 380 HV0.1 | 3.73 | 7.24 | 3.46 | 915.00 | [204] |
| B1400 | 510 HV0.1 | 5.00 | 7.24 | 4.64 | 1147.00 | [204] |
| CrB | 460 HV0.1 | 4.51 | 7.24 | 4.19 | 1021.00 | [204] |
| B360 (HT) | 545 HV0.1 | 5.35 | 7.24 | 4.96 | 1324.00 | [204] |
| B1400 (HT) | 533 HV0.1 | 5.23 | 7.24 | 4.85 | 1260.00 | [204] |
| CrB (HT) | 537 HV0.1 | 5.27 | 7.24 | 4.89 | 1229.00 | [204] |
| R350HT | 365 HV1.0 | 3.58 | 0.90 | 3.55 | 811.00 | [205] |
| N.A. (P) | 415.6 HV100.0 | 4.07 | 0.00 | 4.07 | 911.00 | [206] |
| R260 | 288.3 HV31.25 | 2.83 | 0.00 | 2.83 | 731.00 | [207] |
| R370CrHT | 386.9 HV31.25 | 3.80 | 0.00 | 3.80 | 767.00 | [207] |
| N.A. (P) | 264 HV5.0 | 2.59 | 0.18 | 2.59 | 530.00 | [208] |
| N.A. (B) | 429 HV5.0 | 4.21 | 0.18 | 4.20 | 980.00 | [208] |
| R400HT | 396 HV20.0 | 3.88 | 0.05 | 3.88 | 890.00 | [209] |
| N.A. (P) | 329 HV0.2 | 3.23 | 4.06 | 3.10 | 768.00 | [210] |
| R260 | 299 BHN30 | 2.93 | 0.31 | 2.93 | 531.38 | [211] |
| HP335 | 382 BHN30 | 3.75 | 0.31 | 3.75 | 702.53 | [211] |

The tensile yield strength, k_0 , was then converted to a shear yield strength using Tresca's yield criterion, as given by Equation 3.5.

$$k_0 = \frac{\sigma_y}{2} \quad \text{Equation 3.5}$$

The initial shear yield strength data determined from the bulk undeformed hardness measurements for the three rail steels examined in this work is tabulated in Table 3.3.

Table 3.3: Shear yield strength results of R260, HP335, and R350HT rail steel.

| Rail Steel Grade | Hardness (HV10.0) | Tensile Yield Strength (MPa) | Shear Yield Strength (MPa) |
|------------------|-------------------|------------------------------|----------------------------|
| R260 | 285 | 584 | 292 |
| HP335 | 340 | 748 | 374 |
| R350HT | 350 | 779 | 390 |

3.4.2 Results

Figure 3.24 shows the shear stress-strain curve relationship data obtained for all six conditions investigated. The vertical error bars of the shear stress-strain curve data points represent the $\pm 1 \mu\text{m}$ uncertainty in measuring the depth component of the shear strain data. The horizontal error bars, however, signified the $\pm 0.5^\circ$ uncertainty in measuring the angle of the deformed microstructure used to quantify shear strain. As can be seen, the horizontal error bars increased in size at the higher shear strain data points due to the increased uncertainty associated with the nature of Equation 3.2 as the deformed microstructure approaches 90° . A summary of the coefficients for the modified Voce equation fitted to the shear yield stress against plastic shear strain data is listed in Table 3.4.

Table 3.4: Modified Voce equation coefficients for the shear stress-strain curve relationships for R260 (1500 MPa, 1200 MPa, 900 MPa, 600 MPa), HP335 (1500 MPa), and R350HT (1500 MPa) under dry contact conditions.

| Cond. | Rail Steel Grade | Maximum Contact Pressure (MPa) | Modified Voce Equation Coefficients | | |
|-------|------------------|--------------------------------|-------------------------------------|-------|-------|
| | | | m | n | p |
| 1 | R260 | 1500 | 700.328 | 0.009 | 0.145 |
| 2 | HP335 | 1500 | 726.369 | 0.045 | 0.164 |
| 3 | R350HT | 1500 | 763.459 | 0.048 | 0.168 |
| 4 | R260 | 1200 | 778.490 | 0.003 | 0.143 |
| 5 | R260 | 900 | 657.127 | 0.018 | 0.176 |
| 6 | R260 | 600 | 735.547 | 0.016 | 0.216 |

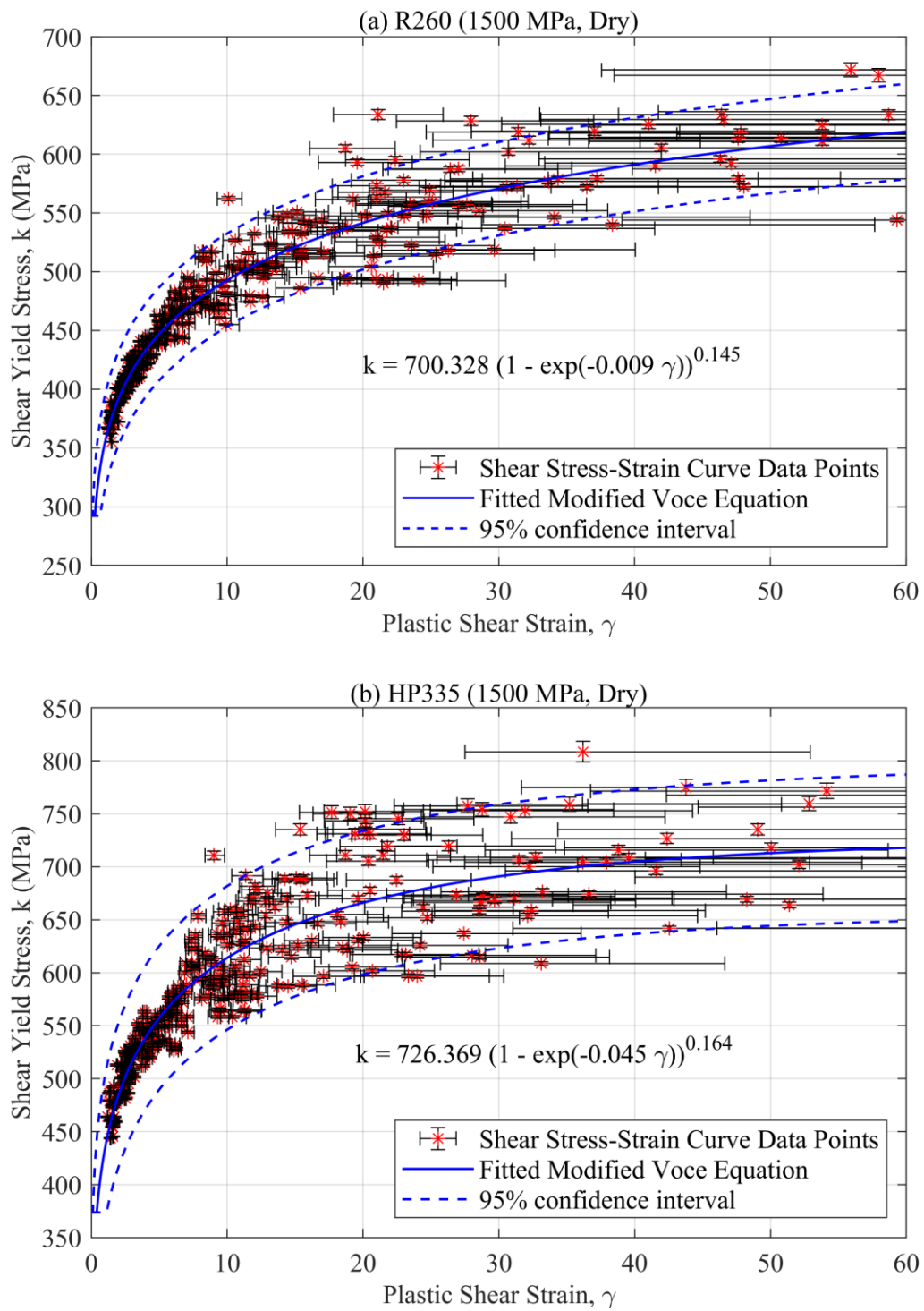


Figure 3.24: Shear stress-strain curve relationship derived for (a) R260 (1500 MPa), (b) HP335 (1500 MPa), (c) R350HT (1500 MPa), (d) R260 (1200 MPa), (e) R260 (900 MPa), and (f) R260 (600 MPa) under dry contact conditions.

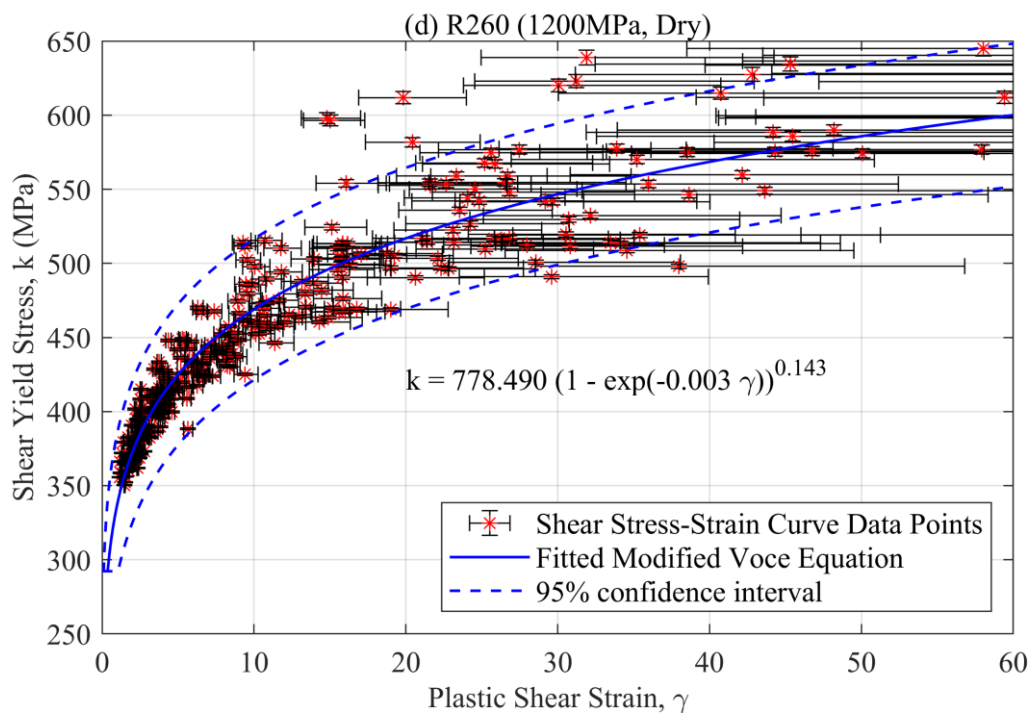
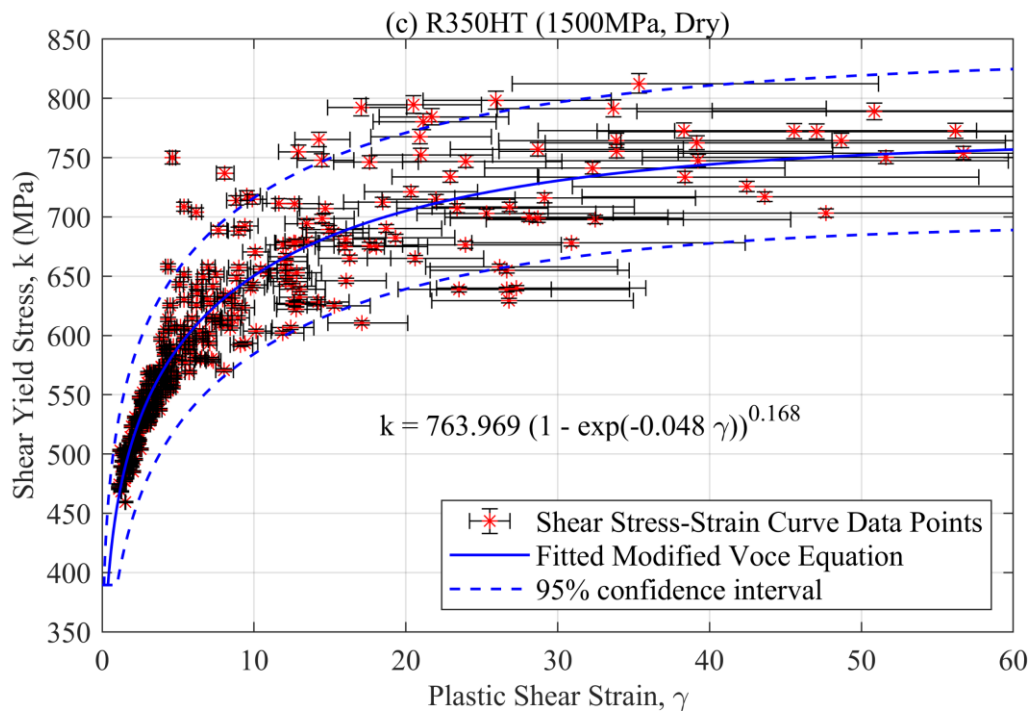


Figure 3.24: Continued.

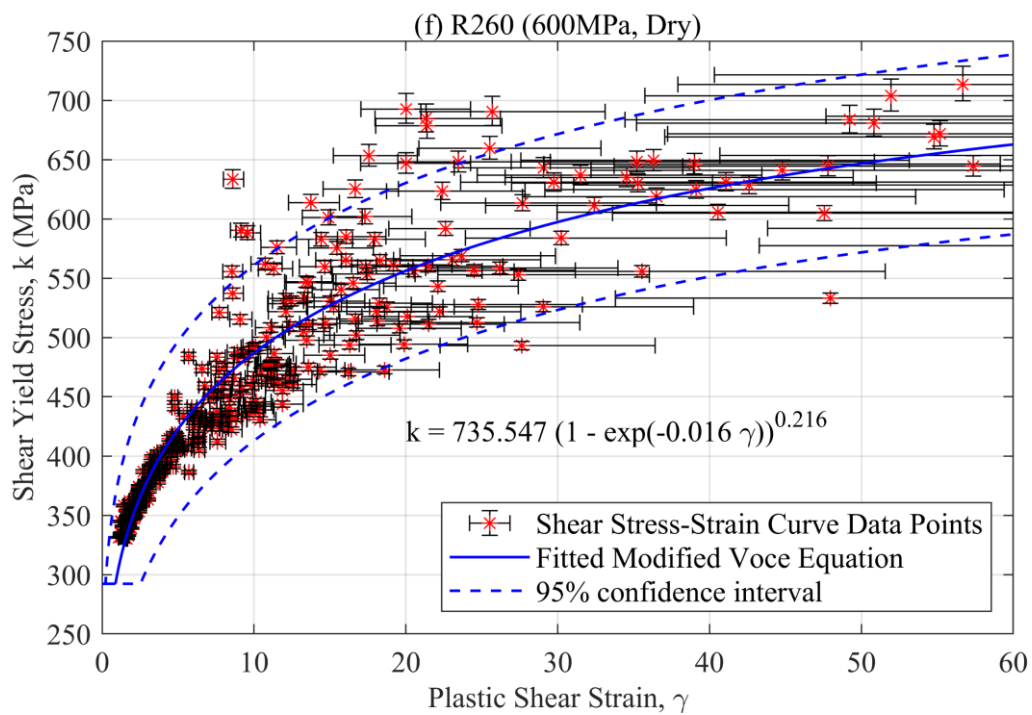
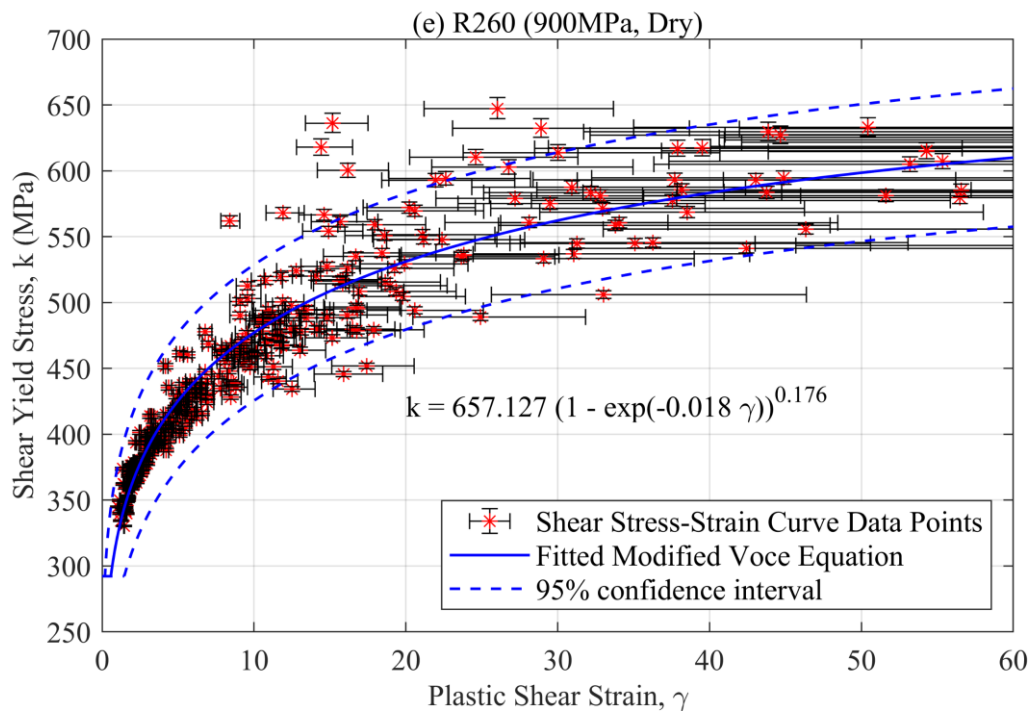


Figure 3.24: Continued.

A comparison of the shear stress-strain curves derived for the six conditions investigated is shown in Figure 3.25(a-b). In Figure 3.25a comparing the three rail steel grades under 1500 MPa, dry contact conditions, a ranking of the shear stress-strain curve could be established. The order in terms of the highest shear yield stress achieved was R350HT, HP335, and then R260. Comparison of the shear stress-strain curve results for R260 tested at 600-1500 MPa contact pressure and dry contact conditions are shown in Figure 3.25b. The results show that the shear stress-strain curves were very

close to one another across the contact pressures tested, showing near independence from the contact pressure, particularly at lower shear strains for which the data was least affected by uncertainties in strain measurement very close to the running surface.

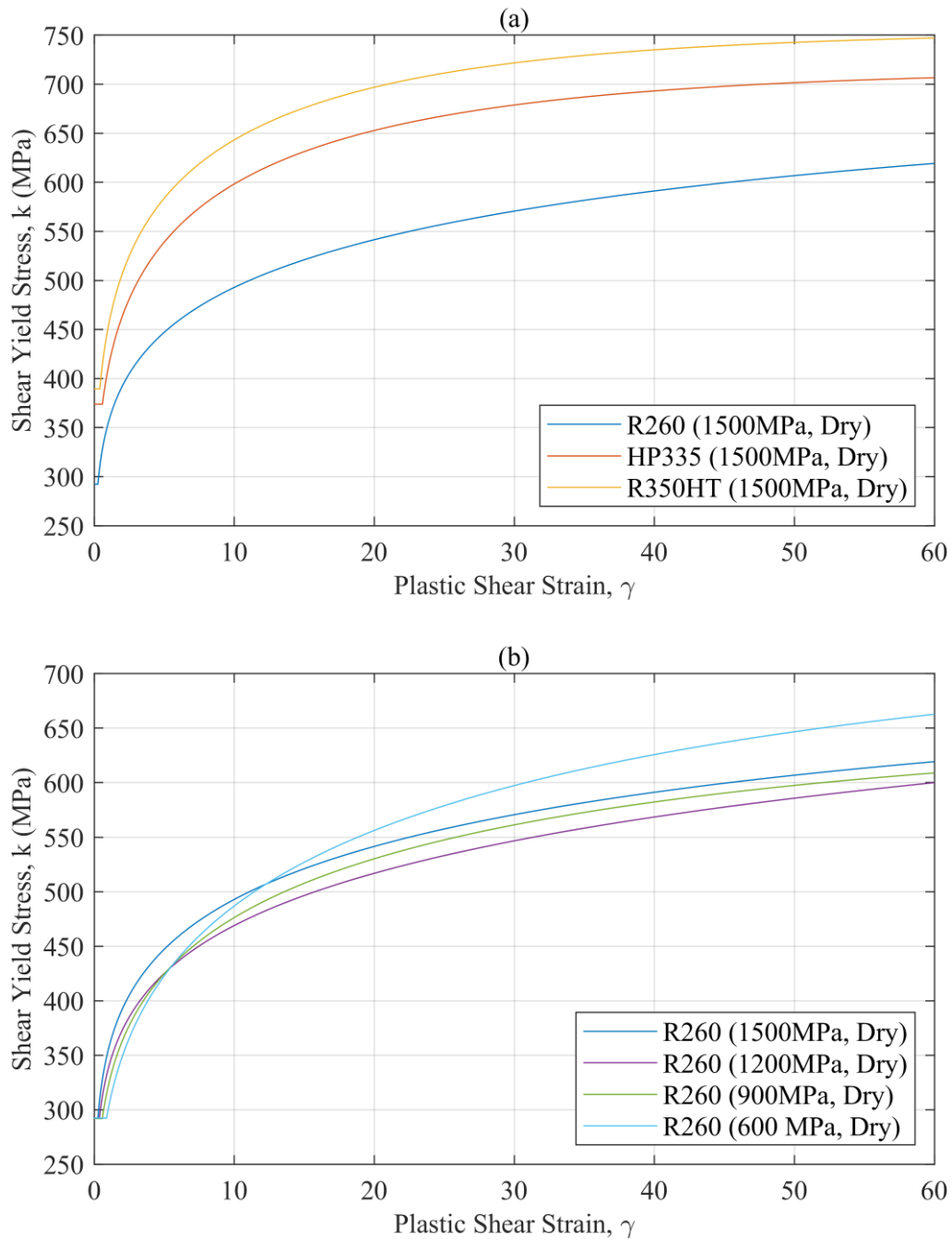


Figure 3.25: Comparison of the shear stress-strain curve relationships derived for (a) R260 (1500 MPa), HP335 (1500 MPa), and R350HT (1500 MPa); and (b) R260 (1500 MPa, 1200 MPa, 900 MPa, 600 MPa) under dry contact conditions.

3.5 Ratcheting Load Conversion Factor

3.5.1 Derivation Procedure

The ratcheting load conversion factor, c (see chapter 2 for clarification of this terminology) is a parameter that describes the conversion from the plastic ratcheting load experienced beneath the rail-wheel contact to incremental shear strain. This parameter was derived from the constant of proportionality between the accumulated shear strain, γ , and the net severity of ratcheting load above the shear yield strength, T_r , over the total number of contact cycles, N , as given by Equation 3.6. To accurately understand this constant of proportionality, the data needs to represent points of material exhibiting a wide range of different accumulated shear strain. In Tyfour et al. [120] method this was done by measuring at a single depth below the running surface from many twin-disc samples tested to various total number of contact cycle durations. To obtain more data and minimise the number of samples tested in this work, the results used to derive the gradient of this linear relationship were instead obtained from a range of different depths, z , for a smaller collection of samples tested to different contact cycles durations. This takes advantage of the shear strain gradient typically observed below the running surface of twin-disc samples and rail steels, similar to the approach in the updated methodology for deriving the shear stress-strain curve [119], [193].

$$\gamma(N, z) = c T_r(N, z) \quad \text{Equation 3.6}$$

From Melan's statical theorem [111], the limiting condition for plastic ratcheting occurs when the orthogonal shear stress, τ_{xz} , exceeds the material yield strength in simple shear, k , as given by Equation 3.7.

$$\tau_{xz} \geq k \quad \text{Equation 3.7}$$

From this underlying rule, the ratcheting load, $\tau_{ratchet}$, could be determined via Equation 3.8.

$$\tau_{ratchet} = \tau_{xz} - k \quad \text{Equation 3.8}$$

By normalising this equation based on the shear yield strength, an expression for the nondimensionalised severity of ratcheting load above the shear yield strength, $T_{ratchet}$, on a per contact cycles basis, n , could be established as given by Equation 3.9.

$$T_{ratchet}(n, z) = \frac{\tau_{xz}(n, z)}{k(n, z)} - 1 \quad \text{Equation 3.9}$$

The net ratcheting load above the shear yield strength over all the contact cycles N of the twin-disc test was, therefore, derived by summing all the positive cyclic contribution as given by Equation

3.10. The negative cyclic contributions were ignored, as they indicate instances when the orthogonal shear stress was below the material shear yield strength and so were insufficient to cause plastic ratcheting.

$$T_r(N, z) = \sum_{n=1}^N T_r(n, z) \quad (T_r(n, z) \geq 0) \quad \text{Equation 3.10}$$

The effect of material wear was considered in the calculation via its influence in decreasing a point of materials depth below the running surface over the duration of the twin-disc test. This implies that the instantaneous depth, z , for any point of material during an experiment was a function of the point of material initial depth, z_0 , and instantaneous contact cycle, n , via Equation 3.11.

$$z(z_0, n) = z_0 - \Delta R(n) \quad \text{Equation 3.11}$$

where ΔR is the cyclic variation of radius loss due to wear experienced by the rail sample. By considering the influence of wear on decreasing a point of materials depth below the running surface, Equations 3.6, 3.8, and 3.9 transform into Equations 3.12-3.14, respectively.

$$\gamma(N, z(z_0, N)) = c T_r(N, (z_0, N)) \quad \text{Equation 3.12}$$

$$T_{ratchet}(n, z(z_0, n)) = \frac{\tau_{xz}(n, z(z_0, n))}{k(n, z(z_0, n))} - 1 \quad \text{Equation 3.13}$$

$$T_r(N, z(z_0, N)) = \sum_{n=1}^N T_r(n, z(z_0, n)) \quad (T_r(n, z(z_0, n)) \geq 0) \quad \text{Equation 3.14}$$

This cyclic radius loss trend ΔR for the rail sample was derived from the mass loss results, Δm , measured from the rail samples of the uninterrupted twin-disc tests. As the direct measurement of twin-disc samples running track diameter change was affected by both the material loss due to wear and the sideways material flow responsible for the bulging of the specimens running track. This bulging of the running track, however, did not contribute to the depth decreasing between the point of subsurface material and the worn running surface with increasing contact cycles. To convert the mass loss results to radius loss, Figure 3.15 was utilised based on the assumption that the material lost due to wear only could be represented as a uniform thickness hollow cylinder.

$$\Delta R = R_0 - \sqrt{R_0^2 - \frac{\Delta m}{\pi \rho l_0}} \quad \text{Equation 3.15}$$

where R_0 is the initial running track radius of the rail sample, ρ is the density of the rail steel, and l_0 is the initial running track width of the rail sample. The density of the rail steels calculated from direct

measurements of the specimen's mass and estimates of the samples volume from SolidWorks are shown in Table 3.5. A relationship was fitted to the data to interpolate the running track cyclic radius loss trend in between twin-disc test conducted. During an ideal twin-disc test where the contact conditions were maintained throughout, the running track radius loss trend would have followed a relationship in the form of Equation 3.16. This is because the rate of the cyclic variation of the running track radius loss was expected to gradually increase from zero during the initial running in period of the experiment followed by increasing at a constant rate after the onset of steady-state wear conditions. This relationship, therefore, would be suitable for fitting onto results obtained from all the R260 experiment due to those tests encountering steady-state wear behaviour. For the HP335 and R350HT uninterrupted experiments, however, which were found in Section 3.3.3 to experience a continuously decreasing coefficient of traction with increasing cycles a different relationship in form of Equation 3.17 was needed to compensate. This was because the continuously decreasing coefficient of traction would have resulted in the twin-disc samples wearing less and the rate of cyclic variation of radius loss to gradually decrease later into the experiment.

Table 3.5: Density estimates for R260, HP335, and R350HT rail steel.

| Rail Steel Grade | Density (g/mm ³) |
|------------------|------------------------------|
| R260 | 0.00781 |
| HP335 | 0.00778 |
| R350HT | 0.00781 |

$$\Delta R(n) = An + \frac{A}{B}(1 - \exp(-Bn)) \quad \text{Equation 3.16}$$

$$\Delta R(n) = \frac{A}{B}(1 - \exp(-Bn)) + \frac{C}{D}(1 - \exp(Dn)) \quad \text{Equation 3.17}$$

where A, B, C, D are coefficients found by fitting the relationship to the calculated radius loss data points for all the uninterrupted twin-disc tests conducted for the same condition investigated. The cyclic variation of the running track radius loss relationships calculated from the mass loss results of the uninterrupted twin-disc tests for the six conditions investigated is shown in Figure 3.26.

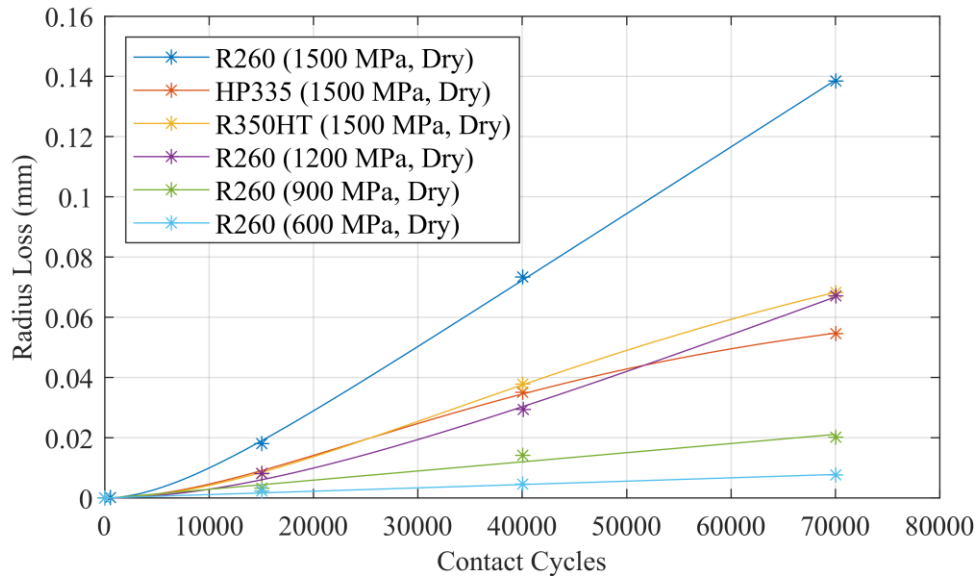


Figure 3.26: Running track radius loss trend calculated from the mass loss measurements of the rail steel samples from the uninterrupted twin-disc tests.

3.5.1.1 Shear Yield Strength

The cyclic variation of the shear yield strength was derived experimentally using the percentage work hardening curves derived for the uninterrupted twin-disc tests presented in Appendix A1 as Figure A1.10. From the percentage work hardening curves, snapshots of the percentage work hardening for the same fixed point of material were deduced at each different contact cycle duration performed, accounting for the point of materials changing depth z due to wear. To interpolate the cyclic variation of the percentage work hardening between the uninterrupted experiment conducted, an estimate was acquired by fitting Equation 3.18 to the data points derived for each fixed point of material investigated.

$$\frac{H(n, z(z_0, n))}{H_0} = A(\exp(-Bn) - 1) + C(\exp(Dn) - 1) + 100 \quad \text{Equation 3.18}$$

where A, B, C, D are coefficients found by fitting the expression to the percentage work hardening data points. The two exponential terms in the expression represented the two driving factors that influences the strain hardening history of a fixed point of material. The first exponential term represents the strain hardening increase contribution from the initial wearing in stage of the twin-disc experiment. The second exponential term, however, describes the strain hardening increase contribution caused by the depth of a fixed point of material decreasing with contact cycles due to wear that would subject the point of material to higher orthogonal shear stress nearer to the surface. An example of one of the percentage work hardening against contact cycles data estimated for a fixed point of subsurface material is shown in Figure 3.26.

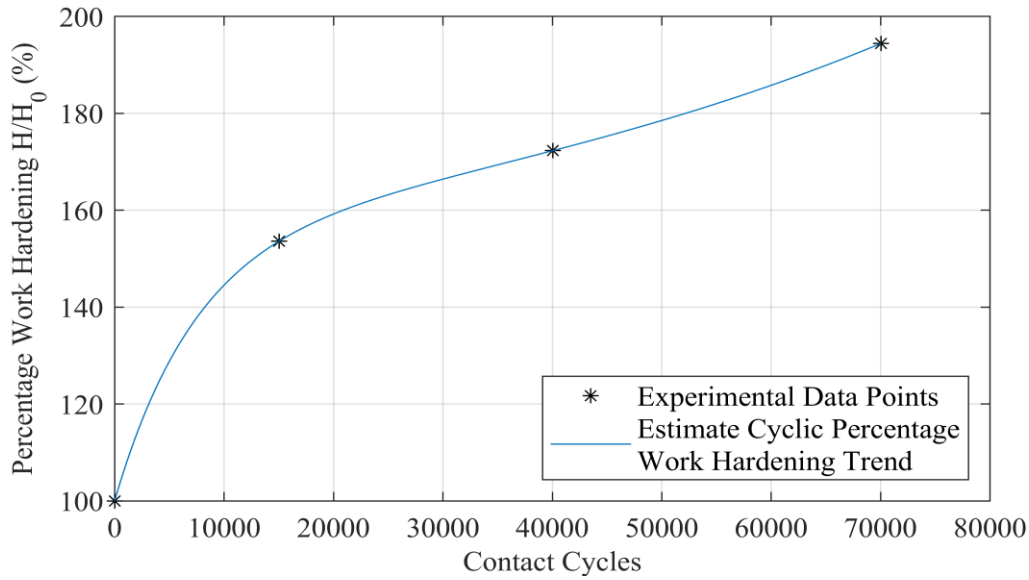


Figure 3.27: Example of the percentage work hardening against contact cycles trend calculated for a fixed point of material from the uninterrupted HP335 twin-disc samples tested under 1500 MPa, dry contact conditions.

By utilising the assumption that the increase in the material percentage work hardening was proportional to the percentage increase in shear yield strength, an estimation of the shear yield strength cyclic variation data for each point of material considered was found via Equation 3.19.

$$k(n, z(z_0, n)) = k_0 \left(\frac{H(n, z(z_0, n))}{H_0} \right) \quad \text{Equation 3.19}$$

3.5.1.2 Orthogonal Shear Stress

The orthogonal shear stress distribution produced by the twin-disc contact was estimated for a rough contact utilising the roughness model developed by Nowell and Hills [48]. The asperity tip radius and separation data characterised from the uninterrupted experiments in section 3.3.4 was used to drive this roughness model. To replicate the natural cyclic variation of surface roughness, a distribution of asperity tip radius and separation parameters were obtained for each contact cycle based on the fitted Birnbaum-Saunders probability distribution functions. The cyclic change of the Birnbaum-Saunders probability distribution functions between the twin-disc tests conducted was accounted for by linearly interpolating the probability distribution functions gamma and beta parameter between the performed experiments. The tip radius parameters were combined by calculating the reduced radius of curvature of the asperity contacts. The separation parameters were merged using the maximum value of the rail and wheel asperity separation parameter at every contact cycle. The Young's modulus and Poisson ratio was approximated as 210 GPa and 0.3, respectively, for all three rail steels investigated.

The maximum contact pressure and half-width dimension of asperity contacts evaluated from the roughness model were then placed into the elastic Hertzian contact based orthogonal shear stress distribution equations developed by M'Ewen [35] given as Equations 2.3-2.5 in the literature review. The orthogonal shear stress distribution contributions from each asperity contact were then summated to determine the orthogonal shear stress distribution of the entire rough twin-disc contact. In addition to surface roughness, the calculation also considered the cyclic variation of coefficient of traction ($\approx 4\%$ accuracy refinement), contact load ($\approx 0.03\%$ accuracy refinement), bulk contact radius of curvature ($\approx 0.8\%$ accuracy refinement), and running track width widening due to bulging ($\approx 28\%$ accuracy refinement) based on measurements collected from the experiments.

For two 47 mm diameter discs rotating under 1% slip conditions as was performed for the twin-disc experiments conducted in this work, the sliding distance from when the sample running surface are initially loaded to fully unloaded during one contact pass is $6.2\ \mu\text{m}$. Relative to the asperity separation, it was predicted that this sliding distance was insufficient to cause multiple stress cycles to occur in the near surface material during each contact pass. Therefore, this analysis had only considered one load cycle at all depths in the material based on the maximum absolute orthogonal shear stress predicted along the same depth plane.

3.5.2 Results

The net severity of ratcheting load above the shear yield strength against shear strain results obtained for all six conditions investigated are shown in Figure 3.28(a-f). To enable the data to follow a roughly linear relationship, the results needed to be calculated using an asperity height criterion based on 35% the value of the roughness profiles Rz roughness parameter. The effect of changing the percentage used for the asperity height criterion is demonstrated in Figure 3.29(a-e). The results show that for an asperity height criterion based on a lower percentage (10%, 20%, and 30%), the severity of ratcheting load above the shear yield strength is underestimated for the higher shear strain data points. An asperity height criterion based on a higher percentage (40% and 50%), however, causes the severity of ratcheting load above the shear yield strength to be overestimated for the higher shear strain data. The two cases both skew the data away from following the linear relationship that was expected to be observed. A summary of the ratcheting load conversion factors determined for the different conditions examined is tabulated in Table 3.6. The error of the ratcheting load conversion factor reported in the table was based on the 95% confidence interval of the linear relationship fitted to the data.

Table 3.6: Ratcheting load conversion factors determined for R260 (1500 MPa, 1200 MPa, 900 MPa, 600 MPa), HP335 (1500 MPa), and R350HT (1500 MPa). The error of the ratcheting load conversion factor was based on the 95% confidence interval of the fitted linear relationship.

| Condition | Rail Steel Grade | Maximum Hertzian Contact Pressure (MPa) | Ratcheting Load Conversion Factor, c |
|-----------|------------------|---|--|
| 1 | R260 | 1500 | 0.00083 ± 0.00003 |
| 2 | HP335 | 1500 | 0.00024 ± 0.00002 |
| 3 | R350HT | 1500 | 0.00021 ± 0.00001 |
| 4 | R260 | 1200 | 0.00062 ± 0.00003 |
| 5 | R260 | 900 | 0.00029 ± 0.00001 |
| 6 | R260 | 600 | 0.00033 ± 0.00002 |

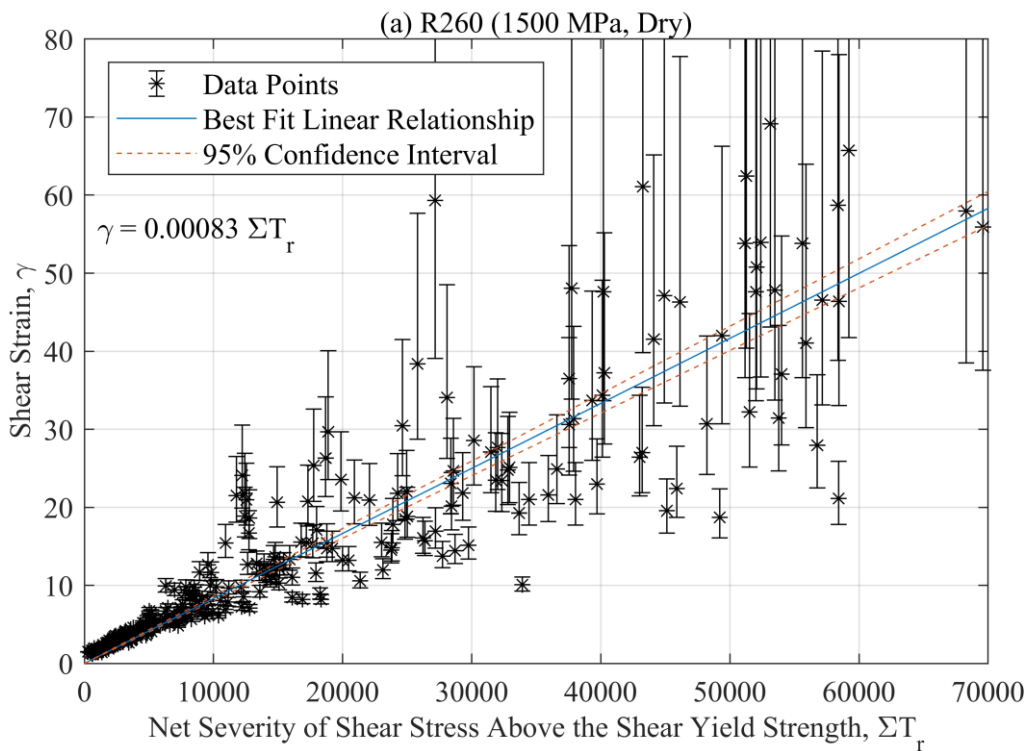


Figure 3.28: Shear Strain against the net ratcheting load above the plastic shakedown limit calculated for (a) R260 (1500 MPa), (b) HP335 (1500 MPa), (c) R350HT (1500 MPa), (d) R260 (1200 MPa), (e) R260 (900 MPa), and (f) R260 (600 MPa) under dry contact conditions.

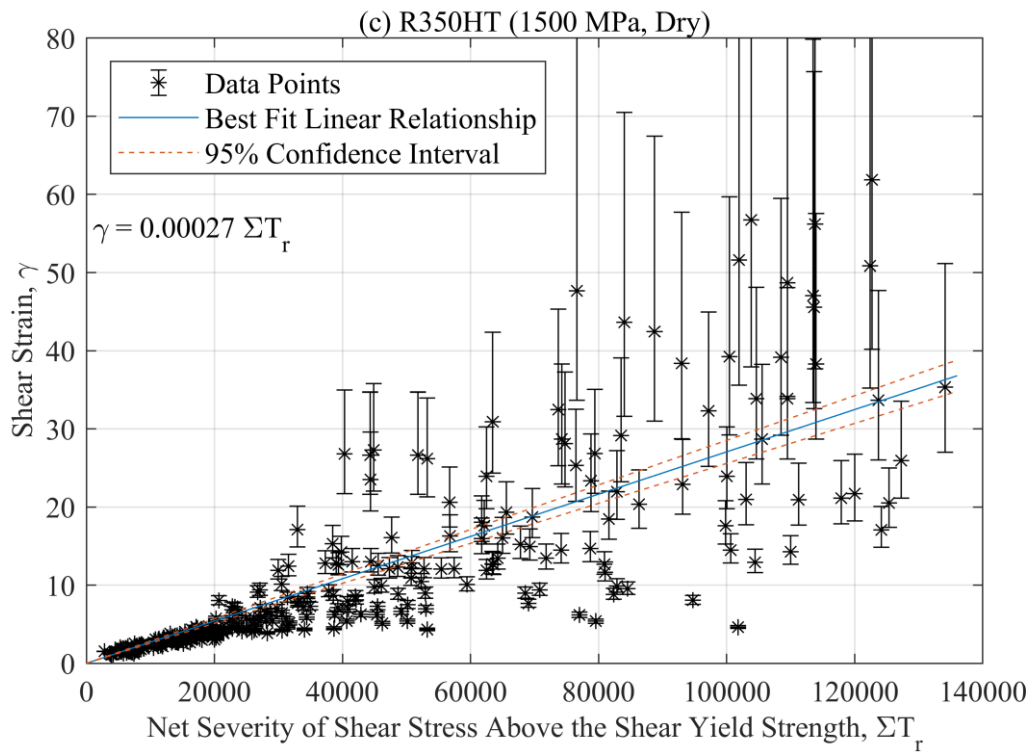
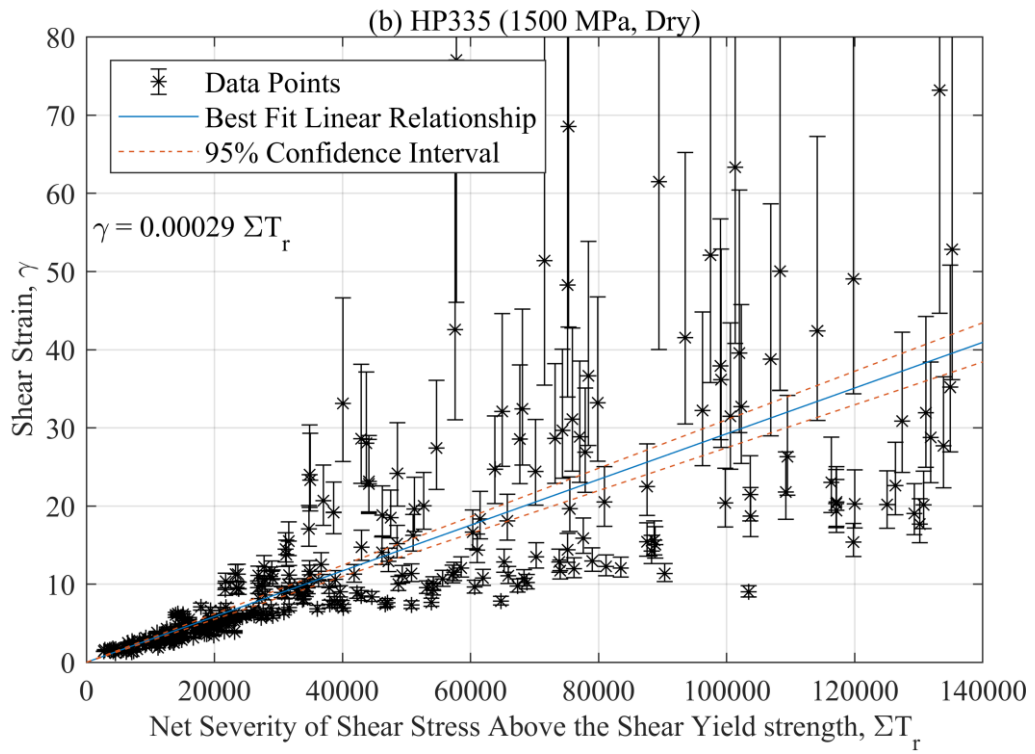


Figure 3.28: Continued.

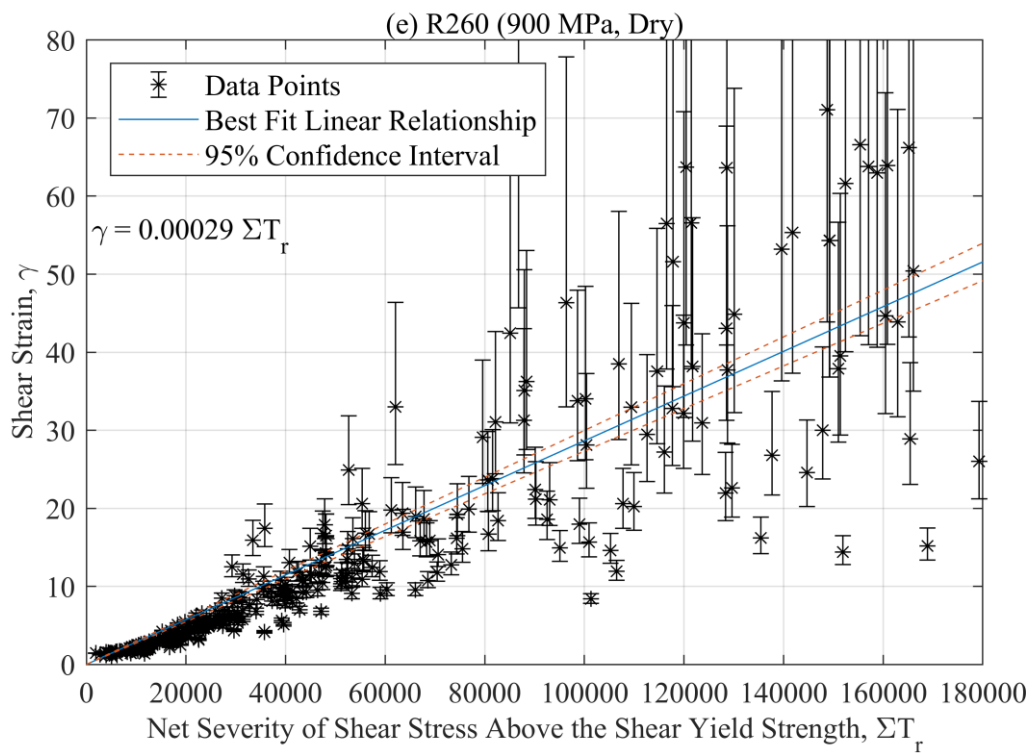
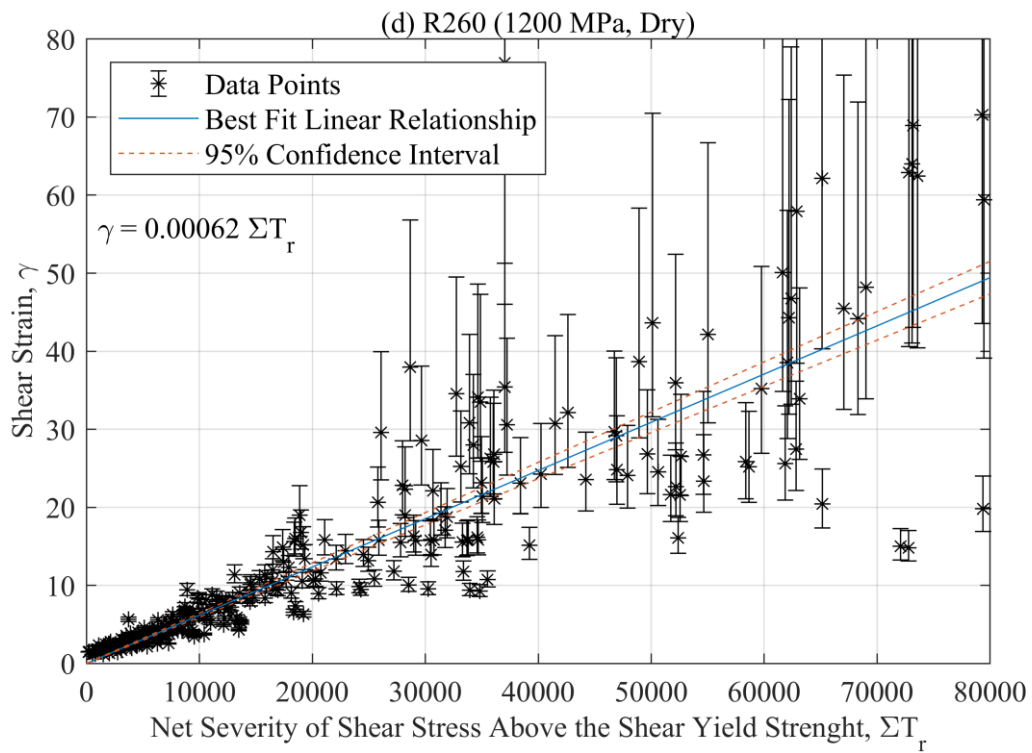


Figure 3.28: Continued.

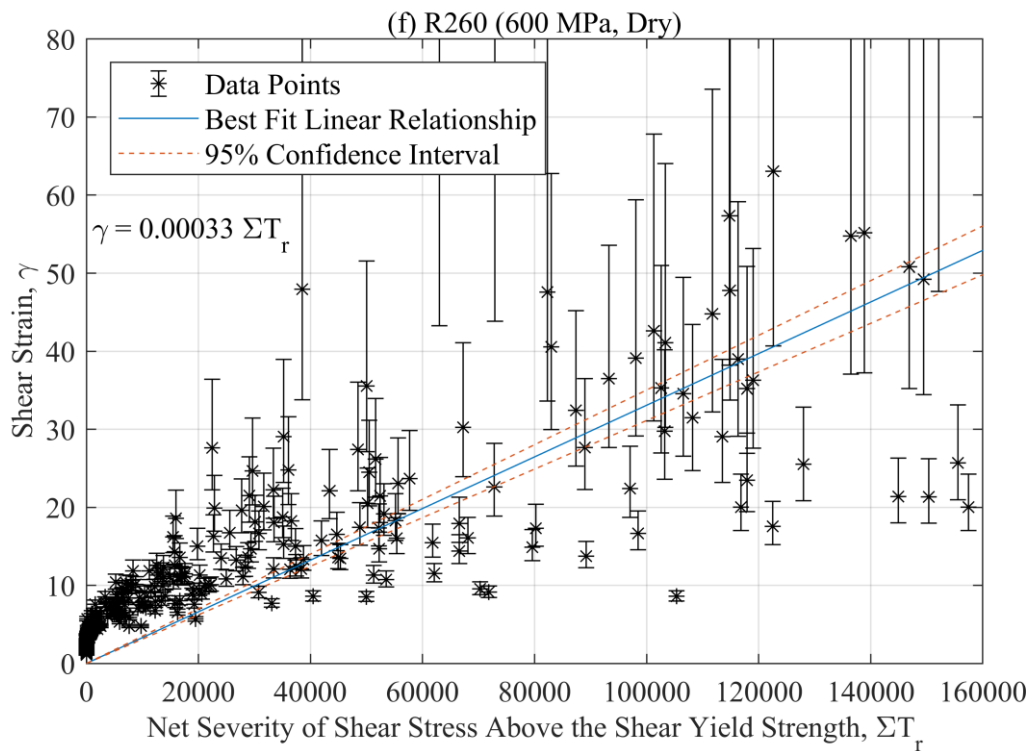


Figure 3.28: Continued.

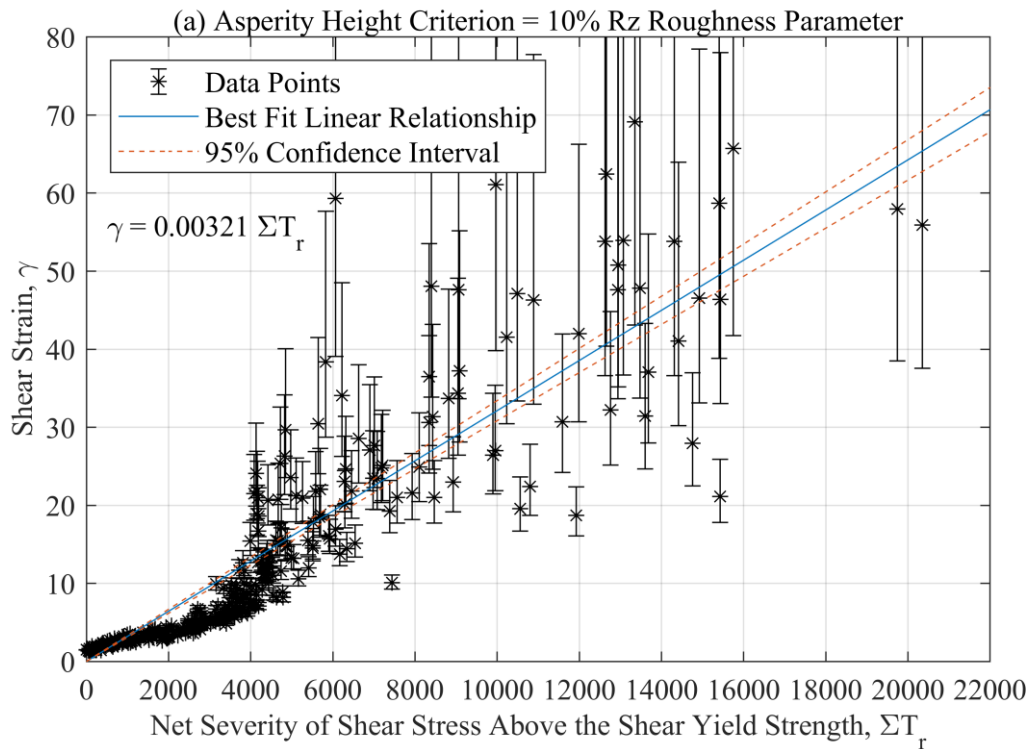


Figure 3.29: Comparison of the net ratcheting load above the plastic shakedown limit against shear strain results generated for R260 under 1500 MPa, dry contact conditions using an asperity height criterion based on (a) 10%, (b) 20%, (c) 30%, (d) 40%, and (e) 50% of the Rz roughness parameter.

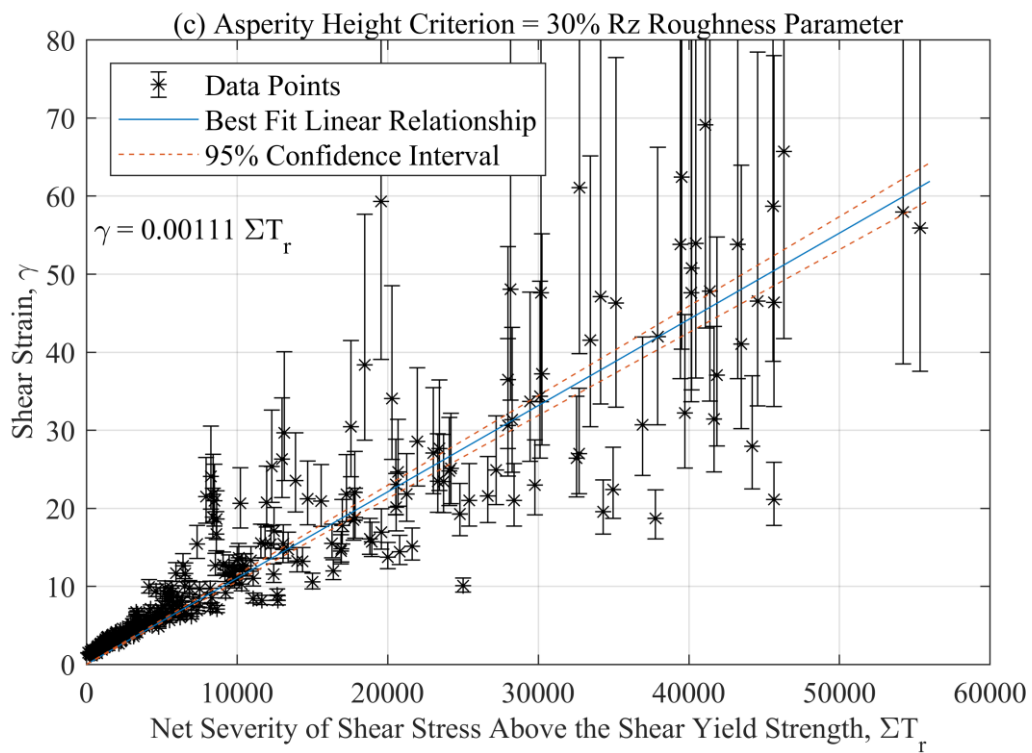
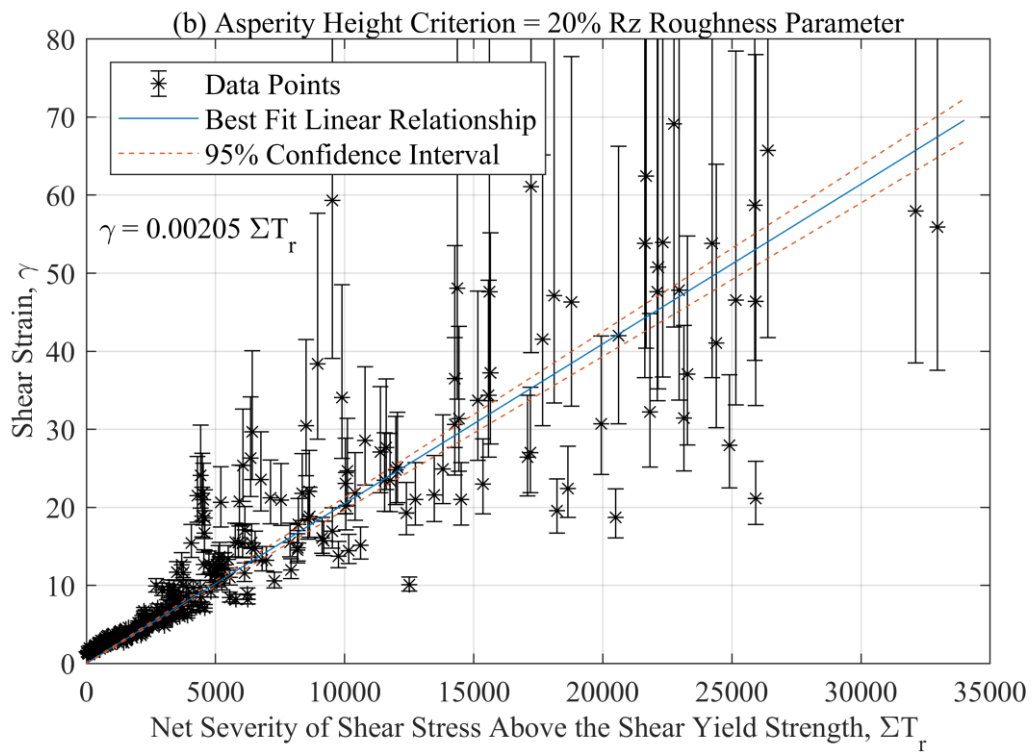


Figure 3.29: Continued.

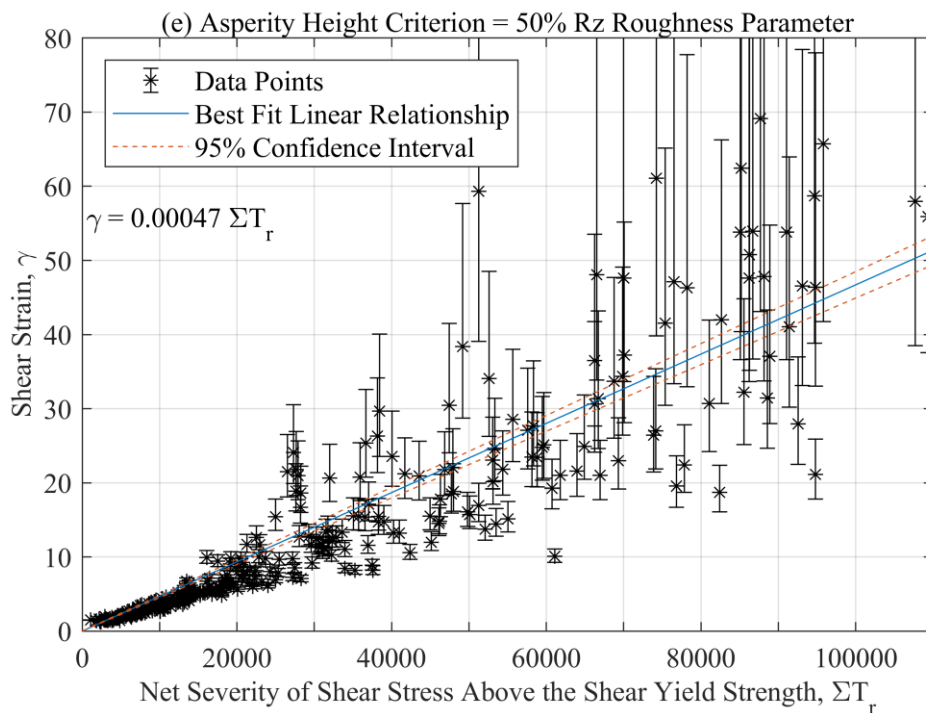
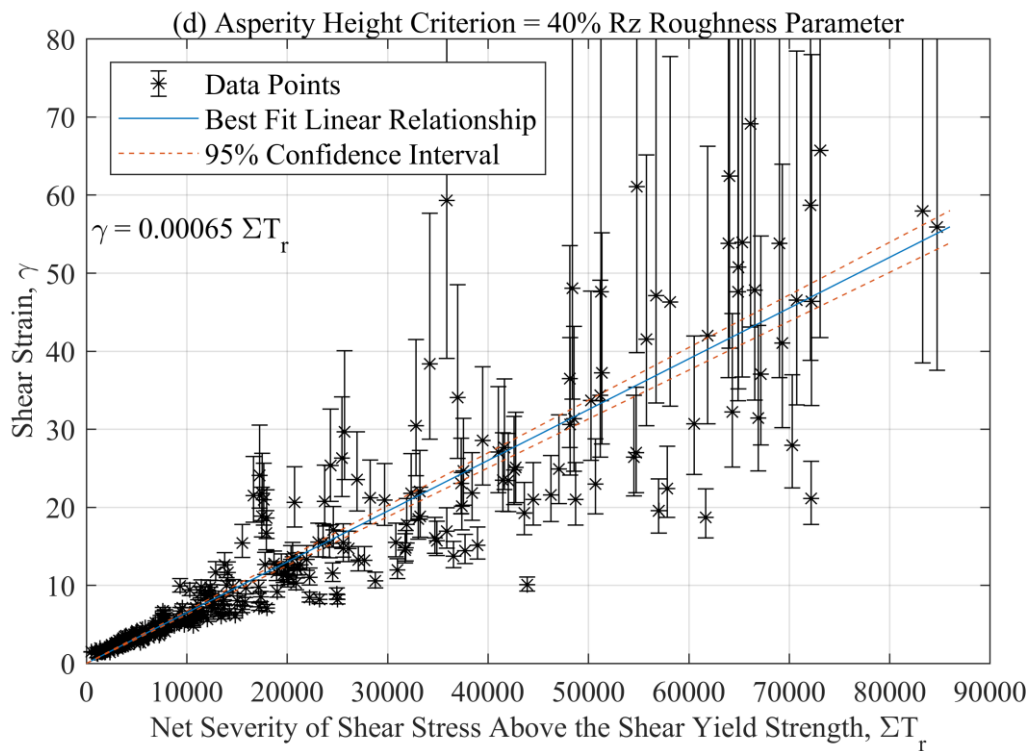


Figure 3.29: Continued.

A comparison of the ratcheting load conversion factors determined for the three rail steels (R260, HP335, R350HT) tested under 1500 MPa, dry contact conditions is plotted in Figure 3.30. The results showed that out of three rail steels under 1500 MPa, dry contact conditions, R260 presented the highest conversion factor at 0.00083. The two premium rail steels tested had significantly smaller

conversion factors compared to R260 tested under the same contact conditions, however, there was negligible difference between the two with 0.00029 for HP335 and 0.00027 for R350HT.

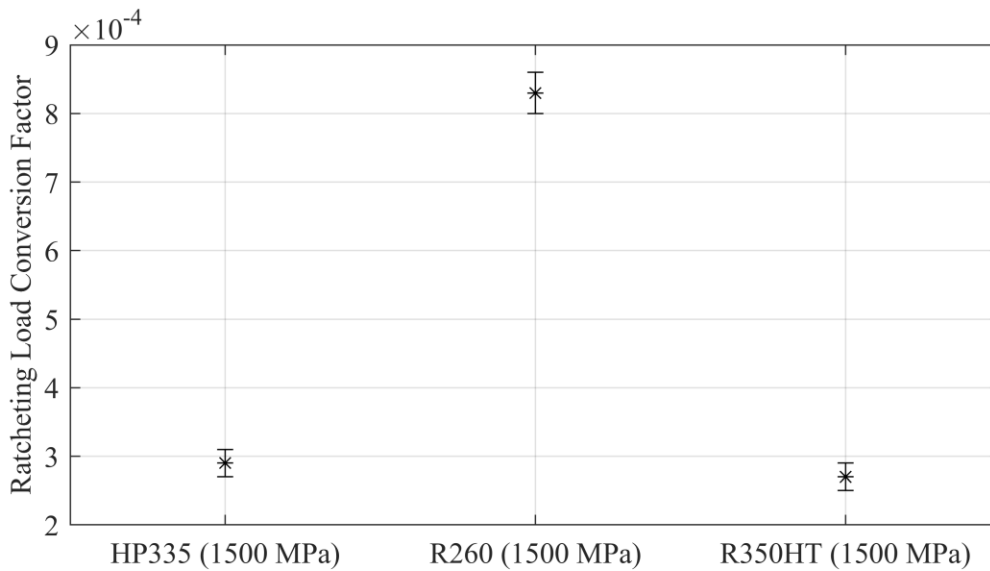


Figure 3.30: Comparison of the ratcheting load conversion factors derived for R260, HP335, and R350HT rail steel under 1500 MPa, dry contact conditions.

A comparison of the ratcheting load conversion factors determined for R260 subject to the four different contact pressure tested (1500 MPa, 1200 MPa, 900 MPa, 600 MPa) is presented in Figure 3.31. The data shows that the ratcheting load conversion factor for R260 was dependent on the maximum nominal Hertzian contact pressure the rail steels were tested under. The trend of this parameter’s dependency with contact pressure showed that the conversion factor was roughly identical for the 600 MPa and 900 MPa twin-disc tests. For twin-disc tests conducted under contact pressures higher than 900 MPa, however, the ratcheting load conversion factor was observed to increase for the higher contact pressure tests conducted.

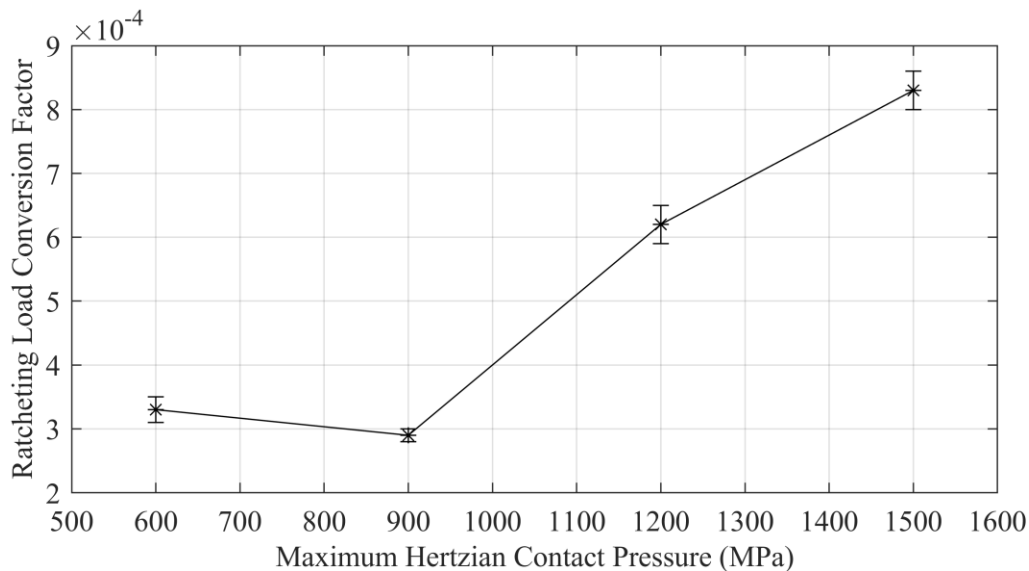


Figure 3.31: Comparison of the ratcheting load conversion factor derived for R260 under the four different maximum Hertzian contact pressures (1500 MPa, 1200 MPa, 900 MPa, 600 MPa) and dry contact conditions.

3.6 Discussion

3.6.1 Cyclic Variation of Rail Steel Surface Roughness

The cyclic variation of surface roughness data on the rail twin-disc samples presented in Figure 3.12 and Figures A1.2-A1.7 in appendix A1 all showed the same trend of both the asperity tip radius and separation decreasing for the worn rail specimens compared to the as-new condition. The implication of these findings points to the asperities becoming sharper and situated closer together as the surface of a rail is worn due to the rail-wheel contact interaction, which contradicts the general belief that they should become duller. An explanation for this cyclic trend behaviour witnessed could be an effect of shear stresses being present in contact causing asymmetrical damage of asperities. In addition, this could also stem from the processes involved in generating wear flakes on the surface of a rail.

Compared to other results published in literature the surface roughness cyclic trend behaviour observed in this work did not match up to similar data published by Tomlinson [63], as shown in Figure 2.10. Their data instead showed a different behaviour occurring with the asperity tip radius generally getting larger and the asperity separation marginally increasing or staying the same for the worn samples compared to the as-new condition. This discrepancy in the results could stem from the different measurement technique utilises between the two studies. This is because in Tomlinson [63] work the tip radius of asperities was measured by fitting a circular relationship to just three data points (asperity peak and two adjacent data points) on the roughness profile. The issue with this approach is

that by only using these three data points, the results generated would generally only capture the top part of each asperity, which would be expected to be flattened when loaded, and disregards the bulk of the asperities. Therefore, a different approach of fitting a circular relationship to all profile data points above the mean line for each significant asperity identified was utilised in this work to better measure the asperity tip radius on a more macro scale. Both of these approaches have got their drawback, though, as the technique used by Tomlinson [63] is susceptible to the profile data spatial resolution; whereas, the method in this work was sensitive to the placement of the mean line on the roughness profiles. On top of this, a different way of defining and locating significant asperities was also used across the two studies, which could also explain the difference in the cyclic trends witnessed in the results. This is because significant asperities were located in Tomlinson [63] work based on a height criterion using the same fixed value; whereas in this work a height criterion based on a percentage of the Rsm roughness parameter was used instead.

3.6.2 Plastic Damage Experimental Observations

The hardness results presented in section 3.3.5 emphasise the importance of understanding asperity driven plastic deformation near the running surface. The influence of asperity-contact driven plastic damage could be observed in the microhardness results presented in Figure 3.15b. At the highest contact pressures subsurface hardening is significantly influenced by the changes in contact pressure. At the lower contact pressures explored, however, subsurface hardening becomes less influenced by bulk contact pressure. This is thought to be because for both 600 MPa and 900 MPa cases the bulk orthogonal shear stress is below the material shear yield strength, whereas localised asperity contact pressures are typically in the order of the materials hardness [60]. The effect of asperity-contact driven plastic damage was also observed in the nanohardness data, shown in Figure 3.17 with the noticeable increase in the hardness-depth data gradient within 50-100 μm of the running surface. The influence of asperity contact driven plastic damage can also help explain why reduced wear was observed for the 900 MPa and 600 MPa contact pressure R260 experiments shown in Figure 3.6b. This is because for the 1500 MPa and 1200 MPa R260 tests, the plastic deformation for these conditions would be observed to be a combination of asperity and bulk plasticity. Tyfour et. al [117] showed that the wear observed for this type of plastic damage accumulation increases initially due to the build-up of bulk subsurface strain. A steady-state wear rate is achieved when the subsurface shear strain against depth profile also becomes steady state. For the 900 MPa and 600 MPa contact pressure experiments, a predominantly asperity contact pressure driven plastic deformation was observed. Under these conditions the orthogonal shear stresses localised at the surface for asperity contacts are significantly higher compared to the stress deeper down. These significantly higher shear stress will then cause the surface material to accumulate shear strain and reach a steady-state strain against depth profile

quicker. Thus, a steady-state wear rate should be achieved for predominantly asperity contact driven plastic deformation sooner than for bulk plasticity.

An interesting finding from the nanohardness results, shown in Figure 3.17, was the similar nanohardness values of about 12 GPa at the surface of the twin-disc samples for all six conditions investigated. This is despite the three rail steels tested having different initial metallurgy and baseline hardness, and the different contact pressures investigated. This could point to the influence of surface roughness leading to very high asperity contact pressures which will cause plastic flow as they exceed the yield stress in a particular material. There is the potential for feedback between asperity pressures, yield point and surface modification resulting in similar amounts of plastic shear strain at the running surface across the tests. An alternative explanation is that the results show a limiting hardness value that the pearlitic microstructure of rail steels can achieve under combined compression-shear loading conditions before failing.

3.6.3 Coefficient of Traction Issues

In section 3.3.3 an issue was spotted with the coefficient of traction data obtained from the uninterrupted twin-disc tests performed for the two conditions 1500 MPa HP335 and 1500 MPa R350HT. The issue raised was that the coefficient of traction data for these tests were observed to continually decrease with increasing contact cycles caused by the dissimilar wear rates of the rail and wheel which altered the slippage within the twin-disc contact. The implication of this was that the wear rates observed for the 1500 MPa HP335 and 1500 MPa R350HT uninterrupted twin-disc tests were observed to taper off with increasing contact cycles rather than exhibit steady-state wear behaviour. To avoid this issue influencing the ratcheting load conversion factor results presented in Section 3.5 an alternative expression was fitted to the cyclic wear depth data for these two conditions. In addition, the cyclic variation of the coefficient of traction was considered in the calculation. In hindsight, however, it would have been best to have avoided this issue in the first place through changing the design of the twin-disc experiments conducted. This could be accomplished in any future twin-disc experiments testing premium rail steel grades, such as HP335 and R350HT, by inputting at the start of each test the estimated cyclic diameter changes to apply this correction. Alternatively, a laser-based disc diameter monitor could be developed to adjust the sample rotation speeds based on the disc diameters measured in real time.

3.6.4 Ratcheting Load Conversion Factor Methodology

In Section 3.5, an updated methodology of calculating the ratcheting load conversion factor for rail steels from experimental twin-disc data was shown. The modifications implemented in this work

were made to help improve the applicability and increase the quantity of results generated available for data fitting to determine more accurately this parameter while using the minimum number of twin-disc samples needed. To enable more meaningful results to be generated from long duration 70,000 contact cycle twin-disc tests, the effect of wear was accounted for in the data analysis. This was accomplished by understanding the influence that wear has in decreasing a point of materials depth below the running surface over the duration of the twin-disc tests via calculating the rail twin-disc samples cyclic radius loss trend from mass loss results, shown in Figure 3.26. The data analysis also utilised the Nowell and Hills roughness model [48] rather than conduct the calculation using the smooth body contact assumption. This modification helped generate more realistic orthogonal shear stress data when analysing the plastic response of the premium rail steels HP335 and R350HT; and the low contact pressure (600 MPa and 900 MPa) R260 twin-disc tests. Due to the simplicity of this roughness model, however, the results generated for data fitting still did not follow a perfectly linear relationship as was expected to be observed with the results for some conditions. This can be seen by the results generated for the 600 MPa R260 contact conditions shown in Figure 3.28f. This is because the data analysis of this contact condition predicted the orthogonal shear stresses to be below the rail steels shear yield strength at depths of 110-150 μm below the running surface. From optical microscopy observations, however, low magnitudes of plastic shear strains were still visible at these depths.

3.6.5 Comparison of the Material Information for Different Rail Steel Grades

A comparison of the shear stress-strain curve and ratcheting load conversion factor for R260, HP335, and R350HT subject to the same contact conditions are presented in Figure 3.25a and Figure 3.29, respectively. The results showed that the ranking of the rail steel grades in terms of the highest shear yield strength achieved is R350HT, HP335, and then R260. The ratcheting load conversion factor data revealed that R260 had the highest conversion factor between ratcheting load and incremental shear strain. Both the premium rail steel grades HP335 and R350HT exhibited comparable ratcheting load conversion factors between the two that were significantly smaller compared to R260. Relating both these results with the wear data collected for the same conditions, presented in Figure 3.6, does not show any direct correlation to explain why HP335 showed a distinctively lower wear rate compared to R350HT, given that R350HT is the harder rail steel out of the two. This lack of a correlation indicates that neither the shear stress-strain curve, shear yield point, and ratcheting load conversion factor by themselves are enough to determine which rail steel will have the lower wear rate. An understanding of the shear strain that the different rail steels can sustain before failure (limit of accumulative shear strain that can occur before the nucleation of voids and microcracks) under

repeated rail-wheel contact is the next logical piece of material information needing to be assessed to help understand the rail steel wear behaviour, which will be explored in the next chapter.

3.6.6 Comparison of the Material Information for Different Normal Contact Pressures

The shear stress-strain curves obtained for R260 under different normal contact pressures (1500 MPa, 1200 MPa, 900 MPa, 600 MPa) are compared in Figure 3.25b. The results showed that the shear stress-strain curves for R260 are roughly similar across the four different contact pressures tested. This shows that within this range of pressures the shear stress-strain curve derived from twin-disc samples is near to independent of the contact pressures at which the data is collected. The shear stress-strain curve obtained can, therefore, be classed as ‘material property’ data rather than ‘system behaviour’ data. Regarding plastic ratcheting-based simulation models, these findings show that the shear stress-strain curve derived from twin-disc samples tested at 1500 MPa, is suitable for describing the material behaviour of rail steel when subjected to different contact pressures ranging from the 600-1500 MPa range tested. This is helpful for simulation models as it implies that separate shear stress-strain curves for different contact pressures are not needed.

The ratcheting load conversion factors determined for R260 at different contact pressures (1500 MPa, 1200 MPa, 900 MPa, 600 MPa) are compared in Figure 3.31. The results generated showed that the ratcheting load conversion factor remains the same between the 600 MPa and 900 MPa contact pressure test, however, increases for the higher contact pressures tested for the tests conducted above 900 MPa. This finding shows that the ratcheting load conversion factor is a ‘system behavioural’ rather than a ‘material property’ parameter. One possible explanation for the variation in conversion factors observed under different normal contact pressure is that this parameter could be linked to the depth of the plastic damage, as illustrated in Figure 3.32. This is because for the lower normal contact pressure tests conducted, a shallower depth of plastic damage was observed which will present a sharper shear strain gradient with depth acting over the same size microstructure. The sharper shear strain gradient could, therefore, exhibit greater resistance to plastic deformation due to needing to bend the individual interlamellar ferrite and cementite lathes by a greater amount. This reason could potentially explain why this parameter is similar when derived from the 900 MPa R260 and 600 MPa R260 contact conditions, as both conditions generated roughly identical depths of plastic damage in the tested samples.

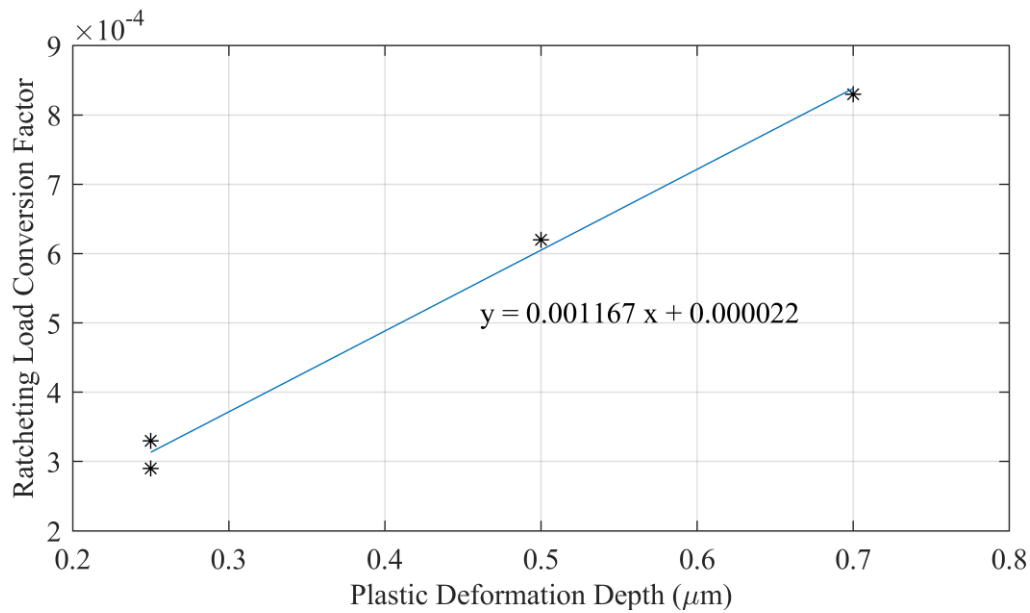


Figure 3.32: Comparison of the ratcheting load conversion factor against the depth of plastic deformation observed from the hardness results for the conditions investigated for R260 rail steel under the four different normal contact pressure tested.

3.7 Conclusions

The rail steel shear stress-strain curve relationship and ratcheting load conversion factor has been derived from characterising the plastic deformation observed in twin-disc samples for a range of different rail steel metallurgies and contact conditions. From this work the following conclusions can be made:

- HP335 was seen to be the better performer in the wear tests showing a distinctly lower overall wear rate compared to R350HT and R260.
- The ranking of the shear stress-strain curves for R260, HP335, and R350HT rail steel subject to 1500 MPa, dry contact conditions was established. The order in terms of highest shear yield stress achieved was R350HT, HP335, and then R260.
- The ratcheting load conversion factor derived for R260, HP335, and R350HT rail steel subject to the same contact conditions was found to be highest for R260. Both the premium rail steels HP335 and R350HT possessed a similar conversion factor between ratcheting load and incremental shear strain that were significantly smaller compared to R260.
- The shear stress-strain curve, ratcheting load conversion factor, and shear yield strength by themselves were found to be insufficient to determine which rail steel will have the lower wear rate.

- The testing of R260 under different normal contact pressures derived roughly identical shear stress-strain curves for all conditions examined. This indicates that (at least within this range of working pressures) the shear stress-strain curves obtained can be classed as ‘material property’ data rather than ‘machine behavioural’ data that is only applicable for the same contact conditions the data was collected with.
- The ratcheting load conversion factor was found to vary depending upon the normal contact pressure the twin-disc experiments were conducted under. This revealed that the ratcheting load conversion factor would be classed as ‘machine behavioural’ data that is only relevant for application in plastic ratcheting-based models simulating the same contact conditions this data was derived under. A possible connection between this parameter and the depth of plastic damage could be observed. This suggests that plastic deformation is slower to accumulate in shallower plastically deformed layers possibly due to the greater resistance created by the sharper shear strain gradient over the same size microstructure, which involves needing to bend individual interlamellar ferrite and cementite lathes by a greater amount.

From the work presented in this chapter, three areas for further work were identified. The first area that could be explored further is to advance the analytical analysis work by using a more sophisticated roughness, such as a fractal-based roughness model [62], to generate a better estimate of the subsurface orthogonal shear stresses. Examining whether the application of a rough contact model that considers the multi-scale nature of the twin-disc samples rough contact helps deliver an improved linear relationship for the data used to determine the ratcheting load conversion factor. The second area of this work that could be expanded upon in the future is to investigate the ratcheting load conversion factor of R260 rail steel subject to few more different normal contact pressures than those conducted in this study. These additional experiments would be beneficial in validating that the ratcheting load conversion factor is related to the depth of plastic damage and help understand what the true relationship is between them. The third area that could be investigated further in the future is to develop a better understanding of the cyclic morphology change happening to asperities subject to compression-shear loading conditions on the running surface of rail and wheel steels. In addition, to researching what mechanisms are occurring that are responsible for this cyclic morphological change of asperities.

Chapter 4: Determining the Shear Strain at Failure of Rail Steels

Novelty and Highlights

- Develop a new methodology to derive the shear strain at failure (limit of accumulative shear strain that can occur before the nucleation of voids and microcracks) for rail steels based on a value optimisation process using a brick-based plastic ratcheting-based model.
- Derivation of the shear strain at failure due to repeated rolling-sliding contacts for the premium rail steels HP335 and R350HT.
- Understanding how the maximum contact pressure influences the shear strain at failure of rail steels due to rolling-sliding contacts.

4.1 Introduction

The work presented in Chapter 3 derived the shear stress-strain curve and ratcheting load conversion factor, which are two of the three pieces of information needed to understand the plastic deformation behaviour of rail steels while in-service. This chapter follows on from that work focusing on determining the third piece of information needed, the shear strain at failure of rail steels under cyclic compression-shear loading conditions. The shear strain at failure describes the highest total amount of localised shear strain that can be accumulated at a localised point of rail steel material before failing. This parameter is important as it helps understand a rail steels ability to resist the creation of wear and rolling contact fatigue (RCF) damage, with a higher value contributing to a higher resistance to damage generation. This is because when the total localised shear strain on a rail surface reaches the shear strain at failure, this failed material becomes a potential source for the nucleation of voids and microcracks that can eventually coalesce to create wear and RCF damage [12].

In the literature review, three different pre-existing methodologies were identified that were developed to determine the shear strain at failure of rail steels under cyclic compression-shear loading conditions from experimental data. These three methodologies are: i) fixed depth methods [13], [121], ii) RCF crack surface inclination angle methods [122], [193], and iii) average plastic deformation angle at the RCF crack tip depth methods [123]–[125]. Each of these approaches, while suited to the studies in which they feature, involve compromises that limit their wider applicability. For example, some methods become highly sensitive to error when dealing with angles approaching 90 degrees - as experienced very near the surface. Others feature assumptions of suitable depths at which to take shear strain measurements that are tied to depth of plastic damage for those materials and does not

translate well to finer grained models. Given this a definitive solution for the problem of determining the shear strain to failure of rail steel has not yet been created.

The general idea for this new methodology was to conduct a value optimisation process using an implementation of the brick-based plastic ratcheting simulation model. This optimisation process entailed varying the materials shear strain at failure until the cyclic wear depth data estimated from the model matches up with the experimental results. This approach was selected rather than any of the pre-existing methods, to take advantage of higher data volumes generated in this work and reduce reliance on discrete measurements, leading to a more widely applicable solution.

The aim of this chapter was to investigate how the shear strain at failure can be derived from rail steels subject to cyclic compression-shear loading conditions. This chapter would first explain the new technique developed in this work to determine the shear strain at failure for rail steels via a value optimisation process using an implementation of the brick-based plastic ratcheting simulation approach. The application of this new technique would then be explored for the two contact conditions (R260 1500 MPa and R260 1200 MPa) where this approach was expected to be most suitable due to the plastic damage in these cases being a combination of bulk and asperity contact driven plasticity. An extension of this work would look at applying this new approach to the other conditions (R260 900 MPa, R260 600 MPa, HP335 1500 MPa, R350HT 1500 MPa) that were predicted to be more challenging due to the plastic damage being more heavily surface roughness driven. Additionally, the brick approach to plastic ratcheting modelling only replicates ratcheting wear mechanism and might potentially miss things like oxidation wear or some wear mechanism that may dominate for the conditions investigating the harder rail steels and lower contact pressures.

4.2 Evaluating Pre-Existing Methods

To highlight the significant variation between prior specialist approaches due to the associated assumptions and compromises, an example of the results generated using all three approaches will be shown in this section. The results presented were derived from experimental data collected from the uninterrupted R260 twin-disc samples subjected to 1500 MPa, dry contact conditions.

4.2.1 Method 1 – Fixed Depth Method

The fixed depth approach [13], [121] is based on the understanding that the shear strain at failure can be determined from the asymptotic value of shear strain measured at a fixed depth below the running surface. From the previous two examples in literature to determine the shear strain at failure of rail steels using this methodology, the results were either derived using data measured at a fixed depth of 200 μm [13] or 30 μm [121] below the running surface. To showcase the results generated using this

approach, 15 measurements of the angle of the deformed microstructure were measured at each fixed depth of 30 μm and 200 μm from every sample tested up to 500, 15,000, 40,000, and 70,000 contact cycles uninterrupted. These angles were then converted to a measure of shear strain using Equation 3.2. The angles of the deformed microstructure and subsequently shear strain results measured at the fixed depths of 30 μm and 200 μm are tabulated in Appendix A3 in Table A3.1 and Table A3.2, respectively.

A plot of the average shear strain against contact cycles results measured at both the 30 μm and 200 μm fixed depths is shown in Figure 4.1. From the data collected at the two fixed depths of 30 μm and 200 μm , an estimate of 27.0 and 3.7, respectively, for the shear strain at failure was established based on the asymptotic value of shear strain against contact cycles observed. This demonstrates that the use of this methodology was sensitive to the length scale chosen, requiring further consideration in any future application.

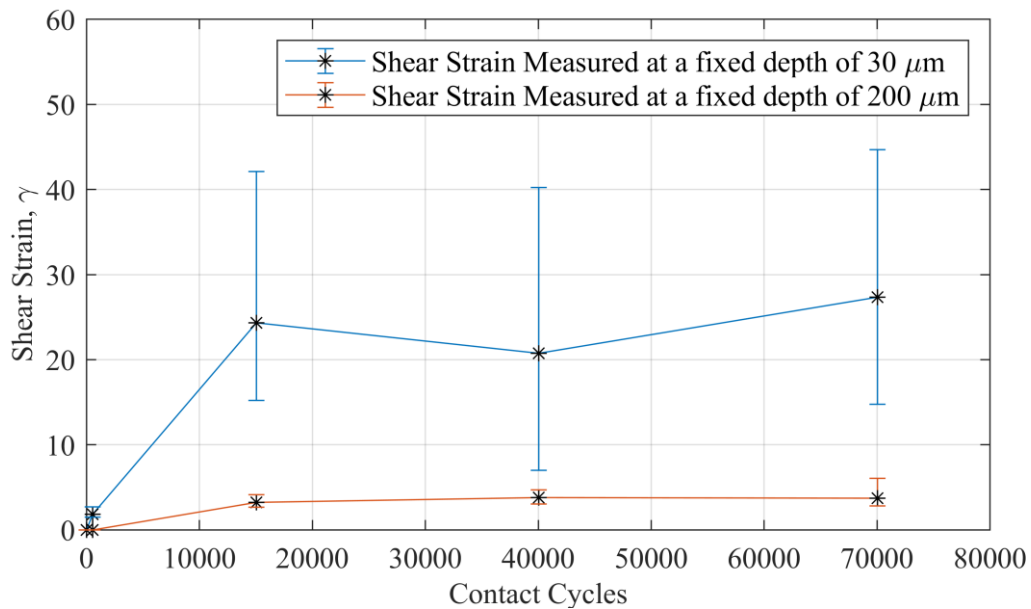


Figure 4.1: Shear strain against contact cycles measured at a fixed of 30 μm and 200 μm below the running surface of R260 twin-disc samples subject to 1500 MPa, dry contact conditions.

4.2.2 Method 2 & 3 – RCF Crack Surface Inclination Angle Method & Average Plastic Deformation Angle at the RCF Crack Tip Depth Method

Both the RCF crack surface inclination angle method and the RCF crack tip plastic deformation use the presence of RCF cracks in rail steels to estimate shear strain at failure of rail steel. The RCF crack surface inclination angle method [122], [193] uses the idea that the shear strain at failure of rail steels can be determined from the average surface inclination angle $\theta_{\text{surface inclination}}$ of RCF cracks observed in the sample. The average plastic deformation angle at the RCF crack tip depth method [123]–[125],

however, is based on the understanding that this parameter can be determined from the angle of the deformed microstructure at the average crack tip depth. To illustrate the results generated using both methods, the surface inclination angle and crack tip depth of 34 RCF cracks were measured from the two R260 twin-disc samples tested uninterrupted for 500 and 70,000 contact cycles. An example of an RCF crack measured is shown in Figure 4.2 and the data collected is presented in Appendix A3 in Table A3.3.

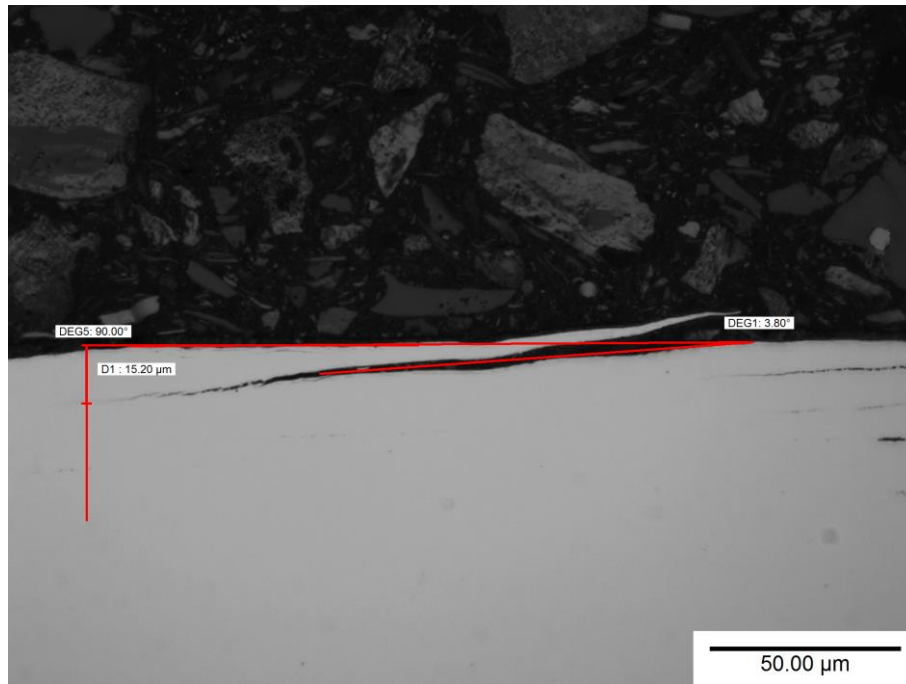


Figure 4.2: Optical micrograph of an RCF crack present on the running surface of the R260 twin-disc samples tested for up to 70,000 contact cycles under 1500 MPa, dry contact conditions.

From the data collected in Table A3.3, an estimate of the rail steel shear strain at failure based on the RCF crack surface inclination angle method was 4.3 and 17.1 from the data collected for the samples tested up to 500 and 70,000 contact cycles, respectively.

For the average plastic deformation angle at the RCF crack tip depth method, the average depth of the RCF crack tip was measured to be 2.78 μm and 10.35 μm for the samples tested to 500 and 70,000 contact cycles uninterrupted, respectively. At these depths for the two corresponding samples, 15 measurements of the plastic deformation angle were recorded and subsequently converted to shear strain, with the results presented in Appendix A3 in Table A3.4. Based on this method, an average estimate of the shear strain at failure was 4.1 and 33.2 from the data collected from the 500 and 70,000 contact cycles sample, respectively.

A comparison of the shear strain at failure estimates derived from using both methods that rely on using the presence of RCF cracks in the sample is shown in Figure 4.3. The difference in the estimates derived from the 500 and 70,000 contact cycles for both methodologies demonstrates that these two approaches were sensitive to the contact cycle duration the sample examined was tested to. Therefore, this aspect of both these approaches will need further consideration for any future application.

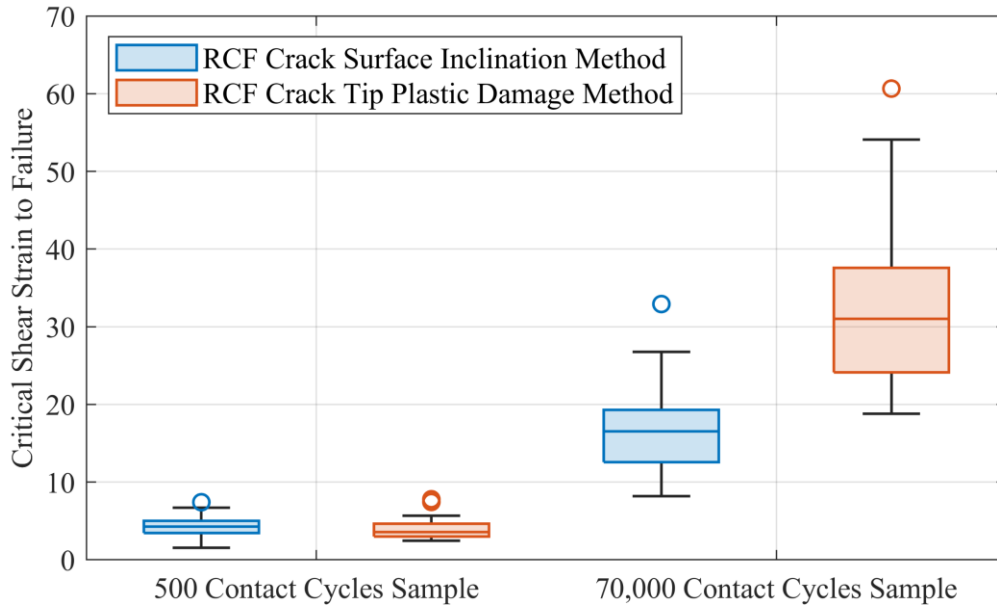


Figure 4.3: Comparison of the Critical shear strain to failure estimated using the RCF crack surface inclination angle method and RCF crack tip plastic damage method for the R260 twin-disc samples tested up to 500 and 70,000 contact under 1500 MPa, dry contact conditions.

Whatever the compromises of the methods discussed in this section, the models were still self-consistent within their own definitions. For example, it is reasonable to simulate the plastic ratcheting behaviour of a rail steel based on the same definitions that the shear strain at failure and other coefficients were derived under. The issues arise when taking the data derived using one definition and applying them within a simulation operating outside the regime of applicability of that definition.

4.3 Value Optimisation Methodology

As mentioned in the introduction, derivation of the rail steel shear strain at failure in this work would be explored via a new value optimisation method using an implementation of the brick technique to plastic ratcheting modelling. The reason for using approach rather than any of the pre-existing methods was to take advantage of the higher data volumes generated in this work. In addition, to reducing the reliance on discrete measurement, leading to a more widely applicable solution.

4.3.1 Optimisation Process

In this new approach, an implementation of the brick technique to plastic ratcheting modelling was used to simulate the rail steels wear behaviour with the cyclic wear depth loss simulation results compared to the twin-disc experimental data. The objective of convergence of this optimisation problem was to minimise the average difference between the two datasets during the steady-state wear behaviour stage exhibited by the simulation results at a range of contact cycle durations in 100 contact cycle increments. The onset of the steady-state wear behaviour phase was detected when a linear increase in the wear depth loss against contact cycles is observed in the simulated data. The start of this linear portion in the cyclic wear depth loss data was defined as the first data point that occurs 1000 contact cycles after the minimum value of the cyclic wear depth loss data first derivative. The rail steels shear strain at failure was setup as the sole variable in these optimisation problems. An initial estimate of 11.5 was given for the materials shear strain at failure, based on the value determined by Tyfour et al. [120] for BS11 rail steel.

During each iteration of the optimisation problem calculation, the model computes the initial objective function evaluation using the current iterate. The gradient of the solution at this iterate was then estimated by performing both forward and backward finite difference function evaluations. The change in the shear strain at failure variable applied for the finite difference function evaluation could be between 0 to infinite. A new estimate for the materials shear strain at failure was then established based on the solution gradient at the current iterate to start the next iteration [212], as illustrated in Figure 4.4. This iteration process was then repeated until either the threshold of the optimality tolerance, function tolerance, or step tolerance of 10^{-4} was met.

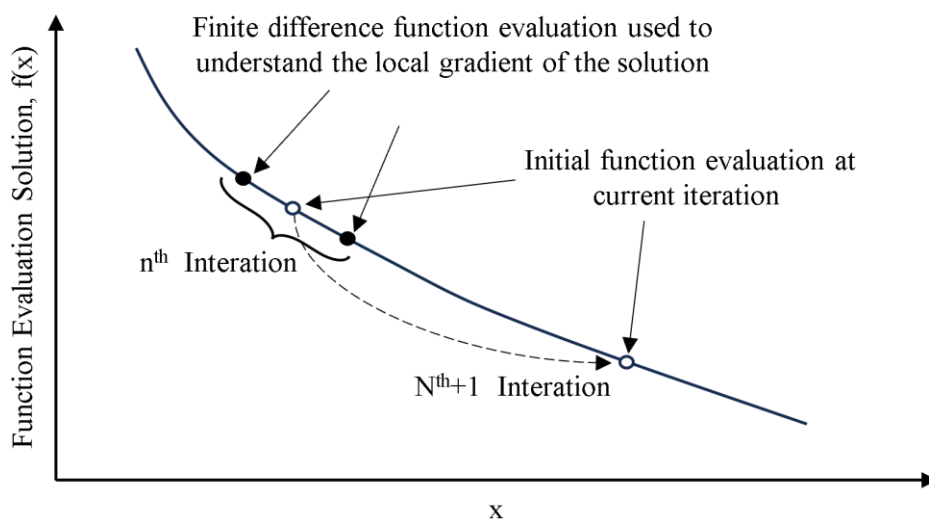


Figure 4.4: Illustrations showing the iteration process conducted during the optimisation problem calculation.

4.3.2 Brick Technique of Plastic Ratcheting Model

The Brick model is a two-dimensional model that subdivides the wearing rail steel material into N_x -by- N_z equally sized bricks along the horizontal and vertical axis. The vertical axis of the model simulated the rail steels plastic deformation behaviour up to a depth of 0.8 mm to capture the full extent of strain accumulation expected to occur for the conditions investigated based on the hardness results presented in Figure 3.14. The suitable number of bricks along the models vertical and horizontal axis to simulate for this optimisation was determined from conducting two convergence studies which will be explore later. To account for the natural variation of mechanical properties in the material, each brick was allocation a different value for the shear strain at failure and initial shear yield strength based on a normal distribution. The standard deviation of this normal distribution was based on the same 5% of the value given for the critical shear strain to failure and initial shear yield strength at each iteration, as used in previous investigation in literature using this type of model [116], [213], [214]. To help with repeatability of the results, the same random number generator seed was used for each iteration of the optimisation calculation.

During each contact cycle, the brick elements were loaded using the same subsurface orthogonal shear stress distribution calculated in Section 3.5.1.2 for the rough contact based on the Nowell and Hills roughness model. This orthogonal shear stress distribution was calculated and loaded onto the top surface of each brick. The incremental shear strain accumulated $\Delta\gamma$ in each brick was calculated from the materials shear yield strength k and absolute maximum orthogonal shear stress along a fix depth plane $\tau_{xz,max}$ using Equation 4.1.

$$\Delta\gamma = c \left(\frac{\tau_{xz,max}}{k} - 1 \right) \quad \text{Equation 4.1}$$

where c is the rail steels ratcheting load conversion factor in which the same parameter determined in chapter 3 for each respective condition investigated was used for this optimisation problem. The shear yield strength k of the brick elements was updated based on the total shear strain accumulated γ using the modified Voce equation, given as Equation 4.2, again using the same respective coefficients m , n , p calculated in Chapter 3.

$$k = m(1 - e^{-n(\gamma)^p}) \quad \text{Equation 4.2}$$

When the total strain accumulated for a brick element reached the materials shear strain at failure, the brick element was classed as a weak, but was not removed from the model straight away. To simulate the removal of wear debris the brick elements were removed from the model based on the nature of their adjacent brick using the same set of 3 x 3 brick heuristics patterns illustrated in Figure 4.5 as

defined in ref. [14] . These heuristic patterns were applied starting from the top left brick searching left to right top down. The two outer vertical edges of the array of bricks wrap around and are connected to create a continuous cylindrical model along the horizontal axis. The wear rate w and wear depth d were calculated using Equations 4.3 and 4.4, respectively, based on the average number of bricks lost for each column in the brick array.

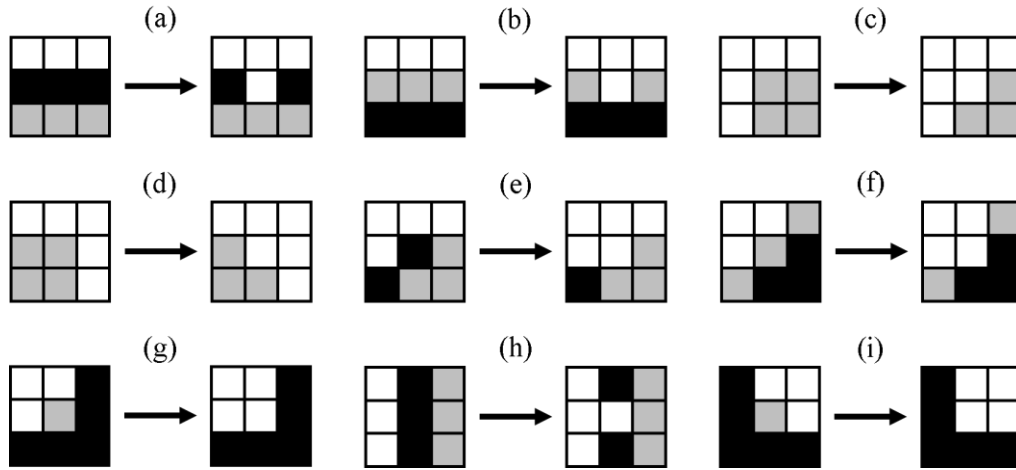


Figure 4.5: 3x3 Heuristic patterns used to determine when a brick is removed from the model as wear debris. White indicates brick that are non-existent, grey indicate bricks that can be either healthy or weak bricks, and black indicates weak bricks.

$$d = \frac{B_{lost} dz}{B_x} \quad \text{Equation 4.3}$$

$$w = \frac{B_{lost} dz}{NB_x} \quad \text{Equation 4.4}$$

where B_{lost} is the total number of brick elements lost in the model, dz is the vertical thickness of the brick elements, N is the total number of contact cycles simulated and B_x is the horizontal number of brick elements in the model.

4.3.3 Validation

The implementation of the brick approach to plastic ratcheting modelling recreated in Matlab for this work was validated against the original Brick model by reproducing the wear rate results presented in Table 2 in ref. [14] averaged over 1,000,000 contact cycles. As per the conditions explored in the original reference, this validation study simulated 100 x 512 bricks ($B_x \times B_z$) with the product $Ndz = 8$ mm. The material parameters of the rail steel consisted of an average shear strain at failure of 11.5 and an average tensile yield strength of 488 MPa, that was converted to a shear yield strength using Von Mises yield criterion. The values allocated to each brick in the model for the critical shear strain to failure and tensile yield strength were randomly sampled using a normal distribution with a

standard deviation based on 10% the mean value. The strain accumulated during each contact cycle was based on a ratcheting load conversion factor of 0.00237 with work hardening of the rail steel material not considered (shear yield strength not updated based on total accumulated shear strain).

The validation simulated a rail-wheel contact with a maximum Hertzian contact pressure of 1500 MPa with a contact half-width dimension of 11mm. Table 4.1 presents the validation results of the average wear rates for a rail-wheel contact simulating coefficient of tractions of 0.3, 0.4, 0.5, and 0.6 under full sliding contact conditions. A graph comparing the validation results against the original model results is shown in Figure 4.6. The average wear rate validation results shows that the implement of the brick model recreated in Matlab was in good agreement with the original model with the difference in the average wear rates within 10% of error. This implementation of the brick-based plastic ratchetting model used a different method of selecting bricks for removal than the original version, checking each brick against all heuristics in a single pass rather than applying the heuristics to the surface in sequence - and this may account for minor variations between the outputs. The close nature of agreement despite this variation gives confidence in the implementation in this thesis.

Table 4.1: Comparison of the average wear results generated by the version of Brick model replicated in this investigation against the results presented in Table 2 in ref. [14] averaged over 1,000,000 contact cycles.

| Run | Coefficient of Traction | | | |
|-----------------|-------------------------|--------|--------|--------|
| | 0.3 | 0.4 | 0.5 | 0.6 |
| 1 | 0.4160 | 0.9777 | 1.2678 | 1.5708 |
| 2 | 0.4159 | 0.9679 | 1.2672 | 1.5708 |
| 3 | 0.4155 | 0.9687 | 1.2674 | 1.5706 |
| 4 | 0.4155 | 0.9682 | 1.2693 | 1.5711 |
| 5 | 0.4162 | 0.9720 | 1.2682 | 1.5717 |
| 6 | 0.4160 | 0.9680 | 1.2685 | 1.5698 |
| Average | 0.4159 | 0.9704 | 1.2681 | 1.5708 |
| Reference Value | 0.4510 | 0.9661 | 1.3263 | 1.6347 |
| Error | 7.79% | 0.45% | 4.39% | 3.91% |

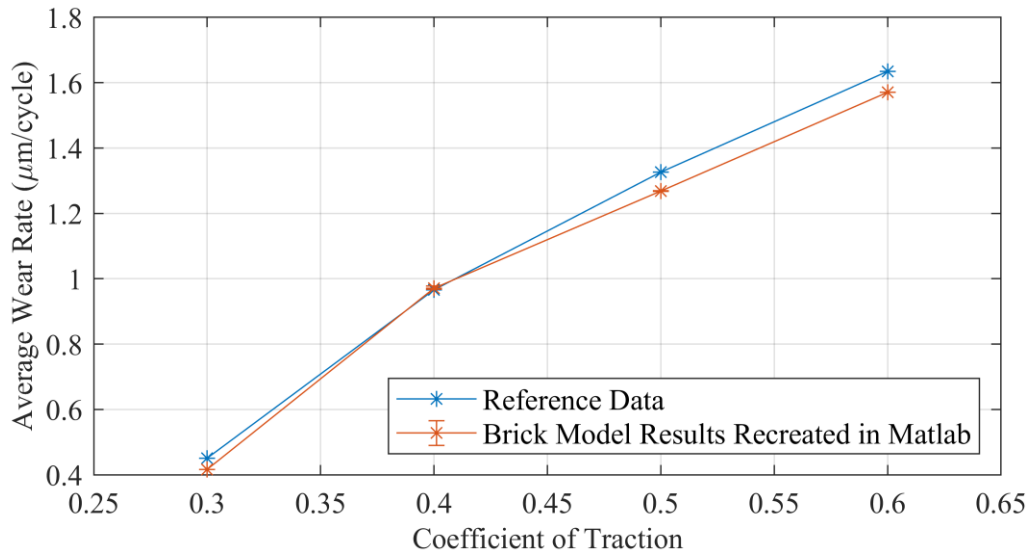


Figure 4.6: Brick Model average wear rate validation results.

In addition to the wear rate, a second validation study was also conducted to confirm that the plastic ratcheting-based simulation model replicated in Matlab correctly replicates the same rate of strain accumulation behaviour. For this study, a 1D ‘layer’ version of the model recreated in Matlab using the same code responsible for determining the cyclic incremental strain accumulation was compared to an earlier version of the ‘layer’ model written in PostgreSQL [215]. This study simulated the strain accumulation behaviour of a rail steel over 40,000 contact cycles for a smooth 1500 MPa Hertzian contact pressure distribution with a contact half-width of 0.31mm to represent a twin-disc contact for a low and high traction coefficient of 0.27 and 0.44, respectively. The material plastic deformation response simulated in this study was BS11 rail steel [13], [120], using the following material information:

- Modified Voce equation coefficients $m = 445.867$, $n = 0.473729$, and $p = 0.795764$
- Ratcheting load conversion factor, $c = 0.00237$
- Initial shear yield strength $k_0 = 234.4$ MPa
- Critical shear strain to failure, $\gamma_c = 11.5$

Both versions of the layer-based plastic ratcheting simulation model estimated the plastic deformation response down to a depth of 4 mm beneath the running surface discretised into equal thickness layers dz of 0.05 mm.

A comparison of the accumulated shear strain against contact cycles results generated by the simulation model Matlab and the PostgreSQL version of the layer model at a depth of 0.175 mm is presented in Figure 4.7. The graph shows that the Matlab simulation model and PostgreSQL version of the layer model produced identical results to one another. This validates that the portion of the

code responsible for calculating the cyclic accumulation of shear strain written in the implementation of the brick based plastic ratcheting simulation model used in this investigation correctly replicated the rate of strain accumulation behaviour observed in the original ‘layer’ and ‘brick’ models.

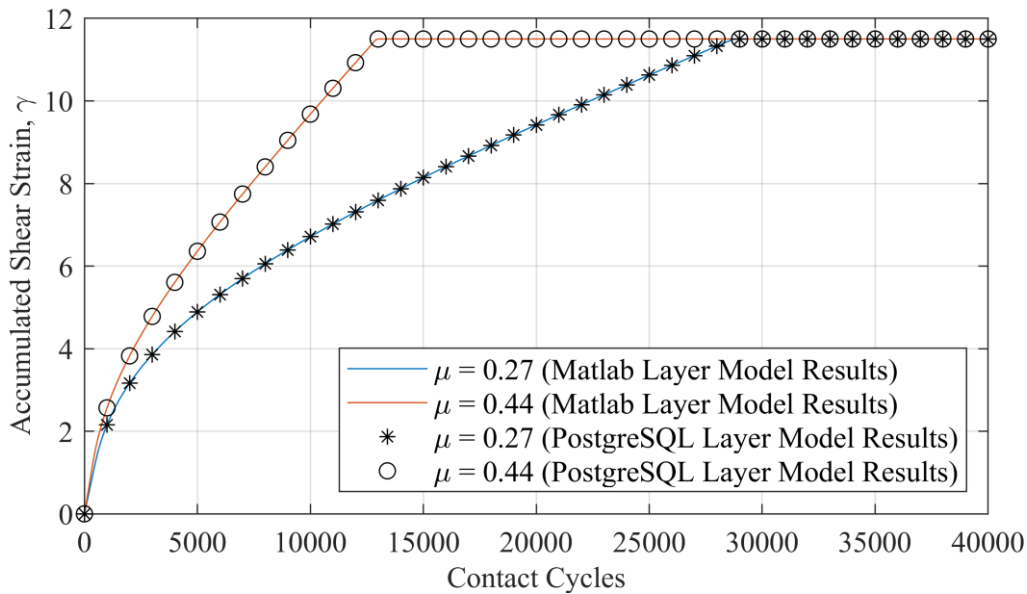


Figure 4.7: Comparison of the total accumulated shear strain against contact cycles at a fixed depth of 0.175 mm below the surface for BS11 rail steel for a rail-wheel contact friction coefficient of 0.27 and 0.44.

4.3.4 Convergence Studies

As mentioned previously, to determine the ideal vertical thickness and horizontal number of brick elements to use, two convergence studies were conducted.

4.3.4.1 Brick Vertical Thickness Convergence Study

The brick vertical thickness convergence study compared the average wear rate w against the vertical brick thickness dz , with the vertical thickness of the bricks varying between $0.25 \mu\text{m} - 32 \mu\text{m}$. The number of elements along the horizontal axis of the brick array was fixed at 200 bricks. The material simulated was R260 rail steel subjected to 1500 MPa, dry contact conditions. Using the same modified Voce equation coefficients and ratcheting loading conversion factor determined in Chapter 3. The materials shear strain at failure was assumed to be the same 11.5 value determined by Tyfour et al. [120] for BS11 rail steel. The wear behaviour of the R260 rail steel was simulated in this study for up to 70,000 contact cycles using a subsurface orthogonal shear stress distribution based on a rough contact.

The results of this first convergence study are shown in Appendix A3 in Table A3.5 and Figure 4.8. The findings from this convergence study showed that the average wear rate calculated became

insensitive to the vertical thickness of bricks when the vertical brick thickness was $\leq 1.0 \mu\text{m}$. Therefore, for this optimisation problem, a vertical brick thickness of $1 \mu\text{m}$ was chosen resulting in the array of bricks consisting of 800 bricks along the vertical axis.

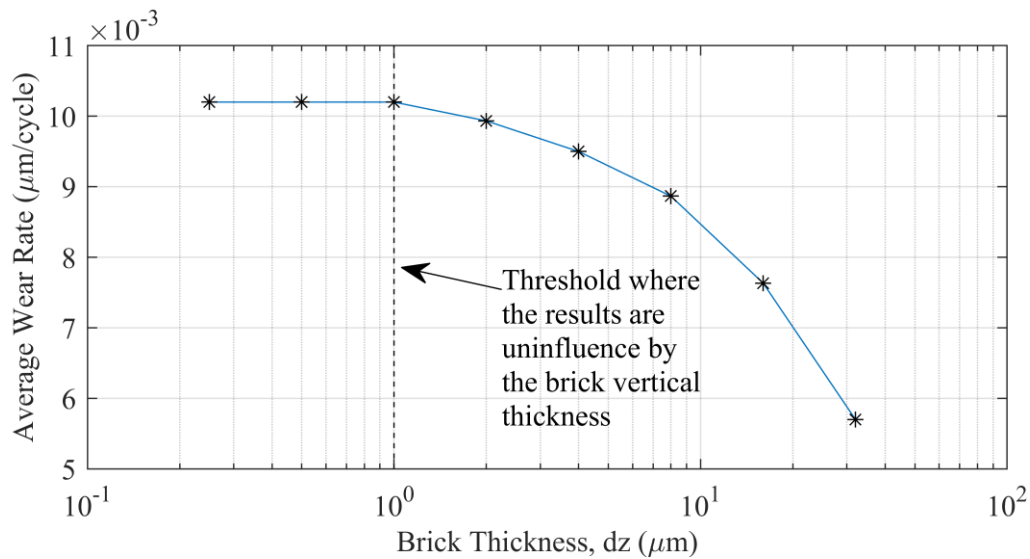


Figure 4.8: Plot comparing the average wear rate against the vertical brick thickness from the first convergence study simulating the wear behaviour of R260 rail steel subjected to 1500 MPa, dry contact conditions for up to 70,000 contact cycles. The results show that the average wear rate become insensitive to the brick vertical thickness when the bricks were $\leq 1.0 \mu\text{m}$ thick.

4.3.4.2 Brick Column Number Convergence Study

The brick column number convergence compared the average wear rate w against the number of brick columns N_x , with the number of brick columns in the simulation model varying between 1 and 1600 bricks. Like the vertical brick thickness convergence study, the material simulated was also R260 rail steel loaded under 1500 MPa, dry contact conditions. Using the same modified Voce equation coefficients and ratcheting loading conversion factor determined in Chapter 3 and the shear strain at failure value of 11.5 as determined by Tyfour et al. [120] for BS11 rail steel. In addition, the wear behaviour was also simulated in this study for up to 70,000 contact cycles using a rough contact based subsurface orthogonal shear stress distribution.

The results of the brick column number convergence study are presented in Appendix A3 in Table A3.6 and Figure 4.9. The results of this convergence study showed that the models average wear rate continued to decrease the more brick columns included in the model. Although the data did not plateau, the wear results rate of change did slow down the more brick columns simulated in the model. This observed behaviour occurs as the higher number of brick columns in the model provide more opportunities for introducing outlier bricks that were given a significantly above average shear yield

strength and critical shear strain to failure. These outlier bricks, therefore, persisted to be healthy for longer than realistically expected at the surface of the modelled rail material, hindering the progression of the rail's surface down to the next row of bricks and thus artificially lowering the wear rate. For this investigation, it was deemed that simulating anything more than 400 brick columns in the models provided minimal improvements in the wear results compared to the significantly higher computational cost.

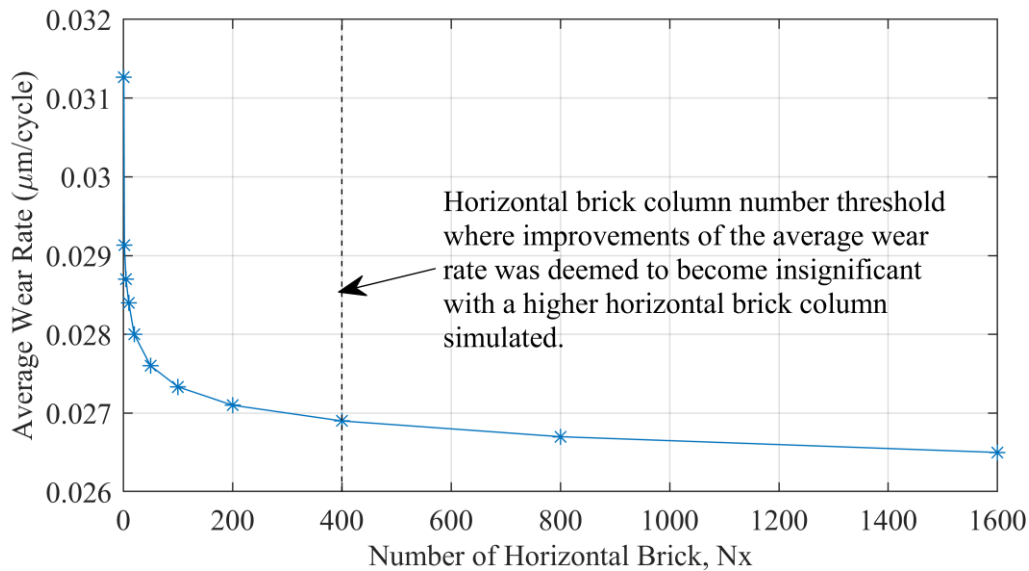


Figure 4.9: Average wear rate against the vertical thickness of the brick convergence study.

4.4 Results

As noted in the introduction, it was expected that this new value optimisation approach would be most suitable for the two contact conditions (1500 MPa and 1200 MPa R260), which display a combination of bulk and asperity driven plasticity. The other conditions (900 MPa R260, 600 MPa R260, 1500 MPa HP335, 1500 MPa R350HT) would be more challenging conditions to apply this new approach to, however, would still be explored in this work.

4.4.1 Combination of Bulk and Asperity Driven Contact Conditions

Figure 4.10(a-b) shows a comparison of the optimal simulation results against the experimental wear depth data for the conditions 1500 MPa R260 and 1200 MPa R260. In addition, an example of the iteration data generated during the optimisation calculation for R260 rail steel under 1500 MPa, dry contact conditions are shown in Figure 4.11. The results presented showed that the optimisation approach undertaken in this investigation worked successfully for these two conditions where it was expected to be most suitable. The shear strain at failure determined for these two conditions was 79.1 and 93.4 for the conditions 1500 MPa R260 and 1200 MPa R260, respectively.

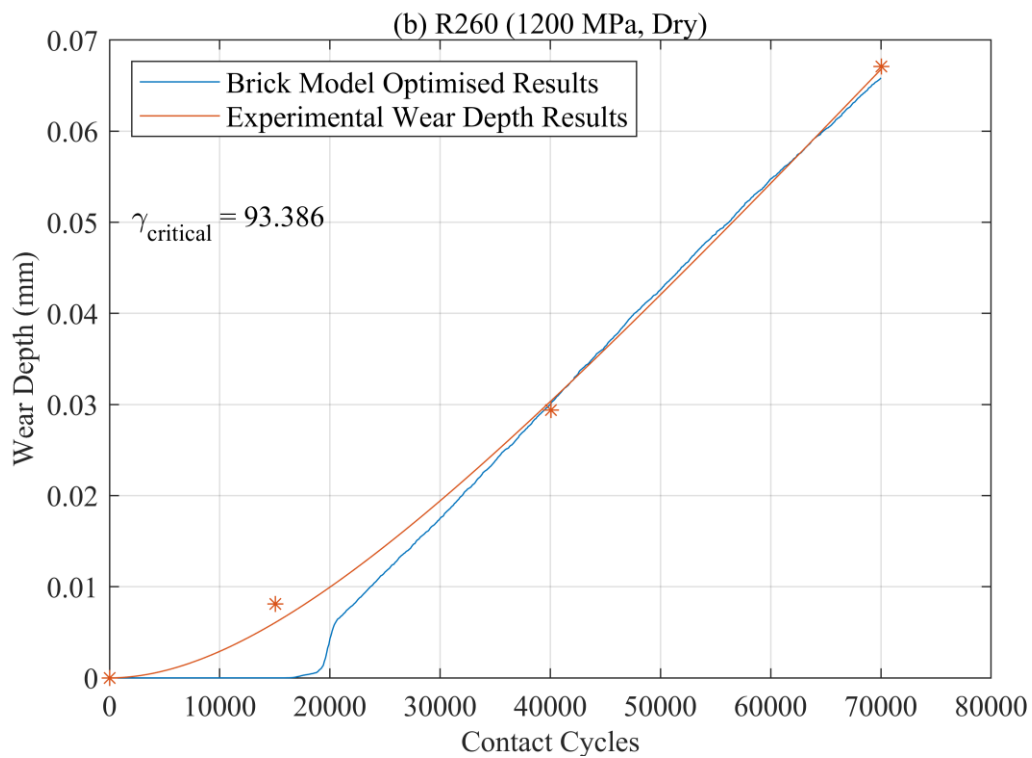
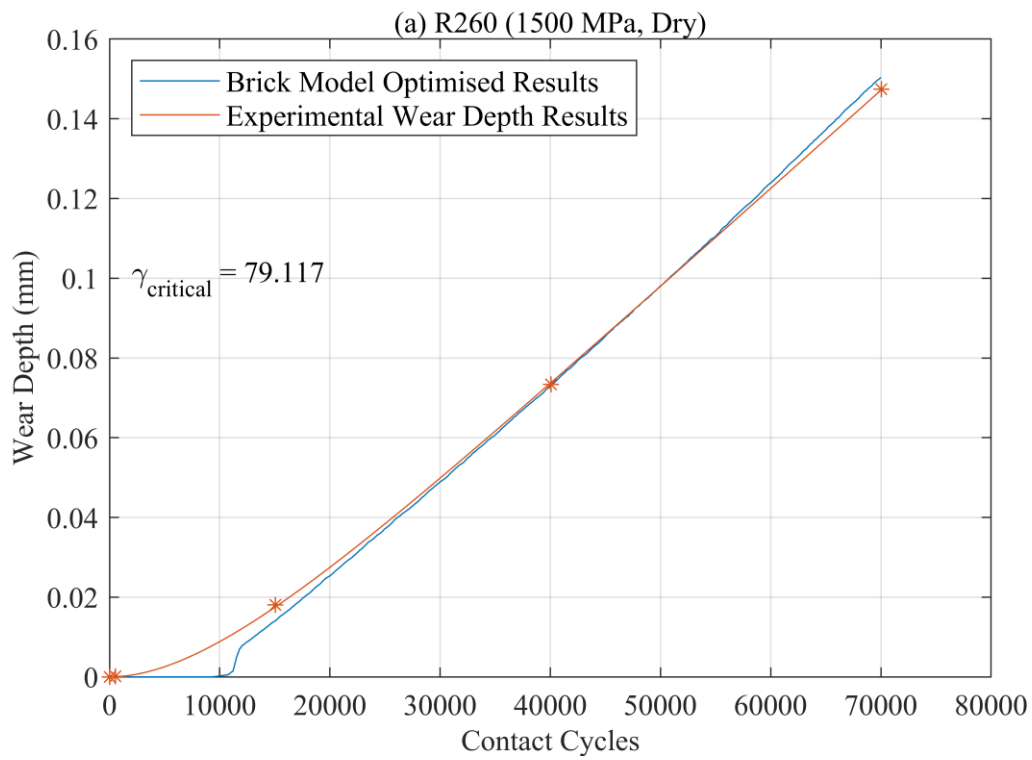


Figure 4.10: Comparison of the wear depth loss against contact cycles for optimal simulation results and the experimental wear depth results for the conditions (a) 1500 MPa R260 and (b) R260 (1200 MPa). The optimal Brick model results were determined using the optimisation objective of minimising the average difference between the simulation and experimental results during the steady-state wear behaviour stage wear behaviour stage exhibited by the simulation results at 100 contact cycles duration increments.

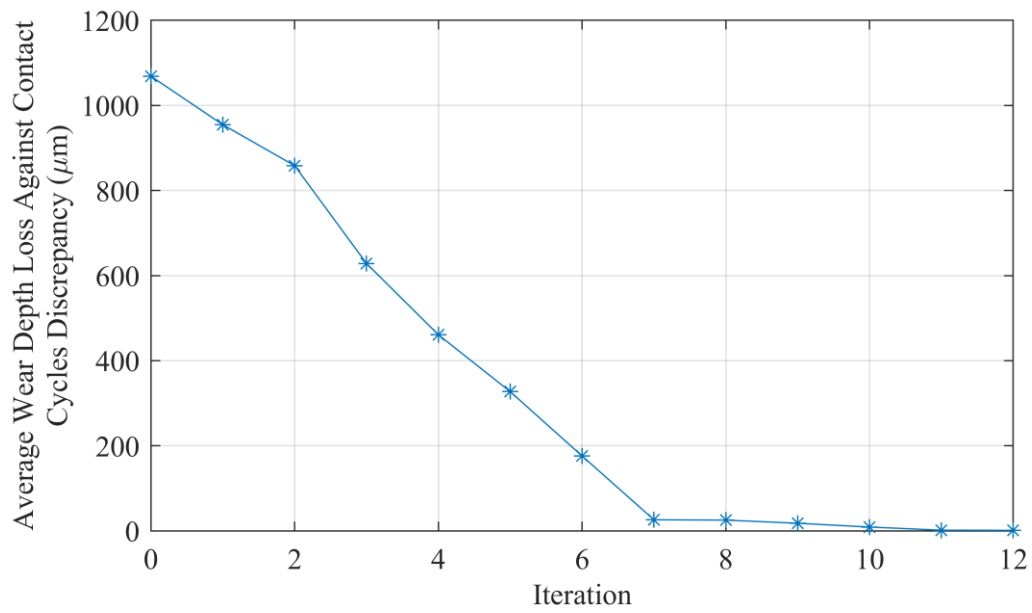


Figure 4.11: Graph showing the iteration results for the optimisation problem calculation conducted for R260 rail steel subjected to 1500 MPa, dry contact conditions.

1.1.1. Partially Asperity Driven Contact Conditions

Figure 4.12(a-d) shows a comparison of the optimal simulation results against the experimental wear depth data for the other four conditions that were expected to be more challenging for application of this method.

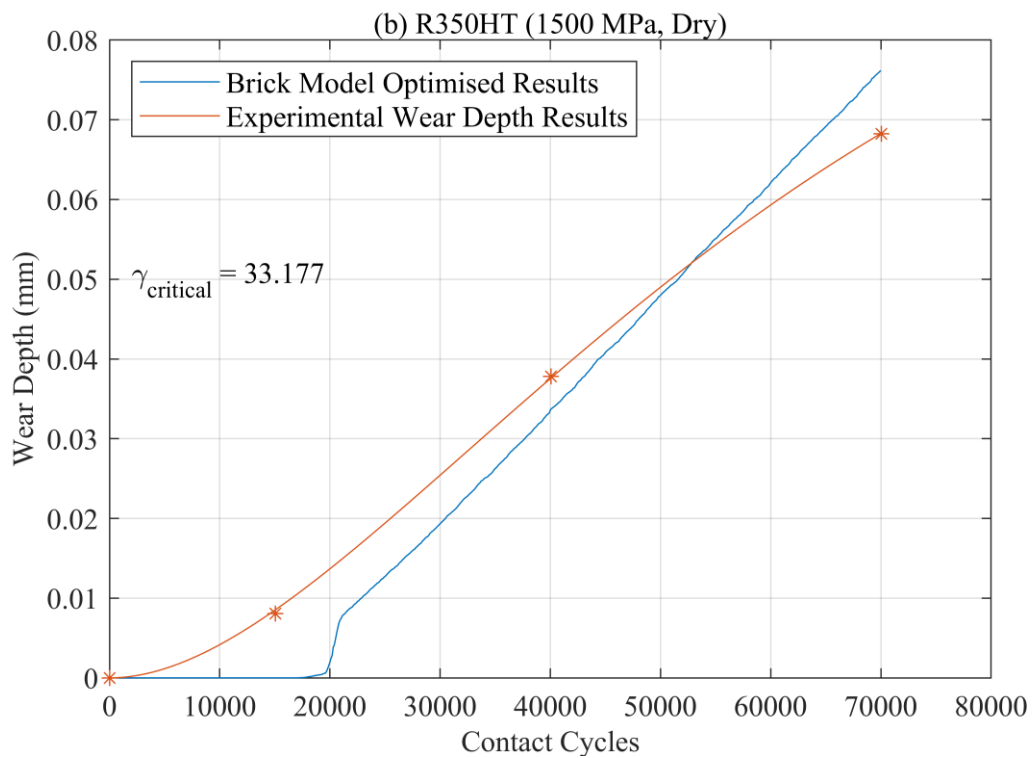
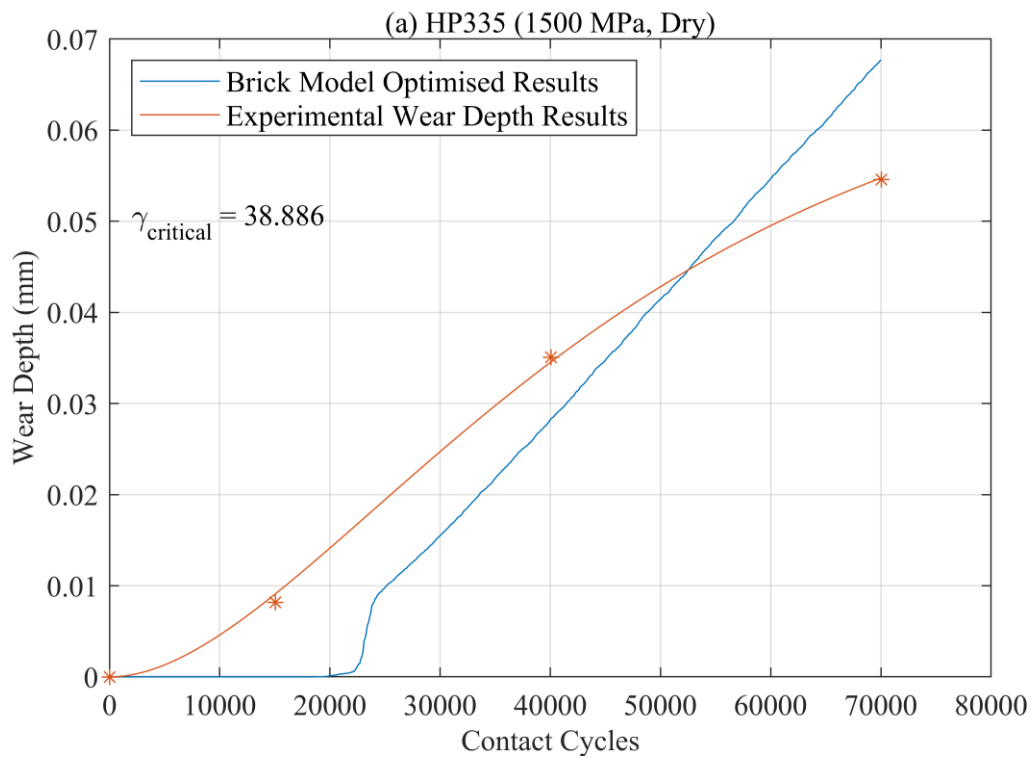


Figure 4.12: Comparison of the wear depth loss against contact cycles for optimal simulation results and the experimental wear depth results for the conditions (a) HP335 (1500 MPa), (b) R350HT (1500 MPa), (c) R260 (900 MPa) and (d) R260 (600 MPa). The optimal Brick model results were determined using the optimisation objective of minimising the average difference between the simulation and experimental results during the steady-state wear behaviour stage wear behaviour stage exhibited by the simulation results at 100 contact cycles duration increments.

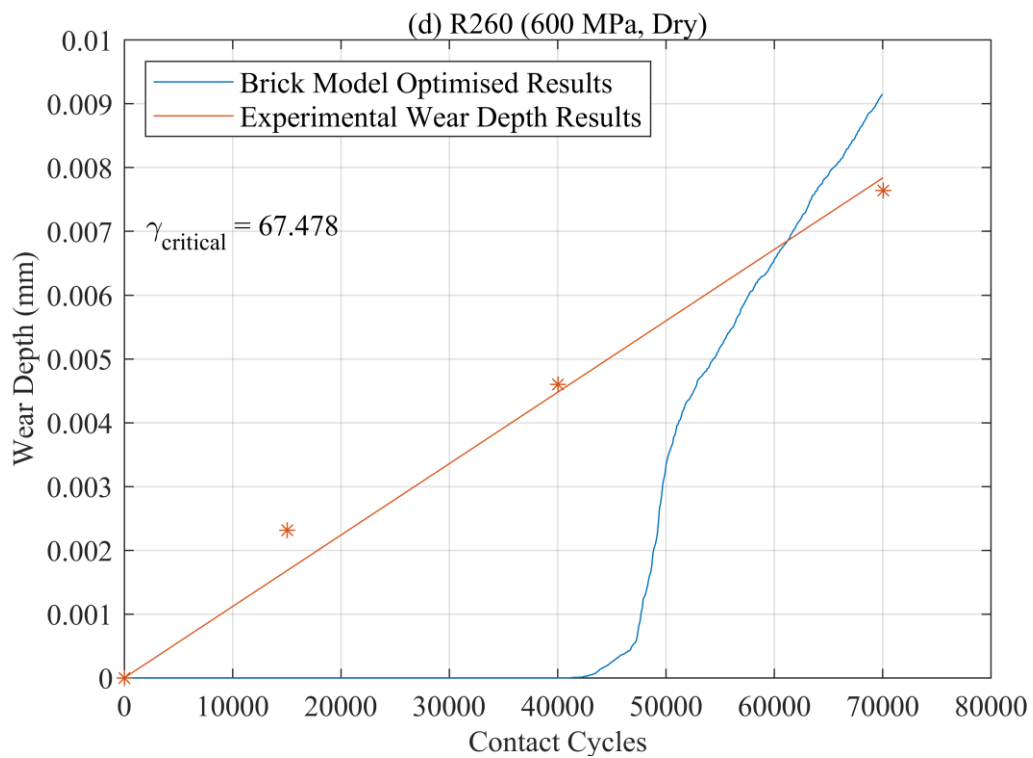
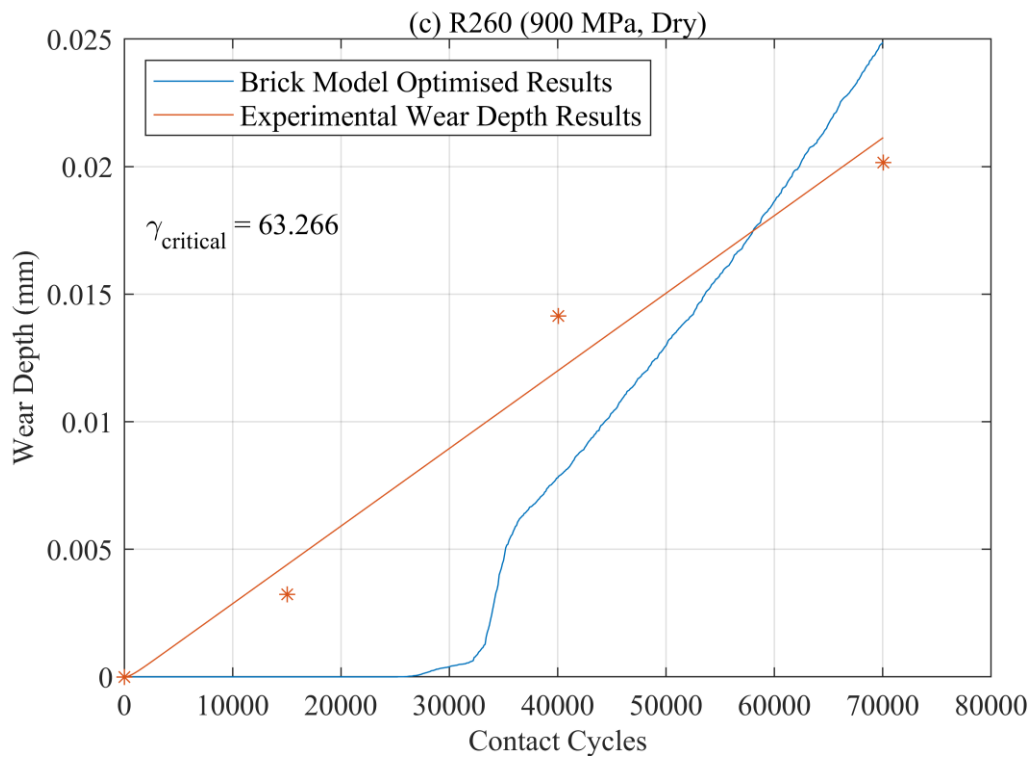


Figure 4.12: Continued.

The results presented showed that this methodology of determined the shear strain at failure was less successful for the four challenging conditions. This was because the approach in its current form was unable to converge onto a shear strain at failure value that allowed the simulation results to be in good agreement with the experimental data. The simulation results generated tended to overestimate the

wear depth loss against contact cycles gradient during steady-state wear conditions and thus forced the simulation results to crossover the experimental data to satisfy mathematical the criteria of the optimisation problems objective of convergence.

4.5 Discussion

The aim of this chapter was to investigate how the shear strain at failure (limit of accumulative shear strain that can occur before the nucleation of voids and microcracks) can be derived from rail steels subject to cyclic compression-shear contact conditions and try to establish a definitive approach to this problem. To do this a new value optimisation process was devised looking at determining this parameter via a value optimisation process using an implementation of the brick approach to plastic ratcheting simulation modelling. For the two conditions, 1500 MPa R260 and 1200 MPa R260, that were expected to be best suited for this methodology, this new approach was found to be successful with the simulation results converging with the experimental data. For the other four conditions (900 MPa and 600 MP R260, 1500 MPa HP335, and 1500 MPa R350HT data), however, this new approach was found to be less successful for these cases. This was somewhat expected, as these four conditions were deemed early on in this investigation to be more challenging conditions to apply this new approach to. This was because compared to the conditions 1500 MPa R260 and 1200 MPa R260 which exhibit a combination of asperity and bulk contact driven plastic damage, the four challenging conditions were instead more significantly influenced by the asperity contact driven plasticity. In addition, this approach only models ratcheting wear mechanisms and potentially might miss things for the harder rail steel or lower normal contact pressure conditions where perhaps oxidation or some other wear mechanism begins to dominate. The other potential reasons for why the Brick model optimisation approach used this investigation was less successful for the four challenging conditions investigated will be examined in this section. On top of this, it is questionable whether the shear strain at failure values determined for the two conditions that did work may be unrealistically larger than the true value.

The first problem identified with the value optimisation approach conducted in this investigation was that the brick elements were potentially being removed too easily from the simulation model. This could stem from the following four areas identified: i) The yet to be fully explored probabilistic nature of a brick getting removed from the model when a heuristic pattern is satisfied. ii) The possible over definition of the heuristic patterns used to outline what brick elements should be removed from the model. iii) The lack of communication between nearby bricks regarding the state of the bricks total accumulated shear strain, that would avoid the sharp variation of accumulated shear strain across nearby bricks. iv) The 2D representation of the simulation model that does not account for the state

of brick elements across the lateral plane in the heuristic patterns. Overall, the easier removal of brick elements due to the areas identified leads to the model overestimating the wear rate, in which forces the optimisation model to converge on an unrealistic high shear strain at failure to match the experimental data. This unrealistic high shear strain at failure created further problems by detrimentally delaying the removal of bricks from the model, which then makes it difficult for the model to match up with the experimental results.

The second issue possibly stems from the pure elastic assumption utilised in the Nowell-Hills roughness used to generate the subsurface orthogonal shear stresses for a rough contact in this study. This is because a common concern associated with pure elastic contact models is that they produce unrealistically high normal contact pressure, which in turn generates unreasonably high subsurface orthogonal shear stresses. This is due to these type of roughness models lacking the ability to account for the flattening out of asperity that would occur from the plastic deformation of the running surface, therefore, increasing the real contact area and decreasing the stresses experienced. Overall, the higher-than-expected orthogonal shear stresses estimated using a pure elastic based contact will result in a faster than normal shear strain accumulation being predicted for the rows of brick close to the surface and, therefore, wear rate. To compensate, the optimisation algorithm must increase the materials shear strain at failure estimated above what would be the true value to dampen the higher-than-expected wear rate predicted by the model to match the experimental data. The rough contact model utilised also does not consider the multi-scale nature of surface roughness, which could have also influenced the results.

The standard deviation of the array of brick initial material was another potential source of error that could be preventing the models from being in good agreement with the experimental results. This was because in this investigation and in other studies using the same model [116], [213], [214], the initial shear yield strength and shear strain at failure for each brick was sampled from a normal distribution with a standard deviation of 5% of the average value supplied. There have been other studies in literature that have used a different standard deviation of 4% [115] and 10% [11] of the average value, however, 5% was the most commonly used. The problem with all the standard deviation percentages mentioned is that they originate from the standard deviation of results observed from microhardness and nanohardness results. This is problematic, as it is difficult to separate out the standard deviation contribution from the actual material variation and the deviation of results introduced from sample surface preparation and the equipment experimental error. A comparison of the effect of different standard deviations percentages on the brick material properties is shown in Figure 4.13 with the optimal shear strain at failure derived tabulated in Table 4.2. The comparison shows that increasing the standard deviation to 10% for the 1500 MPa R260 condition does decrease

the optimised critical shear strain to failure estimated. Like the explanation given for the horizontal brick column convergence study, this observed happens because the higher standard deviation increases the likelihood for outlier bricks to be introduced, which artificially lowers the wear rate of the model. This improvement, however, was insignificant to be the main driving factor causing the simulation model to converge on an unrealistic high shear strain at failure result. In addition, changing the standard deviation percentage from 0.1% to 10% for the 1500 MPa, HP335 conditions was unable to significantly improved the fit between the experimental and simulation results for this case.

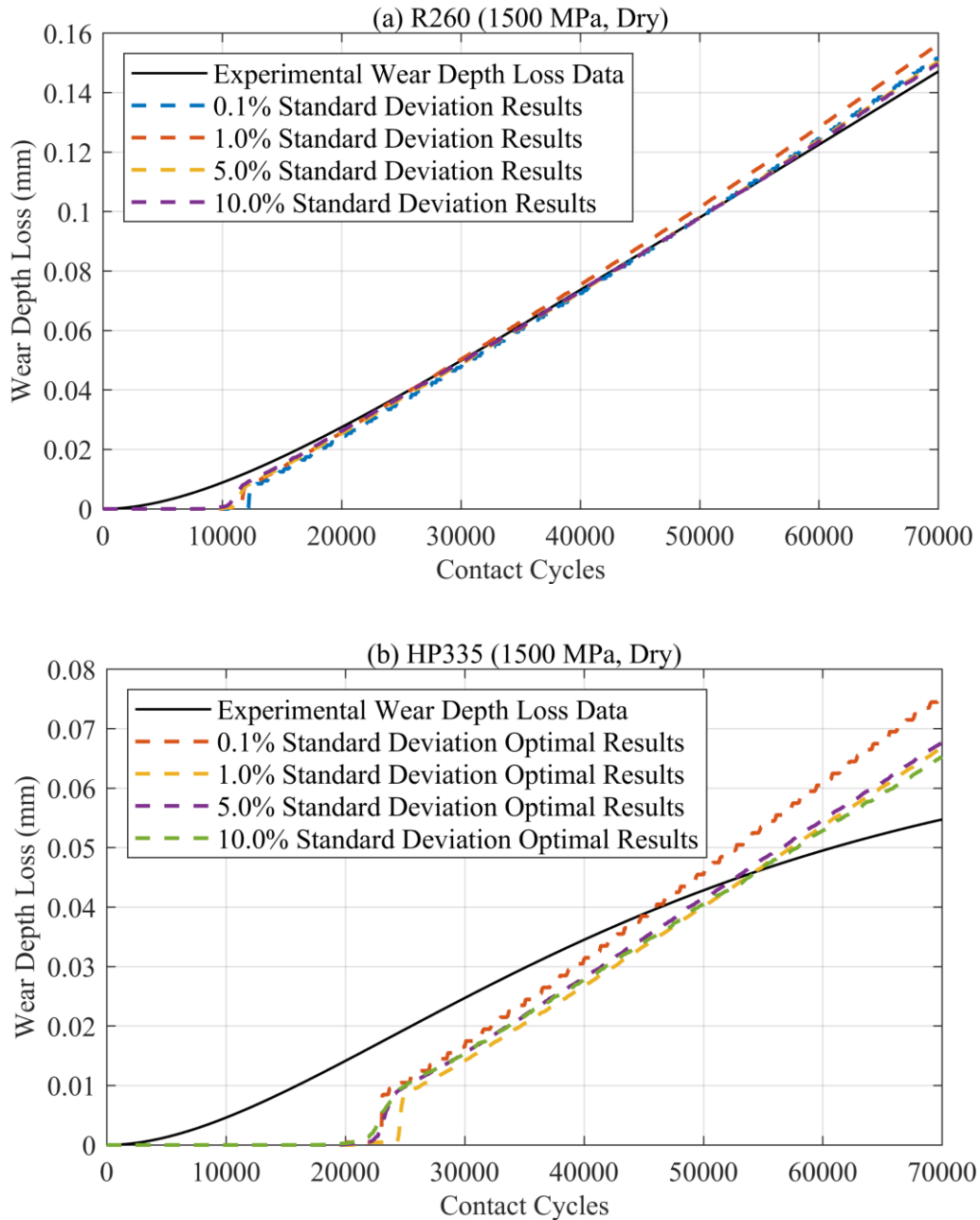


Figure 4.13: Comparison of the effect of different brick material property standard deviation of 0.1%, 1%, 5%, and 10% for (a) R260 and (b) HP335 rail steel subject to 1500 MPa, dry contact conditions.

Table 4.2: Comparison of the optimal shear strain at failure results derived for R260 and HP335 rail steel subject to 1500 MPa, dry contact conditions with the brick material properties sampled using a gaussian distribution with a standard deviation based on 0.1%, 1.0%, 5.0%, and 10.0% of the average values supplied.

| Standard Deviation (%) | R260 (1500 MPa) | HP335 (1500 MPa) |
|------------------------|-----------------|------------------|
| 0.1 | 85.50 | 39.08 |
| 1.0 | 82.24 | 41.41 |
| 5.0 | 79.17 | 39.89 |
| 10.0 | 73.27 | 36.82 |

A final potential issue in this investigation was the uncertainty in the experimental cyclic wear depth data due to the practical constraints on repeat runs of uninterrupted twin-disc tests. This was because in this investigation, a compromise had to be made between exploring different contact conditions and rail and wheel material pairings over conducting any repeat experiments for the uninterrupted experiments. This implies that the experimental wear depth against contact cycles data used to optimise the simulation results towards was only based on one experimental data point at each different contact cycle duration. Therefore, there is a potential problem for the experimental results to be affected by outliers, which can in turn influence the simulation optimisation results.

4.6 Conclusions

Following on from the work started in Chapter 3, this chapter explored the derivation of the rail steel shear strain at failure (limit of accumulative shear strain that can occur before the nucleation of voids and microcracks) under repeated rail-wheel contacts. To derive the rail steel shear strain at failure a new value optimisation process using an implementation of the brick approach to plastic ratcheting modelling was used. In this approach, the rail steel shear strain at failure was varied until the cyclic wear depth loss simulation results converged with the experimental twin-disc data. The results presented in this investigation showed that for the two conditions (1500 MPa R260 and 1200 MPa R260) believed to be suitable for this approach, this technique was found to work very well. For other conditions (900 MPa R260, 600 MPa R260, 1500 MPa HP335, 1500 MPa R350HT) that were considered challenging cases to apply this technique to, the results generated were less successful. In addition, it was also questioned whether the shear strain at failure estimated using this approach derived unrealistically high values for the conditions where it did work.

The potential reasons given for the potential issues observed with this new value optimisation approach are:

1. The bricks potentially being removed too easily removed from the implementation of the brick-based plastic ratcheting simulation model. This could be due to i) the yet to be fully explored probabilistic nature of a brick getting removed from the model when a heuristic pattern is satisfied. ii) The possible over definition of the heuristic patterns used to outline what bricks should be removed from the model. iii) The lack of communication between nearby bricks regarding the state of the bricks total accumulated shear strain, that would avoid the sharp variation of accumulated shear strain across nearby bricks. iv) The 2D representation of the simulation model that does not account for the state of bricks across the lateral plane in the heuristic patterns.
2. The overestimation of the normal contact pressure and subsurface orthogonal shear stress using the Nowell-Hills roughness model caused by the pure elastic contact assumption.
3. The variation of material properties of brick elements is not yet truly representative of actual microstructure (featuring grain boundaries and inclusions and so forth) and is impacted by experimental scatter in the techniques used to quantify it.
4. The uncertainty in the experimental wear loss against contact cycles data due to practical constraints on repeat runs of uninterrupted tests.
5. The inability to replicate all the different wear mechanism usually experienced by rails steel due to the cyclic interaction of rail-wheel contacts.

From this investigation, the following areas for further work have been identified:

- Conduct two additional uninterrupted twin-disc tests for each contact cycle duration to improve the confidence in the experimental data. In addition, a few more experiments to populate the early stages of the experiments should be conducted to improve the understanding of rail steels initial wear behaviour.
- A 3D version of a plastic ratcheting simulation model should be explored with an entire new list of heuristic patterns developed to better represent the plastic deformation of rail steel from twin-disc tests and actual rail-wheel contacts.
- The connectivity of the brick shear strain state would need investigating to prevent unrealistic step changes in the accumulation shear strain across the array of brick elements.
- A better understanding of the rail steels true standard deviation of initial material properties should be investigated.
- The application of an elastic-plastic based roughness contact model should be considered to provide a better estimate of the real orthogonal shear stresses experienced by a rail steel because of surface roughness.

- Examine how the plastic ratcheting simulation models can better replicate all the different wear mechanisms experienced by rail steels due to the cycle interaction of rail-wheel contacts, such as oxidation, ratcheting, and adhesion wear mechanisms.

Chapter 5: Development and Testing of a Novel Optical Monitoring System for Twin-Disc Testing

Novelty and Highlights

- Designed and develop a new optical monitoring system for twin-disc testing capable of photographing in-situ the initiation and development of damage on the running surface of a rail steel twin-disc sample while rotating at 400 rpm.
- Establish a new image analysis approach of understanding the wear behaviour of rail steels from demonstrating the connection between the total wear flake shadow area and the wear rate.

Journal Publication

The work presented in this chapter has been published in the following journal publication:

- A.P.G. Wilby, J. Corteen, R. Lewis, D.I. Fletcher, “Novel in-situ real-time line scan optical monitoring of wear and surface damage initiation in a laboratory twin disc test,” *Proceedings of the Institution of Mechanical Engineers, Part F: Journal of Rail and Rapid Transit*, vol. 0(0), p. 1-11, 2024, doi: 10.1177/09544097241242169.

5.1 Introduction

Twin-disc machines are a common experimental tool used to understand the wear and RCF performance of rail and wheel steels in a laboratory environment. The frequent usage of this experimental approach is attributed to the good balance of characteristics exhibited between accurately representing the rail-wheel contact and accessibility and affordability. However, as highlighted in the literature review in Chapter 2, one inherent drawback of conventional twin-disc machines is that information regarding wear and RCF performance is only obtained after a twin-disc test has finished.

A variety of approaches have been explored previously for implementation with twin-disc tests to expand the amount of information obtained about these damage mechanisms initiation and development. These include regular test interruptions [117], [172], [173], eddy current sensors [174], electro-magnetic array sensors [175], and optical camera systems [123], [181]–[184]. An unexplored opportunity has been spotted, however, for an optical monitoring system that visualises in-situ in real time the morphological initiation and development of wear flakes and RCF cracks on a twin-disc samples running surface while rotating at 400 rpm without needing to interrupt a test.

The aim of this chapter is to describe the development of a new optical monitoring system capable of photographing in detail a twin-disc samples running surface while rotating at speeds up to 400 rpm during tests. To allow the surface morphological development of wear flakes and RCF cracks to be optically observed on the outer running track of twin-disc samples. This chapter will first explain the design and development undertaken to create the optical monitoring system. Followed by preliminary trial experiments conducted to evaluate the performance and capabilities of the system at visualising the surface evolution of wear flakes and RCF cracks on a twin-disc running surface.

5.2 Equipment Description

The optical monitoring system developed, as shown in Figure 5.1, was designed as two detachable modules (camera module and line light driver module) that can be mounted onto the SUROS2 twin-disc machine. When in use, the two modules are connected by an intermediate slider on the machine guarding and the line light driver module is mounted onto the rail roller driveshaft frame to allow the entire system to move with the rail sample. This enables the system to create a stable image of the rail twin-disc sample running track. For alternative test machines or if the wheel sample were of greatest interest the detachable modules can be remounted.

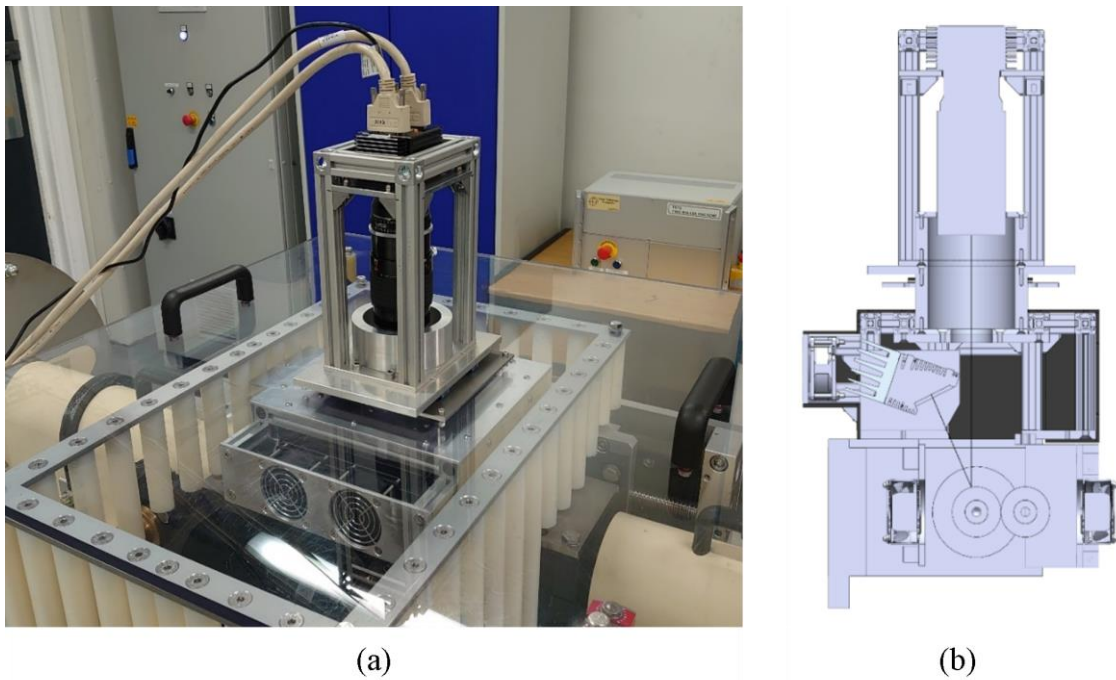


Figure 5.1: Image (a) and cross-section view (b) of the optical monitoring system designed and developed for the SUROS 2 twin-disc machine.

5.2.1 Camera Module

A Basler sprint spl4096-70kc colour line scan camera equipped with a manual focus Nikon f/2.8 105 mm macro lens was used to photograph the running track of the rail sample during tests. A line scan camera was chosen over a more conventional area scan camera for this application as it can observe a cylindrical specimen running surface without the final image being affected by perspective distortion. A sequence of line scans taken at high frequency while the disc is rotating can be stitched together to create a complete 2D photograph of the entire disc circumference, which would be very difficult without introducing distortion when stitching images from an area scan camera. Once captured, the data obtained is recorded using a EPIX PIXCI EL1 frame grabber card [216] connected using CameraLink cables. Postprocessing of the data was carried out using XCAP image processing software developed by EPIX [217] to stitch together individual line scans into a single complete image.

The line scan camera and macro lens combination have a 10 μm sensor pixel size and an optical magnification of 0.5. The spatial resolution, S , for the system can, therefore, be determined by Equation 5.1 [218]:

$$S = \frac{P_{size}}{M} \quad \text{Equation 5.1}$$

where P_{size} is the camera sensor pixel dimensions and M is the equipped lens optical magnification. For the line scan camera and macro lens configuration used, this equates to a spatial resolution for the system of 20 $\mu\text{m}/\text{px}$. A smaller spatial resolution can be achieved by using a higher magnification factor optical lens and/or replacing the camera with one that has a smaller sensor pixel dimension.

The XCAP image processing software is set to capture marginally more lines than needed for one full rotation of the sample allowing complete surface visualisation. The optimal line capture time, $t_{line\ scan}$, and the minimum number of line scans needed to create an image corresponding to one full rotation, $N_{1\ rev}$, are found by Equation 5.2 and 5.3, respectively [218]:

$$t_{line\ scan} = \frac{S}{\pi d_{rail} \omega_{rail}} \quad \text{Equation 5.2}$$

$$N_{1\ rev} = \frac{t_{1\ rev}}{t_{line\ scan}} \quad \text{Equation 5.3}$$

where d_{rail} is the diameter of the rail twin-disc sample, ω_{rail} is the rail twin-disc samples rotation speed, and $t_{1\ rev}$ is the time taken for the rail twin-disc sample to complete one full rotation. For a 47mm diameter twin-disc sample rotating at 400 rpm, this translates to an optimal line capture time

of 20 μs , and a minimum of 7500 line scans are needed to create an image corresponding to one full rotation. To reach these extremely short line capture times and avoid exceeding the system data transfer limits, the camera's horizontal field of view (FOV) needed to be reduced to about 800 pixels wide so that the images captured include just the specimen running track and exclude extraneous data. During testing it was found useful to capture 12000 line scans per image to provide overlap in the case a region of interest lay at the boundary of the image, giving total image size of 9.6 megapixels.

The aperture selected for the optical monitoring system needed to strike a balance between providing sufficient depth of field while maximising light entering the camera to meet the intended exposure time and line capture frequency. This is to allow the rail twin-disc sample to be observed while also accounting for the change in sample diameter during testing because of wear. The depth of field, T , for macro photography can be determined using Equation 5.4 [218]:

$$T = \frac{2fC(1 + M)}{M^2} \quad \text{Equation 5.4}$$

where f is the relative aperture or f-number rated on the camera lens and C is the circle of confusion which is the criterion used for determining acceptable sharpness in the image formed, set equal to the 10 μm pixel size in this case. Experience of testing rail steels showed that a minimum depth of field of 0.6 mm was desirable to cover the expected wear loss during typical test durations. For the camera and lens used ($M = 0.5$), the relative aperture needed to be set at a minimum of $f/5.0$ to provide enough depth of field. As the macro lens for the camera set up had click stops at specific positions, this implied selecting the next highest selectable aperture of $f/5.6$.

Within the XCAP image processing software, the data collected by the line scan camera was captured using a 12-bit 4 channel colour configuration with 0 offset and no shading correction applied. The gain for the green colour channel was reduced by 1.8 dB in the software while the red and blue channels were unchanged, to correct (by eye) the colour of the images collected. This was done because of the greater green colour information obtained by the camera used in this work due to the Bayer sensor pattern which has two green, one red, and one blue sensor for every pixel. As the purpose of the system, however, is to observe the morphological change of surface features, such as wear flakes and RCF cracks, photorealistic colour was not essential.

5.2.2 Line Light Driver Module

Due to the extremely short line capture times needed, it was necessary for the running surface of the rail twin-disc samples observed by the line scan camera to be brightly illuminated. To provide sufficient lighting, a Chromasens Corona II LED line light [219] was used with the optical monitoring

system. This light source can deliver up to 500,000 lux of illuminance onto the sample running track at the required 95 mm operating distance imposed by machine construction and guarding restrictions. The LED line light is controlled by a Chromasens XLC4 control unit that communicates with the optical monitoring computer via an ethernet cable and is programmed using Chromasens XLC4 Commander software.

The position of the LED line light in the module can be changed allowing the light source to provide either brightfield or darkfield illumination. Brightfield illumination, illustrated in Figure 5.2a, involves the LED line light positioned so that the main reflected light path from the sample running surface runs directly into the line scan camera. For darkfield illumination, shown in Figure 5.2b, the line scan camera is instead positioned to receive light that has been reflected from any defects on the twin-disc samples running surface.

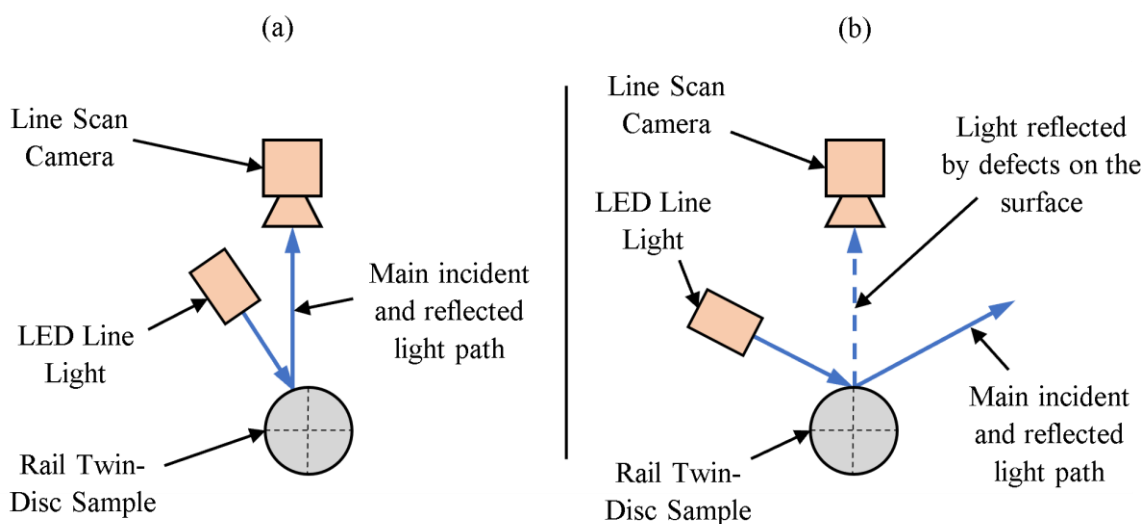


Figure 5.2: Illustration of how the optical monitoring system can be achieved (a) brightfield and (b) darkfield illumination.

5.3 Methodology

To understand the performance of the new optical monitoring system, two experimental studies were undertaken: (i) A preliminary rail damage visualisation assessment using discs of known condition rotating without a counterface, and (ii) a live experimental performance study running with the discs in contact and consequently with surfaces evolving over time.

5.3.1 Rail Damage Visualisation Assessment

The rail damage visualisation assessment study focused on assessing the ability of the optical monitoring system to visualise wear flakes and RCF cracks from a disc running track. To do this,

images were captured using this system for three twin-disc samples rotating at 400 rpm with known existing surface features: (i) a rail sample of R260 grade steel previously tested against an R8T wheel steel with pre-existing wear damage was used for the example of wear flakes; (ii) an eddy current crack detection calibration disc with a crack spark eroded onto the running surface parallel to the disc's lateral direction [220] providing a well-defined surface defect of known geometry; (iii) a new unworn sample that provided a baseline to compare the surface features identified by the optical monitoring system from the two other samples. For each sample examined using the system, images were captured with the LED line light positioned for brightfield and darkfield illumination. This enabled assessment of which illumination method provided the best way of easily visualising wear flakes and RCF cracks from the sample running track.

5.3.2 Live Experimental Performance Study

The live experimental performance study evaluated the capabilities of the optical monitoring system in real time during live tests. For this study, one dry and one water-lubricated contact twin-disc test were performed using the optical monitoring system to photograph in-situ and in real time the development of wear flakes and RCF cracks. The dry contact test was conducted uninterrupted under 1500 MPa, 1% slip, dry contact conditions for a total of 70,000 contact cycles. The water-lubricated twin-disc test was performed under 1500 MPa, 1% slip, dry contact conditions for an initial 500 contact cycles, followed by water-lubrication applied 1 drop every 3 s. For both dry and wet tests these are common combinations of conditions used in SUROS2 twin disc testing for rail and wheel steels. The water-lubricated twin-disc test was stopped when a visible RCF crack was observed in the images captured using the optical monitoring system. For both the dry and water-lubricated tests, R260 rail steel was loaded against R8T wheel steel. The rail and wheel samples used in these experiments were machined, respectively, out of a full-scale rail and railway wheel, as illustrated in Figure 3.3. The running track of all the samples was ground to an average surface roughness (R_a) of 0.5 μm . Prior to and after conducting both tests, the samples were cleaned in an ultrasonic bath using acetone, had their mass recorded, and their running track diameter and width measured.

During the dry contact twin-disc test, the optical monitoring system recorded an image of the rail sample running track every 15 seconds (approximately every 100 contact cycles). In the water-lubricated test, however, an image was recorded of the rail sample running track every 3 seconds (approximately every 20 contact cycles). A faster image capture rate was used due to the unknown nature of how quickly visible RCF cracks initiate in rail steel as it had not been previously possible to observe this phenomenon in a running test. A portion of the sample shoulder was included in the images captured to provide a location of identification markers that were used to help keep track of

the angular position of the sample during the tests. For this purpose, an A, B, C, D marker was written on the twin-disc samples shoulder every quarter revolution.

5.4 Results and Discussion

5.4.1 Rail Damage Visualisation Assessment Study Results

Figure 5.3(a-f) shows the results obtained from the rail damage visualisation assessment study. For brightfield illumination, shown in Figure 5.3c and Figure 5.3e, the outline of the wear flakes and RCF calibration slot can be easily identified by the shadow these defects cast onto the sample running surface, in comparison to Figure 5.3a for an untested surface in which primarily machining marks were visible. In addition, the brightfield illumination images was also able to provide insight on tarnishing and scuffing that occurs on the running track. For the darkfield illumination images (Figure 5.3d and Figure 5.3f) the wear flakes were recognised as bright spots in the image, due to light reflecting off the back of wear flakes peeling away from the running track. Figure 5.3b provides the comparable untested surface indicating some staining of the surface (not visible with the naked eye) even after acetone cleaning but there was no surface flaking. These bright spots were associated with wear flakes; however, bright spots can also be created by surface roughness, making it hard to distinguish between the two. This could especially be the case when wear flakes just start appearing as it would be expected that the size of the bright spots created by wear flakes and surface roughness would be comparable. For the RCF calibration disc, darkfield illumination was unable to illuminate the spark eroded crack as it is recessed below the disc surface, making it less visible compared to brightfield illumination.

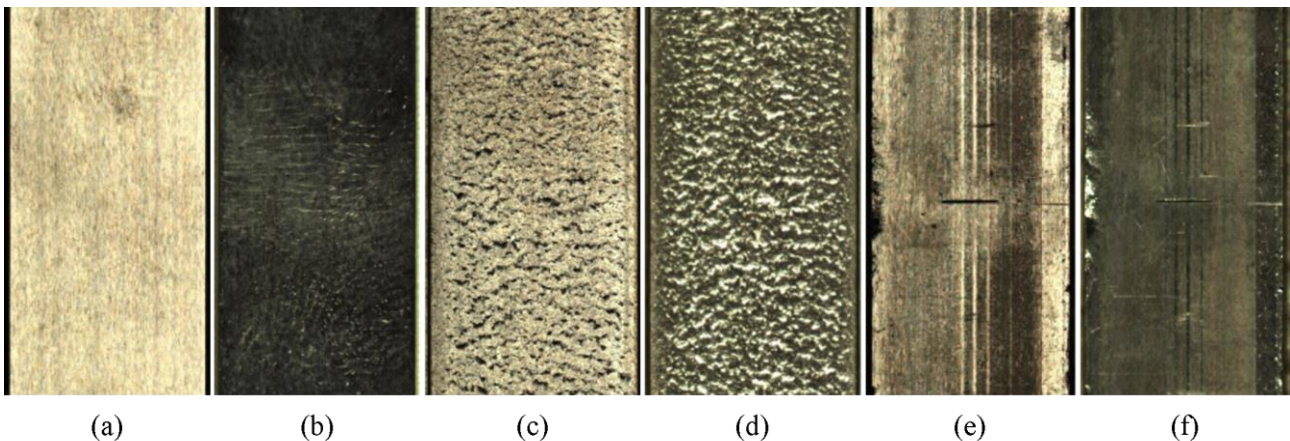


Figure 5.3: Images obtained from the optical monitoring system for a new (a, b), wear (c, d) and RCF calibration (e, f) twin-disc sample rotating at 400 rpm using brightfield (a, c, e) and darkfield (b, d, f) illumination.

5.4.2 Real Time Experimental Performance Study Results

Following assessment of the images from the rail damage visualisation assessment in Section 5.4.1, both dry and water-lubricated live experiment tests were undertaken using brightfield illumination. The photographs captured of the rail running track during the dry contact test are shown in Figure 5.4. The images show that the new optical monitoring system can very effectively visualise the development of wear flakes on the rail sample while the specimens are running in contact. As evident from the lighting intensity of the sample shoulder, it was required to occasionally increase the intensity of the LED line light to ensure the running track retained similar brightness in the images obtained throughout the experiment. This counteracted the change in reflectivity of the twin-disc running track observed during the test, possibly caused by the changing surface roughness and/or accumulation of wear debris on the running track. Manual control of the illumination helps reveal these changes that might be overlooked with automated correction of light levels. In terms of wear flake development, the photographs showed an initial stage of running surface darkening, potentially caused by oxidation, that lasted for around the first 1,000-2,000 contact cycles into the test. No wear flakes were seen on the running surface until after 3,100 cycles when the gradual development of easily recognisable wear flakes was identified via their shadows cast onto the running track. Wear flake size increased until about 10,000-12,000 contact cycles when the size of the wear flakes stabilised for the remainder of the experiment. In addition to wear flakes, the optical monitoring system was also able to observe the occasional creation of regions of dark banding on the twin-disc samples running track.

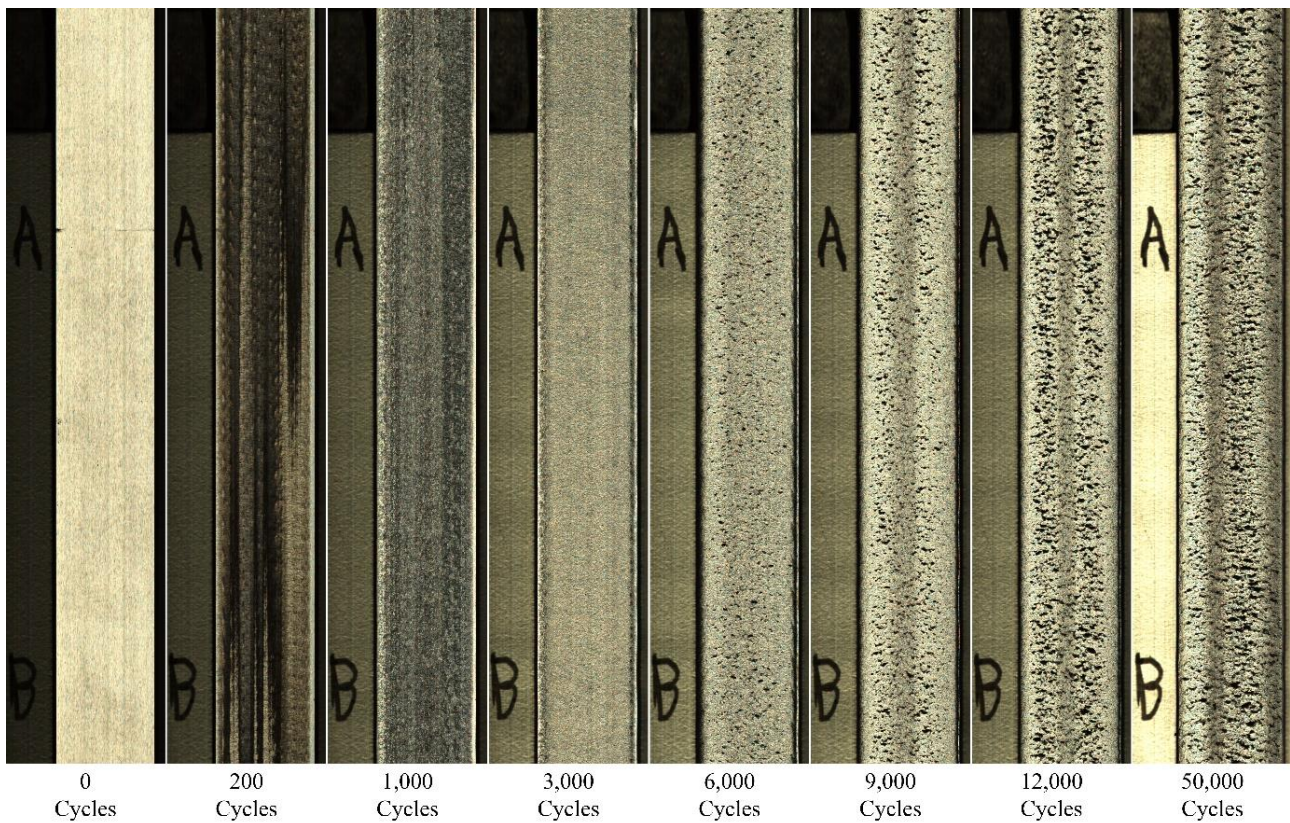
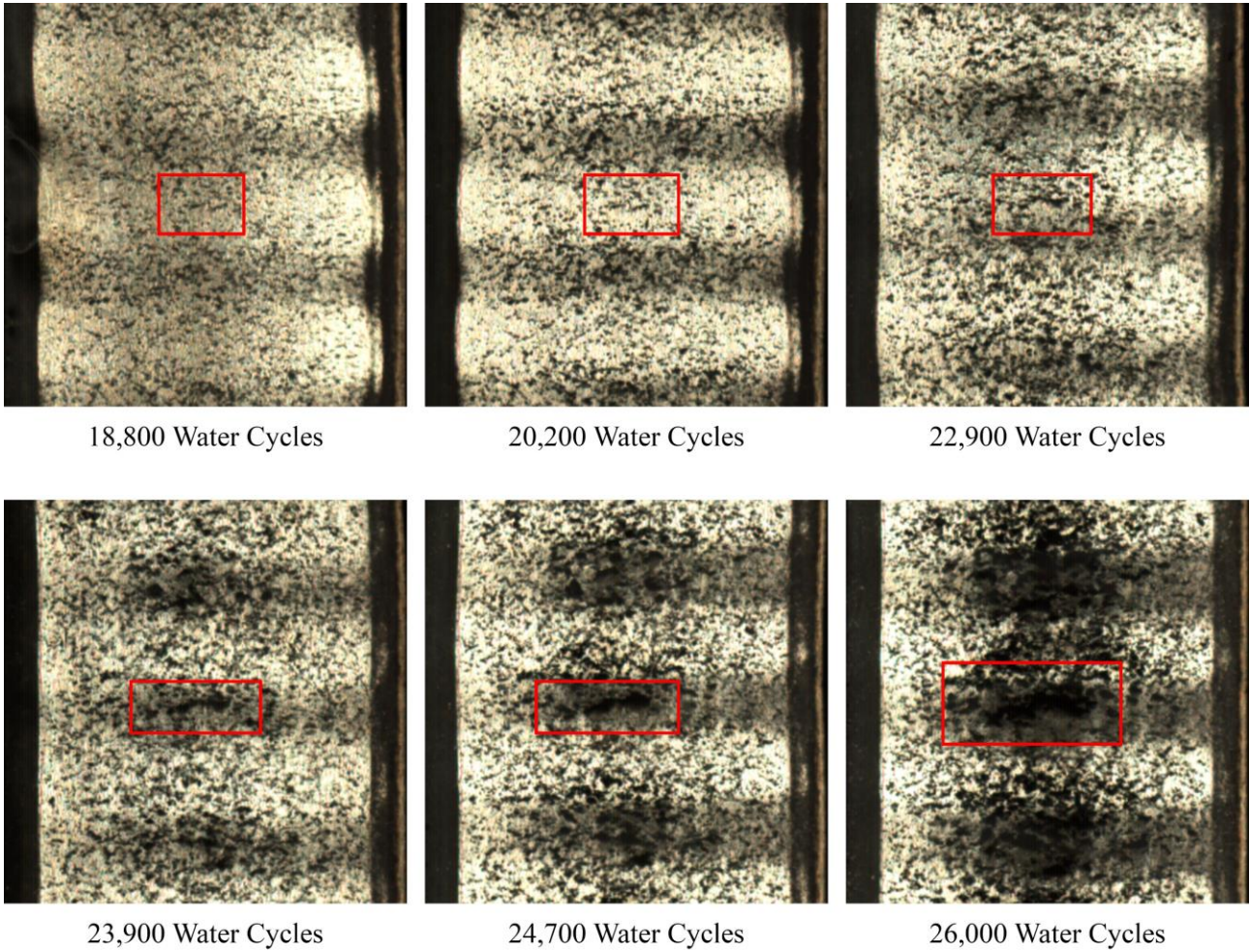


Figure 5.4: Images of the R260 twin-disc samples running track after approximately 0, 200, 1,000, 3,000, 6,000, 9,000, 12,000 and 50,000 contact cycles into the test with 1500MPa, 1% slip, dry contact conditions while rotating at 391.3 rpm. Labels A and B on the sample shoulder were used for identification of angular position.

The photographs captured of the rail sample running track during the water-lubricated contact test are shown in Figure 5.5(a-b). The images obtained show that the optical monitoring system was able to capture images of the disc beneath the water film on the surface to observe the development of damage on the rail running track. Compared with the dry contact experiment, however, the damage observed during the water-lubricated test was not as clear due to interference caused by the water present on the sample. In addition, occasional distortion caused by the water film made it difficult to observe running track features, as shown in Figure 5.6. Despite these issues, the equipment was still able to observe the development of RCF cracks on the running track. The images showed an initial stage of surface damage accumulation like wear flake development during the initial stages of water lubrication. After regions of damage reached a critical size (in this case) approximately 1.2 mm, either by gradual growth or by merging with adjacent regions of damage their growth was observed to accelerate, and a distinct surface feature develops. This feature could be either an RCF crack or a wear flake, but this has not been established. After a surface feature of this type had been identified it was possible to track its development throughout the test from the first appearance of surface damage. A close up of this surface feature at the end of the experiment is shown in Figure 5.7.

(a)



(b)

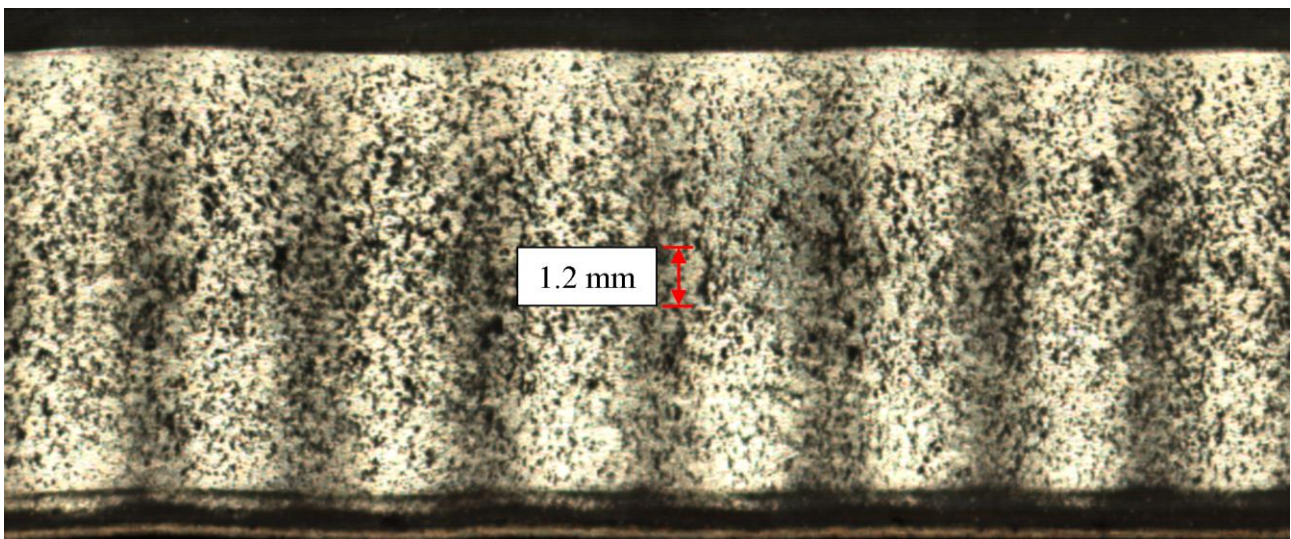


Figure 5.5: (a) Images of the R260 twin-disc samples running track during the water-lubricated contact experiment at approximately 18,800, 20,200, 22,900, 23,900, 24,700, and 26,000 contact cycles into the water-lubricated contact portion of the test. (b) Measurement of the surface features critical length before its growth was observed to accelerate.

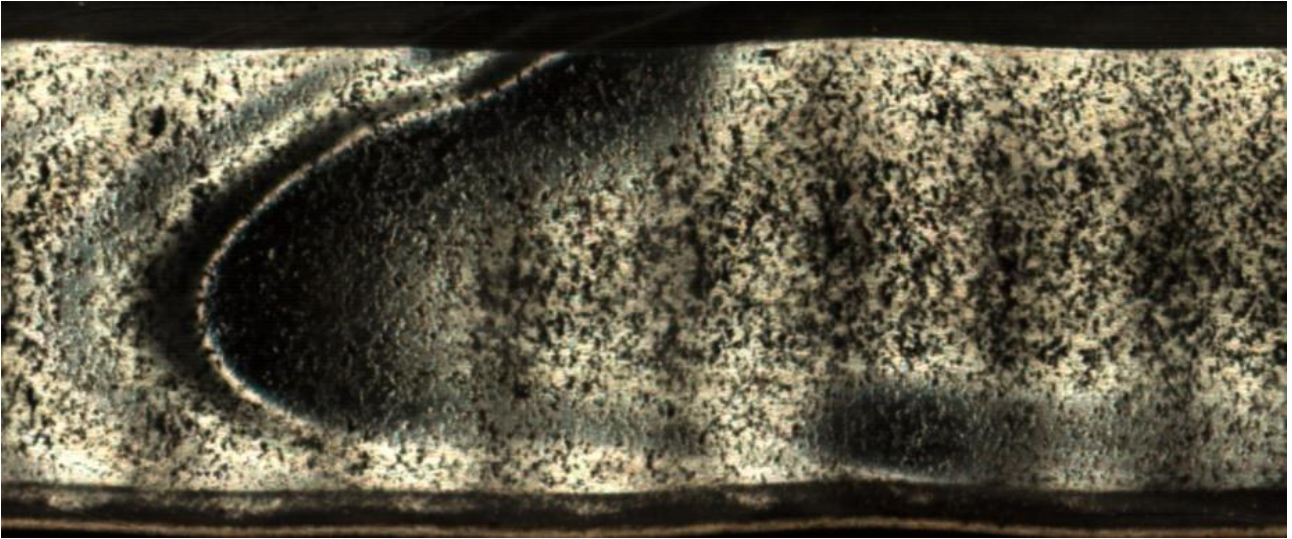


Figure 5.6: An example of the ripples that occasionally occur with the water film on the rail twin-disc sample during the water-lubricated contact twin-disc, which causes visualisation issues for observing defects on the specimens running track.



Figure 5.7: A close up of the surface feature observed using a Alicona infinite focus microscope after the water-lubricated twin-disc test was finished.

The data acquired during water lubricated testing shows the equipment supports identification of RCF crack initiation sites in a way not previously possible with techniques such as eddy current detection that only trigger for cracks in the 100s of microns size range. Improving image quality may be possible using deconvolution techniques like those used to remove atmospheric turbulence in images from ground-based telescopes [221].

5.4.3 Wear Flake Image Analysis

Image analysis using Matlab was conducted on the photographs obtained from the dry contact test (Section 5.4.2) to quantify the total wear flake shadow pixel count in each image over the test

duration. The purpose of this post-processing image analysis was to understand whether wear flake shadows observed in the captured images could be correlated with the rail steel wear rate. To analyse the total wear flake shadow pixel count, the acquired images were converted to greyscale and cropped so that the area analysed was confined to just one revolution of the twin-disc sample running track identified from the location of the disc drive keyways. To define the local reference thresholding values for identifying the wear flake shadows, an average ‘local background intensity image’ was generated using the Matlab function *imfilter* by applying a motion blur filter with a 50 pixel length parallel to the sample running track. The wear flake shadows were then found by locating pixels of below 45% of the average local background intensity using the *imcomplement* function. An example of one of the processed images is shown in figure 5.8 and a copy of the Matlab code for this wear flake image analysis is presented in Appendix A4.

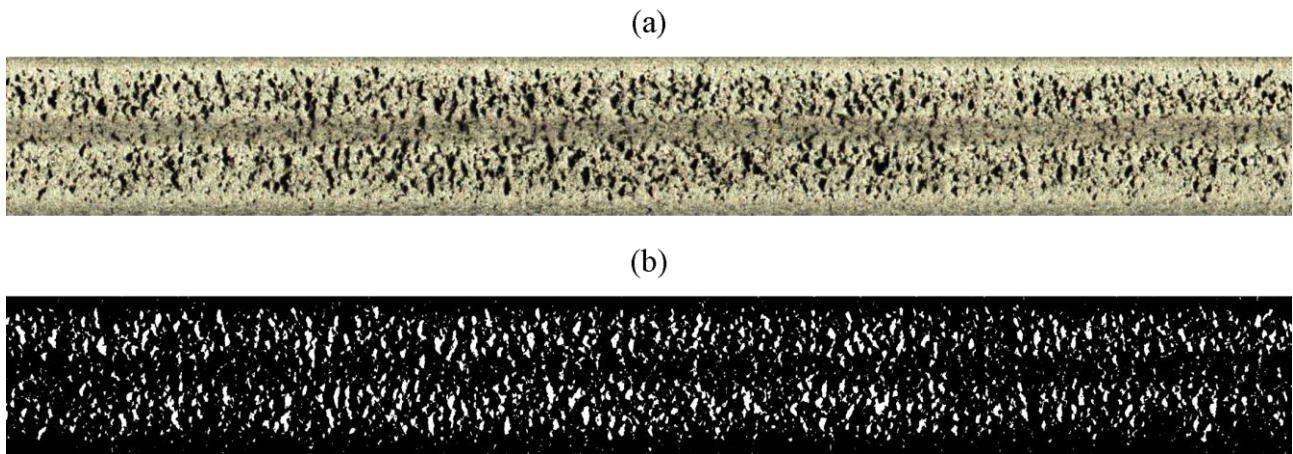


Figure 5.8: An example of (a) wear flake shadows identified from (b) the original image obtained of the twin-disc samples running track using the MATLAB image analysis script written.

The total number of pixels identified as wear flake shadows were then counted for each image throughout the test. The image analysis data collected was then compared with the wear test results presented in Section 3.3.1 for the same material pairings and contact conditions to understand the potential correlation between the two sets of data giving the results in Figure 5.9. From the figure it is possible to identify three stages in the surface morphology development of wear flakes: (i) an initial period of no wear flakes, (ii) a steady rise in the wear flake shadow pixel count, and (iii) a plateauing of the total number of wear flake pixels that persists for the remainder of the experiment. There was variation observed in the total wear flake pixel count after the data plateaued, which coincided with the transient periodic appearance of dark banding on the running track. Fewer pixels were identified belonging to the wear flake shadows within these dark bands, as shown in Figure 5.8. The illumination was changed throughout the experiment, as evident from the sample shoulder presented in Figure 5.4;

however, this influence was accounted for by using the average local background intensity image to identify wear flake shadows. Use of the average local background intensity image inherently corrects the results from the influence of the illumination changing. The cause of the periodically appearing dark bands is unknown, but they are commonly observed in twin disc testing. From the images it is now possible to collect a detailed record of surface change but it cannot yet be determined whether this observed reduction in the wear flake pixel count is due to the lower generation of wear flakes in these bands. An alternative explanation could be that fewer wear flake shadows were observed due to either being obscured by wear debris collecting or the wear flakes tending to be standing less prominently above the surface on the running track in those regions.

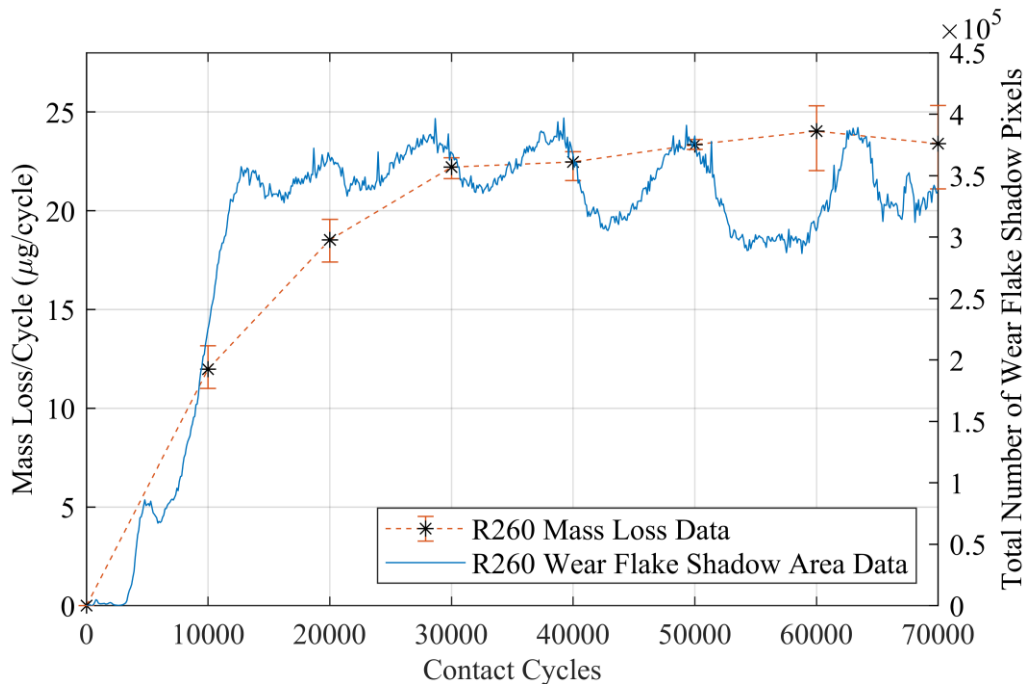


Figure 5.9: Comparison of the total wear flake shadow pixel count against traditional mass loss wear data obtained for an R260 twin-disc sample tested with 1500 MPa, 1% slip, dry contact conditions.

A comparison of the image analysis results with the mass loss wear data presented in Section 3.3.1 shows that there is a good correlation between the two datasets. The total wear flake shadow pixel count plateaus at a similar stage of test as the mass loss wear data. This result indicates that the total wear flake shadow pixel count can provide insight into rail steel wear behaviour without needing to interrupt a twin-disc test. The correlation indicates that changes in wear rate can be identified directly. The optical method also holds the prospect of quantifying wear rates, although it's expected this could only be by calibration against mass loss data for similar materials as visible flake development is likely to differ between materials. By tracking the development of individual wear flakes from their

initiation to eventual detachment from the surface the optical system can provide evidence to understand mechanisms of wear flake formation and removal. Observation of wear flake location relative to the external shoulders of the disc also serves as a marker to observe plastic strain in the running surface, a core aspect of ratchetting failure mechanism [11].

5.5 Conclusions

A new optical monitoring system has been developed to allow the running surface of a wear or RCF sample to be imaged without the need to interrupt the experiment. It has been demonstrated by application on the SUROS2 twin disc machine to observe rail wear and RCF crack initiation in-situ and in real time. The results obtained from dry contact tests showed the equipment can clearly record the development of wear flakes from a running sample surface. This enables the point at which wear flakes first visibly initiate and later stabilise in size to be observed. Analysis of the images obtained showed good correlation between the observed wear flakes and mass loss wear results, indicating the potential for this system to quantify wear behaviour without the need to interrupt the test.

Images acquired during a water-lubricated test showed the equipment was capable of imaging RCF cracks under a water film, but with reduced image sharpness. After an RCF crack was identified it was possible to track its development throughout the test. The data acquired shows the potential for identifying RCF crack initiation sites at a much earlier stage than previously possible with techniques such as eddy current detection. Application of the optical system is not confined to rail-wheel contact testing. However, in its immediate future application it has potential to provide much greater insight than previously possible to the origin of rail surface damage (wear flakes, RCF cracks, plasticity) and the behaviour of products such as flange lubricants or top of rail friction modifiers.

In terms of areas for further developments there is potential to explore how the images captured during water lubricated experiments could be improved using techniques developed for ground-based telescopes affected by atmospheric turbulence. There are opportunities available to train and develop convolution neural network models, such as the U-Net model [223], for this optical monitoring system to improve analysis of the images generated. For example, a convolution neural network model could be developed to help improve the semantic segmentation of wear flake shadows from the running track of dry contact experiments. In addition, a convolution neural network model could also be trained to provide a detector of RCF crack initiation from analysing images taken from water-lubricated tests.

Chapter 6: Rail Steel Damage Development Observed in Real Time

Highlights and Novelty

- Understanding via optical observation the development of individual wear flakes from initiation to removal as wear debris.
- Comparing the surface material plastic flow observed in experiments with simulation results derived from plastic ratcheting-based models.
- Understanding how the rail steels subsurface microstructure affects the development of wear flakes.

Journal Publication

The work presented in this chapter is in preparation for submission for the following journal publication:

- A. Wilby, J. Corteen, R. Lewis, D.I. Fletcher, “Plastic damage development in rolling contact of steels observed in real time correlated with ratcheting strain accumulation,” *In Preparation for submission to the Proceedings of the Royal Society A*, 2023.

6.1 Introduction

The new optical monitoring system developed in Chapter 5 demonstrated that surface features on a twin-disc sample running track can be monitored in-detail during a test while rotating at about 400 rpm. The quality of results obtainable from performing dry contact experiments while using this equipment presented the unique opportunity to visualise and understand in real time the development of rail steel damage, which is the focus of investigation in this chapter.

During dry contact conditions, most damage on a rail is caused by the accumulation of near surface shear strain beneath the running band and the loss of material caused by wear. An understanding of the cyclic behaviour of both these forms of damage is important to help reduce their occurrence and minimise their negative effects. The plastic deformation behaviour of rail steels has been explored in Chapters 3 and 4 by deriving information characterising the strain accumulation observed from twin-disc experiments that can be fed into simulation models [13], [14]. The principles of the rail steel rate of strain accumulation in these models are based upon the plastic ratcheting theory established by Kapoor and Johnson [36]. This theory has previously been validated from copper samples tested under pure sliding contact conditions [36] and via destructive validation of twin-disc samples tested by Tyfour et al. [117] for BS11 rail steel. The capability of observing the surface material plastic flow

in real time provides an opportunity to correlate on a cycle-by-cycle basis the output of these models against twin-disc experiments.

In addition to the surface material plastic flow, the new optical monitoring system has also been shown to clearly visualise wear flakes via the shadows they cast onto the rail running track. In the literature, the formation of wear flakes is commonly observed as the dominant material removal mechanism during severe and catastrophic wear regimes when testing rail-wheel contacts with an applied interfacial traction force [138]. An understanding of how wear flakes are generated and removed from a material are crucial information needed to help comprehending why specific wear behaviours are observed. From previous research, this information has mainly come from inspecting the subsurface microstructure of rail, examination of the rails running band condition, and analysis of the size, shape, and chemical composition of wear debris [138], [142], [145]. The capabilities presented by this new optical monitoring system will provide a new perspective of assessing the wear flake behaviour of rail steels by observing in-situ their formation and removal.

The aim of this chapter was to examine the behaviour of damage development experimentally observed from the surface of rail steel under dry rolling-sliding contact conditions. In addition, to evaluate how this behaviour observed in real time compares with the plastic ratcheting theory from in-situ observation of the surface material plastic flow. The objectives of this chapter were:

- To investigate the wear flake morphological and behavioural differences visualised for R260, HP335, and R350HT rail steel under 1500 MPa, dry contact conditions.
- Develop an understanding of the formation and cyclic change of rail steel wear flakes under dry contact conditions from direct observation.
- Explore how the theory of plastic ratcheting correlates against the rail steel surface material plastic flow observed from twin-disc experiments in real time.

6.1.1 Chapter Outline

Following the introduction, this chapter will first describe the methodology of the experimental twin-disc experiments using the new optical monitoring system and the image analysis work performed. This is followed by reporting the experimental results, in which is grouped into four sub-sections based on the different topics explored about the rail steel damage development. These four sub-sections are: i) an examination of the collective nature of wear flakes looking at the different wear flake morphology and initiation and development behaviour. ii) An investigation into the irregular wear flake behaviour observed from the images captured with results also provided about the samples circumferential hardness variation and specimen orientation relative to the rolling direction. iii) Analyse how individual wear flakes evolve during the experiment from videos produced focusing on

the same portions of the samples over the experiment duration. iv) Examine the cyclic surface material plastic flow observed from the images captured. The next section will compare how the experimental cyclic surface plastic flow correlates with the simulation results generated using an implementation of the Layer model original developed by Kapoor et al. [13]. The chapter will then be concluded with a discussion section and a conclusions and further work section.

6.2 Methodology

Three twin-disc tests were conducted testing the rail steel grades R260, HP335, and R350HT loaded against the wheel steel grade R8T uninterrupted for 70,000 contact cycles under 1500 MPa, dry contact conditions. The twin-disc tests performed in this chapter followed the same methodology outlined in section 5.3.1.2 for conducting the dry contact conditions experiment for the live experimental performance study.

To help understand how individual wear flakes develop on the twin-disc samples running track, the images obtained were cropped to focus on the same specimen location and stitched together into a video for each experiment. To produce these videos, a binary image of the ‘A’ indentation marker on the samples shoulder was initially produced from the first image acquired of each test. This binary image was then compared in Matlab to all later images obtained using the function ‘normxcorr2’ to provide a fixpoint of the same location across all the photographs. The images were then cropped to the same size at a consistent offset from this fixpoint.

Image analysis was also performed in Matlab to track the surface displacement of features on the twin-disc sample running track during the initial stages of experiment for the R260 test only. The purpose of this analysis was to monitor and understand from observation the plastic flow behaviour of the twin-disc samples surface material. For this analysis work, two different features were tracked manually on the R260 twin-disc samples running track: (i) The movement of the surface material itself halfway across the specimens running track observable between 784 – 1,664 contact cycles into the test. (ii) The displacement of the left edge of individual wear flake shadows, in which their location was tracked between 3,327 – 14,969 contact cycles into the experiment. The left edge of the specimen’s keyway captured in the photographs was used to provide a fixpoint in the images used to calculate the horizontal pixel displacement change of the tracked features relative to the initial image the features were first tracked from. The pixel width of the keyway was used to calibrate a new pixel to length conversion for each image to convert the horizontal pixel distance into a physical length. A new pixel to length conversion was calculated for each image to help minimise the small cyclic variation of the rail roller driveshaft rotation speed of ± 0.2 rpm influencing the results.

6.3 Results

6.3.1 Optical Observation of Wear Flake Initiation and Development

A selection of photographs taken of the twin-disc sample running track for the experiments testing R260, HP335, and R350HT rail steel are shown in Figures 6.1-6.3, respectively. The wear results presented in Figure 3.6a showed that for identical contact conditions and rail and wheel material combinations tested in this chapter, steady-state wear behaviour was observed for all three rail grades after accumulating 50,000 contact cycles. Comparing the images in Figures 6.1-6.3 of the twin-disc samples running track at approximately 50,000 contact cycles into the experiment a different surface morphology of the wear flakes was observed. Using the image analysis methodology developed in Section 5.4.3 for the images taken at approximately 50,000 contact cycles, a comparison of the wear flake shadow area probability histogram for the three different rail steels is presented in Figure 6.4. The results presented shows that the size distribution of the wear flakes shadow area was highly skewed towards the small end with the probability decreasing for larger wear flake shadow area. By taking the average and median value of the data as tabulated in Table 6.1, the surface area of the wear flake shadow surface area was observed to be largest on the running track of the R260 sample followed by HP335 and then R350HT. The average number of wear flakes on the running track of the three samples for the roughly 100 images captured between 50,000 – 60,000 contact cycles into the experiment is given in Table 6.2. The results shows that the ranking in terms of the greatest wear flake count on the sample running track was found to be HP335, R350HT, and then R260 rail steel.

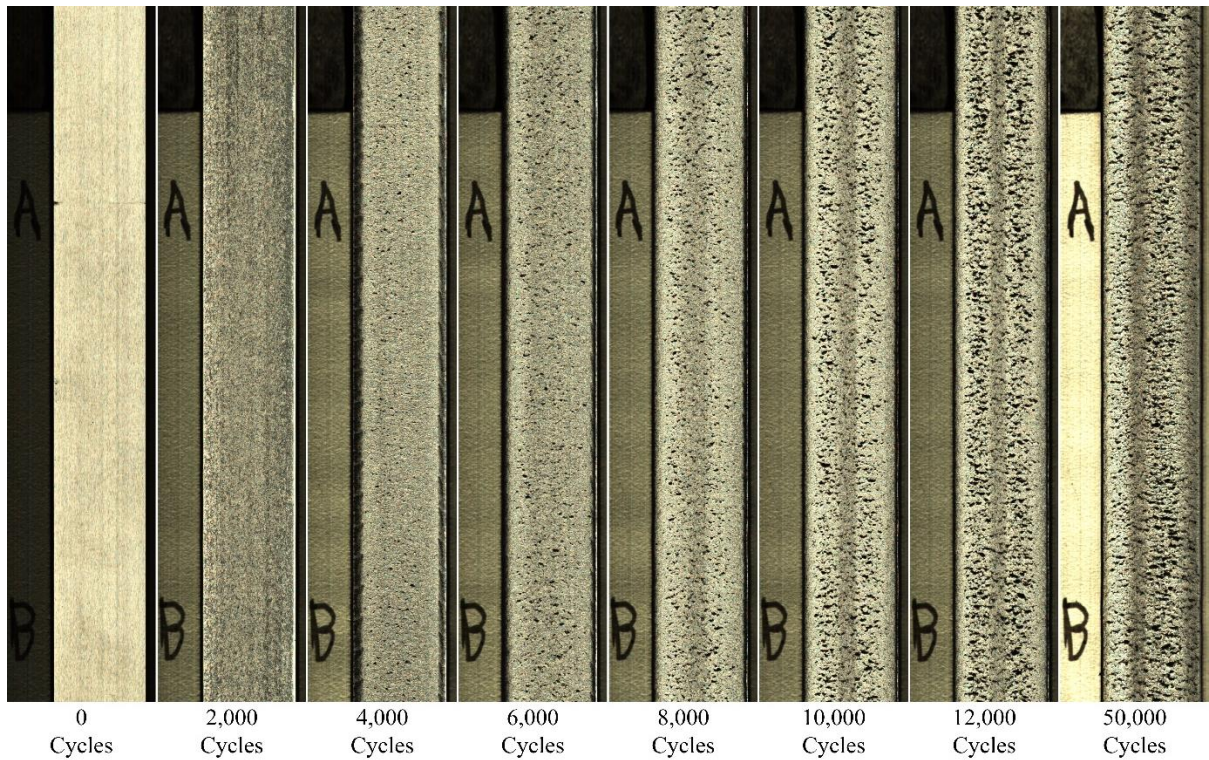


Figure 6.1: Images of the R260 twin-disc samples running track after approximately 0, 2,000, 4,000, 6,000, 8,000, 10,000, 12,000 and 50,000 contact cycles into the test with 1500MPa, 1% slip, dry contact conditions while rotating at about 391.3 rpm.

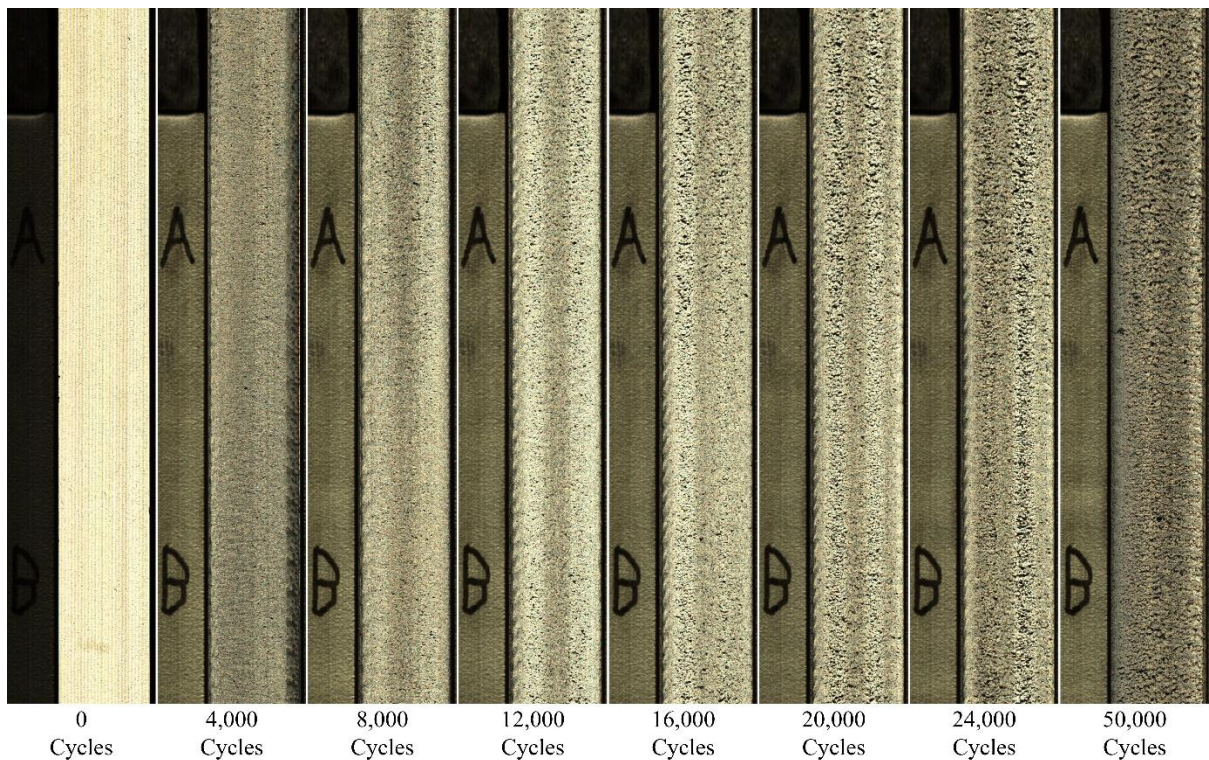


Figure 6.2: Images of the HP335 twin-disc samples running track after approximately 0, 4,000, 8,000, 12,000, 16,000, 20,000, 24,000 and 50,000 contact cycles into the test with 1500MPa, 1% slip, dry contact conditions while rotating at about 391.5 rpm.

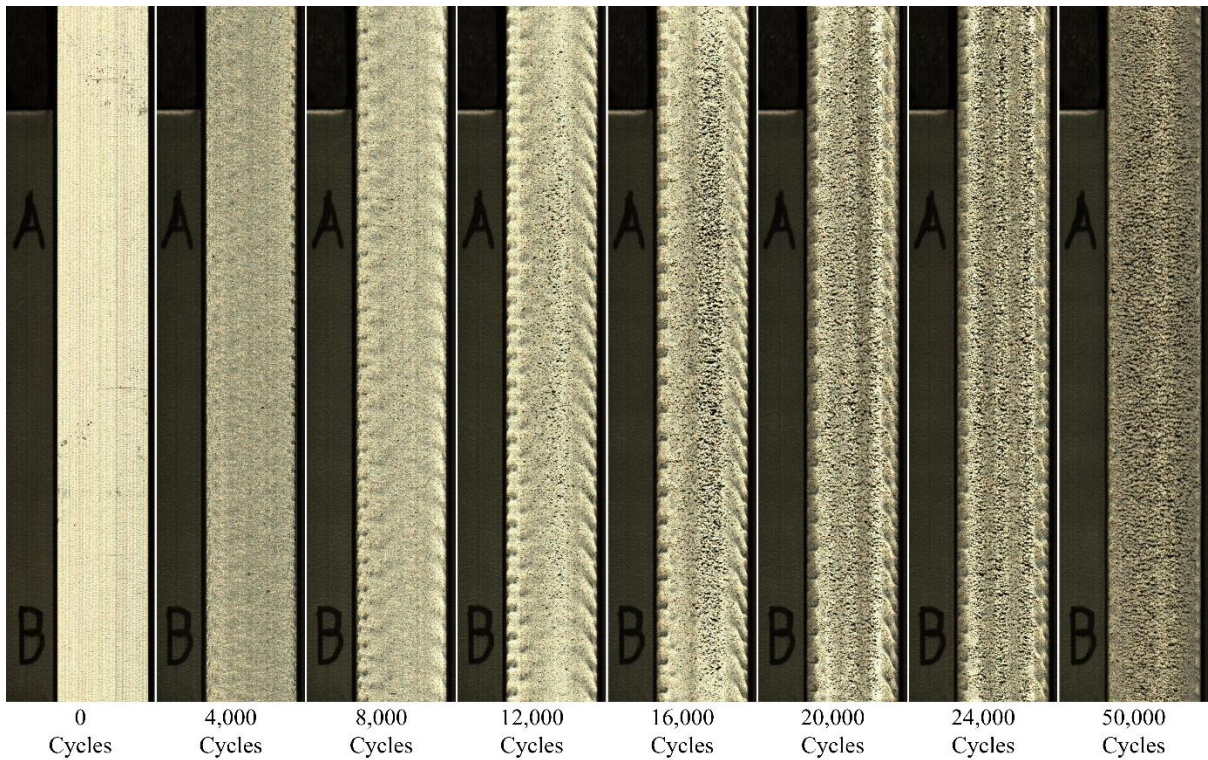


Figure 6.3: Images of the R350HT twin-disc samples running track after approximately 0, 4,000, 8,000, 12,000, 16,000, 20,000, 24,000 and 50,000 contact cycles into the test with 1500MPa, 1% slip, dry contact conditions while rotating at about 392.1 rpm.

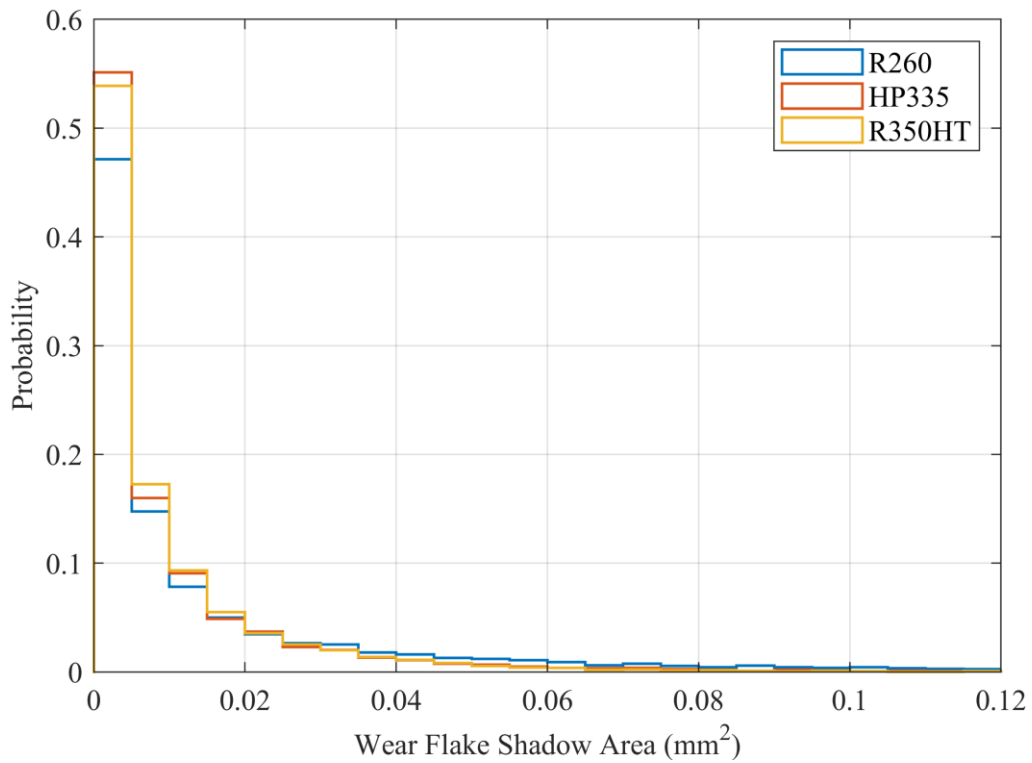


Figure 6.4: Probability histogram comparison the wear flake shadow area incident on the running track of the R260, HP335, and R350HT twin-disc samples running track at approximately 50,000 contact cycles into the experiments.

Table 6.1: Average wear flake shadow pixel and surface area on the R260, HP335, and R350HT twin-disc samples running track at approximately 50,000 contact cycles into the experiment. * The average surface area was calculated by multiplying the pixel area by $400 \mu\text{m}^2$ stemming from the systems $20 \mu\text{m}$ spatial resolution.

| Rail Grade | Wear Flake Shadow Pixels Count | | Wear Flake Shadow Surface Area (μm^2) * | |
|------------|--------------------------------|--------|--|--------|
| | Mean | Median | Average | Median |
| R260 | 55 | 14 | 22000 | 5600 |
| HP335 | 27 | 11 | 10800 | 4400 |
| R350HT | 24 | 10 | 9600 | 4000 |

Table 6.2: Average number of wear flakes on the running track of the R260, HP335, and R350HT twin-disc sample between approximately 50,000 – 60,000 contact cycles into the experiment.

| Rail Grade | Average Number of Wear Flake |
|------------|------------------------------|
| R260 | 8040 ± 125 |
| HP335 | 12907 ± 87 |
| R350HT | 10805 ± 94 |

Overall given the average hardness of the three rails steel grades tested in this work with 285 HV10.0, 340 HV10.0, and 350 HV10.0 for R260, HP335, and R350HT, respectively, as tabulated in Table 3.3. The photographs obtained from the optical monitoring system shows that there was a correlation between the size and the rail steel grade hardness, with smaller wear flakes found on the harder rail steel grades for the same contact conditions. However, a direct correlation could not be established between the wear flake count and the rail steel hardness.

Figure 6.5 shows the image analysis results quantifying the total wear flake shadow pixels count observed in the photographs captured by the optical monitoring system. Examining the onset of the first appearance of wear flakes, they were first detectable at similar durations into the test for the rail grades R260 and HP335 at approximately 3,100 contact cycles. Whereas R350HT rail steel took about double the amount at roughly 6,000 contact cycles for wear flakes to be first visible. In terms of when the wear flake shadow pixel count plateaued this occur at approximately 12,000, 26,000, and 35,000 contact cycles into the test for R260, HP335, and R350HT rail steel, respectively. The point where the pixel count plateaued was defined as when there was a distinct reduction in the pixel count after which variation was of the order of experimental uncertainty. Like the definition used to define the point where the mass loss against contact cycles data plateaus in Section 3.3.1. Comparing the pixel count results with the mass loss data, showed that the two datasets correlated well for identical contact conditions and for the same rail and wheel steel metallurgy pairings.

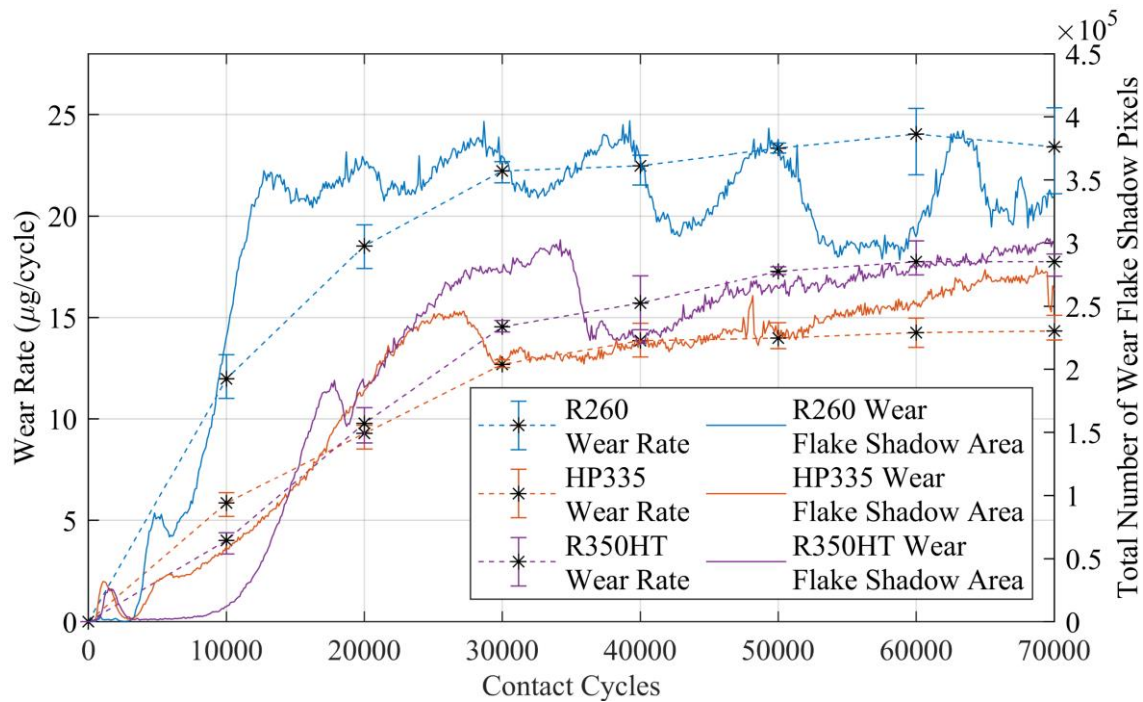


Figure 6.5: Comparison of the total wear flake shadow area quantified from the images obtained by the optical monitoring system against the wear twin-disc test mass loss per cycle results for R260, HP335, and R350HT rail steel tested for 1500 MPa, 1% slip, dry contact conditions.

6.3.2 Irregular Wear Flake Behaviour

An interesting observation from the photographs obtained during the early stages of the twin-disc tests was that wear flakes did not develop uniformly around the twin-disc samples circumference. The specimens instead exhibited an uneven development of wear flakes with all three twin-disc samples able to be segmented into four quadrants based on the degree of wear damage observed. As all three samples presented the same behaviour of two high wear flake damage quadrants situated at opposite ends of the sample separated by two low wear flake damage quadrants. The high wear flake damage quadrants displayed a sooner initiation and a faster development of wear flakes compared to the low wear flake damage quadrants. Additionally, the difference in the rate of the wear damage accumulation was more pronounced for the harder rail steels HP335 and R350HT compared to R260. The location where these high and low wear flake damage quadrants occurred on the specimens did not appear to be linked to any geometrical features of the twin-disc samples, such as the keyways. As the high wear flake damage quadrant appeared adjacent to the keyway for the R260 sample, whereas it occurred about midway between the two keyways for the R350HT sample.

To investigate the root cause of this irregular wear behaviour, an understanding of the sample orientation relatives to the rolling direction was examined from analysing the alignment of the elongated MnS inclusions in the specimens. In addition, an understanding of any potential hardness variation around the circumference of the twin-disc samples was obtained. To observe the alignment of the elongated MnS inclusion, one side of the twin-disc samples, shown in Figure 6.6a, was ground and polished up to a surface finish of 0.05 μm and then examined via optical microscopy.

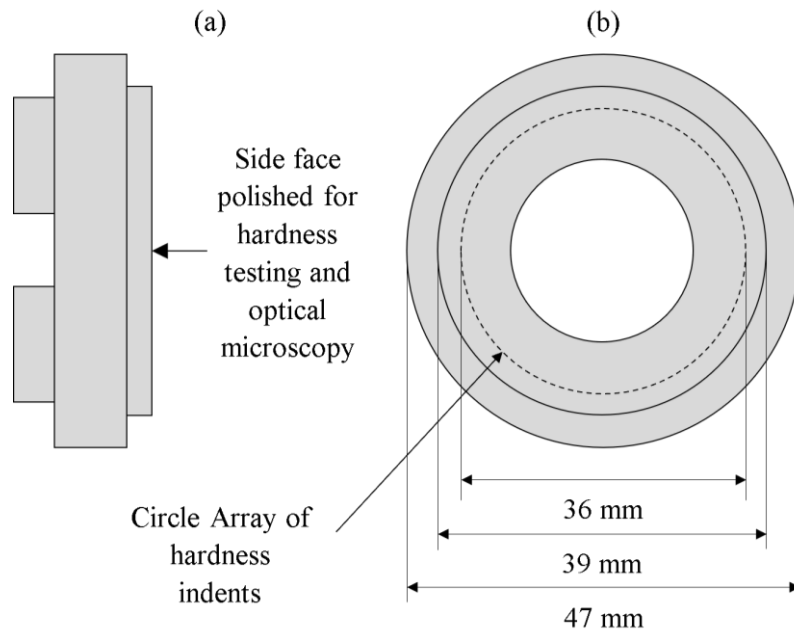


Figure 6.6: Illustration showing (a) the side of the twin-disc samples polished for inspecting the orientation of elongated MnS inclusions, and (b) how the circle array of hardness measurement was conducted on the twin-disc samples to understand the potential hardness variation.

A few examples of the elongated MnS inclusions typically observed via optical microscopy on a polished rail steel surface are shown in Figure 6.7a. The examination of the elongated MnS inclusion showed that the location of the high and low damage quadrants aligned with the same orientation of the elongated MnS inclusions for all three samples. The high wear flake damage quadrants coincided with where the MnS inclusions were perpendicular to the specimens running surface. The low wear flake damage quadrants, however, aligned with where the MnS inclusions were parallel to the running surface. An illustration of this observed behaviour from the twin-disc samples is presented in Figure 6.7b.

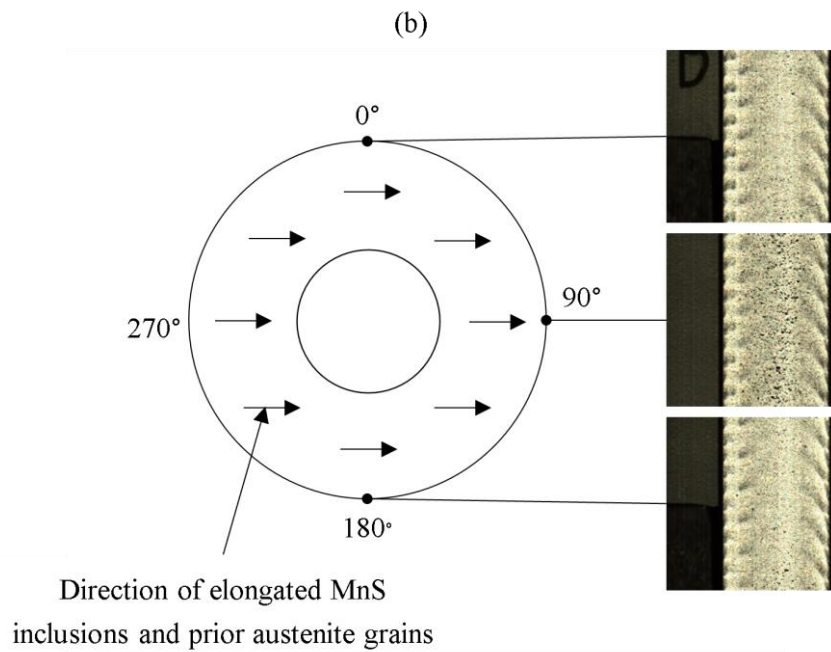
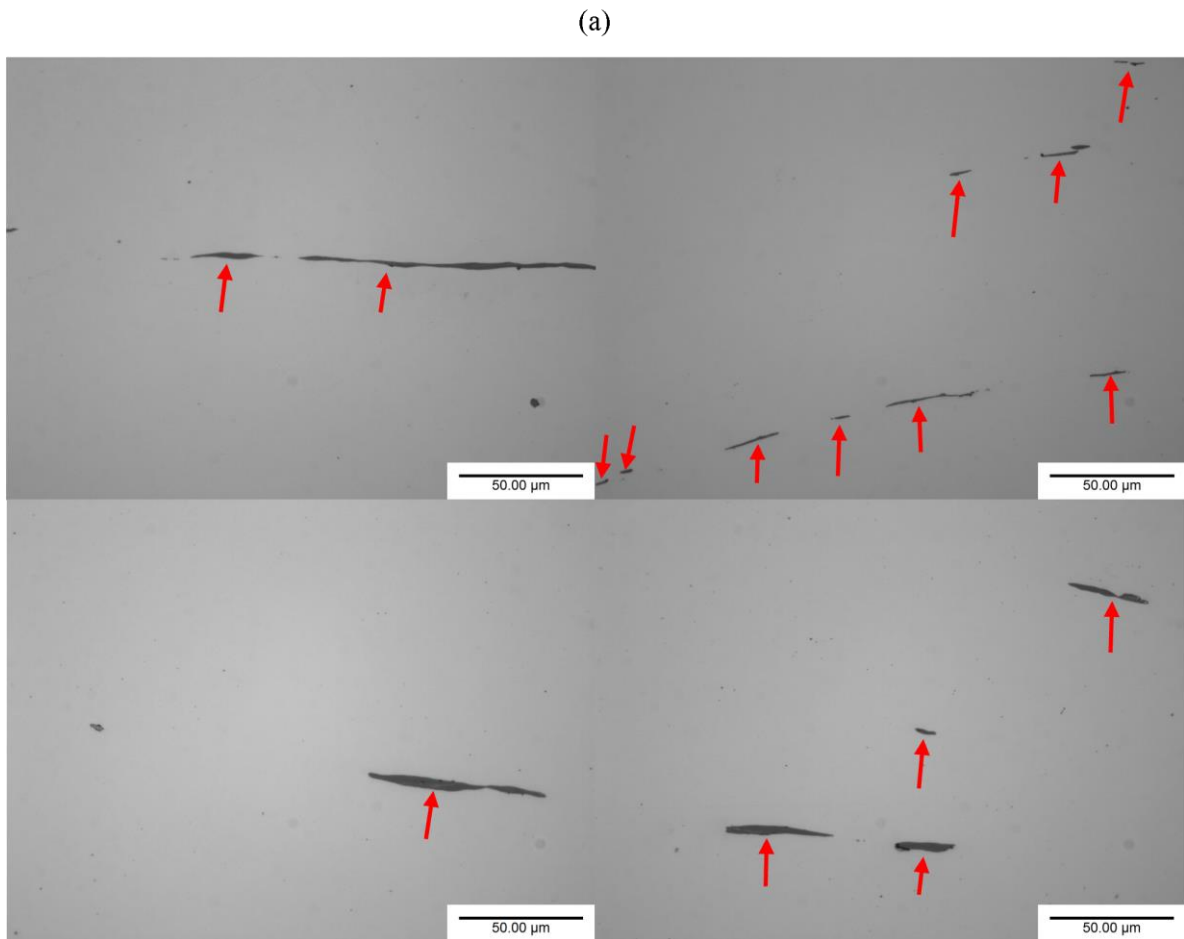


Figure 6.7: (a) Optical micrographs showing examples of the elongated MnS inclusions observed in the twin-disc samples indicated by red arrows. (b) Illustration showing the orientation of the elongation MnS inclusions observed in relation to the location of the high and low wear flake damage quadrants on the twin-disc samples circumference identified via optical microscopy.

For exploring any potential hardness variation around the samples circumference, a Duramin-40 hardness indenter was used to collect macrohardness results from the polished side face on all three twin-disc samples. To conduct these macrohardness tests 56 equally spaced indents situated at a constant distance of approximately 1.5mm from the samples side face outer edge were performed, as illustrated in Figure 6.6b. These indents were all taken using a 10 kg indentation load with a dwell time of 15 sec. The macrohardness data collected around the circumference of the three twin-disc samples is presented in Figure 6.8. The results showed that the specimens did not show any significant variation in hardness around the twin-disc samples circumference, indicating that the circumferential hardness of the specimens was unaffected by the sample orientation relative to the rolling direction.

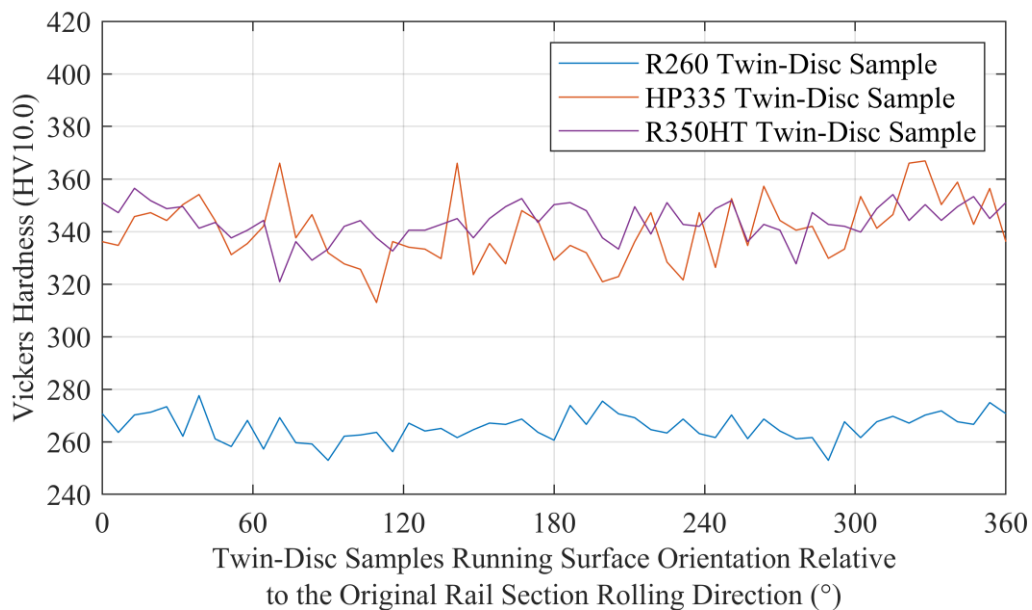


Figure 6.8: Twin-disc sample macrohardness (HV10.0) against twin-disc sample orientation. The theta zero location denotes the angular position where the twin-disc samples running sample is parallel to the longitudinal direction of the rail section the twin-disc samples were section from.

6.3.3 Evolution of Individual Wear Flakes

Stills of the videos created focusing on the same portion of the twin-disc samples running track corresponding to where the high wear flake damage quadrants are located are shown in Figures 6.9-6.11. In the videos created the wear flakes on the twin-disc sample running track were observed to last for 1000s of contact cycles once initiated, with their shadows occasionally growing and shrinking in size over time, but not completely disappearing. The wear flakes were also found to collectively migrate with the underlying flow in the same tangentially direction during the initial stages of the tests, which is caused by the samples surface material plastic flow. After this initial stage of the experiments, the wear flakes appeared roughly stationary relative to the core of the disc.



Figure 6.9: Video of the R260 twin-disc samples running track subjected to 1500 MPa, dry contact conditions focusing on the high wear flake damage quadrant. See the supplement mp4 video named ‘R260 and R8T (1500 MPa, 1% Slip, Dry, 400 rpm, 70000 Contact Cycles) Twin-Disc Test Video’.

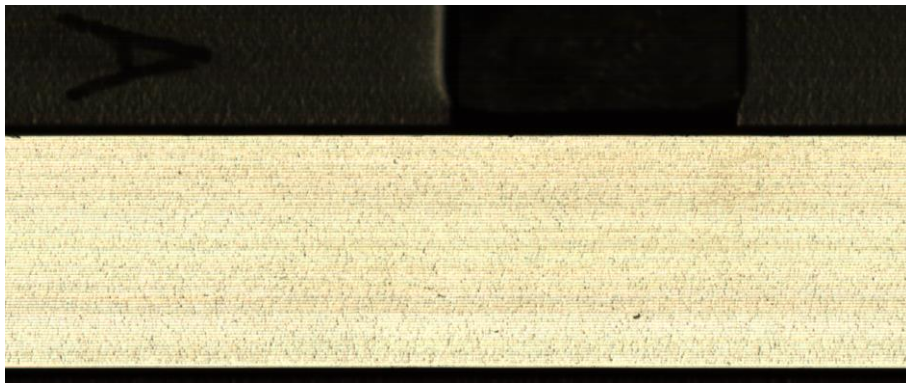


Figure 6.10: Video of the HP335 twin-disc samples running track subjected to 1500 MPa, dry contact conditions focusing on the high wear flake damage quadrant. See the supplement mp4 video named ‘HP335 and R8T (1500 MPa, 1% Slip, Dry, 400 rpm, 70000 Contact Cycles) Twin-Disc Test Video’.

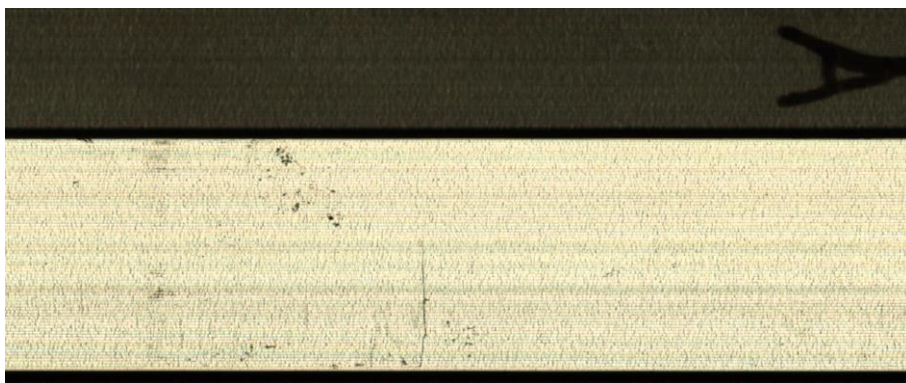


Figure 6.11: Video of the R350HT twin-disc samples running track subjected to 1500 MPa, dry contact conditions track focusing on the high wear flake damage quadrant. See the supplement mp4 video named ‘R350HT and R8T (1500 MPa, 1% Slip, Dry, 400 rpm, 70000 Contact Cycles) Twin-Disc Test Video’.

6.3.4 Surface Material Plastic Flow Analysis

Figures 6.12 and 6.13 shows the horizontal displacement results obtained from tracking the observable surface material plastic flow and left edge of wear flake shadows, respectively. For both features, the horizontal displacement was monitored for ten different points of surface material or wear flakes and then averaged. The results presented in Figures 6.12 and 6.13 shows a steady increase in the horizontal displacement of the twin-disc samples surface material during the early stages of the experiment from both features tracked. Monitoring the migration of the wear flakes during the later stages of the experiment does show this horizontal displacement slowing down over time. From both sets of results, there was quite a bit noise for each individual feature with the horizontal displacement going backwards in some locations. This noise in the results stemmed from the ± 0.2 rpm variation of the rail roller driveshaft speed and human error introduced from tracking both the wear flake movement and surface material flow manually.

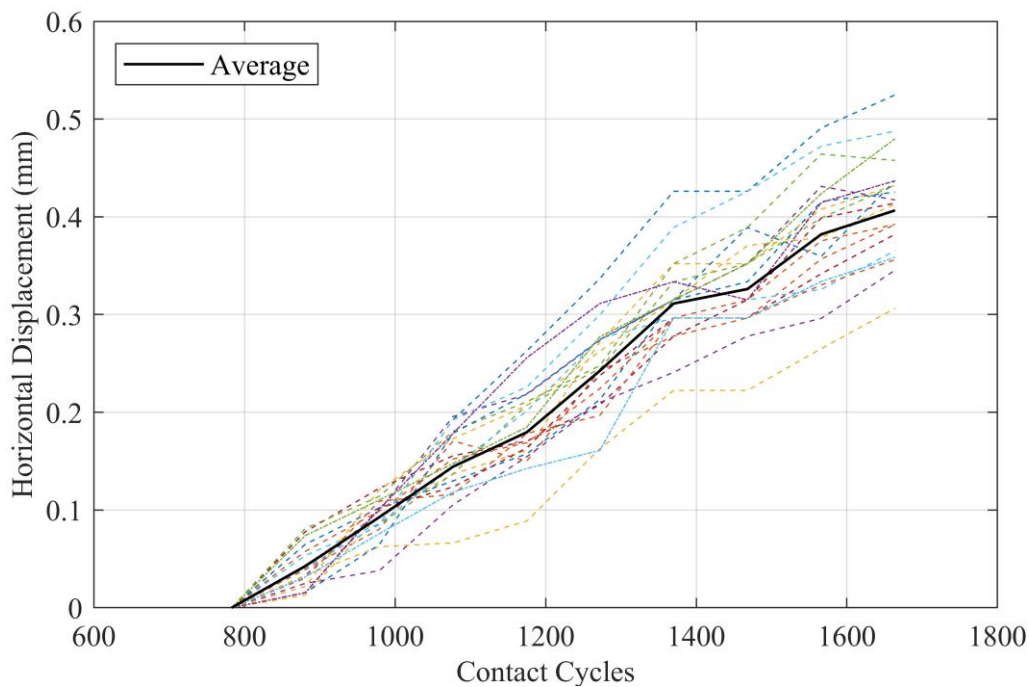


Figure 6.12: Horizontal displacement change relative to the initial location at the start of monitoring for points of the surface material plastic flow monitored between 784 – 1664 contact cycles into the experiment on the R260 twin-disc samples running track.

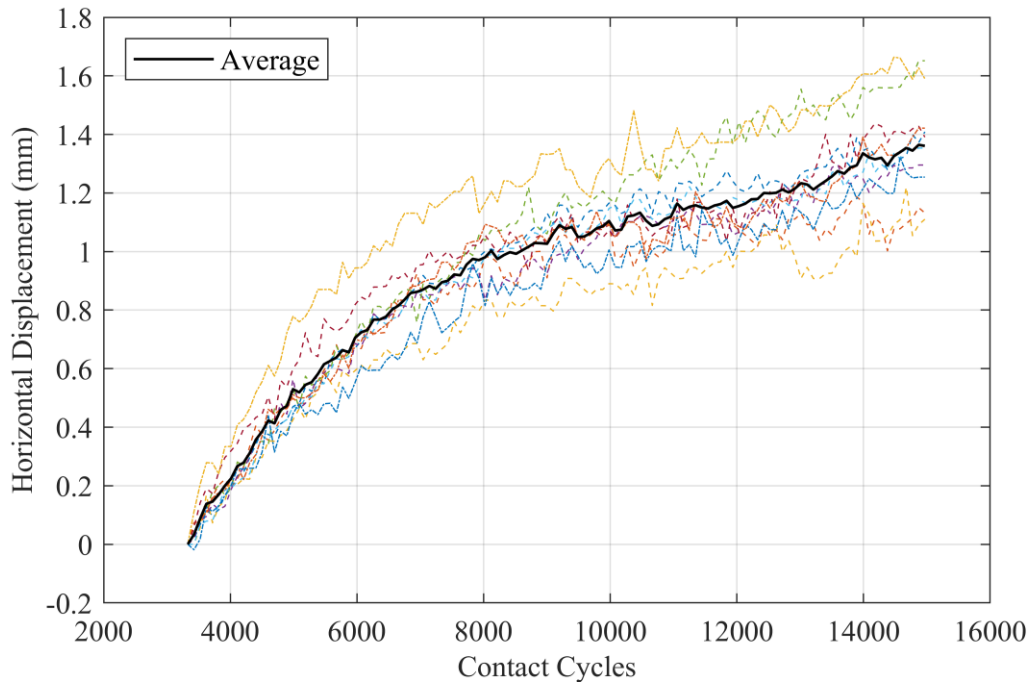


Figure 6.13: Horizontal displacement change relative to the initial location at the start of monitoring of the left edge of wear flake shadows tracked between 3327 – 5969 contact cycles into the experiment on the R260 twin-disc samples running track.

6.4 Plastic Ratcheting Theory Correlation with Real Time Experimental Data

An implement of the Layer model originally developed by Kapoor et al. [13] was used to correlate the real time experimental surface material plastic flow data against the plastic ratcheting theory. The model used in this study was set up to simulate the plastic deformation behaviour of R260 up to a depth of 0.8mm below the running track. The model was discretised into 800 layers with a uniform vertical thickness dz of $1\mu\text{m}$ based on the convergence study results shown in Figure 4.5 in Chapter 4. Based on the results generated in Chapter 3, the material data used to simulate the plastic deformation behaviour of R260 rail steel under 1500 MPa, dry contact conditions are:

- Initial shear yield strength, $k_0 = 292.26 \text{ MPa}$
- Ratcheting load conversion factor, $c = 0.00083$
- Modified Voce equation coefficients, $m = 700.328$, $n = 0.009$, and $p = 0.145$

The conclusions derived from the work presented in Chapter 4 is that a definitive method has still not been found for determining the shear strain to failure (limit of accumulative shear strain that can occur before the nucleation of voids and microcracks) of rail steels under cyclic shear compression loading conditions. Therefore, the simulation work shown in this section will compare the real time surface material plastic flow experimental results against a few model outputs calculated using a range of

different values (15, 20, 25, 30) for the rail steel shear strain at failure. The horizontal displacement of each layer dx was calculated from the shear strain γ using.

$$dx = \gamma dz \tag{Equation 6.1}$$

The total displacement of the rail top surface was found by summing the horizontal displacement contribution of all layers in the model. The layers were loaded during each contact cycle using an orthogonal shear stress distribution for a rough contact calculated via the same approach described in Section 3.5.1.2, factoring the cyclic variation in traction coefficient and surface roughness.

A comparison of the surface displacement simulated by the layer model and experimental data measured from the surface material plastic flow and movement of wear flake are shown in Figures 6.14 and 6.15, respectively. The results in Figure 6.14 shows that during the early stages of the R260 experiment, the plastic deformation behaviour estimated from the simulation model correlated well with the experimental observation of the surface material plastic flow. For Figure 6.15 the experimental and simulation results only provided a good correlation with the simulation results calculated using a rail steel shear strain at failure of 25 and 30. However, they only remained in good agreement up until approximately 9,000-11,000 contact cycles into the experiment, before the model starts to overestimate the horizontal displacement of the rail surface due to plastic deformation.

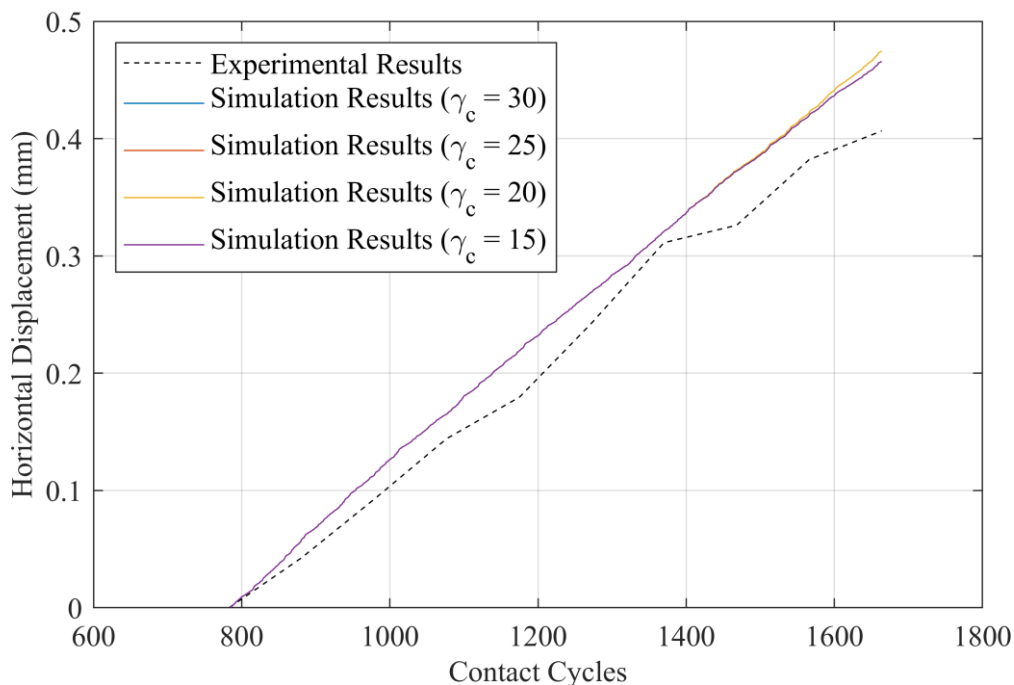


Figure 6.14: Comparison of the rail surface displacement measured from the wear flake movement measured experimentally and the Layer model simulation results for the R260 between 784 – 1664 contact cycles using a shear strain to failure of 15, 20, 25, and 30.

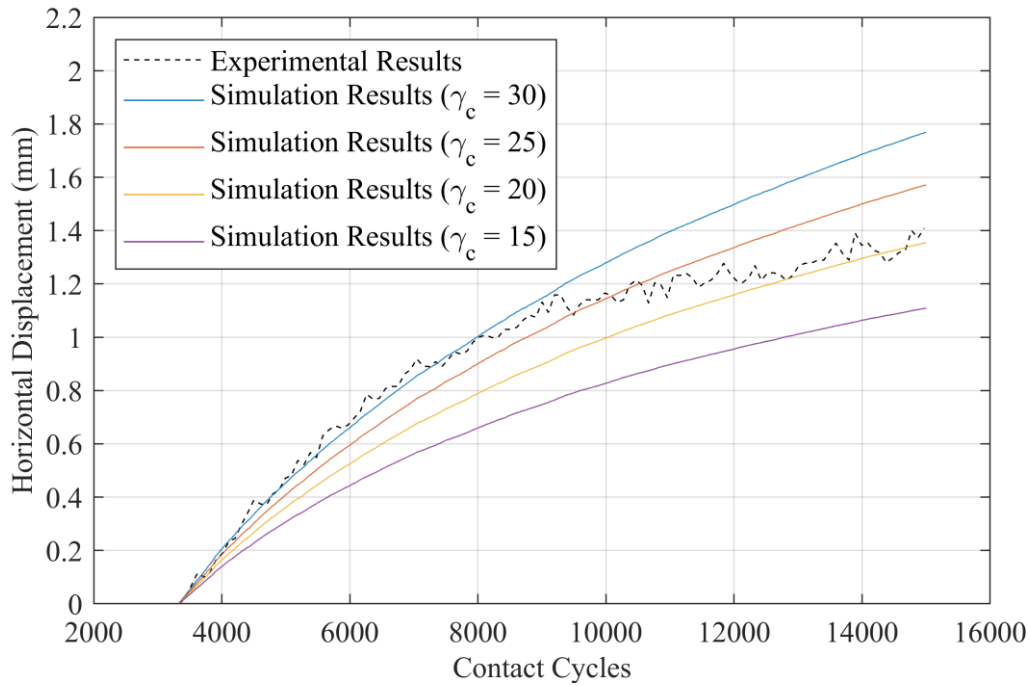


Figure 6.15: Comparison of the rail surface displacement measured from the wear flake movement measured experimentally and the Layer model simulation results for the R260 between 3,327 – 14,969 contact cycles using a shear strain to failure of 15, 20, 25, and 30.

6.5 Discussion

6.5.1 Wear Flake Morphological Size and Distribution

The images obtained from the optical monitoring system presented a different wear flake behaviour across the three pearlitic rail steels investigated. As the harder rail steels tended to produce wear flakes smaller in size, with the average wear flake produced by the rail grades HP335 and R350HT being 56.4 % and 50.1 % smaller, respectively, compared to the wear flakes produced by R260. The average total wear flake count was also observed to be higher for the harder rail grades HP335 and R350HT compared to R260. However, the average total wear flake count on the twin-disc sample running track did not appear to correlate with the rail grade hardness, with the slightly softer HP335 generating more wear flakes at 12,907 compared to 10,805 for R350HT. The average true interlamellar spacing and pearlite colony size measured from SEM (scanning electron microscope) micrographs of the undeformed region of the three rail steel grades tested in this work are tabulated in Table 6.3. These results were measured by using the line intersect method with twenty measurements conducted for each parameter and sample, with each interlamellar spacing line measurement taken from a different pearlite colony. A correction factor of $2/\pi$ [222] was applied to the apparent interlamellar spacing measured directly from the micrographs to account for the different orientation of the pearlite lamellae in the section plane to determine the true interlamellar spacing of the three materials. A

comparison with the wear flake morphology results, did not appear to show the size of the wear flakes correlate with either the true interlamellar spacing or the pearlite colony size. This was because both the true interlamellar spacing and the pearlite colony was found to be comparable between R260 and HP335, but significantly smaller for R350HT; however, the size of the wear flakes was observed to be similar between HP335 and R350HT, but noticeably larger for R260.

Table 6.3: Average interlamellar spacing and pearlite colony size measured from the undeformed matrix of the twin-disc samples tested in this thesis far away from any observable plastic damage for the three rail grades: R260, HP335, and R350HT.

| Rail Steel Grade | True Interlamellar Spacing (nm) | Pearlite Colony Size (μm) |
|------------------|---------------------------------|--|
| R260 | 189 ± 38 | 10.9 ± 1.5 |
| HP335 | 146 ± 46 | 8.7 ± 1.5 |
| R350HT | 69 ± 15 | 4.5 ± 0.7 |

Instead, this correlation observed between rail steel hardness and wear flake size could, therefore, potentially stem from the dissimilar depths of plastic deformation produced beneath the surface of the rail steels. As from the hardness against depth results presented in Figure 3.15a in Chapter 3 for the same rail steels tested under identical contact conditions and contact cycle durations, the harder rail steels produced shallower depths of plastic deformation compared to R260. The explanation is that the shallower depth of plastic deformation for harder rail steels implies that less material would be available to produce the wear flakes and so will end up growing to a smaller size. In addition, the shallower depth of plastic deformation would also mean a sharper shear strain against depth gradient, which would imply the wear flake would not have to follow the deformed microstructure for as far compared to R260 before reaching less deformed material that has not yet failed.

Alternatively, this observed behaviour between wear flake size and rail steels hardness could potentially stem from different microstructural features present in the rail steels tested. This is because for R260, which has a near eutectoid chemical composition, there would have been small amounts of proeutectoid ferrite along the prior austenite grain boundaries present in the microstructure of this rail steel. From literature the presence of proeutectoid ferrite in rail steels is known to facilitate the creation of RCF cracks and wear flake [69], [94], implying that the wear flakes generated on the R260 would have been influenced by the prior austenite grain size. In contrast, both HP335 and R350HT would have been expected to have no proeutectoid ferrite present in the microstructure, inferring that wear flake influenced by the pearlite colony size would have instead been expected for these two rail steels.

6.5.2 Delayed R350HT Wear Flake Development

The wear flake shadow pixel area analysis results shown in Figure 6.5 showed that for R350HT rail steel roughly double the contact cycle duration was needed for wear flakes to be seen in the output from the optical monitoring system compared to R260 and HP335. For HP335 rail steel, which has a similar hardness of 340 HV10.0 compared to 350HV10.0 for R350HT, suggests that the difference in contact cycle durations for wear flakes development to be observable was not due to the steel's higher hardness. In addition, the comparable chemical content between R260 and R350HT rail steels, excludes the idea that this behaviour was caused by composition. Having eliminated hardness and composition, this left the refined pearlitic microstructure of R350HT rail steel created by the heat treatment process as the cause of this observed delayed wear flake development behaviour. This was supported by Wen et al. [103], in which suggested that the smaller initial interlamellar spacing coupled with the smaller pearlite and nodule size created a higher resistance to plastic deformation in the heat treated rail steel because of the formation of strong dislocation cells. In addition, the finer interlamellar spacing helps to increase the cleavage fracture stress and the toughness of a eutectoid rail steel, which help to delay the initiation of wear flakes [72]. Once these wear flakes have been initiated previous experimental studies have also shown that rail steels with a finer interlamellar spacing possess slower fatigue crack growth rates [207]

This delayed wear flake development behaviour could help to explain the difference witnessed in the mass loss results observed between HP335 and R350HT rail steel at the 10,000 contact cycles mark. As this delayed wear flake development helps to inhibit the rail steels wear rate and thus experience less mass loss compared to HP335 at the 10,000 contact cycles mark. This was even though once wear flakes have fully developed, R350HT wore more compared to HP335 rail steel under the same contact conditions.

6.5.3 Irregular Circumferential Wear Flake Development

In section 6.3.2 an irregular development of wear flakes around the sample running track was observed from the images taken by the optical monitoring system. The three samples tested presented the same wear flake development patterns around the sample circumference with two high wear flake damage quadrants separated by two low wear flake damage quadrants. The different position around the circumference of the specimen for where the high wear flake damage quadrants were located showed that this irregular development was not linked to design features of the specimens, such as the keyway. In addition, no significant out of round issues were observed with any of the samples tested when measuring their diameter using a vernier calliper. An examination of the elongated MnS inclusion orientation in the sample did show that the high wear flake damage quadrants coincided on

the point of the discs where the elongated inclusions were orientated perpendicular to the running surface. The implications of this result showed that there was a connection between this irregular development and the original location of the samples parent material from the sectioned rail steel. As the high and low wear flake damage quadrants came from portions of the discs where the material was originally located, respectively, from the centre and the side edges of the rail head. An examination of the hardness around the twin-disc samples circumference presented in Figure 6.8 showed that a variation of hardness around the specimens was not the reason for this behaviour. The results instead pointed to microstructural features aligned with the longitudinal direction of the rail they were section from, such as the elongated MnS inclusions and/or prior austenite grains, responsible for this observed behaviour.

Both the elongated MnS inclusions and prior austenite grain boundaries have previously been found to influence the initiation and propagation behaviour of wear flakes in rail steels [93], [94], [96]. In hypo-eutectoid rail steels, proeutectoid ferrite exists along the prior austenite grains boundaries which detrimental promotes the formations due to strain partitioning between proeutectoid ferrite and pearlite. The importance of the prior austenite grain boundaries in encouraging wear flakes, however, diminishes with decreasing proeutectoid content in the microstructure. This influence becomes insignificant compared to wear flakes assisted by MnS inclusions when no proeutectoid ferrite exists [94]. As the three rail steels tested in this investigation were near or fully pearlitic, this suggests that the irregular wear flake behaviour observed must be due to the different elongation MnS inclusions orientation rather than the prior austenite grains boundaries.

Overall, the results presented in this chapter indicate that elongated MnS inclusions orientated perpendicular to the running surface were contributing to wear flake formation compared to parallel MnS inclusions. The implication of this observed irregular wear flake behaviour is that it implies that the rail-wheel contacts direction of traction force relative to the rail's longitudinal direction is a significant factor influencing the rail steels wear performance. In addition to the delayed wear flake initiation discussed in Section 6.5.2, the results in this section provide another instance where just relying on the rail steel hardness does not provide the whole picture of the rail steels wear performance. For real rail-wheel contacts, the angle of the traction force relative to the longitudinal direction changes depending on the track section a train is travelling on. As a train going down a straight section of track will see the traction force acting close to parallel to the longitudinal direction. A train negotiating around a curved section of track, however, would instead see the traction forces acting at an angle. Implying that the angle of the traction force relative to the longitudinal could be another potential factor influencing the wear performance of rail steels for different track sections. For twin-disc testing, the different approaches of sectioning a sample out of a railhead could,

therefore, be used to characterise the rail steels wear behaviour at the two limiting angles the traction force can act relative to the elongated MnS inclusions orientation. As parts of a twin-disc sample sectioned horizontally out of a rail head, shown in Figure 6.16a, will provide wear data of the traction force acting at 0° to the elongated MnS inclusions. However, a specimen removed laterally, as shown in Figure 6.16b, would instead provide wear data of the traction force acting at 90° to the elongated MnS inclusions.

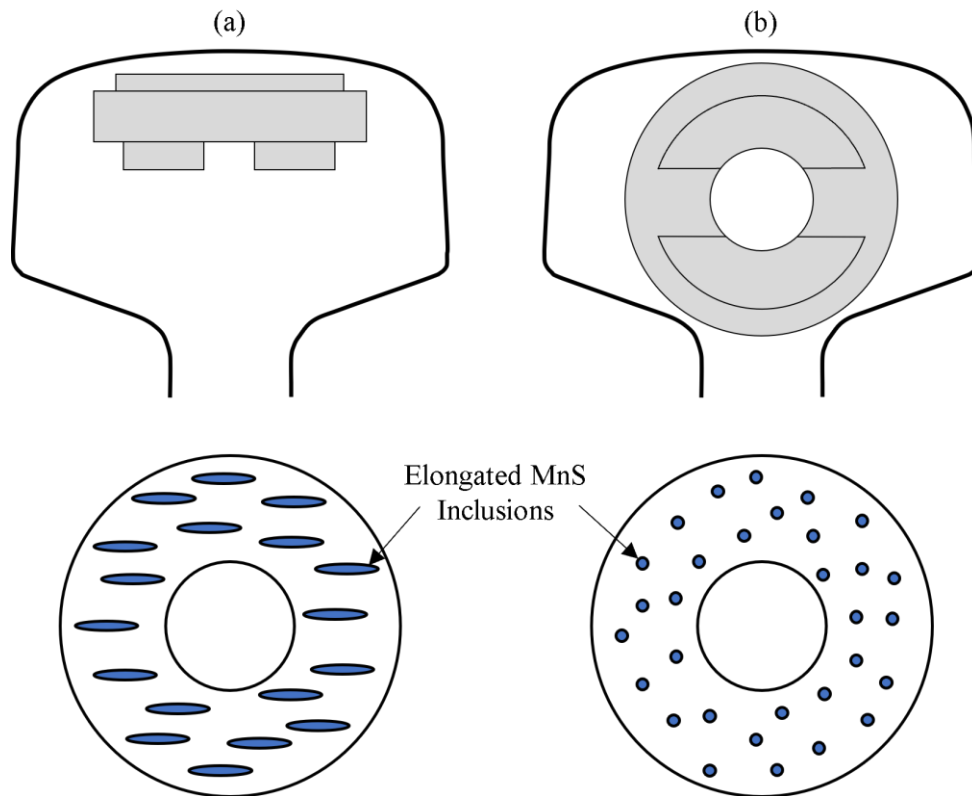


Figure 6.16: Illustration showing a twin-disc sample sectioned (a) horizontally and (b) laterally out of a railhead and the resulting orientation of the elongated MnS inclusions in the specimens. MnS inclusions in the laterally cut twin-disc sample are elongated into the page

Compared to the wider literature, the wear flake behaviour observed in this chapter supports the work published by Nakai et al. [128]. As their experimental finding also demonstrated a higher RCF life associated with parallel MnS inclusions in steels compared to either perpendicular or transverse orientated MnS inclusions relative to the rolling direction. However, the results in this chapter disagrees with the simulation results presented by Madhavi et al. [129] in which showed that the stress concentration around a parallel MnS inclusion is 87.8% higher compared to a perpendicularly orientated MnS inclusion. This observed behaviour with orientation could stem from the idea that parallel MnS inclusions in the plastically deformed surface material creates planes of weaknesses that run alongside the surface of a rail. These planes of weaknesses in turn would only encourage a thin

sliver of material above the inclusions to be removed as wear debris. For perpendicular MnS inclusions, however, the plane of weaknesses created would instead go down into the material encouraging the generation of flake-like features. The more pronounced difference between the low and high wear flake damage quadrants for the harder premium rail steels compared to R260 could be caused by the higher hardness difference between the hard steel matrix and the soft MnS inclusions. As this higher hardness difference will cause higher strain partitioning to be observed between the steel matrix and MnS inclusions, similar to the behaviour observed between proeutectoid ferrite and pearlite [93], [94], [96].

6.5.4 Wear Flake Removal Behaviour

The accumulation of plastic deformation on a rail surface leads to the initiation of voids and microcracks that eventually coalesce to form a crack that runs parallel to the surface. The material above this crack peels away from the surface and it was the shadow cast by this peeling material that was observed by the optical monitoring system. Tracking the development of these individual wear flakes showed that they tended to remain present for 1000's contact cycles. In addition, their shadows were observed to occasionally grow and shrink, but not disappear completely. This information demonstrates that the flake-like features that form on the running surface of the rail sample are not completely detaching at their base. Instead, it was evidence that material was being removed as wear debris from only the tips of these flake-like features, leaving portions of the base of the wear flakes still attached to allow them to regrow again at the same location.

6.5.5 Surface Material Plastic Flow Correlation

The analysis of the surface material plastic flow showed that there was good agreement between the experimental and simulated R260 surface displacement results during the early stages of the experiment. However, this correlation was observed to break down after about 9,000-11,000 contact cycles into the tests, as shown in Figure 6.15. One reason for this discrepancy was that during the later stages of the test, the propagation and removal of the wear flake tip counteracts their movement due to plastic deformation, as illustrated in Figure 6.17. Therefore, as this removal of rail steel material due to wear becomes more significant, the wear flake displacement thus becomes an increasingly inaccurate feature to use for understanding the surface plastic flow. This could potentially cause the experimental results to underestimate the true plastic flow behaviour during the later stages of the experiment.

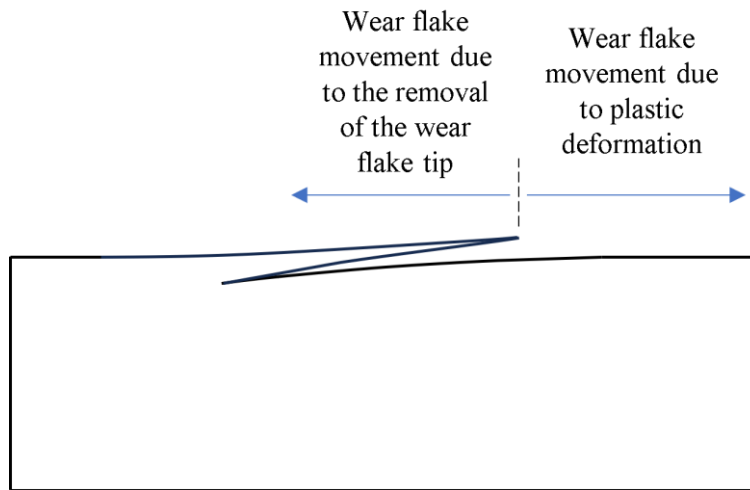


Figure 6.17: Illustration showing how plastic deformation and the removal of the wear tip as wear debris influences the movement on the rail; running surface.

Another explanation for this discrepancy potentially stems from the layer-based plastic ratcheting simulation used in this investigation being a 2D model. This was because the contact pressure produced by the twin-disc contact was never completely uniform across the width of the specimens running track, due to edges effects lowering the contact pressure at the samples edge. The rail steel material situated at the edges of the samples running track would, therefore, not plastically deform as much as the material in the running tracks centre due to the lower contact pressure. This overall results in the material located at the edges of the samples running track dragging on the central running track material, as demonstrated in Figure 6.18, producing residual stresses which were not accounted for in this simulation model due to its 2D nature.

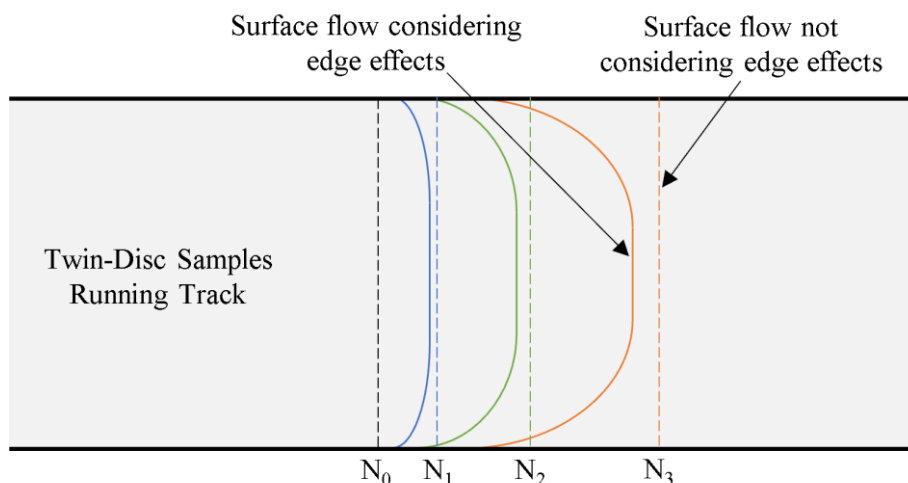


Figure 6.18: Illustration showing the influence of the edge effects on the surface plastic flow across a twin-disc samples running track and how this is expected to be compared against the surface plastic flow predicted if the edge effects were not considered.

6.6 Conclusions

In this investigation, three tests were conducted using the SUROS2 twin-disc machine with the new optical monitoring system to evaluate the plastic damage behaviour between R260, HP335, and R350HT rail steel under 1500 MPa, dry contact conditions. From the results collected, the following conclusions were established:

- The size of the wear flake on the twin-disc samples running track correlated with the rail steel undeformed hardness. The wear flakes for HP335 and R350HT were observed on average to be 56.4 % and 50.1 %, respectively, smaller compared to the wear flakes produced by R260. This correlation was believed to be caused by the shallower depth of plastic deformation present in the harder rail steel grades due to less damaged material being available to create the wear flakes via delamination.
- The harder rail steel grades HP335 and R350HT were observed to possess a higher wear flake count on the twin-disc sample running surface compared to the standard grade R260. However, the wear flake count did not seem to be correlated with rail steel hardness with the slightly softer HP335 having more wear flakes than R350HT.
- The development of wear flakes for R350HT rail steel was observed to take roughly double the contact cycle duration compared to R260 and HP335 rail steel for them to become noticeable with the new optical monitoring system. This delayed wear flake behaviour for R350HT was believed to be caused by the refined pearlitic microstructure due to the heat treatment process.
- An irregular wear flake development of two high damage quadrants separated by two low damage quadrants was observed across all three samples. This irregular development was narrowed down to be caused by the different orientation of elongation MnS inclusions in the rail steel relative to the running surface around the sample circumference. The MnS inclusions orientated perpendicular to the samples running track were found to initiate and develop wear flakes sooner compared to regions on the sample where MnS were orientated parallel to the running surface. This observed behaviour potentially comes from parallel MnS inclusions creating planes of weakness that run along the surface of a rail that only promote the detachment of a thin sliver of material above the inclusion as wear debris. The perpendicular MnS inclusions, however, would create planes of weakness that go down into rail and thus facilitate the generation of flake-like structures on the rail surface. Overall, in rail, the elongated MnS inclusions are always oriented parallel with the longitudinal direction and thus the running surface. The direction of traction in rail-wheel contacts, however, will

change depending upon the track section a train is traveling on, which cannot be changed in twin-disc tests. The result is the same situation where the rail-wheel contact traction forces act at an angle relative to the elongated MnS inclusion orientation, which can negatively affect the wear performance of certain track sections, such as tight curves.

- Tracking the development of individual wear flakes showed them tending to remain present for 1000's contact cycles. In addition, their shadows were observed to occasionally grow and shrink, but not disappear completely. This observed behaviour showed that wear flakes were not completely removed as wear debris from the base of the flake. Instead, it suggests that material was being removed as wear debris from only the wear flake tips, leaving the wear flakes base still attached to allow the wear flakes to regrow again at the same location.
- The comparison between the R260 surface plastic flow simulated using an implement of the layer model and experimental data showed a good correlation during the early stages of the experiment. The experimental and simulation results, however, were observed to diverge after between 9,000-11,000 contact cycles into the experiment. This lack of agreement was noted to be possibly caused by the propagation and removal of the wear flakes tips as wear debris counteracting the movement of wear flakes due to plastic deformation. In addition, due to the limitations of the simulation model being 2D, some residuals stresses caused by the material on the running track edges not plastically deforming as much due to edge effects were not replicated.

From this investigation, the following areas for further work have been identified:

- A new heat-treated rail steel grade based around the chemical composition of HP335 potentially offers improved wear performance. This is based on the idea of combining the higher wear resistance provided by HP335 chemical composition and delayed wear flake development behaviour observed with R350HT due to the refinement of the pearlitic microstructure created by the heat treatment process.
- An examination of the distribution and size of the MnS inclusion present in the three rail steels tested in this investigation could be conducted. This would help to understand whether the distribution and size of MnS inclusions is an influential factor that could explain why a more pronounced difference in the wear flake developments with MnS inclusion orientation was observed for the harder rail steels.
- The comparison of the plastic ratcheting-based simulation results against the experimental plastic flow results captured using the optical monitoring system could form the basis for a new methodology determining the rail steel shear strain at failure (limit of accumulative shear strain that can occur before the nucleation of voids and microcracks). This approach would

involve a value optimisation approach that varied the rail steel shear strain at failure until the predicted cyclic surface displacement matches with the experimentally observed plastic flow.

- The comparison of the simulation and experimental surface material flow results could be advanced by using a 3D plastic ratcheting-based simulation model.

Chapter 7: Conclusions and Further Work

7.1 Introduction

Highlighted in the introduction, rail transportation is important because it is one of the safest and fastest forms of land-based transportation available. In addition, to being one of the more energy efficient and environmentally friendlier modes of transport that will play a crucial role in reducing worldwide carbon emissions. The desire to expand the utilisation of rail transportation is contributing to the current trend in the industry for higher speeds, greater axle loads and more frequent track usage, which is resulting in a higher propensity for wear and RCF damage. Therefore, improving the quantification of rail steel plastic damage development is imperative to allow better decisions regarding rail maintenance programmes and the selection of most suitable rail steel grade, helping to support the installation of premium rail steel metallurgies. In addition, to providing potential cost savings through possibly helping to optimise maintenance programmes and the prevention of rail failures.

The overarching aim set out at the beginning of this thesis was to expand the knowledge and understanding of how plastic damage develops in rail steels due to the cyclic interaction of rail-wheel contacts. This has been achieved by characterising the plastic deformation behaviour of rail steel under cyclic combined shear-compression loading conditions from experimental twin-disc data in Chapters 3 and 4. In addition, a novel optical monitoring system for twin-disc tests was developed in Chapter 5 and then Chapter 6 explored the unique output this new technique could deliver in terms of visualising in real time the initiation and development of rail steel damage. On top of these primary research challenges, a considerable amount had been achieved in commissioning the SUROS2 twin-disc machine, which has been used extensively during this project. This commissioning work involved conducting a sensitivity study of the operating parameters and for making the following modifications:

- Adding mounting points for additional equipment, such as the optical monitoring system
- Implementing a new linear slider to provide better support during dry contact tests
- Changing the roller driveshafts to accommodate the pre-existing SUROS1 sample design [171]
- Enhancing safety with the installation of guarding around the driveshafts.

The information documented in this thesis presents some of the collaboration work conducted between the University of Sheffield and British Steel Ltd under the umbrella of UKRRIN. The

UKRRIN framework has enable investment into new experimental equipment, such as the SUROS2 twin-disc machine, Bruker Hysitron TS 77 select nanoindentor, and Alicona PortableRF infinite focus microscope. Both this collaboration and investment have also been indispensable in allowing the research questions in this thesis to be explored.

7.2 Project Conclusions

The following are brought out as highlights of the overall thesis:

- Characterising near-surface behaviour in modern premium rail steels using novel techniques, such as high throughput nano-indentation, and implementing this roughness dominated behaviour into models of plastic damage and wear behaviour to showcase its importance in predicting damage.
- Demonstrating the shear stress-strain curve and the relationship between ratcheting load to incremental shear strain are material property and system behaviour, respectively.
- Optical monitoring system developed for in-situ plastic flow and wear monitoring without test interruption.
- Observed for the first time and in real time plastic ratcheting take place as predicted by models. Revealing never-before-seen wear flake initiation and evolution under repeat contact loading.

Having highlighted these items, the following presents detailed conclusions. To characterise the plastic deformation behaviour of rail steel a large quantity of experimental data has been collected from tested twin-disc samples for a range of different rail steel metallurgies and contact conditions. This data was then subsequently analysed to derive the shear stress-strain curve, ratcheting load conversion factor (conversion factor between ratcheting load and incremental shear strain), and shear strain to failure (limit of accumulative shear strain that can occur before the nucleation of voids and microcracks) for each condition investigated. The design of the experimental methodology conducted enabled an understanding of the rail steel plastic damage response across the three different rail steel grades, R260, HP335, and R350HT subjected to 1500 MPa, dry contact conditions. In addition to providing knowledge on the plastic damage response of R260 subjected to different maximum Hertzian contact pressures (1500 MPa, 1200 MPa, 900 MPa, 600 MPa) and dry contact conditions. The intention of which was to assess whether the material information derived should be classified as either ‘material property’ or ‘system behavioural’ information that are only suitable for application to a limit range of contact conditions.

For the three different rail steels investigated, a ranking of the shear stress-strain curves was established. The ranking in terms of the highest shear yield stress achieved, was R350HT, followed by HP335, and then R260. The ratcheting load conversion factor results showed that R260 presented the highest conversion factor at 0.00083, however, both premium rail steels exhibit near similar conversion factors of 0.00029 and 0.00027 for HP335 and R350HT, respectively. Compared with the rail steel wear rate results, which revealed HP335 wearing the least out of the three materials, the data showed that neither the shear stress-strain curve, ratcheting load conversion factor, shear yield strength provided an explanation for the higher wear resistance of HP335.

For R260 rail steel subject to different maximum Hertzian contact pressures, the shear stress-strain curves were found to be mostly identical across the four contact pressures tested. The ratcheting load conversion factor, however, did exhibit some dependency with contact pressure. The results showing that the conversion factor decreased for the lower contact pressures tested, however, remains broadly the same between the 600 MPa and 900 MPa contact pressure tests. This contact pressure dependency observed was believed to be linked to the depth of plastic deformation in the rail steels. This was because it was suspected that the strain accumulation was slower in the shallower plastically deformed layers due to the greater resistance created by the sharper shear strain gradient over the same size microstructure, which involves needing to bend individual interlamellar ferrite and cementite lathes by a greater amount. Overall, these results demonstrated that the shear stress-strain curve could be regarded as material property information, whereas the ratcheting load conversion factor was system behaviour information.

A new value optimisation approach using an implementation of the brick-based plastic ratcheting simulation model was devised in this work to estimate the shear strain at failure for each of the conditions investigated. This was done by varying the materials shear strain at failure in the model until the cyclic wear depth loss simulation results converged with the experimental data. At the time of conducting this work, the two conditions (1500 MPa R260 and 1200 MPa R260) were expected to be most suitable for this technique due to them experiencing a combination of bulk and asperity contact driven plasticity. The other conditions, however, where plastic damage was expected to be more heavily surface roughness driven were predicted to be more challenging conditions to apply this approach to. Additionally, the brick approach to plastic ratcheting model only models ratcheting wear mechanisms and potentially misses things like oxidation wear or some other wear mechanism that may dominate for the conditions investigating the harder rail steels and lower contact pressures. The application of this technique was found to be successful when applied to the 1500 MPa R260 and 1200 MPa R260 conditions. The extension of this work to consider the remaining condition believed to be challenging was found to be less successful. For these conditions, the simulation model was

observed to exhibit a longer than expected delay in displaying any wear. Leading to an overestimate of the wear loss against contact cycles gradient during the steady-state wear state for these conditions.

The novel optical monitoring system developed in this work showed that the running surface of a wear or RCF sample can be imaged without the need to interrupt an experiment. The application of this new technique on the SUROS2 twin-disc machine, demonstrated the capability of this system to observe in real time the initiation and development of rail wear and RCF crack damage. The optical information obtained captured details down to a spatial resolution of 20 $\mu\text{m}/\text{px}$ while a 47 mm diameter twin-disc sample rotates at around 400 rpm.

The undertaking of dry contact tests showed that the equipment can clearly record the development of wear flakes from the running sample surface via the shadows they cast. This enables the point at which wear flakes first visibly initiate and later stabilise in size to be observed. Analysis of these images collected showed good correlation between the observed wear flakes pixel count and mass loss wear results, indicating the potential for this system to quantify wear behaviour without the need to interrupt the test.

The comparison of the development of wear flakes from R260, HP335, and R350HT rail steel subjected to 1500 MPa, dry contact conditions showed that the size of the wear flakes correlated with the rail steel undeformed hardness. This potentially stems from the shallower depth of plastic damage present in the higher hardness rail steel samples due to less damaged material being available to create the wear flakes. The premium rail steels R350HT and HP335, were also observed to have a higher wear flake count compared to the standard grade R260. This characteristic, however, was not found to be related to the rail steel hardness, with the slightly softer rail steel grade HP335 exhibiting on average more wear flakes than R350HT. The cyclic initiation point of wear flakes between the three rail steels was also observed to be different, with R350HT rail steel requiring roughly 6,000 contact cycles compared to about 3,100 contact cycles for both R260 and HP335 for wear flakes to be larger than at least 10 μm to be observed. After eliminating hardness and composition, the refined pearlitic microstructure of R350HT was left as the sole explanation for the observed delay in wear flake initiation. This result of a delayed cyclic initiation point helps explain one of the interesting aspects of the wear results collected for the same rail steels. This was the noticeably lower wear rate for R350HT rail steel at the 10,000 contact cycles mark compared HP335, even though R350HT wears faster during steady-state wear conditions.

The comparison between the R260 surface plastic flow simulated using an implementation of the layer model and experimental plastic flow data showed a good correlation during the early stages of the experiment. This correlation, however, was observed to break down after about 9,000-11,000

contact cycles into the test. This lack of agreement was noted to be possibly caused by the propagation and removal of the wear flakes tips as wear debris counteracting the movement of wear flakes due to plastic deformation. In addition, due to the limitations of the simulation model being 2D based, some residual stresses caused by material on the running track edges not plastically deforming as much due to the edge effects were not replicated. An implementation of the 2D plastic ratcheting-based models (Layer and Brick simulation approaches) were also used during the plastic deformation characterisation work, which was deemed to be a sensible approach at the time of doing that work. However, after reviewing the work presented in this thesis these 2D models now would be considered as a too simplistic representation, which could potentially be contributing to some of the issues observed. For example, the difficulty in obtaining a linear relationship between the net severity of ratcheting load above the shear yield strength against shear strain results for determining the ratcheting load conversion factor. In addition, to the problems encountered with converging the simulated wear against contact cycle data against the experimental results used to predict the shear strain at failure for some of the conditions investigated. This approach of correlation between the experimental surface plastic flow against the simulation models also presented a new way of determining the shear strain to failure of rail steels, in which a definitive approach of determining this parameter has still yet to be found.

An irregular development of wear flakes was also observed across all the samples tested with the same arrangement of two high damage quadrants separated by two low damage quadrants on exact opposite ends of the specimens. This irregular wear flake development was narrowed down to the different orientation of the elongated MnS inclusions in the rail steel relative to the running surface around the specimen circumference. The results showing that when the elongated MnS inclusions were orientated perpendicular to the running track the wear flakes tended to initiate and develop sooner compared to portions of the sample where the inclusions were parallel. In rail, the elongated MnS inclusions are always oriented parallel with the longitudinal direction and thus the running surface. The direction of traction in rail-wheel contacts, however, will change depending upon the track section a train is traveling on, which cannot be changed in twin-disc tests. The result is the same situation where the rail-wheel contact traction forces act at an angle relative to the elongated MnS inclusion orientation, which can negatively affect the wear performance of certain track sections, such as tight curves.

The tracking of the development of individual wear flakes showed that they tended to remain present for 1000's contact cycles. In addition, their shadows were observed to occasionally grow and shrink, but not disappear completely. This observed behaviour showed that wear flakes were not completely removed as wear debris from the base of the flake. Instead, it was evidence that suggested material

was being removed as wear debris from only the tip of wear flakes, leaving portions of the base of wear flakes to still be attached that allows them to regrow again at the same location.

7.3 Recommendation for Further Work

The experimental equipment developed in this EngD project, such as the SUROS2 twin-disc machine and novel optical monitoring system, are already in 2023 enabling a new intake of research.

In addition to the new experimental outputs that can be obtained from the equipment developed, there are several research areas identified in this thesis, which could be undertaken in the future to expand the knowledge and understanding of rail steel plastic deformation behaviour. The analytical work conducted in this thesis utilised significantly 2D plastic ratcheting-based simulation techniques coupled with the Nowell-Hills roughness model. From the results generated, however, it was thought that the too simplistic nature of this roughness model may have been a potential issue causing the results to not fit as well as expected for some conditions. For this purpose, a potential area for further work would be to look at advancing the analytical work but using a more sophisticated roughness model, such as a fractal-based roughness model [62], to more accurately represent the rough contact. The 2D nature of these simulation models was also noted as a potential reason for the divergence of the simulation results compared against the plastic flow experimental data, which would have also affected the plasticity derivation work. Therefore, work could be conducted in the future to look at developing an expanded 3D version of these plastic ratcheting-based models, which would enable them to account for the residual stresses created by the edge effect on twin-disc samples. To accomplish this, careful consideration would be needed to expand the heuristic patterns used to remove elements from the 2D brick approach to 3D. A review of the heuristic patterns used currently to remove elements from the implementation of the brick model approach would also be needed to ensure they are not allowing elements to be removed as wear debris too easily. The connectivity between elements should also be investigated in the future to help prevent unrealistic step changes in the accumulation shear strain across the array of elements in this plastic ratcheting-based models. In addition, a better understanding of the rail steels true standard deviation of initial material properties could also be explored.

To determine the shear strain to failure in this work, a new value optimisation approach was developed using an implementation of the brick approach to plastic ratcheting modelling. This approach in its current form was found to be imperfect for some of the challenging conditions investigated that were expected to be heavily asperity contact driven plasticity, which would need further exploration to improve the results for those conditions. This, therefore, leaves a partially accomplished objective of the work presented in this thesis, which was to find a definitive approach

of deriving the shear strain at failure of rail steels. Another new approach of potentially deriving the shear strain to failure has been identified in this thesis involving the new optical monitoring system developed. This approach would entail another value optimisation process varying the shear strain at failure until the predicted surface cyclic plastic flow results from plastic ratcheting-based simulation models converges with the experimental plastic flow data collected from the new optical monitoring system.

One of the interesting findings from the experimental wear tests presented in thesis was the lower wear rate observed for HP335 compared to R350HT rail steel under the same contact conditions. This result was intriguing because of the higher undeformed hardness possessed by R350HT compared to HP335 rail steel. The evaluation of the shear stress-strain curve and ratcheting load conversion factor results for the same condition did not pinpoint an explanation for why HP335 wore at a slower rate. This, therefore, leaves the shear strain to failure as the last remaining parameter needed for comparison after a definitive approach of deriving this information has been established to help pinpoint the reason for this observed wear behaviour. A detailed comparison of the microstructure evolution between R260, HP335, and R350HT rail steel would also be important to conduct in a future study to understand the fundamental microstructural reason behind this higher wear resistance with HP335 rail steel. Another interesting opportunity that could also be explored in the future is an investigation into whether a new heat-treated rail steel grade based around the chemical composition of HP335 potentially offers further enhancements in wear performance. This is based on the idea of combining the higher wear resistance provided by the HP335 chemical composition and the delayed wear flake development behaviour observed with R350HT due to the refinement of the pearlitic microstructure created by the heat treatment process. The work conducted investigating the influence of normal contact pressure on the ratcheting load conversion factor could also be expanded upon by testing R260 rail steel under a few more different normal contact pressures than those conducted in this thesis. These additional experiments would be beneficial in validating that the ratcheting load conversion factor is related to the depth of plastic damage and help understand what the true relationship is between them. A better understanding of the cyclic morphology change happening to asperities subject to compression-shear loading conditions on the running surface of rail and wheel steels could also be investigated. In addition, to researching what mechanisms are occurring that are responsible for this cyclic morphological change of asperities.

The research performed to develop a novel optical monitoring system for use on twin-disc testing demonstrated that the system was capable of clearly seeing the initiation and development of wear flakes from a dry contact test. An aspect of the dry contact tests that could be investigated further is looking at whether a conversion factor between the wear flake shadow pixel count and the wear rates

could be established. This would potentially enable an indirect estimate of the rail steel wear performance during twin-disc experiments.

During the water-lubricated experiments, however, the optical monitoring system was found to be less successfully at clearly visualising the initiation and development of RCF cracks. A key reason for this observed lack of clarity was the interference caused by the water-film present on the samples running track. An idea of improving the image quality during water-lubricated tests in the future is the possible application of deconvolution techniques, such as those used to remove atmospheric turbulence in images from ground-based telescopes [221]. After improving image quality, this research could be extended through simultaneously using eddy current detection techniques with this new optical monitoring system during water-lubricated tests. To investigate how the development of RCF cracks from eddy current data about subsurface behaviour compares against the surface information provided by the optical monitoring system.

There are also opportunities available to train and develop convolution neural network models, such as the U-Net model [223], for this optical monitoring system to help improve the analysis of image generated. For example, a convolution neural network model could be trained to look out for RCF cracks so that the optical monitoring system could automatically alert operators during water-lubricating test when this damage is created. Similarly, a convolutional neural network model could also be trained to detect wear flakes to potentially improve the semantic segmentation of wear flakes shadow from images collected during dry contact experiments.

The optical monitoring system explored in this thesis has also provided further evidence to show that the orientation of the elongated MnS inclusion relative to the running direction influences the initiation and development of wear flakes. The influence of the elongated MnS inclusion orientation has also been observed and explored in the references [128], [129], however, the full understanding of why this is occurring has yet to be established and will require further investigation. In addition, microstructural examination of MnS inclusions in the plastically deformed layer could also be conducted to provide a comprehensive explanation behind why this influence of the MnS inclusion orientation was observed to be more distinct for the harder rail steels.

References

- [1] Department for Transport, “Rail Factsheet: 2019,” Dec. 2019. <https://www.gov.uk/government/statistics/rail-factsheet-2019>.
- [2] UK Government, “Modal comparisons (TSGB01),” *Passenger transport by mode from 1952*, 2023. <https://www.gov.uk/government/statistical-data-sets/tsgb01-modal-comparisons#passenger-transport> (accessed May 01, 2023).
- [3] UK Government, “Final UK greenhouse gas emissions national statistics: 1990 to 2020,” *2020 UK greenhouse gas emissions: final figures - data tables (Excel)*, 2022. <https://www.gov.uk/government/statistics/final-uk-greenhouse-gas-emissions-national-statistics-1990-to-2020> (accessed May 01, 2023).
- [4] Department for Transport, “Rail Freight Strategy,” Sep. 2016. <https://www.gov.uk/government/publications/rail-freight-transport>.
- [5] RSSB, “Transport Decarbonisation Plan,” 2021. <https://www.rssb.co.uk/sustainability/decarbonisation/transport-decarbonisation-plan> (accessed May 01, 2023).
- [6] HS2, “Why HS2?,” 2023. <https://www.hs2.org.uk/why/> (accessed May 01, 2023).
- [7] O. of R. and Road, “Annual Passenger Journeys,” *Passenger Rail Usage*, 2019. <https://dataportal.orr.gov.uk/statistics/usage/passenger-rail-usage/> (accessed May 01, 2023).
- [8] Department for Transport, “Daily domestic transport use by mode,” *Domestic Transport Usage by Mode (CSV)*, 2023. https://assets.publishing.service.gov.uk/government/uploads/system/uploads/attachment_data/file/1149684/full_data_clean.csv.
- [9] R. Lundén and B. Paulsson, “Introduction to wheel-rail interface research,” in *Wheel-Rail Interface Handbook*, 2009.
- [10] Network Rail, “Network Rail Infrastructure Limited: Regulatory Financial Statements 2021/22,” 2022. [Online]. Available: <https://www.networkrail.co.uk/who-we-are/publications-and-resources/financial/>.
- [11] A. Kapoor, D. I. Fletcher, and F. J. Franklin, “The role of wear in enhancing rail life,” *Tribol. Ser.*, vol. 41, pp. 331–340, Jan. 2003, doi: 10.1016/S0167-8922(03)80146-3.
- [12] N. P. Suh, “The delamination theory of wear,” *Wear*, vol. 25, no. 1, pp. 111–124, Jul. 1973, doi: 10.1016/0043-1648(73)90125-7.
- [13] A. Kapoor, J. H. Beynon, D. I. Fletcher, and M. Loo-Morrey, “Computer simulation of strain accumulation and hardening for pearlitic rail steel undergoing repeated contact,” *J. Strain Anal. Eng. Des.*, vol. 39, no. 4, pp. 383–396, May 2004, doi: 10.1243/0309324041223935.
- [14] F. J. Franklin, T. Chung, and A. Kapoor, “Ratcheting and fatigue-led wear in rail–wheel contact,” *Fatigue Fract. Eng. Mater. Struct.*, vol. 26, no. 10, pp. 949–955, Oct. 2003, doi: 10.1046/j.1460-2695.2003.00703.x.
- [15] R. Lewis and U. Olofsson, “Basic tribology of the wheel–rail contact,” in *The Wheel Rail Interface Handbook*, R. Lewis and U. Olofsson, Eds. Cambridge, UK: Woodhead Publishing Ltd., 2009, pp. 34–57.

- [16] T. Telliskivi and U. Olofsson, "Contact mechanics analysis of measured wheel-rail profiles using the finite element method," *Proc. Inst. Mech. Eng. Part F J. Rail Rapid Transit*, vol. 215, no. 2, pp. 65–72, Mar. 2001, doi: 10.1243/0954409011531404.
- [17] M. A. Arslan and O. Kayabaşı, "3-D Rail–Wheel contact analysis using FEA," *Adv. Eng. Softw.*, vol. 45, no. 1, pp. 325–331, 2012, doi: <https://doi.org/10.1016/j.advengsoft.2011.10.009>.
- [18] G. G. Sirata, H. G. Lemu, K. Waclawiak, and Y. D. Jelila, "Study of rail-wheel contact problem by analytical and numerical approaches," *IOP Conf. Ser. Mater. Sci. Eng.*, vol. 1201, no. 1, p. 12035, 2021, doi: 10.1088/1757-899X/1201/1/012035.
- [19] S. K. Sharma and A. Kumar, "Dynamics Analysis of Wheel Rail Contact Using FEA," *Procedia Eng.*, vol. 144, pp. 1119–1128, 2016, doi: <https://doi.org/10.1016/j.proeng.2016.05.076>.
- [20] N. Burgelman, Z. Li, and R. Dollevoet, "A new rolling contact method applied to conformal contact and the train–turnout interaction," *Wear*, vol. 321, pp. 94–105, 2014, doi: <https://doi.org/10.1016/j.wear.2014.10.008>.
- [21] H. Tournay, "Support Technologies Vehicle Track Interaction," in *Guidelines to best practices for heavy haul railway operations: wheel and rail interface issues.*, Virginia Beach, VA, USA: International Heavy Haul Association, 2001, pp. 2.1-2.73.
- [22] K. L. Johnson, *Contact Mechanics*. Cambridge, UK: Cambridge University Press, 1985.
- [23] S. Iwnicki, S. Björklund, and R. Enblom, "Wheel–rail contact mechanics," in *Wheel–Rail Interface Handbook*, R. Lewis and U. Olofsson, Eds. Cambridge, UK: Woodhead Publishing Ltd., 2009, pp. 58–92.
- [24] J. J. Kalker, "Wheel-rail rolling contact theory," *Wear*, vol. 144, no. 1–2, pp. 243–261, Apr. 1991, doi: 10.1016/0043-1648(91)90018-P.
- [25] F. W. Carter, "On the action of a locomotive driving wheel," *Proc. R. Soc. London. Ser. A, Contain. Pap. a Math. Phys. Character*, vol. 112, no. 760, pp. 151–157, Aug. 1926, doi: 10.1098/rspa.1926.0100.
- [26] D. V Gutsulyak, L. J. E. Stanlake, and H. Qi, "Twin disc evaluation of third body materials in the wheel/rail interface," *Tribol. - Mater. Surfaces Interfaces*, vol. 15, no. 2, pp. 115–126, Apr. 2021, doi: 10.1080/17515831.2020.1829878.
- [27] E. A. Gallardo-Hernandez and R. Lewis, "Twin disc assessment of wheel/rail adhesion," *Wear*, vol. 265, no. 9, pp. 1309–1316, 2008, doi: <https://doi.org/10.1016/j.wear.2008.03.020>.
- [28] C. Chang, B. Chen, Y. Cai, and J. Wang, "An experimental study of high speed wheel-rail adhesion characteristics in wet condition on full scale roller rig," *Wear*, vol. 440–441, p. 203092, 2019, doi: <https://doi.org/10.1016/j.wear.2019.203092>.
- [29] A. Matsumoto *et al.*, "Creep force characteristics between rail and wheel on scaled model," *Wear*, vol. 253, no. 1, pp. 199–203, 2002, doi: [https://doi.org/10.1016/S0043-1648\(02\)00100-X](https://doi.org/10.1016/S0043-1648(02)00100-X).
- [30] U. Olofsson and K. Sundvall, "Influence of leaf, humidity and applied lubrication on friction in the wheel-rail contact: Pin-on-disc experiments," *Proc. Inst. Mech. Eng. Part F J. Rail Rapid Transit*, vol. 218, no. 3, pp. 235–242, May 2004, doi: 10.1243/0954409042389364.
- [31] W. J. Wang, H. F. Zhang, H. Y. Wang, Q. Y. Liu, and M. H. Zhu, "Study on the adhesion behavior of wheel/rail under oil, water and sanding conditions," *Wear*, vol. 271, no. 9–10, pp.

2693–2698, Jul. 2011, doi: 10.1016/J.WEAR.2010.12.019.

- [32] O. Arias-Cuevas, Z. Li, and R. Lewis, “A laboratory investigation on the influence of the particle size and slip during sanding on the adhesion and wear in the wheel–rail contact,” *Wear*, vol. 271, no. 1–2, pp. 14–24, May 2011, doi: <https://doi.org/10.1016/j.wear.2010.10.050>.
- [33] M. Burstow, “Whole Life Rail Model Application and Development for RSSB - Development of an RCF Damage Parameter,” RSSB, Derby, UK, Paper AEATR-ES-2003-832, Oct. 2003.
- [34] A. Gabelli, J. Lai, T. Lund, K. Rydén, I. Strandell, and G. E. Morales-Espejel, “The fatigue limit of bearing steels – Part II: Characterization for life rating standards,” *Int. J. Fatigue*, vol. 38, pp. 169–180, May 2012, doi: 10.1016/J.IJFATIGUE.2011.12.006.
- [35] E. M’Ewen, “Stresses in elastic cylinders in contact along a generatrix (including the effect of tangential friction),” *London, Edinburgh, Dublin Philos. Mag. J. Sci.*, vol. 40, no. 303, pp. 454–459, Apr. 1949, doi: 10.1080/14786444908521733.
- [36] A. Kapoor and K. L. Johnson, “Plastic ratchetting as a mechanism of metallic wear,” *Proc. R. Soc. London. Ser. A Math. Phys. Sci.*, vol. 445, no. 1924, pp. 367–384, May 1994, doi: 10.1098/rspa.1994.0066.
- [37] A. Kapoor, F. J. Franklin, S. K. Wong, and M. Ishida, “Surface roughness and plastic flow in rail wheel contact,” *Wear*, vol. 253, no. 1–2, pp. 257–264, Jul. 2002, doi: 10.1016/S0043-1648(02)00111-4.
- [38] J. A. Greenwood, J. B. P. Williamson, and F. P. Bowden, “Contact of nominally flat surfaces,” *Proc. R. Soc. London. Ser. A Math. Phys. Sci.*, vol. 295, no. 1442, pp. 300–319, Jan. 1966, doi: 10.1098/rspa.1966.0242.
- [39] A. W. Bush, R. D. Gibson, and T. R. Thomas, “The elastic contact of a rough surface,” *Wear*, vol. 35, no. 1, pp. 87–111, 1975, doi: [https://doi.org/10.1016/0043-1648\(75\)90145-3](https://doi.org/10.1016/0043-1648(75)90145-3).
- [40] J. A. Greenwood and J. H. Tripp, “The Contact of Two Nominally Flat Rough Surfaces,” *Proc. Inst. Mech. Eng.*, vol. 185, no. 1, pp. 625–633, Jun. 1970, doi: 10.1243/PIME_PROC_1970_185_069_02.
- [41] W. R. Chang, I. Etsion, and D. B. Bogy, “An Elastic-Plastic Model for the Contact of Rough Surfaces,” *J. Tribol.*, vol. 109, no. 2, pp. 257–263, Apr. 1987, doi: 10.1115/1.3261348.
- [42] R. L. Jackson and I. Green, “A statistical model of elasto-plastic asperity contact between rough surfaces,” *Tribol. Int.*, vol. 39, no. 9, pp. 906–914, 2006, doi: <https://doi.org/10.1016/j.triboint.2005.09.001>.
- [43] M. Ciavarella, J. A. Greenwood, and M. Paggi, “Inclusion of ‘interaction’ in the Greenwood and Williamson contact theory,” *Wear*, vol. 265, no. 5, pp. 729–734, 2008, doi: <https://doi.org/10.1016/j.wear.2008.01.019>.
- [44] G. F. Wang, J. M. Long, and X. Q. Feng, “A self-consistent model for the elastic contact of rough surfaces,” *Acta Mech.*, vol. 226, no. 2, pp. 285–293, 2015, doi: 10.1007/s00707-014-1177-2.
- [45] C.-Y. Li, Y. Ding, X.-M. Liang, and G.-F. Wang, “An improved elastic–plastic contact model with asperity interactions based on Greenwood–Williamson theory,” *Acta Mech.*, 2023, doi: 10.1007/s00707-023-03662-8.
- [46] C.-Y. Li and G.-F. Wang, “A modified Greenwood–Williamson contact model with asperity interactions,” *Acta Mech.*, vol. 234, no. 7, pp. 2859–2868, 2023, doi: 10.1007/s00707-023-03538-x.

- [47] J. A. Greenwood and J. H. Tripp, “The Elastic Contact of Rough Spheres,” *J. Appl. Mech.*, vol. 34, no. 1, pp. 153–159, Mar. 1967, doi: 10.1115/1.3607616.
- [48] D. Nowell and D. A. Hills, “Hertzian Contact of Ground Surfaces,” *J. Tribol.*, vol. 111, no. 1, pp. 175–179, Jan. 1989, doi: 10.1115/1.3261869.
- [49] D. A. Hills, D. Nowell, and A. Sackfield, “Chapter 4 - Plane contacts: partial slip,” D. A. Hills, D. Nowell, and A. B. T.-M. of E. C. Sackfield, Eds. Oxford: Butterworth-Heinemann, 1993, pp. 107–157.
- [50] A. Majumdar and B. Bhushan, “Fractal Model of Elastic-Plastic Contact Between Rough Surfaces,” *J. Tribol.*, vol. 113, no. 1, pp. 1–11, Jan. 1991, doi: 10.1115/1.2920588.
- [51] Y. Morag and I. Etsion, “Resolving the contradiction of asperities plastic to elastic mode transition in current contact models of fractal rough surfaces,” *Wear*, vol. 262, no. 5, pp. 624–629, 2007, doi: <https://doi.org/10.1016/j.wear.2006.07.007>.
- [52] X. Miao and X. Huang, “A complete contact model of a fractal rough surface,” *Wear*, vol. 309, no. 1, pp. 146–151, 2014, doi: <https://doi.org/10.1016/j.wear.2013.10.014>.
- [53] J. C. Chung and J. F. Lin, “Fractal Model Developed for Elliptic Elastic-Plastic Asperity Microcontacts of Rough Surfaces,” *J. Tribol.*, vol. 126, no. 4, pp. 646–654, Nov. 2004, doi: 10.1115/1.1792680.
- [54] Y. Yuan, J. Chen, and L. Zhang, “Loading-unloading contact model between three-dimensional fractal rough surfaces,” *AIP Adv.*, vol. 8, no. 7, p. 75017, Jul. 2018, doi: 10.1063/1.5027437.
- [55] B. N. J. Persson, “Elastoplastic Contact between Randomly Rough Surfaces,” *Phys. Rev. Lett.*, vol. 87, no. 11, p. 116101, Aug. 2001, doi: 10.1103/PhysRevLett.87.116101.
- [56] B. N. J. Persson, “Contact mechanics for randomly rough surfaces,” *Surf. Sci. Rep.*, vol. 61, no. 4, pp. 201–227, 2006, doi: <https://doi.org/10.1016/j.surfrep.2006.04.001>.
- [57] S. Hyun, L. Pei, J.-F. Molinari, and M. O. Robbins, “Finite-element analysis of contact between elastic self-affine surfaces,” *Phys. Rev. E*, vol. 70, no. 2, p. 26117, Aug. 2004, doi: 10.1103/PhysRevE.70.026117.
- [58] G. Carbone and F. Bottiglione, “Asperity contact theories: Do they predict linearity between contact area and load?,” *J. Mech. Phys. Solids*, vol. 56, no. 8, pp. 2555–2572, 2008, doi: <https://doi.org/10.1016/j.jmps.2008.03.011>.
- [59] Y. Xu and R. L. Jackson, “Statistical models of nearly complete elastic rough surface contact-comparison with numerical solutions,” *Tribol. Int.*, vol. 105, pp. 274–291, 2017, doi: <https://doi.org/10.1016/j.triboint.2016.10.003>.
- [60] J. F. Archard and T. E. Allibone, “Elastic deformation and the laws of friction,” *Proc. R. Soc. London. Ser. A. Math. Phys. Sci.*, vol. 243, no. 1233, pp. 190–205, Jan. 1997, doi: 10.1098/rspa.1957.0214.
- [61] M. Ciavarella, G. Demelio, J. R. Barber, and Y. H. Jang, “Linear elastic contact of the Weierstrass profile†,” *Proc. R. Soc. London. Ser. A Math. Phys. Eng. Sci.*, vol. 456, no. 1994, pp. 387–405, Feb. 2000, doi: 10.1098/rspa.2000.0522.
- [62] Y.-F. Gao and A. F. Bower, “Elastic–plastic contact of a rough surface with Weierstrass profile,” *Proc. R. Soc. A Math. Phys. Eng. Sci.*, vol. 462, no. 2065, pp. 319–348, Nov. 2005, doi: 10.1098/rspa.2005.1563.

- [63] K. Tomlinson, “Additive manufacturing for railway track component life extension with premium laser clad coating,” 2021.
- [64] J. C. Haven and G. L. Vose, “Economy of steel rails,” *The American Railway Times*, vol. 22, p. 86, Jan. 1870.
- [65] D. Brooke, “The advent of the steel rail, 1857-1914,” *J. Transp. Hist.*, vol. 7, no. 1, pp. 18–31, Mar. 1986.
- [66] *Railway applications - Track - Rail - Part 1: Vignole railway rails 46 kg/m and above*. BS EN13674-1, 2011.
- [67] C. Esveld, *Modern railway track*, 2nd ed. Duisburg, Germany: MRT Productions, 2001.
- [68] D. T. Llewellyn and R. Hudd, *Steels: metallurgy and applications*, 3rd ed. Oxford, UK: Butterworth-Heinemann, 1998.
- [69] J. E. Garnham, R. G. Ding, and C. L. Davis, “Ductile inclusions in rail, subject to compressive rolling–sliding contact,” *Wear*, vol. 269, no. 11–12, pp. 733–746, Oct. 2010.
- [70] O. P. Modi, N. Desmukh, D. P. Mondal, A. K. Jha, A. H. Yegneswaran, and H. K. Khaira, “Effect of interlamellar spacing on the mechanical properties of 0.65% C steel,” *Mater. Charact.*, vol. 46, no. 5, pp. 347–352, 2001, doi: [https://doi.org/10.1016/S1044-5803\(00\)00113-3](https://doi.org/10.1016/S1044-5803(00)00113-3).
- [71] A. M. Elwazri, P. Wanjara, and S. Yue, “The effect of microstructural characteristics of pearlite on the mechanical properties of hypereutectoid steel,” *Mater. Sci. Eng. A*, vol. 404, no. 1, pp. 91–98, 2005, doi: <https://doi.org/10.1016/j.msea.2005.05.051>.
- [72] F. P. L. Kavishe and T. J. Baker, “Effect of prior austenite grain size and pearlite interlamellar spacing on strength and fracture toughness of a eutectoid rail steel,” *Mater. Sci. Technol.*, vol. 2, no. 8, pp. 816–822, Aug. 1986, doi: [10.1179/mst.1986.2.8.816](https://doi.org/10.1179/mst.1986.2.8.816).
- [73] B. Bhattacharya, T. Bhattacharyya, and A. Halder, “Influence of Microstructure on the Mechanical Properties of a Pearlitic Steel,” *Metall. Mater. Trans. A*, vol. 51, no. 7, pp. 3614–3626, 2020, doi: [10.1007/s11661-020-05793-2](https://doi.org/10.1007/s11661-020-05793-2).
- [74] A. Rajput, J. Ramkumar, and K. Mondal, “Effect of pearlitic morphology with varying fineness on the cavitation erosion behavior of eutectoid rail steel,” *Ultrason. Sonochem.*, vol. 71, p. 105399, 2021, doi: <https://doi.org/10.1016/j.ultsonch.2020.105399>.
- [75] A. Fernández-Vicente, M. Carsí, F. Peñalba, E. Taleff, and O. A. Ruano, “Toughness dependence on the microstructural parameters for an ultrahigh carbon steel (1.3 wt.% C),” *Mater. Sci. Eng. A*, vol. 335, no. 1, pp. 175–185, 2002, doi: [https://doi.org/10.1016/S0921-5093\(01\)01916-5](https://doi.org/10.1016/S0921-5093(01)01916-5).
- [76] J. J. Lewandowski and A. W. Thompson, “Effects of the prior austenite grain size on the ductility of fully pearlitic eutectoid steel,” *Metall. Trans. A*, vol. 17, no. 3, pp. 461–472, Mar. 1986, doi: [10.1007/BF02643953](https://doi.org/10.1007/BF02643953).
- [77] X. C. Li, H. H. Ding, W. J. Wang, J. Guo, Q. Y. Liu, and Z. R. Zhou, “Investigation on the relationship between microstructure and wear characteristic of rail materials,” *Tribol. Int.*, vol. 163, p. 107152, 2021, doi: <https://doi.org/10.1016/j.triboint.2021.107152>.
- [78] B. L. Bramfitt, “Structure/Property Relationships in Irons and Steels,” in *Metals Handbook Desk Edition*, 2nd ed., J. R. Davis, Ed. Metals Park, OH, USA: ASM International, 1998, pp. 153–173.

- [79] G. K. Bouse, I. M. Bernstein, and D. H. Stone, “Role of Alloying and Microstructure on the Strength and Toughness of Experimental Rail Steels,” in *Rail Steels—Developments, Processing, and Use*, D. H. Stone and G. G. Knupp, Eds. West Conshohocken, PA: ASTM International, 1978, pp. 145–161.
- [80] E. Kozeschnik and H. K. D. H. Bhadeshia, “Influence of silicon on cementite precipitation in steels,” *Mater. Sci. Technol.*, vol. 24, no. 3, pp. 343–347, Mar. 2008, doi: 10.1179/174328408X275973.
- [81] K. Han, D. V Edmonds, and G. D. W. Smith, “Optimization of mechanical properties of high-carbon pearlitic steels with Si and V additions,” *Metall. Mater. Trans. A*, vol. 32, no. 6, pp. 1313–1324, Jun. 2001, doi: 10.1007/s11661-001-0222-7.
- [82] J. Maciejewski, “The Effects of Sulfide Inclusions on Mechanical Properties and Failures of Steel Components,” *J. Fail. Anal. Prev.*, vol. 15, no. 2, pp. 169–178, Feb. 2015, doi: 10.1007/s11668-015-9940-9.
- [83] W. Solano-Alvarez, M. J. Peet, E. J. Pickering, J. Jaiswal, A. Bevan, and H. K. D. H. Bhadeshia, “Synchrotron and neural network analysis of the influence of composition and heat treatment on the rolling contact fatigue of hypereutectoid pearlitic steels,” *Mater. Sci. Eng. A*, vol. 707, pp. 259–269, Nov. 2017, doi: 10.1016/J.MSEA.2017.09.045.
- [84] Y. E. Smith and F. B. Fletcher, “Alloy steels for high-strength, as-rolled rails,” in *Rail Steels—Developments, Processing, and Use*, no. 644, G. G. Knupp, Ed. West Conshohocken, PA, USA: ASTM International, 1978, pp. 212–232.
- [85] S. K. Mondal, *Steel metallurgy: properties, specifications and applications*. New York, NY, USA: McGraw-Hill Education, 2015.
- [86] S. A. Parsons and D. V Edmonds, “Microstructure and mechanical properties of medium-carbon ferrite–pearlite steel microalloyed with vanadium,” *Mater. Sci. Technol.*, vol. 3, no. 11, pp. 894–904, Nov. 1987, doi: 10.1179/mst.1987.3.11.894.
- [87] F. Katsuki, K. Watari, H. Tahira, and M. Umino, “Abrasive wear behavior of a pearlitic (0.4%C) steel microalloyed with vanadium,” *Wear*, vol. 264, no. 3–4, pp. 331–336, Feb. 2008, doi: <https://doi.org/10.1016/j.wear.2007.03.023>.
- [88] W. Solano-Alvarez, L. Fernandez Gonzalez, and H. K. D. H. Bhadeshia, “The effect of vanadium alloying on the wear resistance of pearlitic rails,” *Wear*, vol. 436–437, pp. 1–6, Oct. 2019, doi: 10.1016/J.WEAR.2019.203004.
- [89] British Steel, “Steel compositions and properties,” *Rail Product Guide*, 2017. <https://britishsteel.co.uk/media/40810/steel-grade-dimensions-and-properties.pdf>.
- [90] R. Stock and R. Pippan, “RCF and wear in theory and practice—The influence of rail grade on wear and RCF,” *Wear*, vol. 271, no. 1–2, pp. 125–133, May 2011, doi: 10.1016/J.WEAR.2010.10.015.
- [91] P. Pointner, “High strength rail steels—The importance of material properties in contact mechanics problems,” *Wear*, vol. 265, no. 9–10, pp. 1373–1379, Oct. 2008, doi: 10.1016/J.WEAR.2008.03.015.
- [92] H. C. Eden, J. E. Garnham, and C. L. Davis, “Influential microstructural changes on rolling contact fatigue crack initiation in pearlitic rail steels,” *Mater. Sci. Technol.*, vol. 21, no. 6, pp. 623–629, Jun. 2005.
- [93] J. E. Garnham and C. L. Davis, “Very early stage rolling contact fatigue crack growth in

pearlitic rail steels,” *Wear*, vol. 271, no. 1–2, pp. 100–112, May 2011.

- [94] J. E. Garnham and C. L. Davis, “The role of deformed rail microstructure on rolling contact fatigue initiation,” *Wear*, vol. 265, no. 9–10, pp. 1363–1372, Oct. 2008, doi: 10.1016/J.WEAR.2008.02.042.
- [95] F. J. Franklin, J. E. Garnham, D. I. Fletcher, C. L. Davis, and A. Kapoor, “Modelling rail steel microstructure and its effect on crack initiation,” *Wear*, vol. 265, no. 9–10, pp. 1332–1341, Oct. 2008.
- [96] J. E. Garnham, F. J. Franklin, D. I. Fletcher, A. Kapoor, and C. L. Davis, “Predicting the life of steel rails,” *Proc. Inst. Mech. Eng. Part F J. Rail Rapid Transit*, vol. 221, no. 1, pp. 45–58, Jan. 2007.
- [97] A. J. Perez-Unzueta and J. H. Beynon, “Microstructure and wear resistance of pearlitic rail steels,” *Wear*, vol. 162–164, pp. 173–182, Apr. 1993, doi: 10.1016/0043-1648(93)90498-B.
- [98] T. Teshima, M. Kosaka, K. Ushioda, N. Koga, and N. Nakada, “Local cementite cracking induced by heterogeneous plastic deformation in lamellar pearlite,” *Mater. Sci. Eng. A*, vol. 679, pp. 223–229, 2017, doi: <https://doi.org/10.1016/j.msea.2016.10.018>.
- [99] Y. Satoh and K. Iwafuchi, “Crystal orientation analysis of running surface of rail damaged by rolling contact,” *Wear*, vol. 258, no. 7–8, pp. 1126–1134, Mar. 2005, doi: 10.1016/J.WEAR.2004.03.048.
- [100] L. Zhou *et al.*, “Comparison of the damage and microstructure evolution of eutectoid and hypereutectoid rail steels under a rolling-sliding contact,” *Wear*, vol. 492–493, p. 204233, 2022, doi: <https://doi.org/10.1016/j.wear.2021.204233>.
- [101] H. Sunwoo, M. E. Fine, M. Meshii, and D. H. Stone, “Cyclic deformation of pearlitic eutectoid rail steel,” *Metall. Trans. A*, vol. 13, no. 11, pp. 2035–2047, Nov. 1982, doi: 10.1007/BF02645949.
- [102] D. A. Hughes and N. Hansen, “High angle boundaries formed by grain subdivision mechanisms,” *Acta Mater.*, vol. 45, no. 9, pp. 3871–3886, Sep. 1997, doi: 10.1016/S1359-6454(97)00027-X.
- [103] J. Wen, J. Marteau, S. Bouvier, M. Risbet, F. Cristofari, and P. Secordel, “Comparison of microstructure changes induced in two pearlitic rail steels subjected to a full-scale wheel/rail contact rig test,” *Wear*, vol. 456–457, p. 203354, Sep. 2020, doi: 10.1016/J.WEAR.2020.203354.
- [104] M. Matsui and Y. Kamiya, “Evaluation of material deterioration of rails subjected to rolling contact fatigue using x-ray diffraction,” *Wear*, vol. 304, no. 1–2, pp. 29–35, Jul. 2013, doi: 10.1016/J.WEAR.2013.04.018.
- [105] M. Masoumi, E. A. Ariza, A. Sinatora, and H. Goldenstein, “Role of crystallographic orientation and grain boundaries in fatigue crack propagation in used pearlitic rail steel,” *Mater. Sci. Eng. A*, vol. 722, pp. 147–155, Apr. 2018, doi: 10.1016/J.MSEA.2018.03.028.
- [106] W. Lojkowski, M. Djahanbakhsh, G. Bürkle, S. Gierlotka, W. Zielinski, and H.-J. Fecht, “Nanostructure formation on the surface of railway tracks,” *Mater. Sci. Eng. A*, vol. 303, no. 1–2, pp. 197–208, May 2001, doi: 10.1016/S0921-5093(00)01947-X.
- [107] V. N. Gridnev, V. V Nemoskalkenko, Y. Ya. Meshkov, V. G. Gavrilyuk, V. G. Prokopenko, and O. N. Razumov, “Mössbauer effect in deformed Fe–C alloys,” *Phys. status solidi*, vol. 31, no. 1, pp. 201–210, Sep. 1975, doi: 10.1002/pssa.2210310122.

- [108] J. Languillaume, G. Kapelski, and B. Baudelet, "Cementite dissolution in heavily cold drawn pearlitic steel wires," *Acta Mater.*, vol. 45, no. 3, pp. 1201–1212, Mar. 1997, doi: 10.1016/S1359-6454(96)00216-9.
- [109] G. Roberts, R. M. Ward, M. Strangwood, and C. L. Davis, "Use of misorientation values to further understand deformation in rail steels," *Ironmak. Steelmak.*, vol. 40, no. 2, pp. 92–97, Feb. 2013, doi: 10.1179/1743281212Y.0000000058.
- [110] J. Hua *et al.*, "Study on Microstructure Evolution and Property Change of U75V Rail Steel under Rolling–Sliding Conditions," *J. Mater. Eng. Perform.*, vol. 30, no. 11, pp. 8157–8168, 2021, doi: 10.1007/s11665-021-06040-4.
- [111] A. R. S. Ponter, A. D. Hearle, and K. L. Johnson, "Application of the kinematical shakedown theorem to rolling and sliding point contacts," *J. Mech. Phys. Solids*, vol. 33, no. 4, pp. 339–362, Jan. 1985, doi: 10.1016/0022-5096(85)90033-X.
- [112] J. W. Ringsberg, "Life prediction of rolling contact fatigue crack initiation," *Int. J. Fatigue*, vol. 23, no. 7, pp. 575–586, Aug. 2001, doi: 10.1016/S0142-1123(01)00024-X.
- [113] C. P. Jones, W. R. Tyfour, J. H. Beynon, and A. Kapoor, "The effect of strain hardening on shakedown limits of a pearlitic rail steel," *Proc. Inst. Mech. Eng. Part F J. Rail Rapid Transit*, vol. 211, no. 2, pp. 131–140, Mar. 1997, doi: 10.1243/0954409971530978.
- [114] A. Kapoor and F. J. Franklin, "Tribological layers and the wear of ductile materials," *Wear*, vol. 245, no. 1–2, pp. 204–215, Oct. 2000, doi: 10.1016/S0043-1648(00)00480-4.
- [115] F. J. Franklin, I. Widiyarta, and A. Kapoor, "Computer simulation of wear and rolling contact fatigue," *Wear*, vol. 251, no. 1–12, pp. 949–955, Oct. 2001, doi: 10.1016/S0043-1648(01)00732-3.
- [116] F. J. Franklin and A. Kapoor, "Modelling wear and crack initiation in rails," *Proc. Inst. Mech. Eng. Part F J. Rail Rapid Transit*, vol. 221, no. 1, pp. 23–33, Jan. 2007, doi: 10.1243/0954409JRRT60.
- [117] W. R. Tyfour, J. H. Beynon, and A. Kapoor, "The steady state wear behaviour of pearlitic rail steel under dry rolling-sliding contact conditions," *Wear*, vol. 180, no. 1–2, pp. 79–89, Jan. 1995, doi: 10.1016/0043-1648(94)06533-0.
- [118] K. Tomlinson, D. I. Fletcher, and R. Lewis, "Measuring material plastic response to cyclic loading in modern rail steels from a minimum number of twin-disc tests," *J. Rail Rapid Transit*.
- [119] F. A. M. Alwahdi, A. Kapoor, and F. J. Franklin, "Subsurface microstructural analysis and mechanical properties of pearlitic rail steels in service," *Wear*, vol. 302, no. 1–2, pp. 1453–1460, Apr. 2013, doi: 10.1016/j.wear.2012.12.058.
- [120] W. R. Tyfour, J. H. Beynon, and A. Kapoor, "Deterioration of rolling contact fatigue life of pearlitic rail steel due to dry-wet rolling-sliding line contact," *Wear*, vol. 197, no. 1–2, pp. 255–265, Sep. 1996, doi: 10.1016/0043-1648(96)06978-5.
- [121] M. Akama and T. Kimata, "Numerical simulation model for the competition between short crack propagation and wear in the wheel tread," *Wear*, vol. 448–449, p. 203205, 2020, doi: <https://doi.org/10.1016/j.wear.2020.203205>.
- [122] A. Namura, F. Urakawa, H. Tanimoto, and D. Nakajima, "Rail Surface Fatigue Assessment Using Numerical Simulation of the Concurrence of Short Crack Propagation and Wear," *Q. Rep. RTRI*, vol. 57, no. 4, pp. 311–317, 2016, doi: 10.2219/rtriqr.57.4_311.
- [123] G. Donzella, M. Faccoli, A. Mazzù, C. Petrogalli, and R. Roberti, "Progressive damage

assessment in the near-surface layer of railway wheel–rail couple under cyclic contact,” *Wear*, vol. 271, no. 1–2, pp. 408–416, May 2011, doi: 10.1016/J.WEAR.2010.10.042.

- [124] A. Mazzù, “Experimental and Numerical Characterization of a Rail Steel Behavior under Cyclic Contact Stresses,” *Key Eng. Mater.*, vol. 348–349, pp. 569–572, 2007, doi: 10.4028/www.scientific.net/KEM.348-349.569.
- [125] R. Halama, R. Fajkoš, P. Matušek, P. Bábková, F. Fojtík, and L. Václavek, “Contact defects initiation in railroad wheels – Experience, experiments and modelling,” *Wear*, vol. 271, no. 1, pp. 174–185, 2011, doi: <https://doi.org/10.1016/j.wear.2010.10.053>.
- [126] D. I. Fletcher, F. J. Franklin, and A. Kapoor, “Rail surface fatigue and wear,” in *Wheel–Rail Interface Handbook*, R. Lewis and U. Olofsson, Eds. Cambridge, UK: Woodhead Publishing Ltd., 2009, pp. 280–310.
- [127] Y. H. He, X. Q. Hou, C. H. Tao, and F. K. Han, “Recrystallization and fatigue fracture of single crystal turbine blades,” *Eng. Fail. Anal.*, vol. 18, no. 3, pp. 944–949, 2011, doi: <https://doi.org/10.1016/j.engfailanal.2010.11.012>.
- [128] Y. Nakai *et al.*, “Inclusion orientation dependent flaking process in rolling contact fatigue observed by laminography using ultrabright synchrotron radiation X-ray,” *Fatigue Fract. Eng. Mater. Struct.*, vol. 45, no. 8, pp. 2200–2214, Aug. 2022, doi: <https://doi.org/10.1111/ffe.13728>.
- [129] H. Mahdavi, K. Poulis, and C. F. Niordson, “Effect of superimposed compressive stresses on rolling contact fatigue initiation at hard and soft inclusions,” *Int. J. Fatigue*, vol. 134, p. 105399, May 2020, doi: 10.1016/j.ijfatigue.2019.105399.
- [130] D. I. Fletcher, P. Hyde, and A. Kapoor, “Investigating fluid penetration of rolling contact fatigue cracks in rails using a newly developed full-scale test facility,” *Proc. Inst. Mech. Eng. Part F J. Rail Rapid Transit*, vol. 221, no. 1, pp. 35–44, Jan. 2007, doi: 10.1243/09544097JRRT63.
- [131] A. F. Bower, “The Influence of Crack Face Friction and Trapped Fluid on Surface Initiated Rolling Contact Fatigue Cracks,” *J. Tribol.*, vol. 110, no. 4, pp. 704–711, Oct. 1988, doi: 10.1115/1.3261717.
- [132] S. Bogdański, “A rolling contact fatigue crack driven by squeeze fluid film,” *Fatigue Fract. Eng. Mater. Struct.*, vol. 25, no. 11, pp. 1061–1071, Oct. 2002, doi: 10.1046/j.1460-2695.2000.00563.x.
- [133] W. J. Wang, R. Lewis, M. D. Evans, and Q. Y. Liu, “Influence of Different Application of Lubricants on Wear and Pre-existing Rolling Contact Fatigue Cracks of Rail Materials,” *Tribol. Lett.*, vol. 65, no. 58, pp. 1–15, Mar. 2017, doi: 10.1007/s11249-017-0841-9.
- [134] N. Larijani, J. Brouzoulis, M. Schilke, and M. Ekh, “The effect of anisotropy on crack propagation in pearlitic rail steel,” *Wear*, vol. 314, no. 1–2, pp. 57–68, Jun. 2014, doi: 10.1016/J.WEAR.2013.11.034.
- [135] J. F. Archard, “Contact and Rubbing of Flat Surfaces,” *J. Appl. Phys.*, vol. 24, no. 8, pp. 981–988, Aug. 1953, doi: 10.1063/1.1721448.
- [136] P. J. Bolton and P. Clayton, “Rolling—sliding wear damage in rail and tyre steels,” *Wear*, vol. 93, no. 2, pp. 145–165, Jan. 1984, doi: 10.1016/0043-1648(84)90066-8.
- [137] J. F. Santa *et al.*, “Twin disc assessment of wear regime transitions and rolling contact fatigue in R400HT – E8 pairs,” *Wear*, vol. 432–433, p. 102916, Aug. 2019, doi:

10.1016/J.WEAR.2019.05.031.

- [138] Y. Hu *et al.*, “Wear of driving versus driven discs in a twin disc rolling-sliding test,” *Wear*, vol. 512–513, p. 204528, 2023, doi: <https://doi.org/10.1016/j.wear.2022.204528>.
- [139] R. Lewis and R. S. Dwyer-Joyce, “Wear mechanisms and transitions in railway wheel steels,” *Proc. Inst. Mech. Eng. Part J J. Eng. Tribol.*, vol. 218, no. 6, pp. 467–478, Jun. 2004, doi: 10.1243/1350650042794815.
- [140] E. A. Gallardo-Hernandez, R. Lewis, and R. S. Dwyer-Joyce, “Temperature in a twin-disc wheel/rail contact simulation,” *Tribol. Int.*, vol. 39, no. 12, pp. 1653–1663, Dec. 2006.
- [141] British Steelmakers Creep Committee, *BSCC high temperature data : British long term creep rupture and elevated temperature tensile data on steels for high temperature service*. London, UK: Iron and Steel Institute for the British Steelmakers Creep Committee, 1973.
- [142] H. Al-Maliki, A. Meierhofer, G. Trummer, R. Lewis, and K. Six, “A new approach for modelling mild and severe wear in wheel-rail contacts,” *Wear*, vol. 476, p. 203761, 2021, doi: <https://doi.org/10.1016/j.wear.2021.203761>.
- [143] T. Sasada, “Wear research in Japan: Trends and future directions,” *Wear*, vol. 100, no. 1, pp. 561–577, 1984, doi: [https://doi.org/10.1016/0043-1648\(84\)90033-4](https://doi.org/10.1016/0043-1648(84)90033-4).
- [144] I. Hutchings and P. Shipway, “5 - Sliding wear,” in *Tribology: Friction and Wear of Engineering Materials*, 2nd ed., I. Hutchings and P. B. T.-T. (Second E. Shipway, Eds. Butterworth-Heinemann, 2017, pp. 107–164.
- [145] A. Athukorala and D. V De Pellegrin, “Experimental Depiction of the Hypothesis of Flake-Like Wear Debris Generation in Rolling Contact Fatigue of the Rail–Wheel Contact Interface,” *Tribol. Trans.*, vol. 60, no. 4, pp. 581–591, Jul. 2017, doi: 10.1080/10402004.2016.1188189.
- [146] N. Tosangthum *et al.*, “Dry rolling-sliding wear behavior of ER9 wheel and R260 rail couple under different operating conditions,” *Wear*, vol. 518–519, p. 204636, 2023, doi: <https://doi.org/10.1016/j.wear.2023.204636>.
- [147] C. Hardwick, R. Lewis, and D. T. Eadie, “Wheel and rail wear—Understanding the effects of water and grease,” *Wear*, vol. 314, no. 1–2, pp. 198–204, Jun. 2014, doi: 10.1016/J.WEAR.2013.11.020.
- [148] W. J. Wang, R. Lewis, B. Yang, L. C. Guo, Q. Y. Liu, and M. H. Zhu, “Wear and damage transitions of wheel and rail materials under various contact conditions,” *Wear*, vol. 362–363, pp. 146–152, 2016, doi: <https://doi.org/10.1016/j.wear.2016.05.021>.
- [149] R. Lewis and R. S. Dwyer-Joyce, “Wear at the wheel/rail interface when sanding is used to increase adhesion,” *Proc. Inst. Mech. Eng. Part F J. Rail Rapid Transit*, vol. 220, no. 1, pp. 29–41, Jan. 2006, doi: 10.1243/095440905X33260.
- [150] Y. Lyu, Y. Zhu, and U. Olofsson, “Wear between wheel and rail: A pin-on-disc study of environmental conditions and iron oxides,” *Wear*, vol. 328–329, pp. 277–285, Apr. 2015, doi: 10.1016/J.WEAR.2015.02.057.
- [151] UIC, “Recommendations for the use of rail steel grades,” 2015.
- [152] INNOTRACK Guidelines, “Definitive guidelines on the use of different rail grades,” 2006.
- [153] M. Hiensch and M. Steenberg, “Rolling Contact Fatigue on premium rail grades: Damage function development from field data,” *Wear*, vol. 394–395, pp. 187–194, Jan. 2018, doi: 10.1016/J.WEAR.2017.10.018.

- [154] R. Stock and R. Pippan, “Rail grade dependent damage behaviour – Characteristics and damage formation hypothesis,” *Wear*, vol. 314, no. 1, pp. 44–50, 2014, doi: <https://doi.org/10.1016/j.wear.2013.11.029>.
- [155] R. Heyder and M. Brehmer, “Empirical studies of head check propagation on the DB network,” *Wear*, vol. 314, no. 1, pp. 36–43, 2014, doi: <https://doi.org/10.1016/j.wear.2013.11.035>.
- [156] R. Lewis, P. Christoforou, W. J. Wang, A. Beagles, M. Burstow, and S. R. Lewis, “Investigation of the influence of rail hardness on the wear of rail and wheel materials under dry conditions (ICRI wear mapping project),” *Wear*, vol. 430–431, pp. 383–392, 2019, doi: <https://doi.org/10.1016/j.wear.2019.05.030>.
- [157] S. Lewis, A. Vickerstaff, S. Fretwell-Smith, R. Lever, and A. Trowsdale, “Experiences of using premium rail on an urban metro network,” 2022.
- [158] M. Burstow, “Experience of premium grade rail steels to resist rolling contact fatigue (RCF) on GB network,” *Ironmak. Steelmak.*, vol. 40, no. 2, pp. 103–107, Feb. 2013, doi: 10.1179/1743281212Y.0000000042.
- [159] A. Vickerstaff, A. Bevan, and P. Boyacioglu, “Predictive wheel–rail management in London Underground: Validation and verification,” *Proc. Inst. Mech. Eng. Part F J. Rail Rapid Transit*, vol. 234, no. 4, pp. 393–404, Oct. 2019, doi: 10.1177/0954409719878616.
- [160] Y. Hu *et al.*, “Comparison of wear and rolling contact fatigue behaviours of bainitic and pearlitic rails under various rolling-sliding conditions,” *Wear*, vol. 460–461, p. 203455, 2020, doi: <https://doi.org/10.1016/j.wear.2020.203455>.
- [161] C. C. Viáfara, M. I. Castro, J. M. Vélez, and A. Toro, “Unlubricated sliding wear of pearlitic and bainitic steels,” *Wear*, vol. 259, no. 1–6, pp. 405–411, Jul. 2005, doi: 10.1016/J.WEAR.2005.02.013.
- [162] J. Sundh and U. Olofsson, “Relating contact temperature and wear transitions in a wheel–rail contact,” *Wear*, vol. 271, no. 1–2, pp. 78–85, May 2011, doi: 10.1016/J.WEAR.2010.10.046.
- [163] G. Tressia, A. Sinatora, H. Goldenstein, and M. Masoumi, “Improvement in the wear resistance of a hypereutectoid rail via heat treatment,” *Wear*, vol. 442–443, p. 203122, Feb. 2020, doi: 10.1016/J.WEAR.2019.203122.
- [164] F. C. Robles Hernández, N. G. Demas, K. Gonzales, and A. A. Polycarpou, “Correlation between laboratory ball-on-disk and full-scale rail performance tests,” *Wear*, vol. 270, no. 7–8, pp. 479–491, Mar. 2011, doi: 10.1016/J.WEAR.2011.01.001.
- [165] F. C. Robles Hernández, N. G. Demas, D. D. Davis, A. A. Polycarpou, and L. Maal, “Mechanical properties and wear performance of premium rail steels,” *Wear*, vol. 263, no. 1–6, pp. 766–772, Sep. 2007, doi: 10.1016/J.WEAR.2006.12.021.
- [166] S. M. Shariff, T. K. Pal, G. Padmanabham, and S. V Joshi, “Comparative Study on Dry Sliding Wear Behavior of Various Railroad Steels,” *J. Tribol.*, vol. 133, no. 2, Mar. 2011, doi: 10.1115/1.4003485.
- [167] R. S. Miranda, A. B. Rezende, S. T. Fonseca, F. M. Fernandes, A. Sinatora, and P. R. Mei, “Fatigue and wear behavior of pearlitic and bainitic microstructures with the same chemical composition and hardness using twin-disc tests,” *Wear*, vol. 494–495, p. 204253, 2022, doi: <https://doi.org/10.1016/j.wear.2022.204253>.
- [168] Y. Jin, M. Ishida, and A. Namura, “Experimental simulation and prediction of wear of wheel flange and rail gauge corner,” *Wear*, vol. 271, no. 1–2, pp. 259–267, May 2011, doi:

10.1016/J.WEAR.2010.10.032.

- [169] U. Olofsson and T. Telliskivi, “Wear, plastic deformation and friction of two rail steels—a full-scale test and a laboratory study,” *Wear*, vol. 254, no. 1–2, pp. 80–93, Jan. 2003, doi: 10.1016/S0043-1648(02)00291-0.
- [170] R. Lewis *et al.*, “Towards a standard approach for the wear testing of wheel and rail materials,” *Proc. Inst. Mech. Eng. Part F J. Rail Rapid Transit*, vol. 231, no. 7, pp. 760–774, Apr. 2017, doi: 10.1177/0954409717700531.
- [171] D. I. Fletcher and J. H. Beynon, “Development of a Machine for Closely Controlled Rolling Contact Fatigue and Wear Testing,” *J. Test. Eval.*, vol. 28, no. 4, pp. 267–275, Jul. 2000, doi: 10.1520/JTE12104J.
- [172] P. Christoforou, D. I. Fletcher, and R. Lewis, “Benchmarking of premium rail material wear,” *Wear*, vol. 436–437, p. 202990, Oct. 2019, doi: 10.1016/J.WEAR.2019.202990.
- [173] B. Rodríguez-Arana, A. San Emeterio, M. Panera, A. Montes, and D. Álvarez, “Investigation of a relationship between twin-disc wear rates and the slipping contact area on R260 grade rail,” *Tribol. Int.*, vol. 168, p. 107456, Apr. 2022, doi: 10.1016/J.TRIBOINT.2022.107456.
- [174] J. E. Garnham and J. H. Beynon, “The early detection of rolling-sliding contact fatigue cracks,” *Wear*, vol. 144, no. 1–2, pp. 103–116, Apr. 1991, doi: 10.1016/0043-1648(91)90009-J.
- [175] S.-J. Kwon, J.-W. Seo, J.-M. Kim, and M.-S. Kim, “Observation of the damage process of rolling contact fatigue using a non-contact electro-magnetic array sensor,” *Wear*, vol. 390–391, pp. 220–227, Nov. 2017, doi: 10.1016/J.WEAR.2017.08.003.
- [176] M. P. Papaelias, M. C. Lugg, C. Roberts, and C. L. Davis, “High-speed inspection of rails using ACFM techniques,” *NDT E Int.*, vol. 42, no. 4, pp. 328–335, 2009, doi: <https://doi.org/10.1016/j.ndteint.2008.12.008>.
- [177] J. L. Shen, L. Zhou, H. Rowshandel, G. L. Nicholson, and C. L. Davis, “Determining the propagation angle for non-vertical surface-breaking cracks and its effect on crack sizing using an ACFM sensor,” *Meas. Sci. Technol.*, vol. 26, no. 11, p. 115604, 2015, doi: 10.1088/0957-0233/26/11/115604.
- [178] Y. Hou, J. Shen, J. Fang, Z. Meng, G. Liu, and L. Zhou, “Characterization of intersecting and bifurcating rolling contact fatigue (RCF) cracks in railway rails using ACFM sensor,” *Measurement*, vol. 217, p. 113075, 2023, doi: <https://doi.org/10.1016/j.measurement.2023.113075>.
- [179] J. Shen, L. Zhou, H. Rowshandel, G. L. Nicholson, and C. L. Davis, “Prediction of RCF clustered cracks dimensions using an ACFM sensor and influence of crack length and vertical angle,” *Nondestruct. Test. Eval.*, vol. 35, no. 1, pp. 1–18, Jan. 2020, doi: 10.1080/10589759.2019.1611817.
- [180] J. Shen *et al.*, “Analysis on asymmetrical RCF cracks characterisation using an ACFM sensor and the influence of the rail head profile,” *Measurement*, vol. 194, p. 111008, 2022, doi: <https://doi.org/10.1016/j.measurement.2022.111008>.
- [181] I. Bodini *et al.*, “Evaluation of wear in rolling contact tests by means of 2D image analysis,” *Wear*, vol. 400–401, pp. 156–168, Apr. 2018, doi: 10.1016/J.WEAR.2017.12.023.
- [182] I. Bodini, G. Sansoni, M. Lancini, S. Pasinetti, and F. Docchio, “A novel optical apparatus for the study of rolling contact wear/fatigue based on a high-speed camera and multiple-source laser illumination,” *Review of Scientific Instruments*, vol. 87, no. 8. American Institute of

Physics Inc., Aug. 01, 2016, doi: 10.1063/1.4959981.

- [183] I. Bodini, G. Sansoni, M. Lancini, S. Pasinetti, and F. Docchio, “Feasibility study of a vision system for on-line monitoring of rolling contact fatigue tests,” *J. Phys. Conf. Ser.*, vol. 778, p. 12007, 2017, doi: 10.1088/1742-6596/778/1/012007.
- [184] I. Bodini, C. Petrogalli, A. Mazzù, S. Pasinetti, T. Kato, and T. Makino, “A vision-based approach for rolling contact fatigue evaluation in twin-disc tests on a railway wheel steel,” *Tribol. - Mater. Surfaces Interfaces*, vol. 15, no. 2, 2021, doi: 10.1080/17515831.2020.1825062.
- [185] P. Andersson and B. Hemming, “Determination of wear volumes by chromatic confocal measurements during twin-disc tests with cast iron and steel,” *Wear*, vol. 338–339, pp. 95–104, 2015, doi: <https://doi.org/10.1016/j.wear.2015.05.011>.
- [186] I. Bodini, N. Zani, C. Petrogalli, A. Mazzù, T. Kato, and T. Makino, “Analysis of damage evolution in alternated wet-dry contact tests on a railway wheel steel by a vision system,” 2022.
- [187] G. Donzella, A. Mazzù, and C. Petrogalli, “Competition between wear and rolling contact fatigue at the wheel—rail interface: some experimental evidence on rail steel,” *Proc. Inst. Mech. Eng. Part F J. Rail Rapid Transit*, vol. 223, no. 1, pp. 31–44, Jan. 2009, doi: 10.1243/09544097JRRT161.
- [188] J.-W. Seo, S.-J. Kwon, D.-H. Lee, and H.-Y. Choi, “Analysis of contact fatigue crack growth using twin-disc tests and numerical evaluations,” *Int. J. Fatigue*, vol. 55, pp. 54–63, Oct. 2013, doi: 10.1016/J.IJFATIGUE.2013.05.005.
- [189] M. Kráčalík, G. Trummer, and W. Daves, “Application of 2D finite element analysis to compare cracking behaviour in twin-disc tests and full scale wheel/rail experiments,” *Wear*, vol. 346–347, pp. 140–147, Jan. 2016, doi: 10.1016/J.WEAR.2015.11.013.
- [190] C. Kammerhofer, A. Hohenwarter, and R. Pippan, “A novel laboratory test rig for probing the sensitivity of rail steels to RCF and wear – first experimental results,” *Wear*, vol. 316, no. 1–2, pp. 101–108, Aug. 2014, doi: 10.1016/J.WEAR.2014.04.008.
- [191] L. Ma, L. B. Shi, J. Guo, Q. Y. Liu, and W. J. Wang, “On the wear and damage characteristics of rail material under low temperature environment condition,” *Wear*, vol. 394–395, pp. 149–158, 2018, doi: <https://doi.org/10.1016/j.wear.2017.10.011>.
- [192] A. Kapoor and K. L. Johnson, “Effect of changes in contact geometry on shakedown of surfaces in rolling/sliding contact,” *Int. J. Mech. Sci.*, vol. 34, no. 3, pp. 223–239, Mar. 1992, doi: 10.1016/0020-7403(92)90073-P.
- [193] K. Tomlinson, D. I. Fletcher, and R. Lewis, “Measuring material plastic response to cyclic loading in modern rail steels from a minimal number of twin-disc tests,” *Proc. Inst. Mech. Eng. Part F J. Rail Rapid Transit*, vol. 235, no. 10, pp. 1203–1213, Feb. 2021, doi: 10.1177/0954409721993615.
- [194] Phoenix Tribology Ltd, “TE 72 two roller machine,” 2017. <http://www.phoenix-tribology.com/at2/leaflet/te72>.
- [195] “British Standards. Metallic materials. Vickers hardness test. Test method,” BS EN ISO 6507-1:2018, 2018.
- [196] W. C. Oliver and G. M. Pharr, “An improved technique for determining hardness and elastic modulus using load and displacement sensing indentation experiments,” *J. Mater. Res.*, vol. 7, no. 6, pp. 1564–1583, 1992, doi: 10.1557/JMR.1992.1564.

- [197] “British Standards. Geometrical product specification (GPS). Surface texture: Profile method. Terms, definitions and surface texture parameters,” BS EN ISO 4287, 1998.
- [198] Z. W. Birnbaum and S. C. Saunders, “A New Family of Life Distributions,” *J. Appl. Probab.*, vol. 6, no. 2, pp. 319–327, Feb. 1969, doi: 10.2307/3212003.
- [199] N. A. Fleck, G. M. Muller, M. F. Ashby, and J. W. Hutchinson, “Strain gradient plasticity: Theory and experiment,” *Acta Metall. Mater.*, vol. 42, no. 2, pp. 475–487, Feb. 1994, doi: 10.1016/0956-7151(94)90502-9.
- [200] D. I. Fletcher and J. H. Beynon, “The influence of lubricant type on rolling contact fatigue of pearlitic rail steel,” in *Lubrication at the Frontier*, vol. 36, D. Dowson, M. Priest, C. M. Taylor, P. Ehret, T. H. C. Childs, G. Dalmaz, Y. Berthier, L. Flamand, J. M. Georges, and A. A. Lubrecht, Eds. Elsevier, 1999, pp. 299–310.
- [201] D. Nikas, X. Zhang, and J. Ahlström, “Evaluation of local strength via microstructural quantification in a pearlitic rail steel deformed by simultaneous compression and torsion,” *Mater. Sci. Eng. A*, vol. 737, pp. 341–347, 2018, doi: <https://doi.org/10.1016/j.msea.2018.09.067>.
- [202] K. A. Meyer, M. Ekh, and J. Ahlström, “Modeling of kinematic hardening at large biaxial deformations in pearlitic rail steel,” *Int. J. Solids Struct.*, vol. 130–131, pp. 122–132, 2018, doi: <https://doi.org/10.1016/j.ijsolstr.2017.10.007>.
- [203] O. Yazici, S. Yilmaz, and S. Yildirim, “Microstructural and Mechanical Properties Examination of High-Power Diode Laser-Treated R260 Grade Rail Steels Under Different Processing Temperatures,” *Metall. Mater. Trans. A*, vol. 50, no. 2, pp. 1061–1075, 2019, doi: 10.1007/s11661-018-5041-1.
- [204] O. Hajizad, A. Kumar, Z. Li, R. H. Petrov, J. Sietsma, and R. Dollevoet, “Influence of Microstructure on Mechanical Properties of Bainitic Steels in Railway Applications,” *Metals*, vol. 9, no. 7, 2019, doi: 10.3390/met9070778.
- [205] A. Kumar *et al.*, “Design of high-strength and damage-resistant carbide-free fine bainitic steels for railway crossing applications,” *Mater. Sci. Eng. A*, vol. 759, pp. 210–223, Jun. 2019, doi: 10.1016/j.msea.2019.05.043.
- [206] A. C. Athukorala, D. V De Pellegrin, and K. I. Kourousis, “Characterisation of head-hardened rail steel in terms of cyclic plasticity response and microstructure for improved material modelling,” *Wear*, vol. 366–367, pp. 416–424, Nov. 2016, doi: 10.1016/j.wear.2016.03.024.
- [207] S. Maya-Johnson, A. J. Ramirez, and A. Toro, “Fatigue crack growth rate of two pearlitic rail steels,” *Eng. Fract. Mech.*, vol. 138, pp. 63–72, Apr. 2015, doi: 10.1016/j.engfracmech.2015.03.023.
- [208] W. Hui, Z. Xu, Y. Zhang, X. Zhao, C. Shao, and Y. Weng, “Hydrogen embrittlement behavior of high strength rail steels: A comparison between pearlitic and bainitic microstructures,” *Mater. Sci. Eng. A*, vol. 704, pp. 199–206, Sep. 2017, doi: 10.1016/j.msea.2017.08.022.
- [209] H. Su *et al.*, “Ratcheting behaviour of flash butt welds in heat-treated hypereutectoid steel rails under uniaxial and biaxial cyclic loadings,” *Int. J. Mech. Sci.*, vol. 176, p. 105539, Jun. 2020, doi: 10.1016/j.ijmecsci.2020.105539.
- [210] R. R. Porcaro, G. L. Faria, L. B. Godefroid, G. R. Apolonio, L. C. Cândido, and E. S. Pinto, “Microstructure and mechanical properties of a flash butt welded pearlitic rail,” *J. Mater. Process. Technol.*, vol. 270, pp. 20–27, Aug. 2019, doi: 10.1016/j.jmatprotec.2019.02.013.

- [211] British Steel, “R260 and HP335 Tensile and Hardness Test Results.” 2021.
- [212] Matlab, “Iterations and Function Counts,” 2023. https://uk.mathworks.com/help/optim/ug/iterations-and-function-counts.html#mw_dc044841-a6b6-43c0-8b29-0af2fbbcb66c.
- [213] A. M. S. Asih, K. Ding, and A. Kapoor, “Modelling rail wear transition and mechanism due to frictional heating,” *Wear*, vol. 284–285, pp. 82–90, 2012, doi: <https://doi.org/10.1016/j.wear.2012.02.017>.
- [214] F. Alwahdi, F. J. Franklin, and A. Kapoor, “The effect of partial slip on the wear rate of rails,” *Wear*, vol. 258, no. 7, pp. 1031–1037, 2005, doi: <https://doi.org/10.1016/j.wear.2004.03.052>.
- [215] IN2TRACK, “Research into enhanced tracks, switches and structures,” 2016. doi: 10.3030/730841.
- [216] EPIX, “PIXCI EL1 PCIe x1 Base, Medium, Full Camera Link Frame Grabber,” 2023. https://www.epixinc.com/products/pixci_el1.htm (accessed Jul. 15, 2023).
- [217] EPIX, “XCAP Software Ready-to-Run Image Analysis Software for PIXCI Frame Grabbers,” 2023. <https://www.epixinc.com/products/xcap.htm> (accessed Jul. 15, 2023).
- [218] E. Allen and S. Triantaphillidou, *The manual of photography*, 10th ed. Oxford: Oxford, 2011.
- [219] Chromasens, “Corona II LED line scan light,” 2023. <https://chromasens.de/en/product/corona> (accessed Jul. 15, 2023).
- [220] J. E. Garnham and J. H. Beynon, “The early detection of rolling-sliding contact fatigue cracks,” *Wear*, vol. 144, no. 1–2, pp. 103–116, Apr. 1991, doi: 10.1016/0043-1648(91)90009-J.
- [221] X. Zhu and P. Milanfar, “Removing Atmospheric Turbulence via Space-Invariant Deconvolution,” *IEEE Trans. Pattern Anal. Mach. Intell.*, vol. 35, no. 1, pp. 157–170, 2013, doi: 10.1109/TPAMI.2012.82.
- [222] G. F. Vander Voort and A. Roósz, “Measurement of the interlamellar spacing of pearlite,” *Metallography*, vol. 17, no. 1, pp. 1–17, 1984, doi: [https://doi.org/10.1016/0026-0800\(84\)90002-8](https://doi.org/10.1016/0026-0800(84)90002-8).
- [223] O. Ronneberger, P. Fischer, and T. Brox, “U-Net: Convolutional Networks for Biomedical Image Segmentation BT - Medical Image Computing and Computer-Assisted Intervention – MICCAI 2015,” 2015, pp. 234–241.

Appendix A1: Supplementary Information for Chapter 3

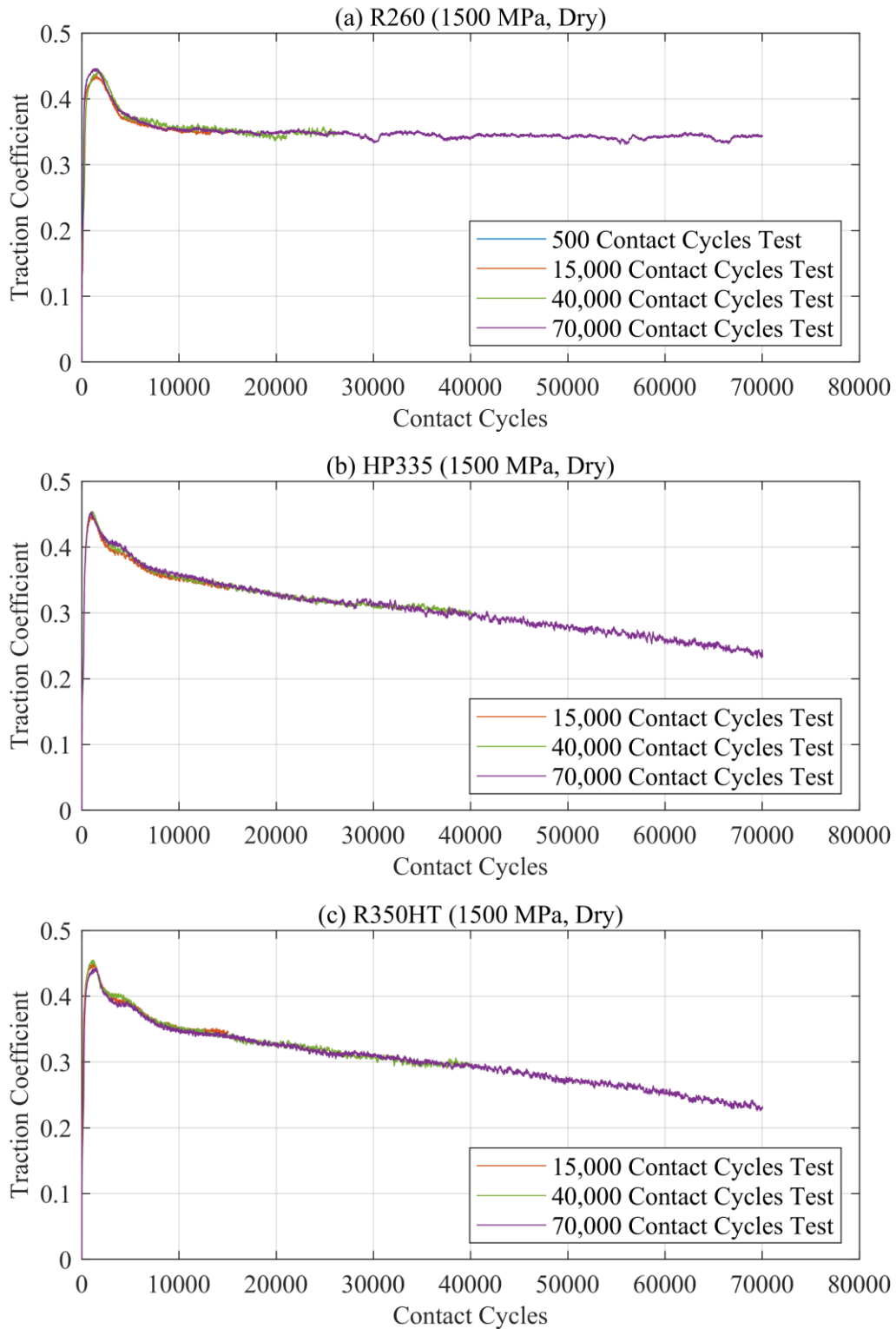


Figure A1.1: Coefficient of traction results collected during the uninterrupted twin-disc test from the SUROS2 twin-disc machine for R260 (1500 MPa, 1200 MPa, 900 MPa, 600 MPa), HP335 (1500 MPa), and R350HT (1500 MPa) for dry contact conditions.

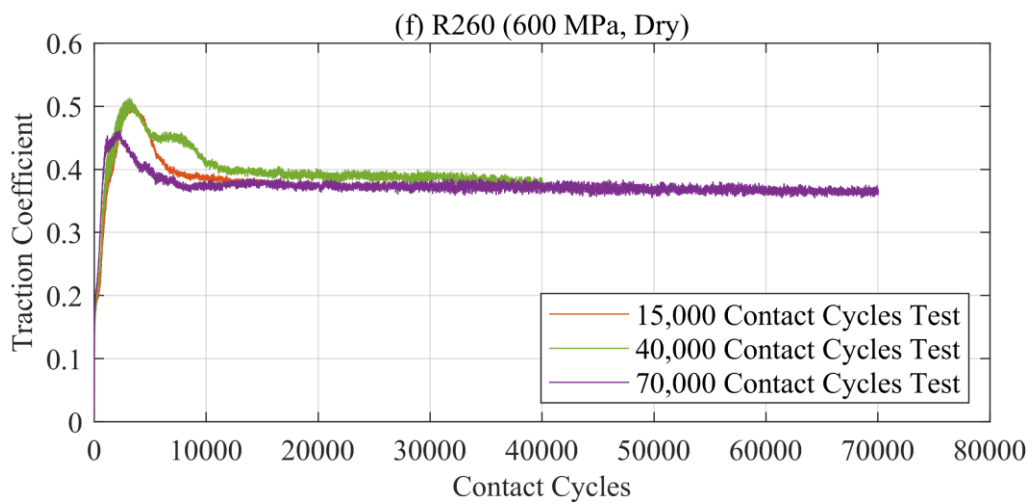
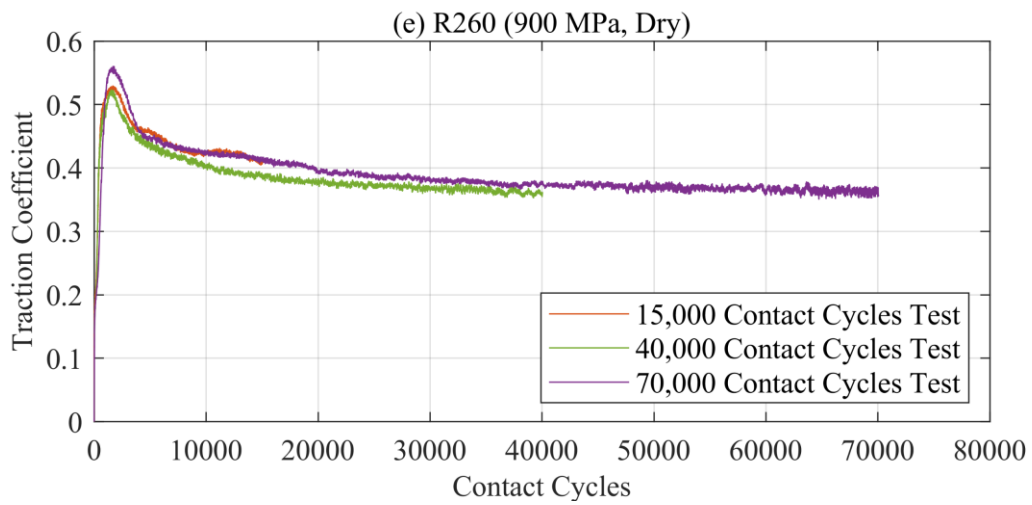
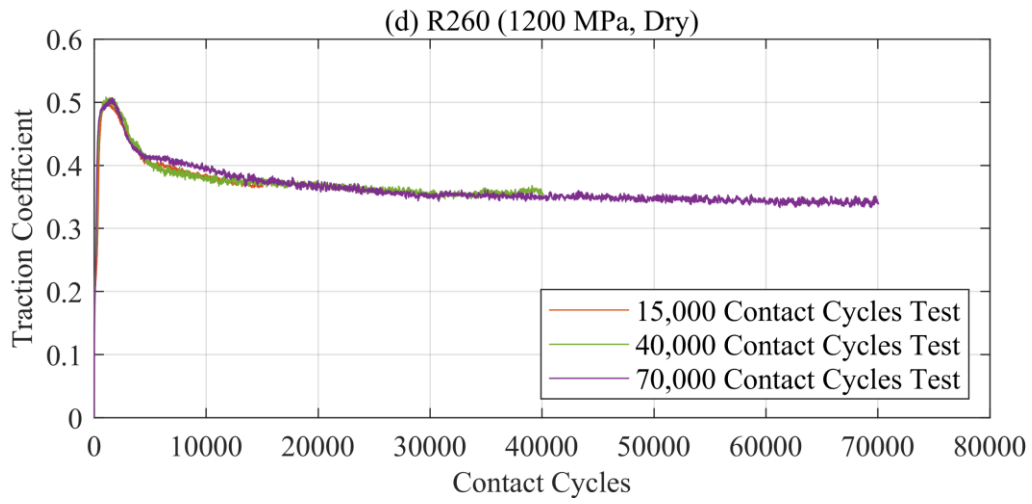


Figure A1.1: Continued.

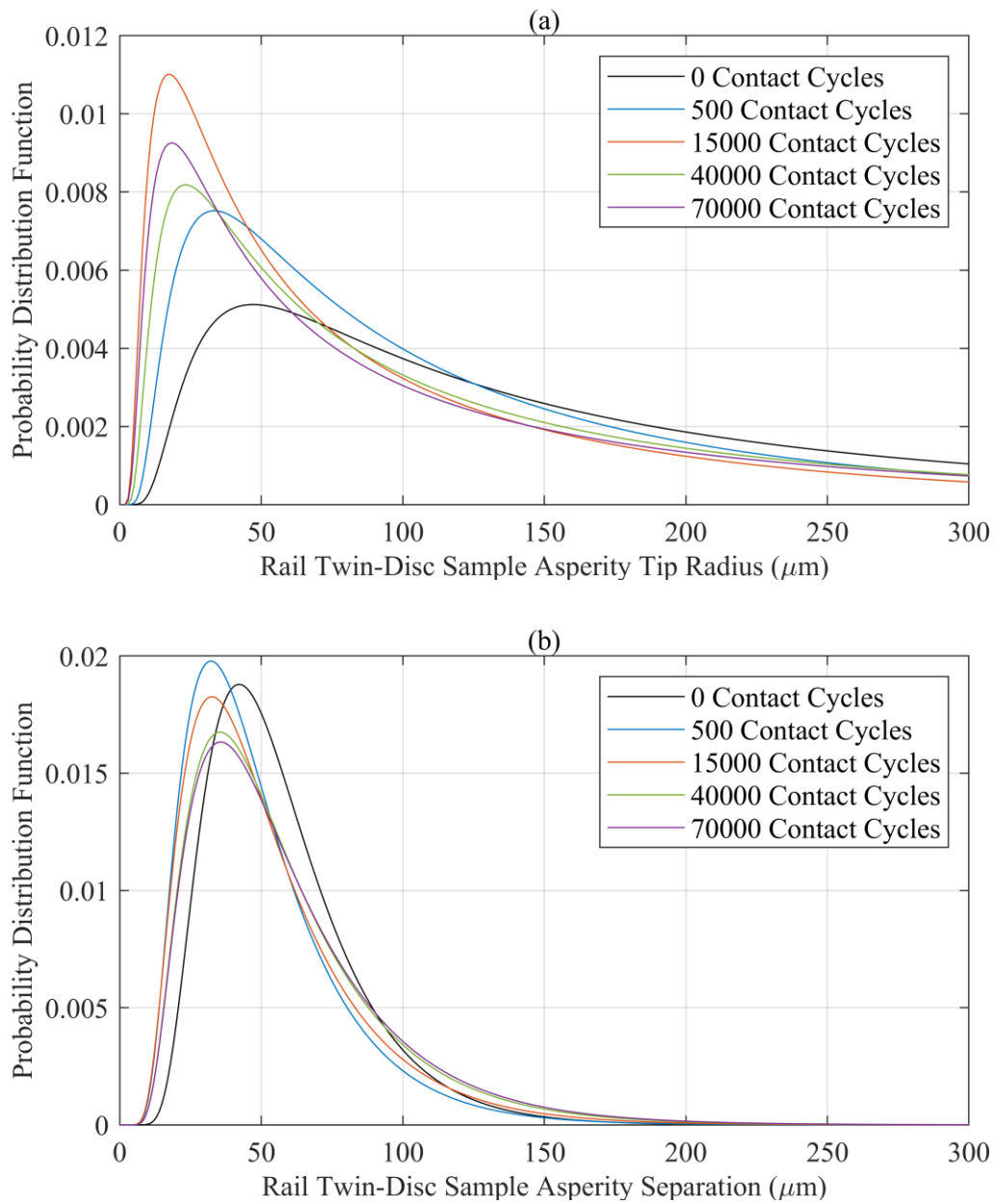


Figure A1.2: Comparison of the Birnbaum-Saunders distributions fitted to the (a, c) asperity tip radius and (b, d) asperity separation results from the (a, b) rail and (c, d) wheel twin-disc sample from the R260 and R8T uninterrupted twin-disc test conducted under 1500 MPa, dry contact conditions.

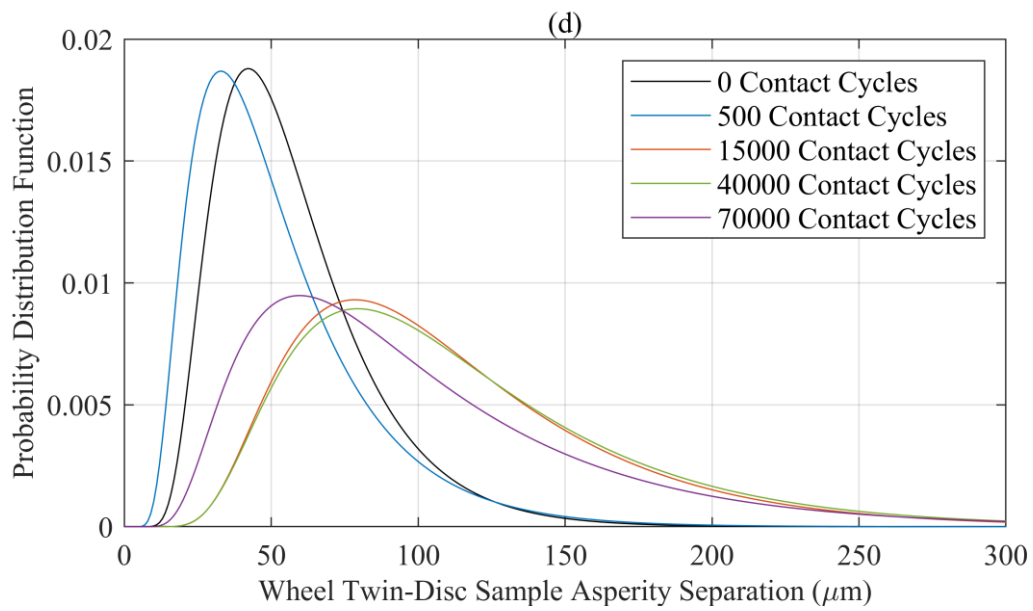
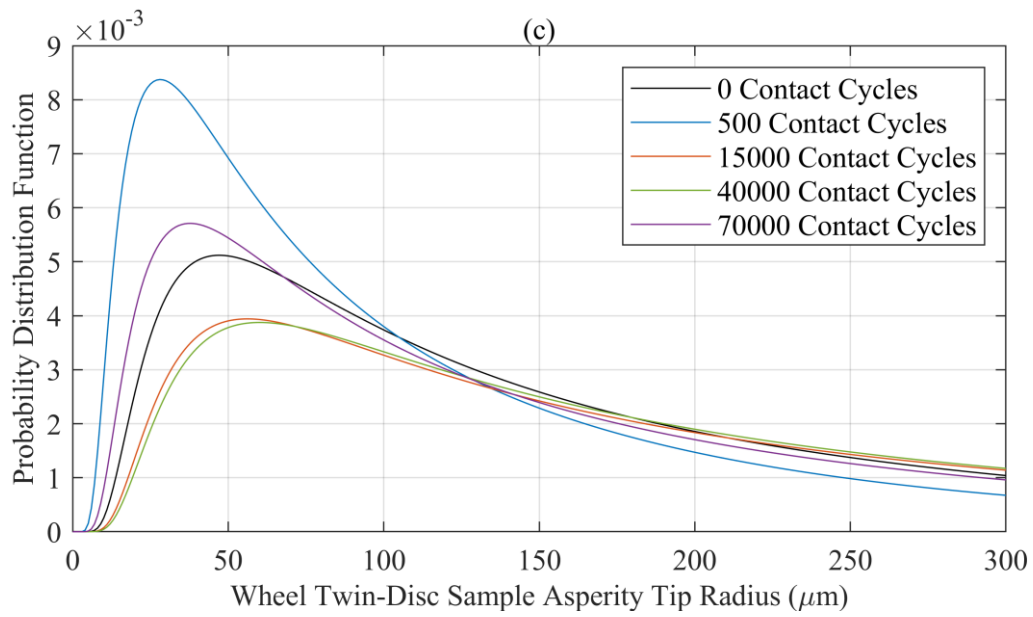


Figure A1.2: Continued.

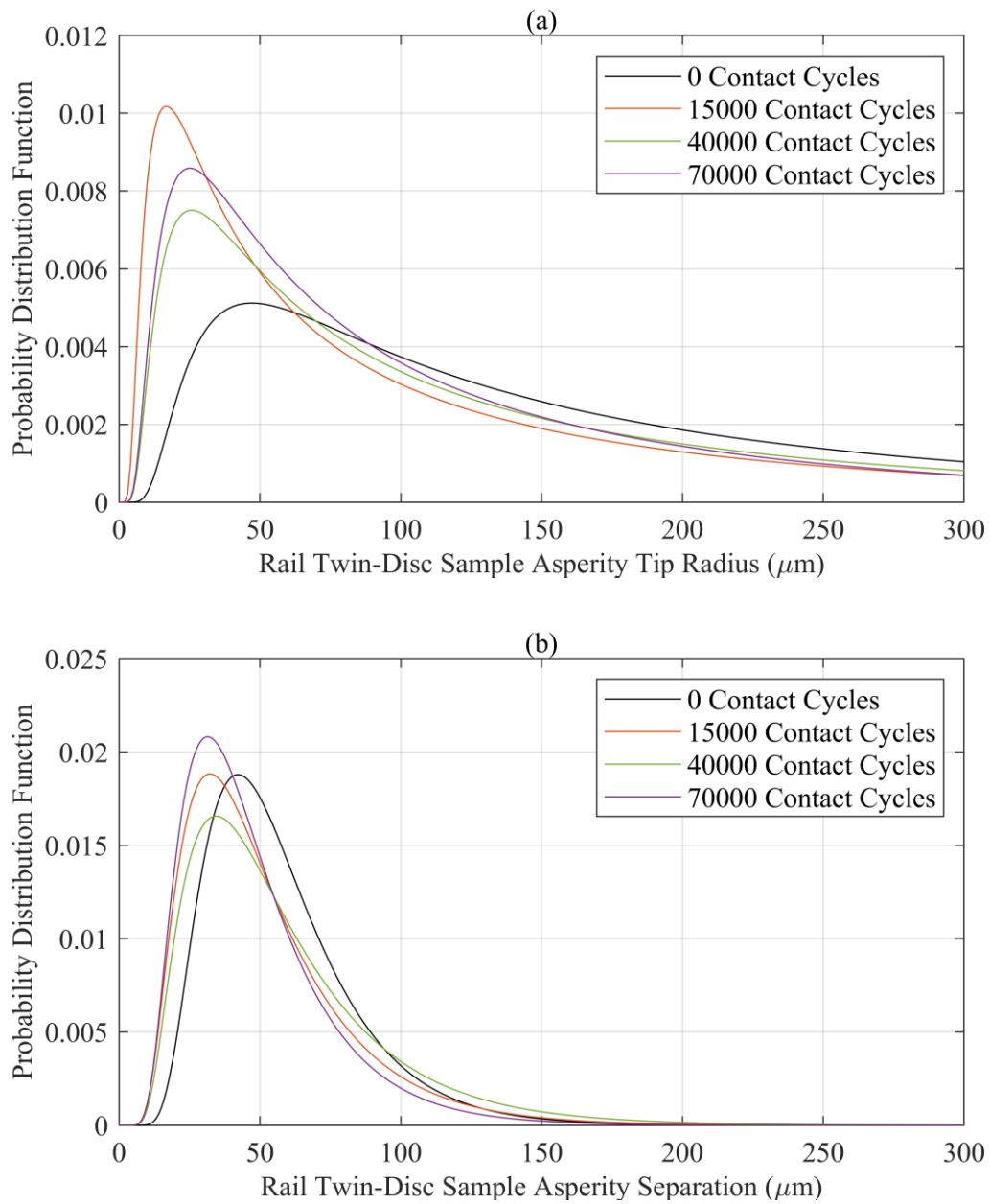


Figure A1.3: Comparison of the Birnbaum-Saunders distributions fitted to the (a, c) asperity tip radius and (b, d) asperity separation results from the (a, b) rail and (c, d) wheel twin-disc sample from the HP335 and R8T uninterrupted twin-disc test conducted under 1500 MPa, dry contact conditions.

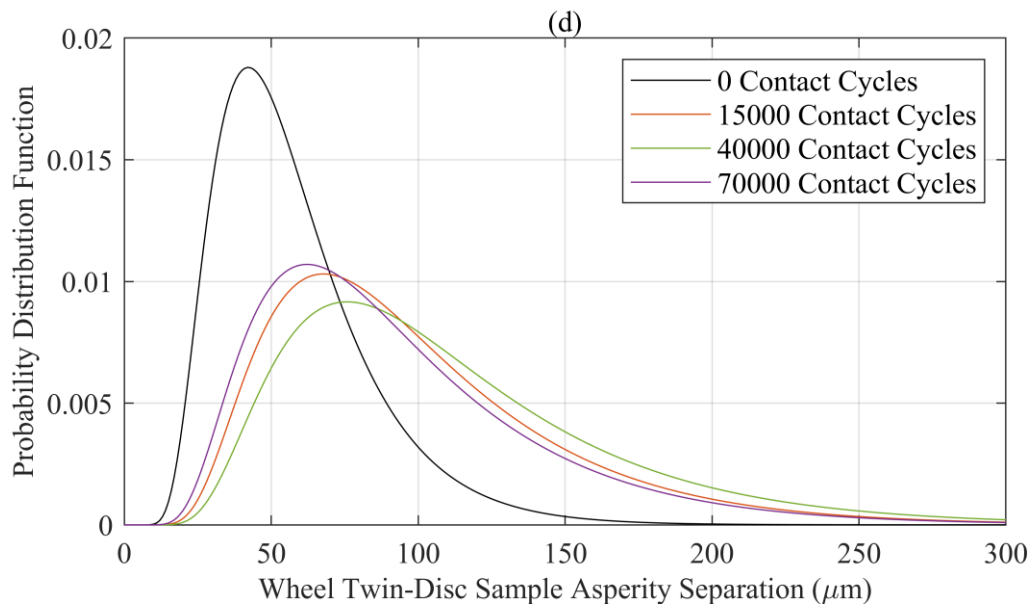
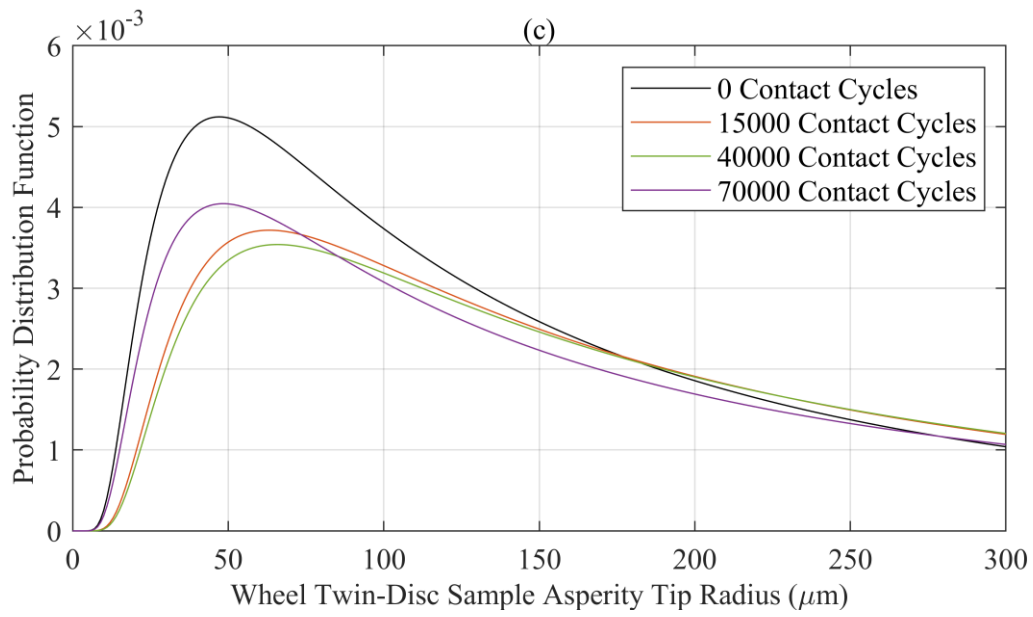


Figure A1.3: Continued.

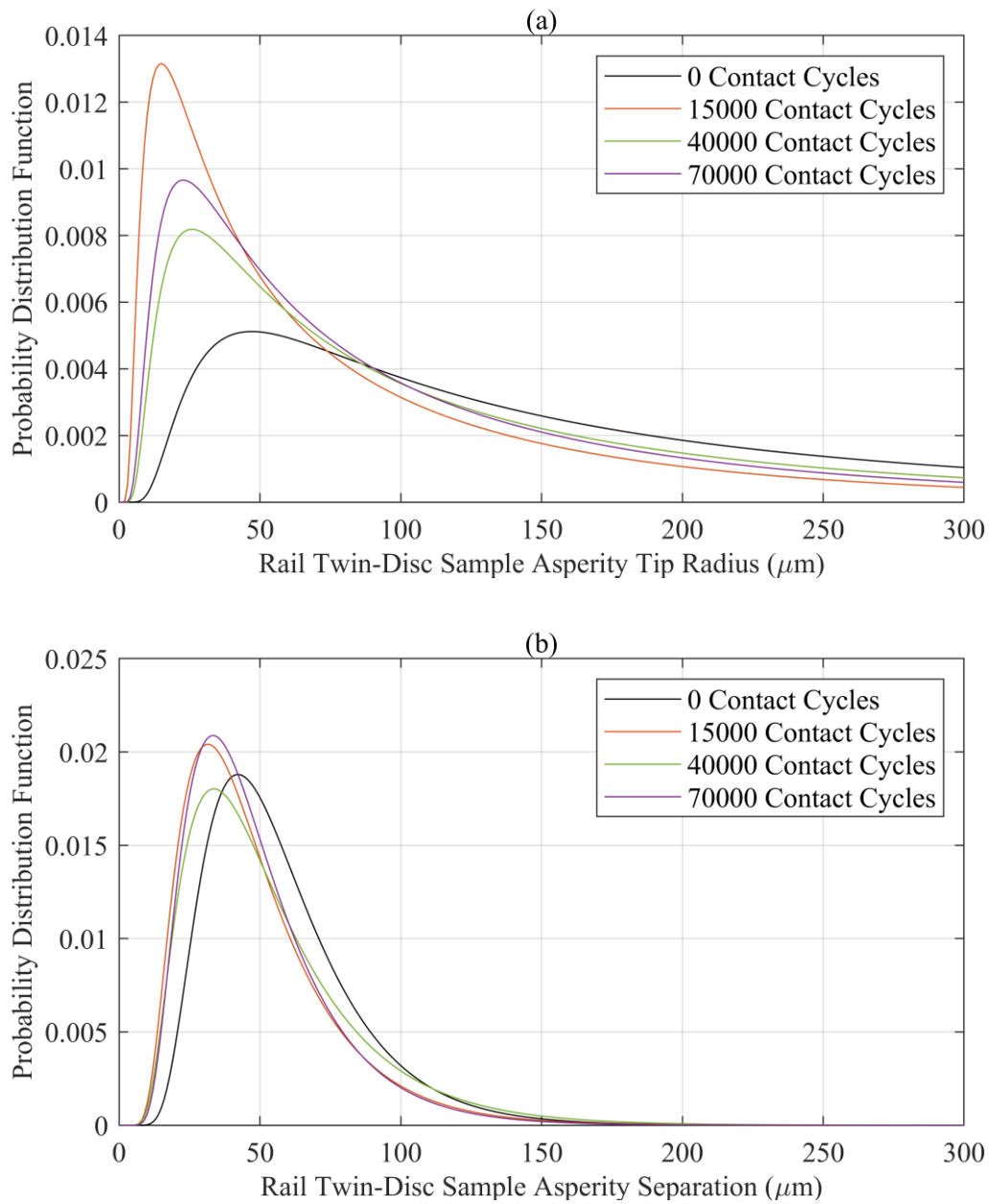


Figure A1.4: Comparison of the Birnbaum-Saunders distributions fitted to the (a, c) asperity tip radius and (b, d) asperity separation results from the (a, b) rail and (c, d) wheel twin-disc sample from the R350HT and R8T uninterrupted twin-disc test conducted under 1500 MPa, dry contact conditions.

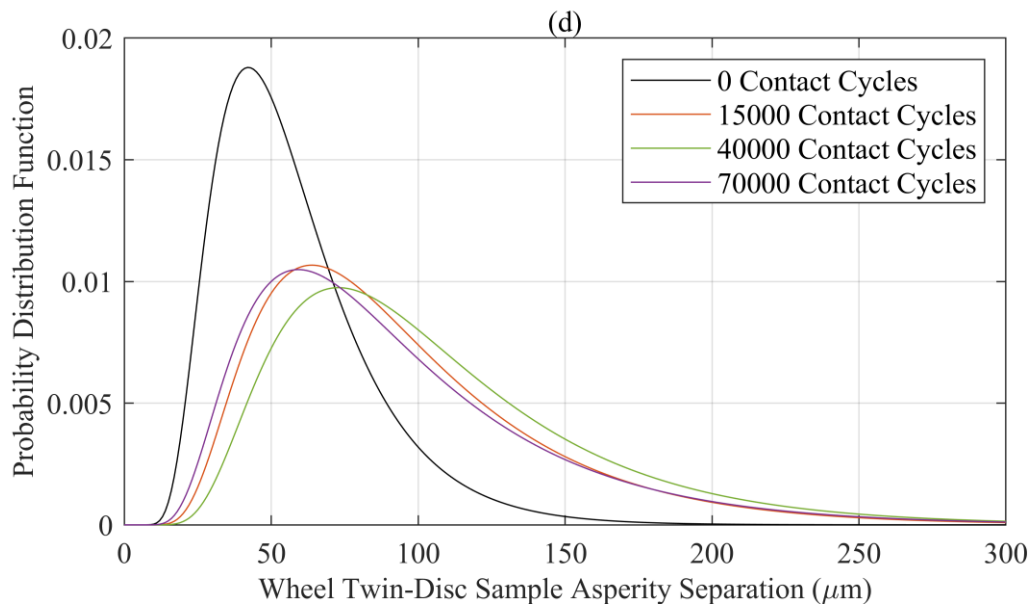
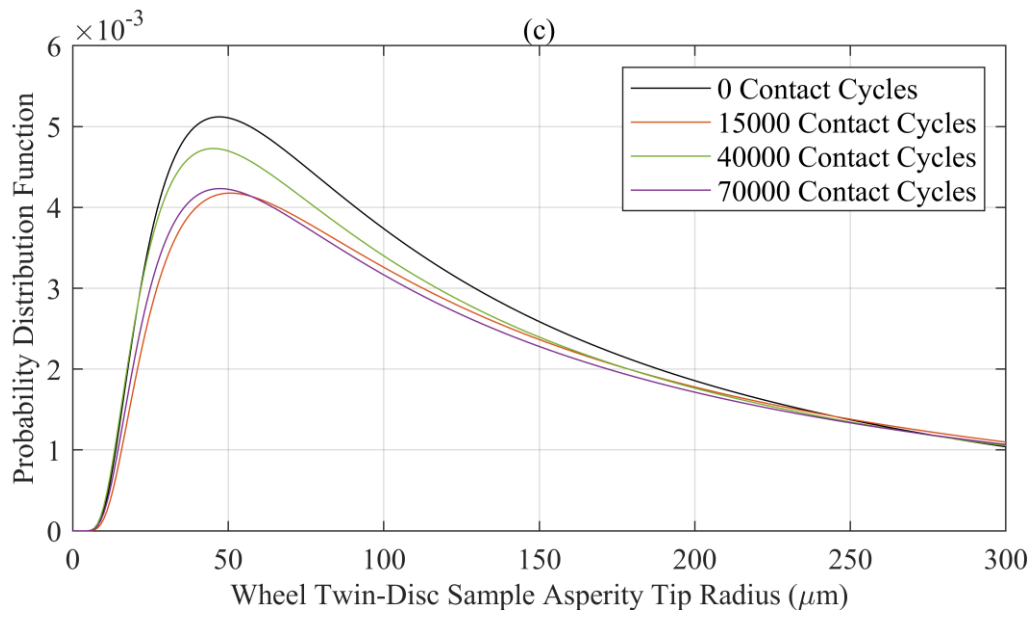


Figure A1.4: Continued.

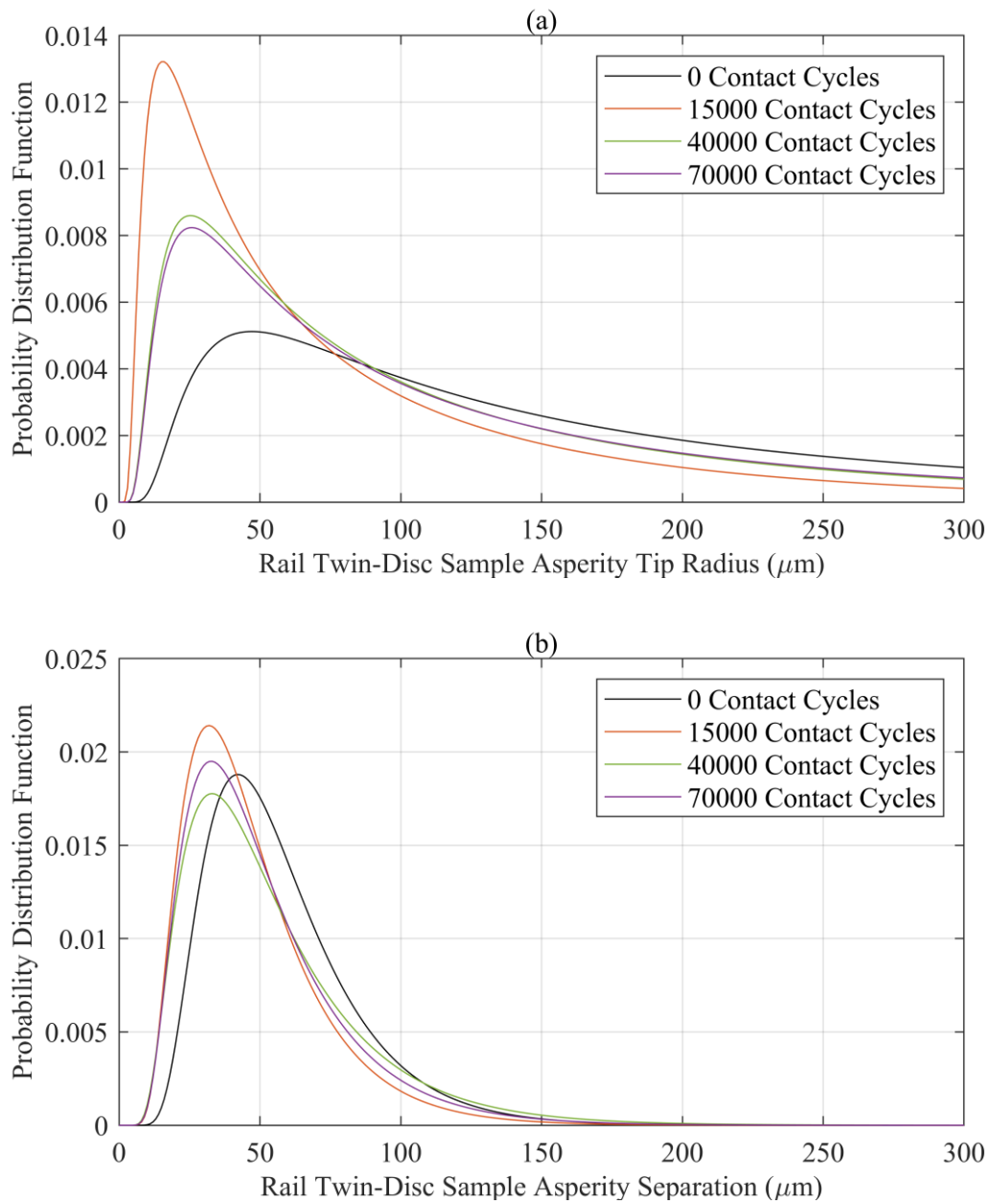


Figure A1.5: Comparison of the Birnbaum-Saunders distributions fitted to the (a, c) asperity tip radius and (b, d) asperity separation results from the (a, b) rail and (c, d) wheel twin-disc sample from the R260 and R8T uninterrupted twin-disc test conducted under 1200 MPa, dry contact conditions.

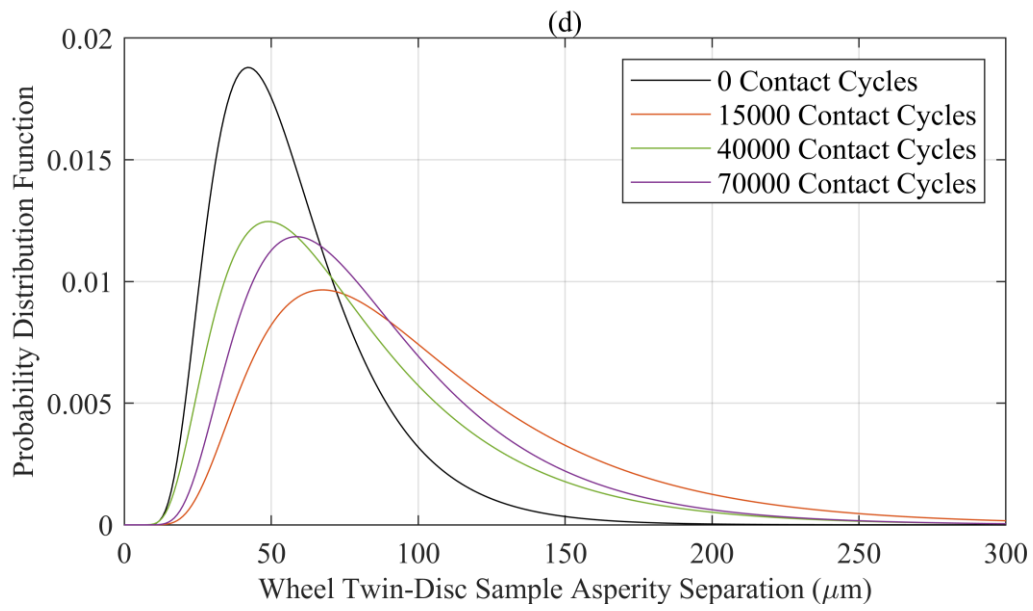
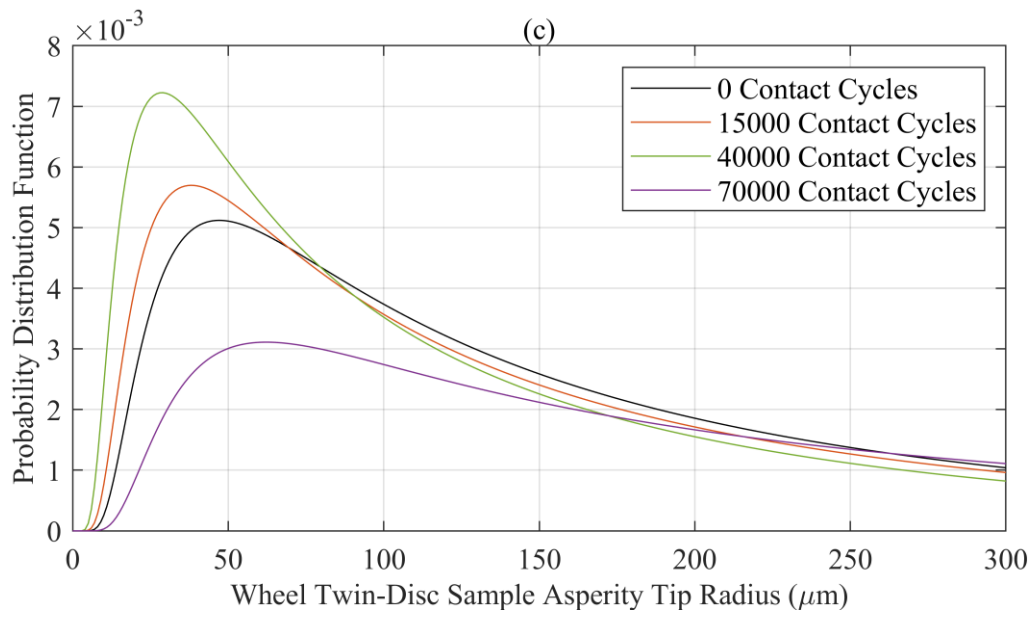


Figure A1.5: Continued.

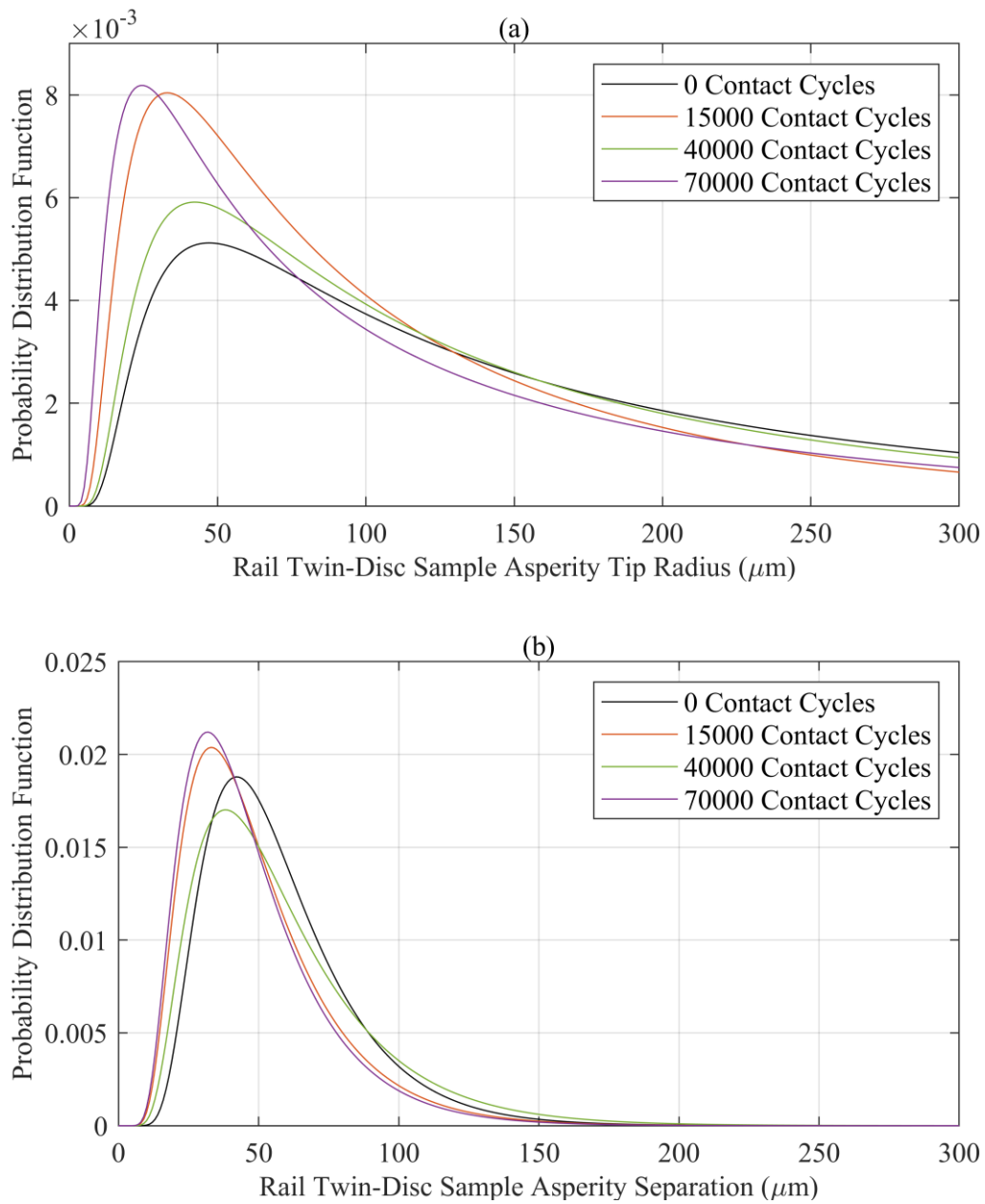


Figure A1.6: Comparison of the Birnbaum-Saunders distributions fitted to the (a, c) asperity tip radius and (b, d) asperity separation results from the (a, b) rail and (c, d) wheel twin-disc sample from the R260 and R8T uninterrupted twin-disc test conducted under 900 MPa, dry contact conditions.

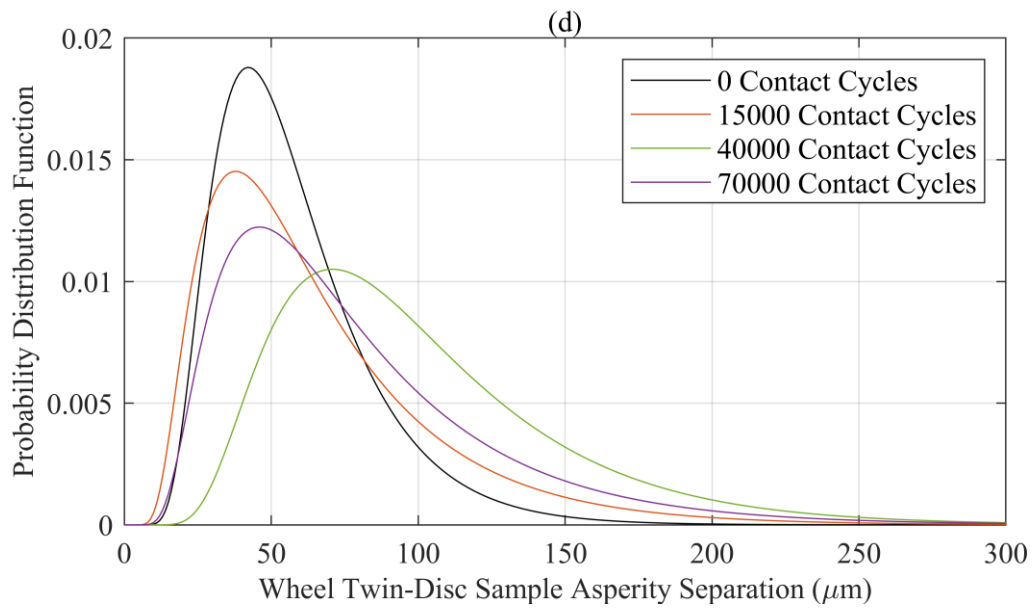
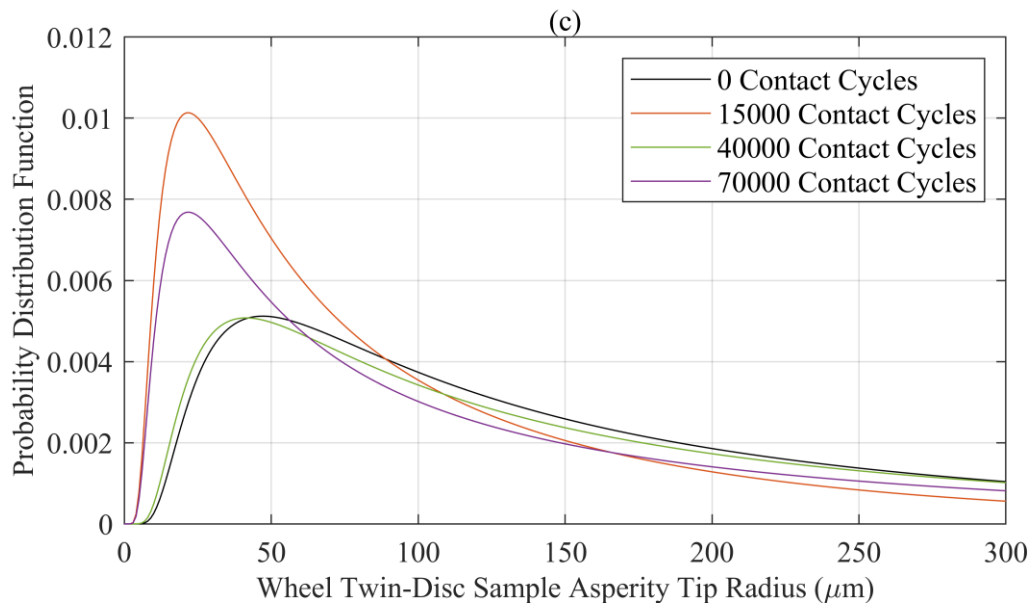


Figure A1.6: Continued.

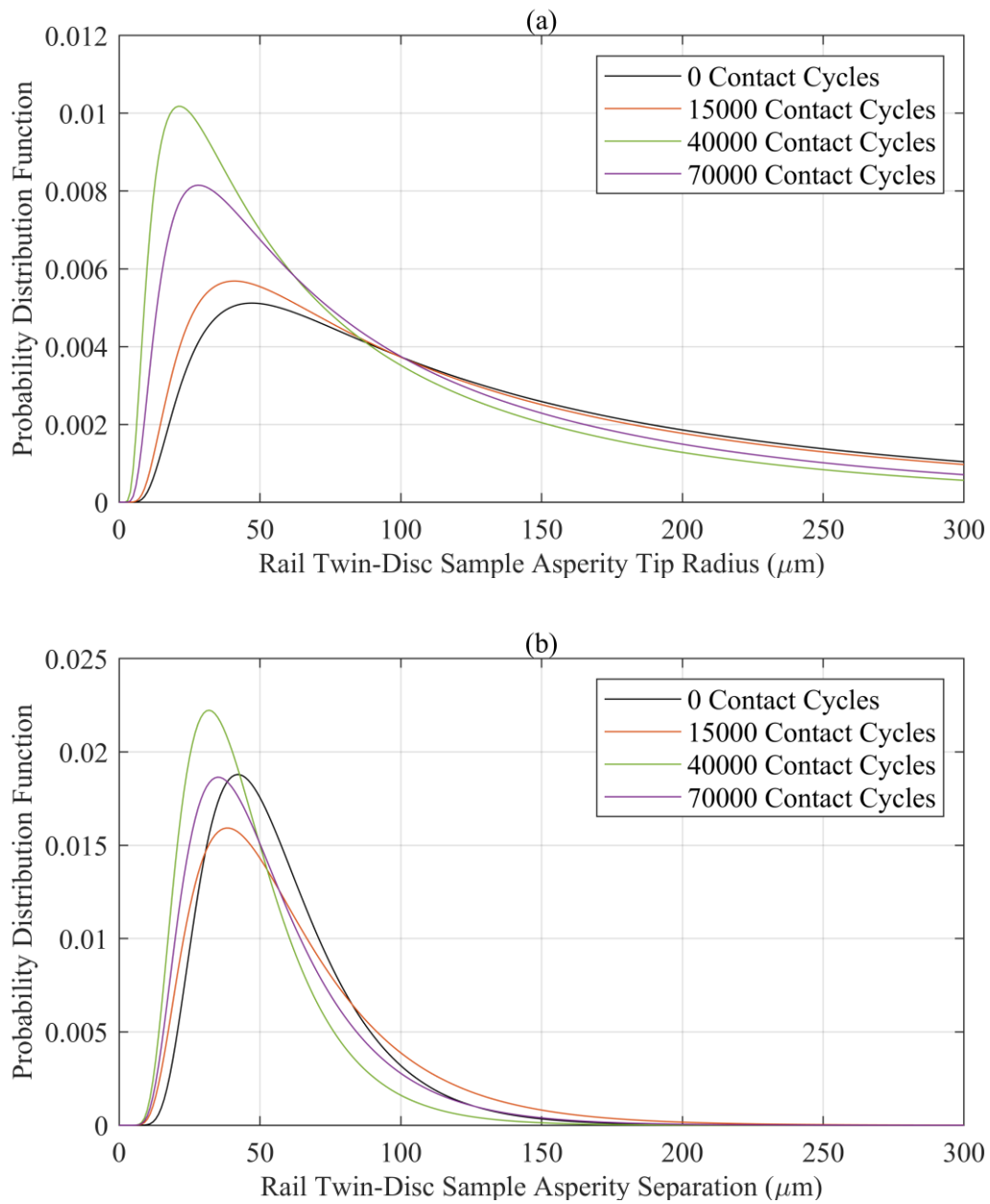


Figure A1.7: Comparison of the Birnbaum-Saunders distributions fitted to the (a, c) asperity tip radius and (b, d) asperity separation results from the (a, b) rail and (c, d) wheel twin-disc sample from the R260 and R8T uninterrupted twin-disc test conducted under 600 MPa, dry contact conditions.

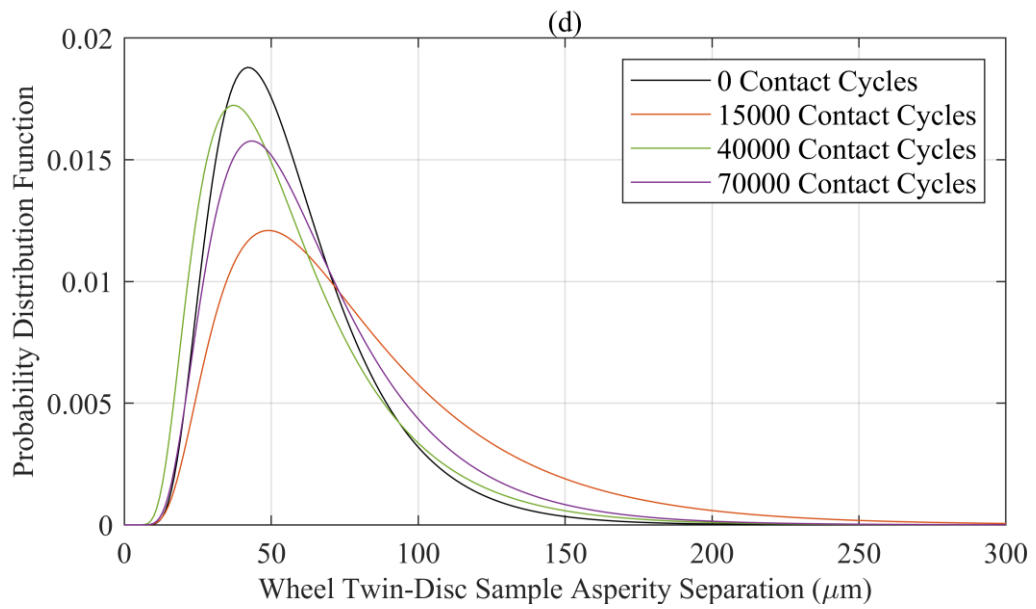
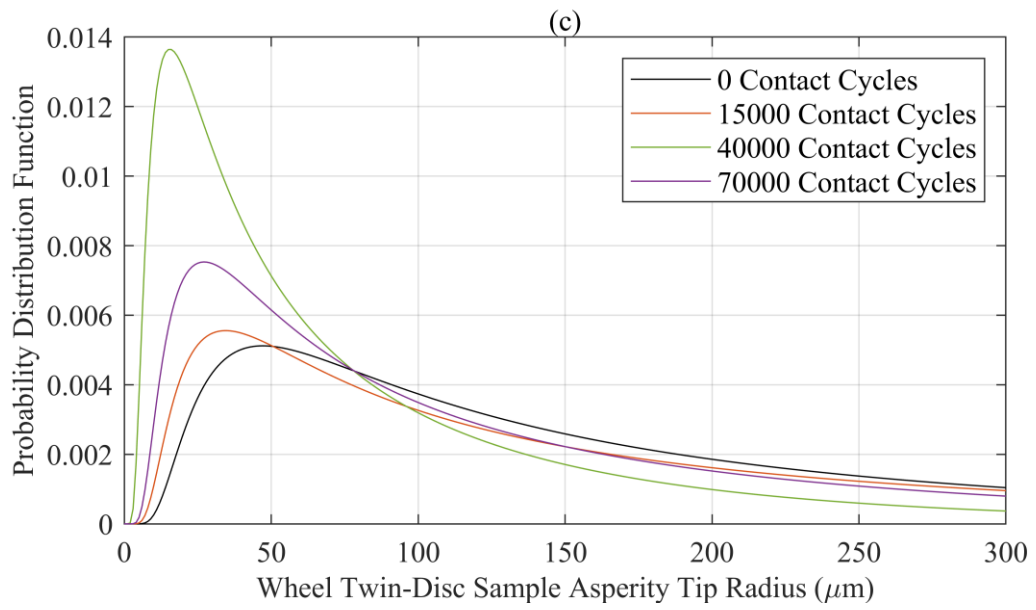


Figure A1.7: Continued.

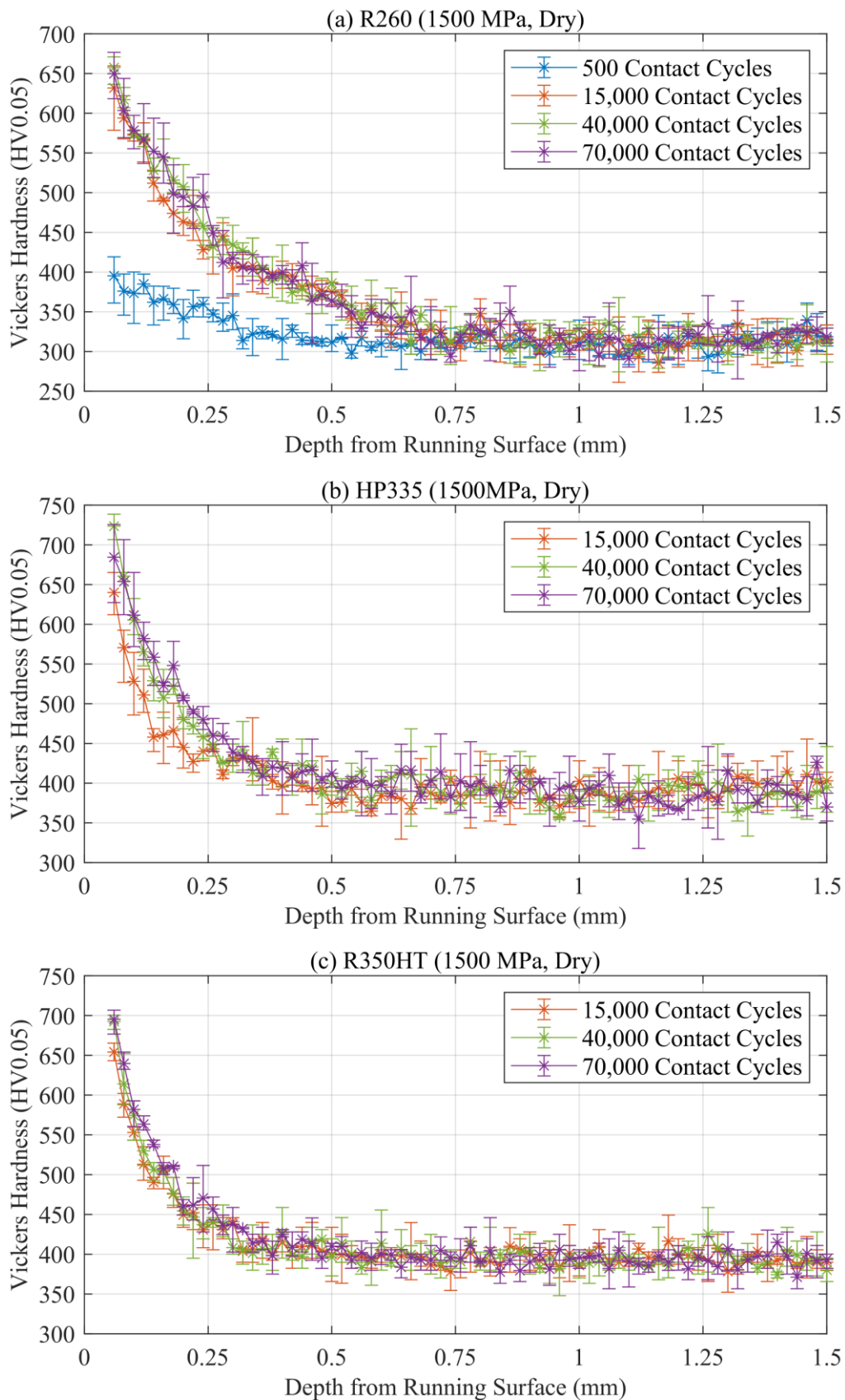


Figure A1.8: Microhardness against depth below surface results obtained from the uninterrupted twin-disc samples for R260 (1500 MPa, 1200 MPa, 900 MPa, 600 MPa), HP335 (1500 MPa), and R350HT (1500 MPa) and dry contact conditions.

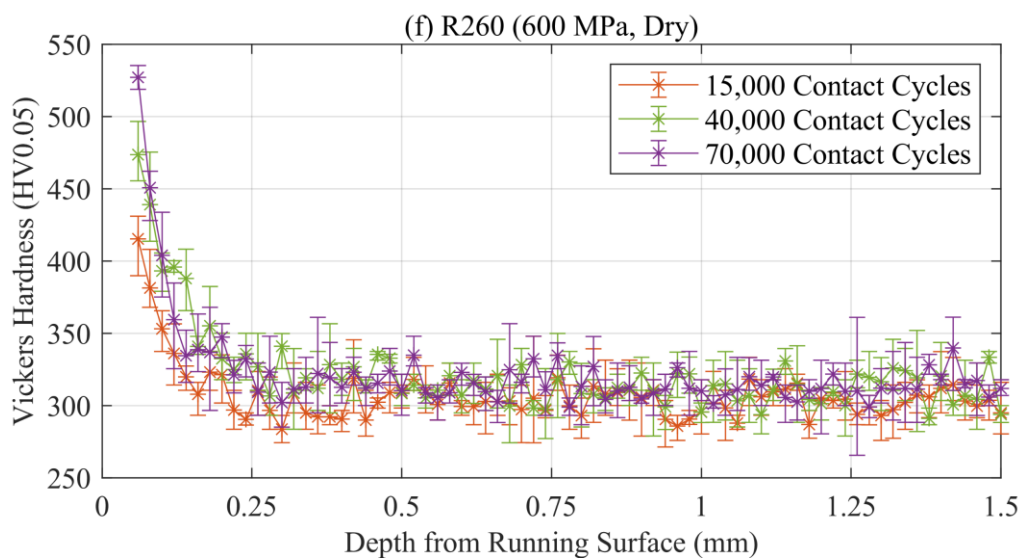
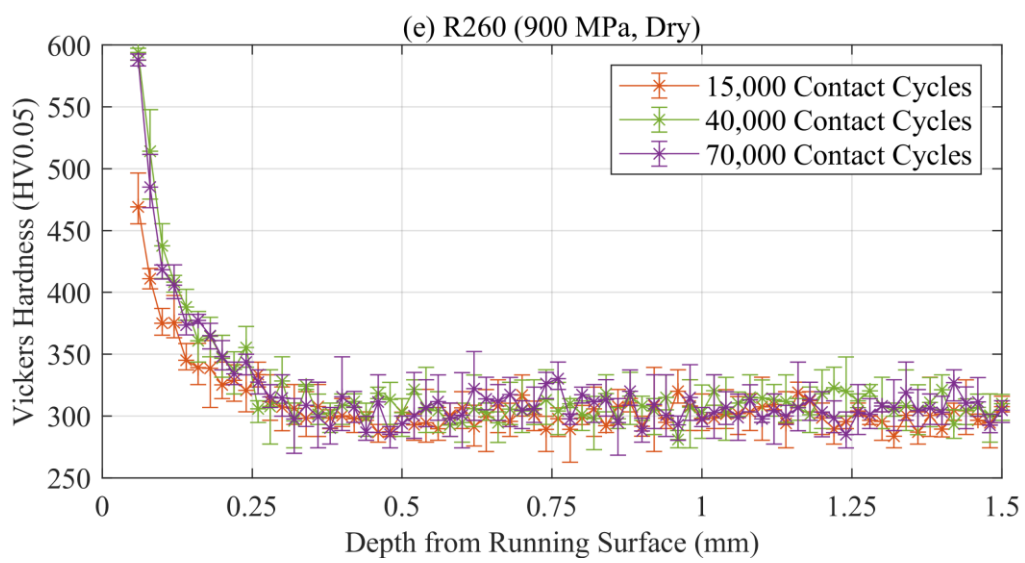
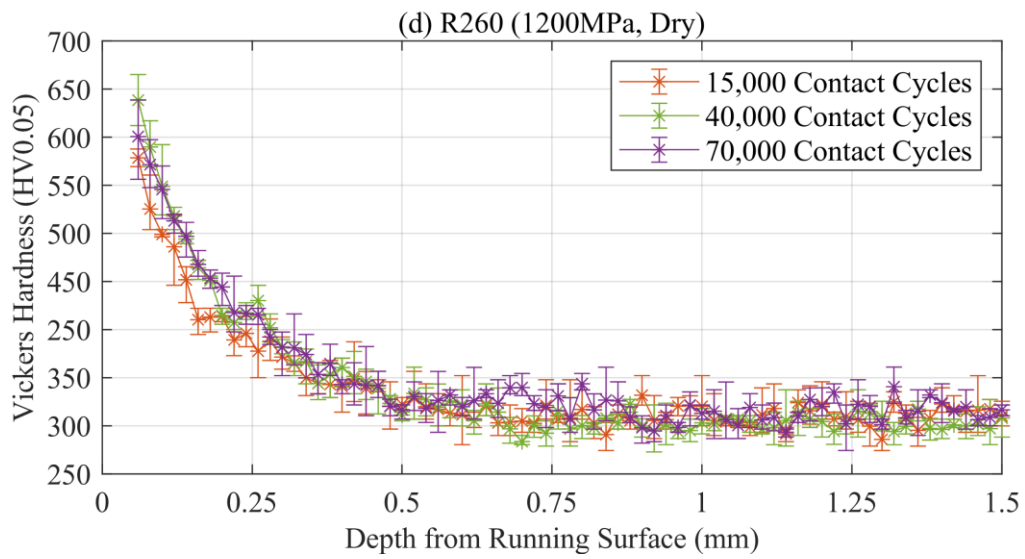
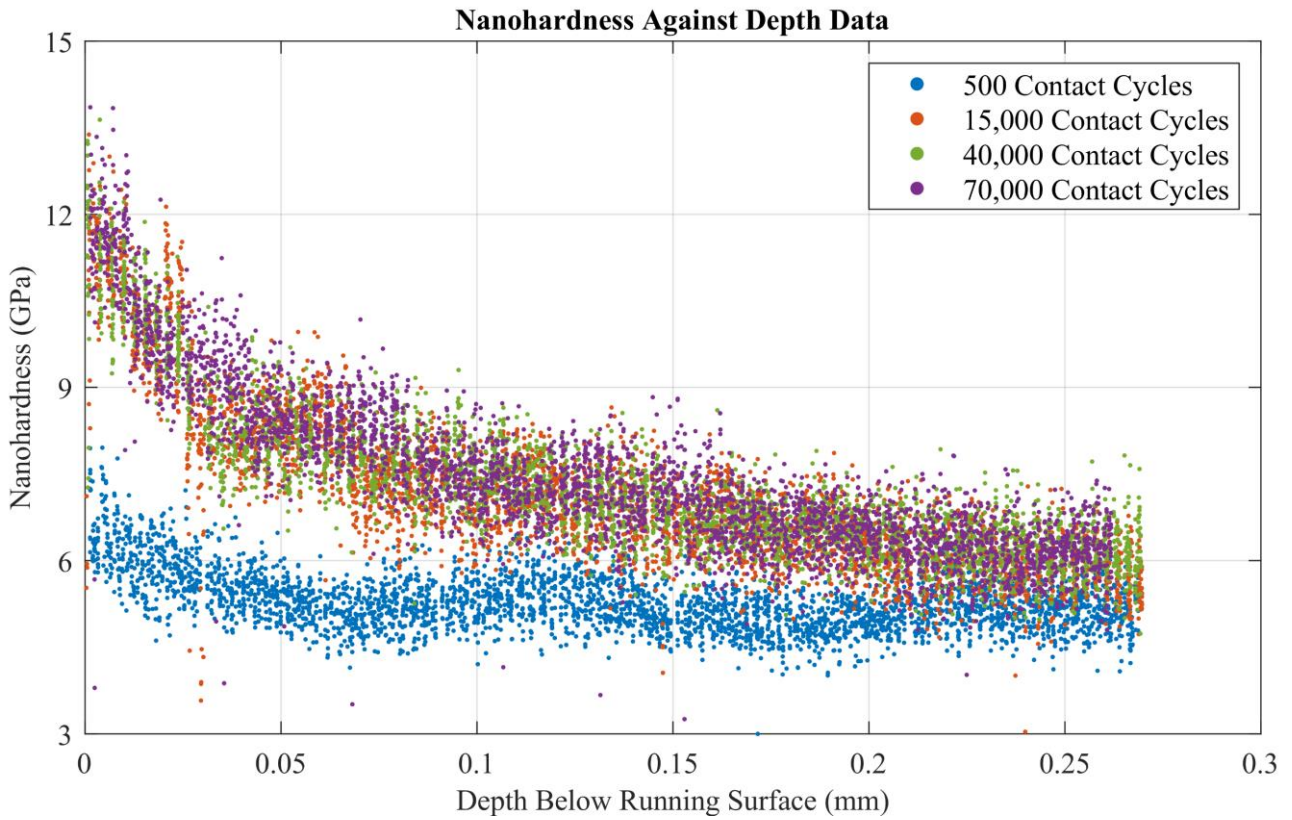


Figure A1.8: continued.

(a) R260 (1500 MPa, Dry)



Nanohardness Undeformed Bulk Data

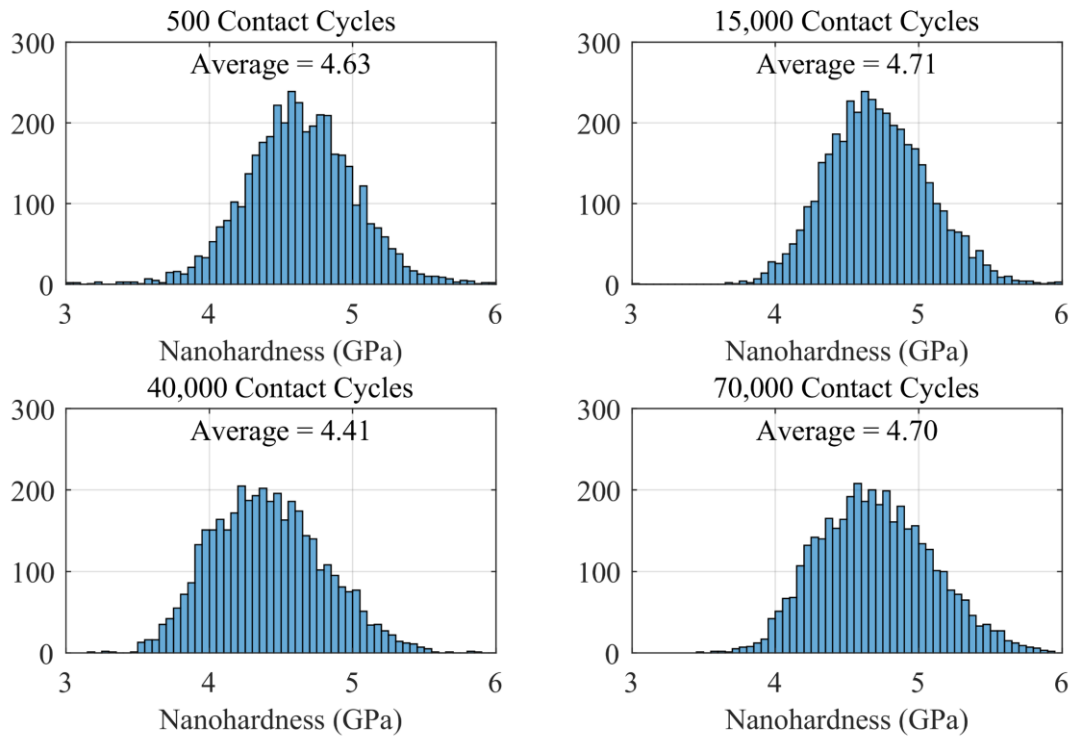
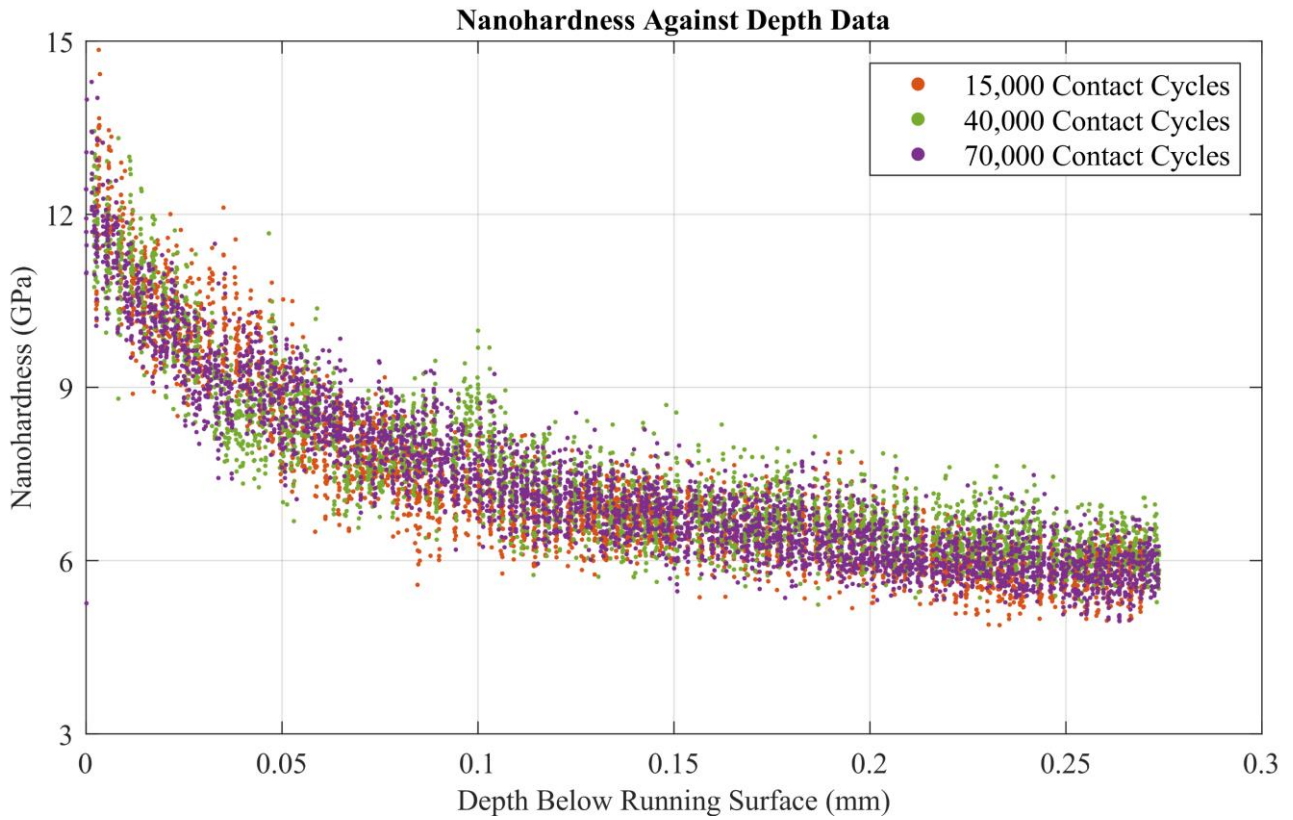


Figure A1.9: Nanohardness data collected from the uninterrupted twin-disc samples for R260 (1500 MPa, 1200 MPa, 900 MPa, 600 MPa), HP335 (1500 MPa), and R350HT (1500 MPa) and dry contact conditions.

(b) HP335 (1500 MPa, Dry)



Nanohardness Undeformed Bulk Data

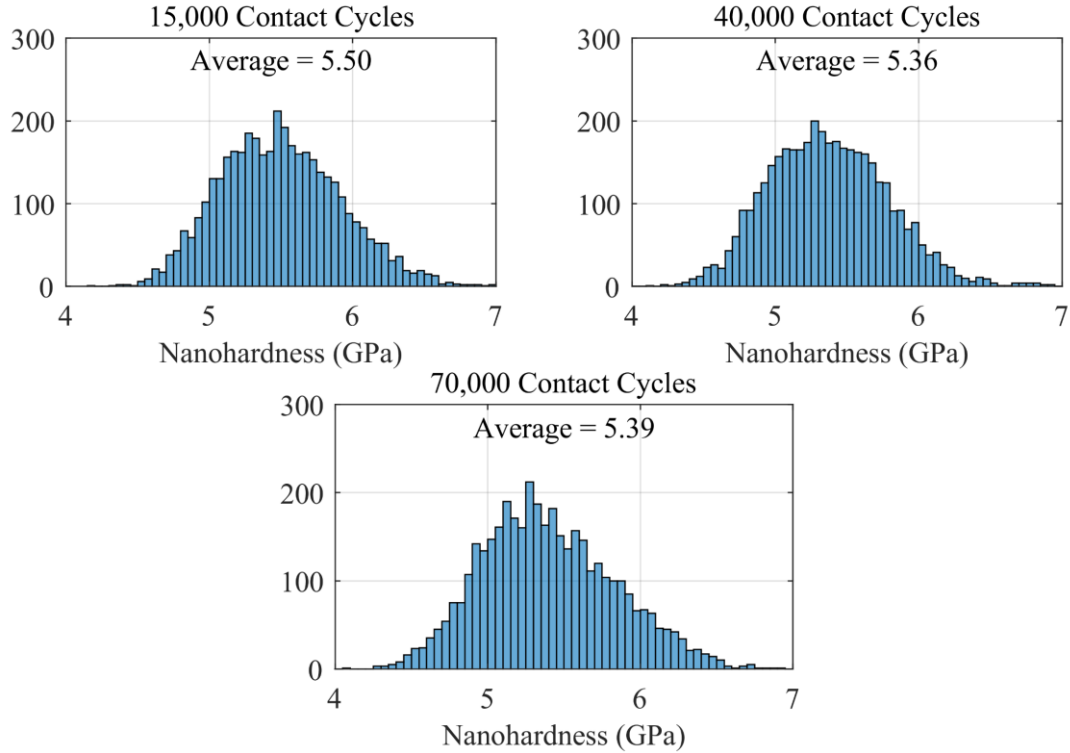
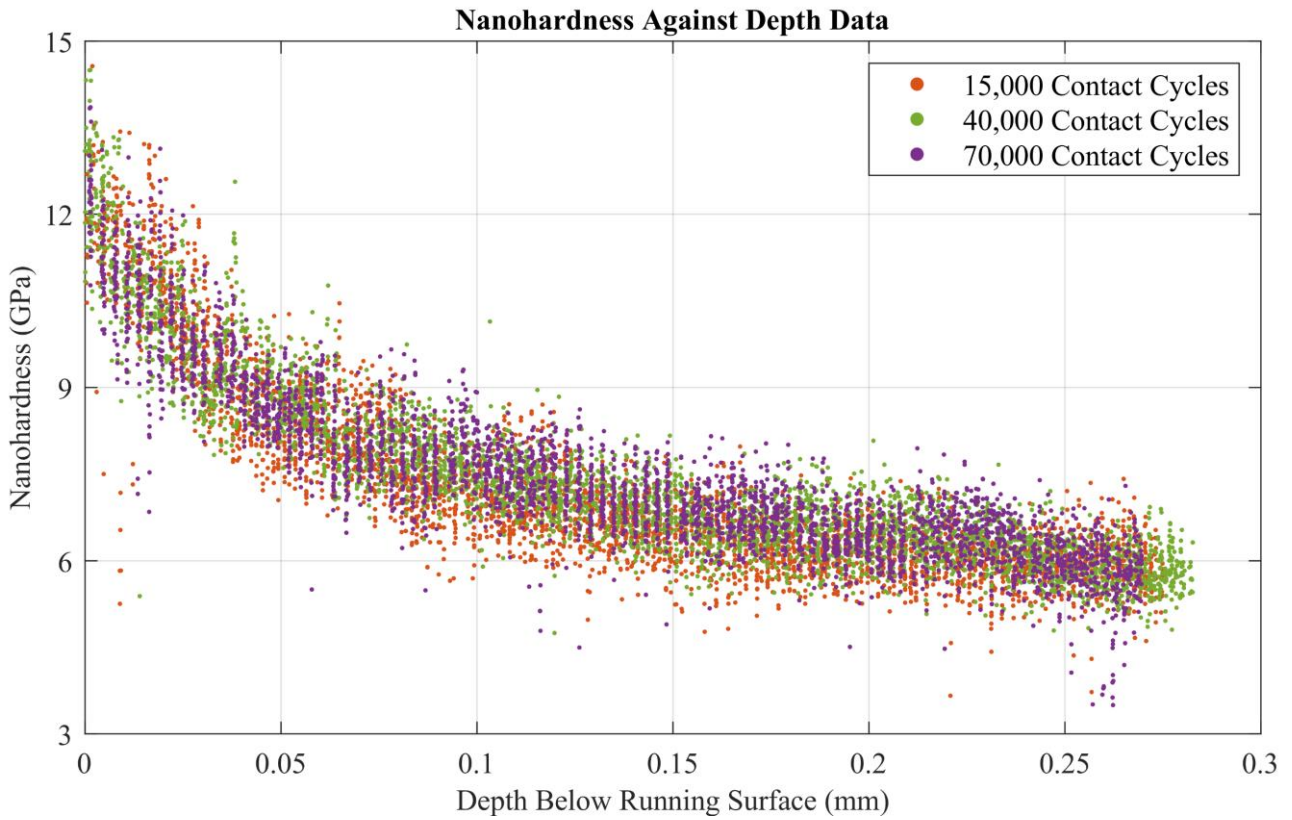


Figure A1.9: Continued.

(c) R350HT (1500 MPa, Dry)



Nanohardness Undeformed Bulk Data

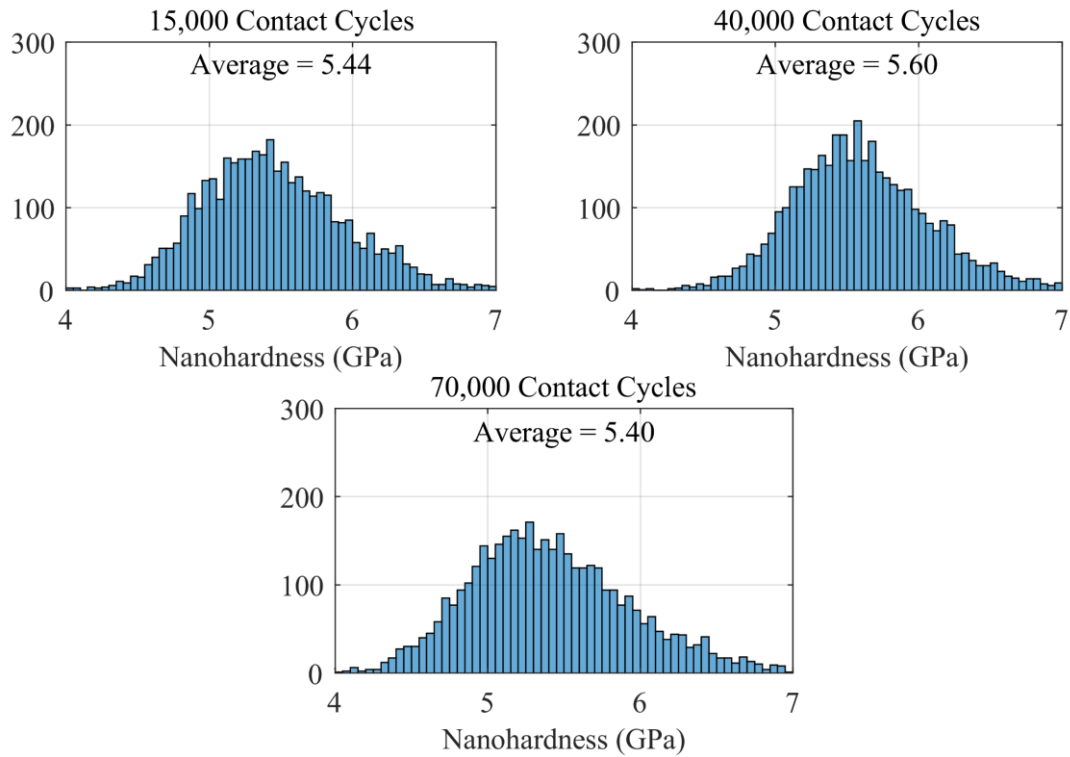
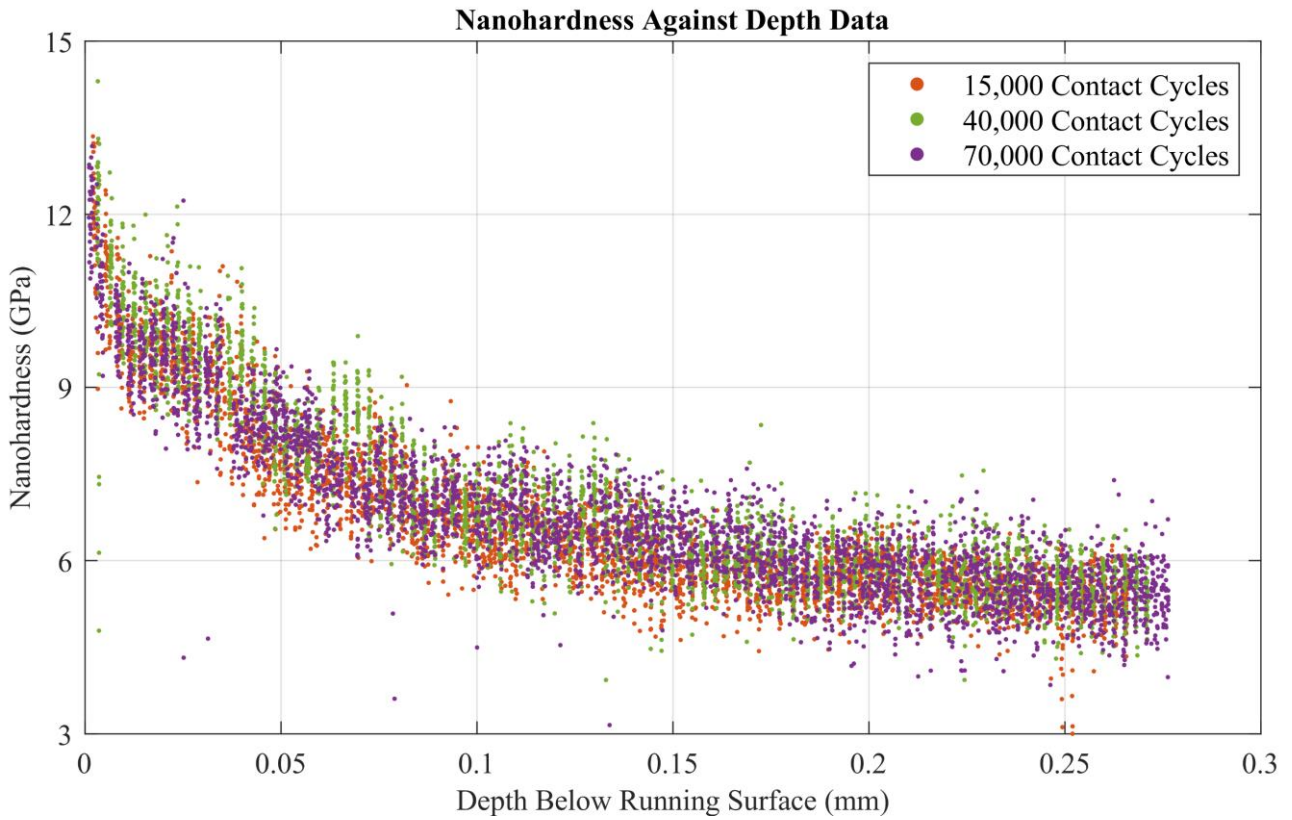


Figure A1.9: Continued.

(d) R260 (1200 MPa, Dry)



Nanohardness Undeformed Bulk Data

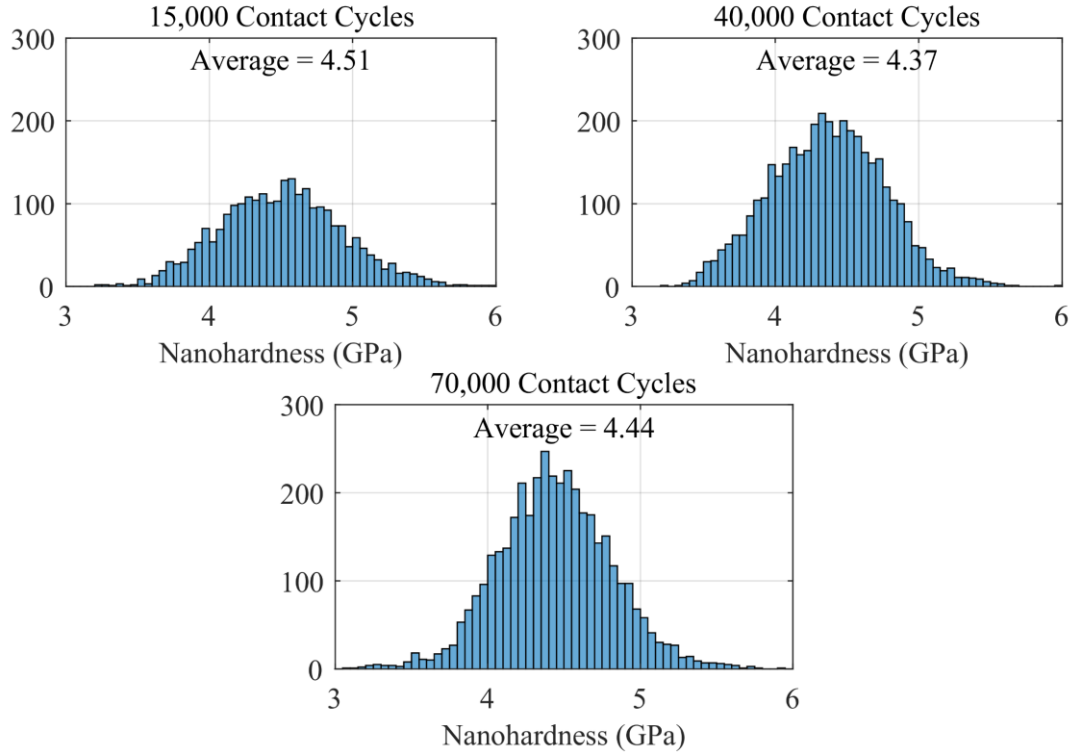


Figure A1.9: Continued.

(e) R260 (900 MPa, Dry)

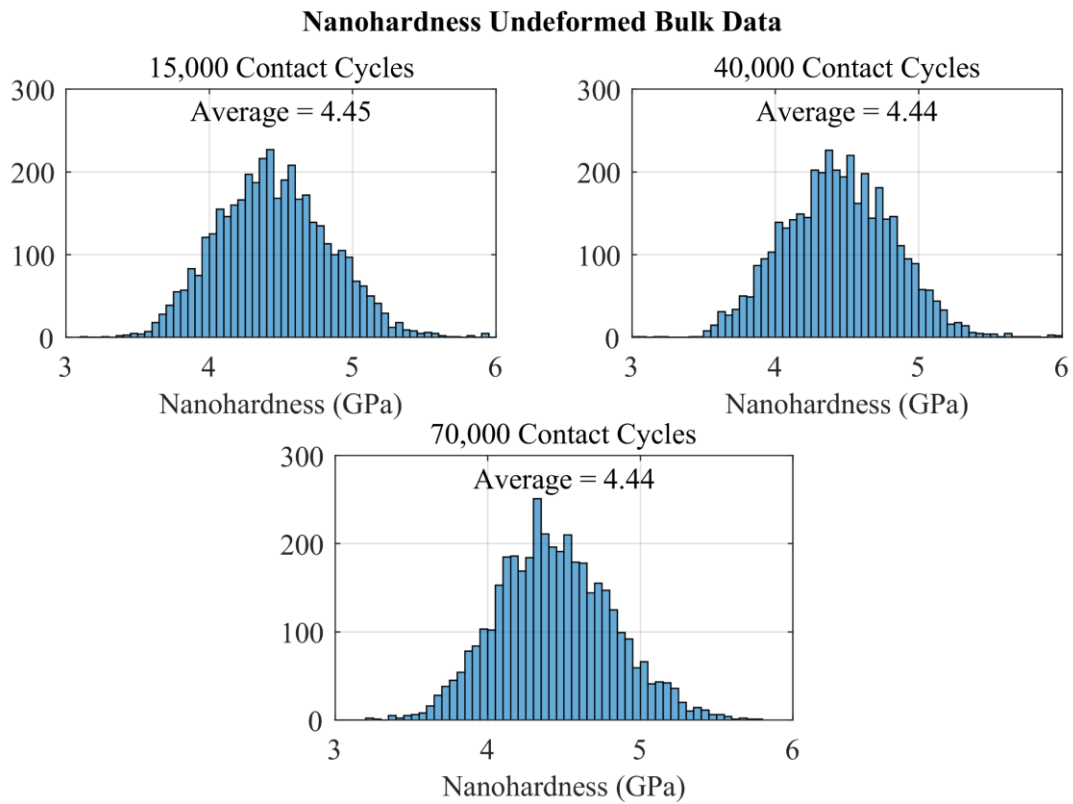
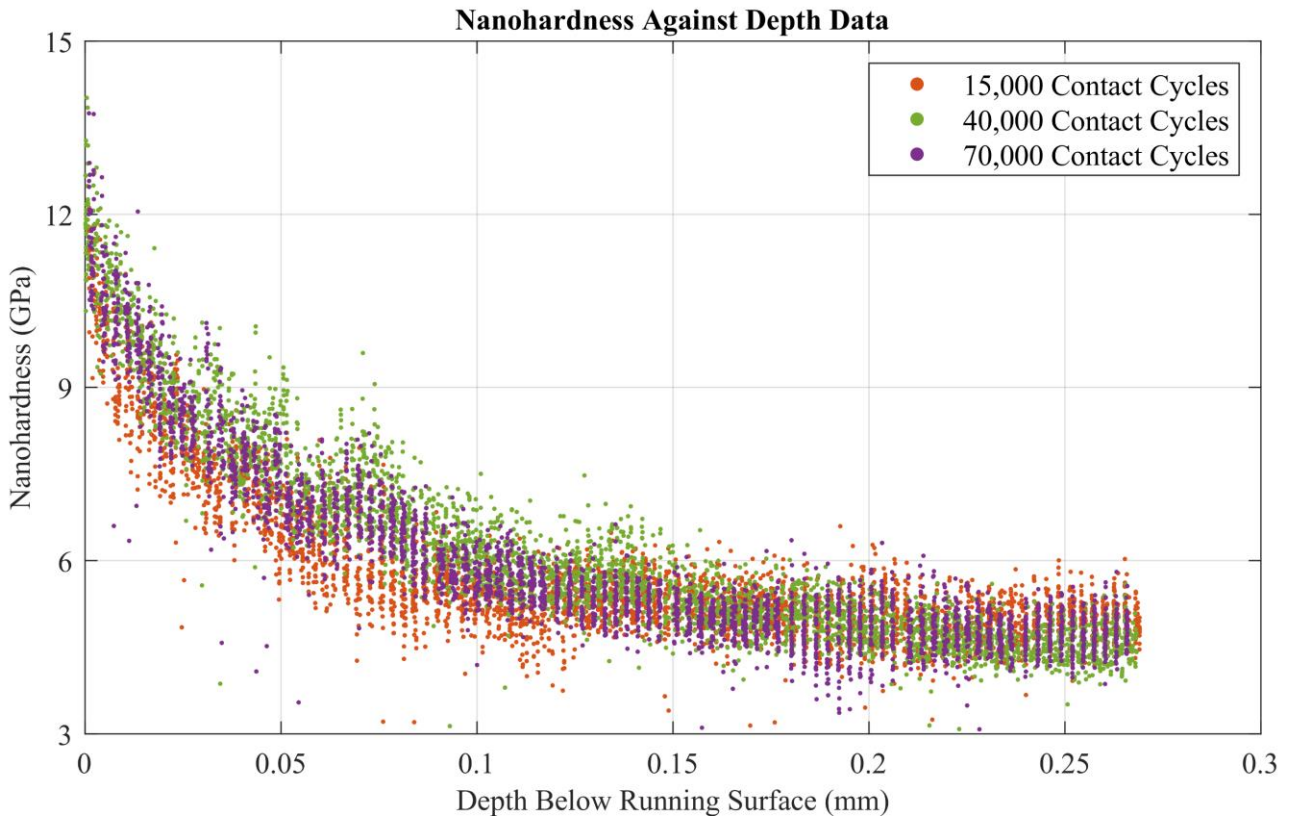
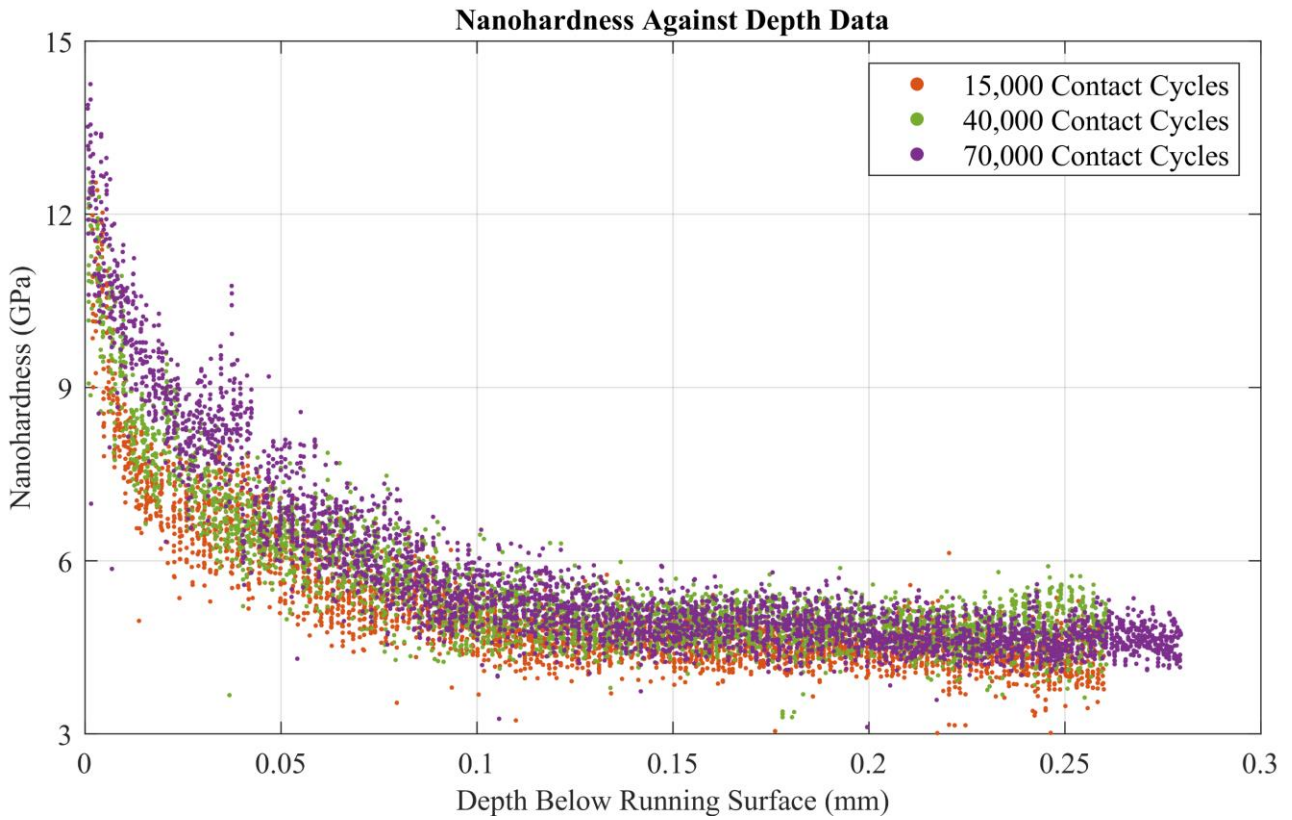


Figure A1.9: Continued.

(f) R260 (600 MPa, Dry)



Nanohardness Undeformed Bulk Data

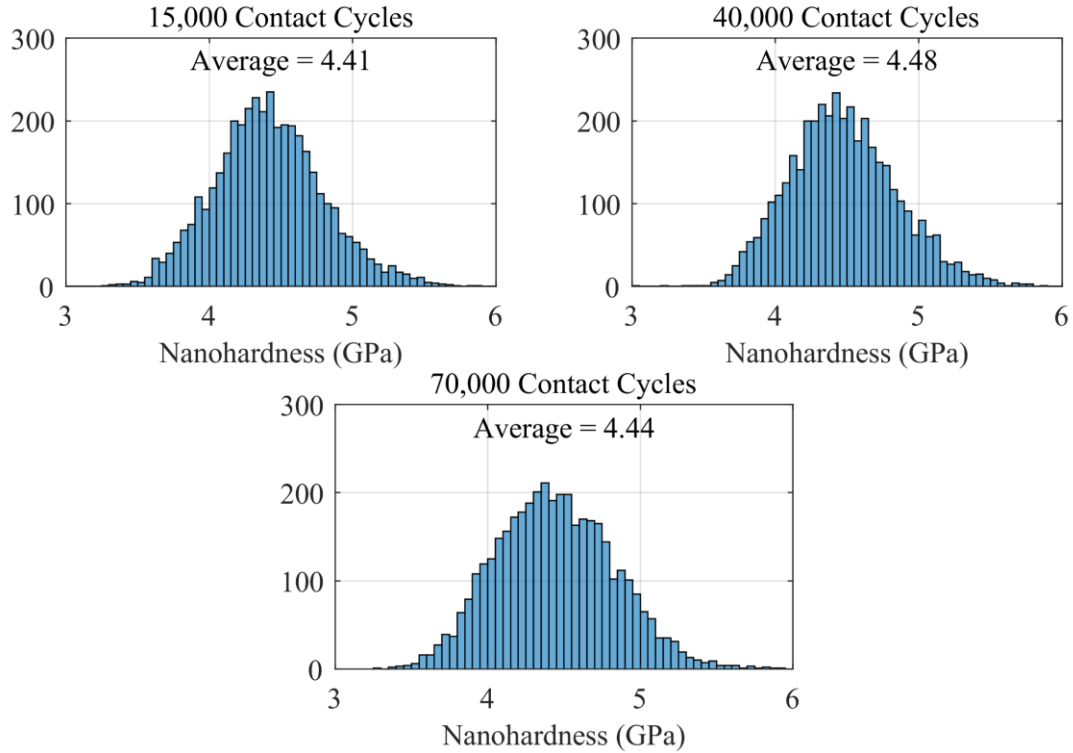


Figure A1.9: Continued.

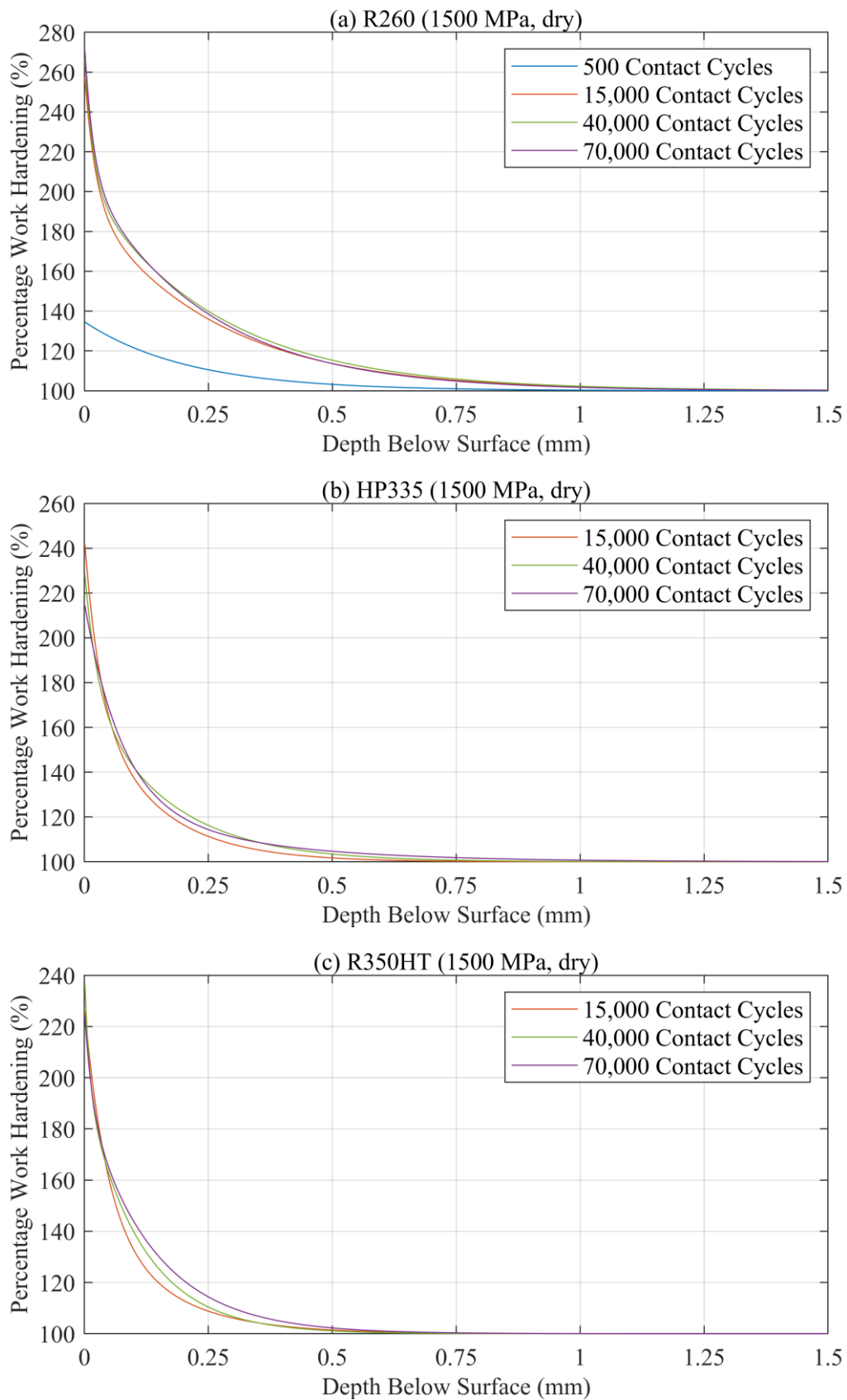


Figure A1.10: Percentage work hardening against depth below surface results obtained from the uninterrupted twin-disc samples for R260 (1500 MPa, 1200 MPa, 900 MPa, 600 MPa), HP335 (1500 MPa), and R350HT (1500 MPa) and dry contact conditions.

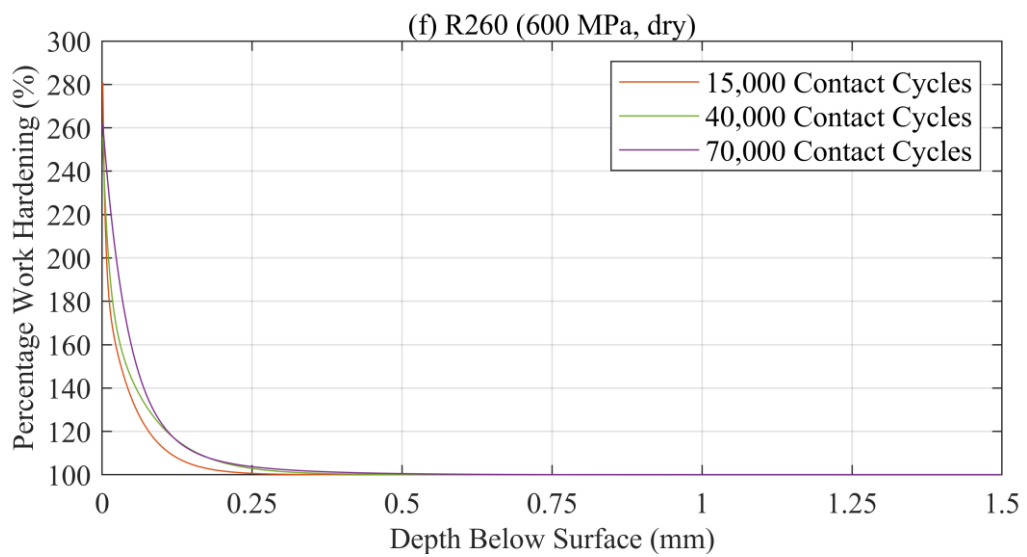
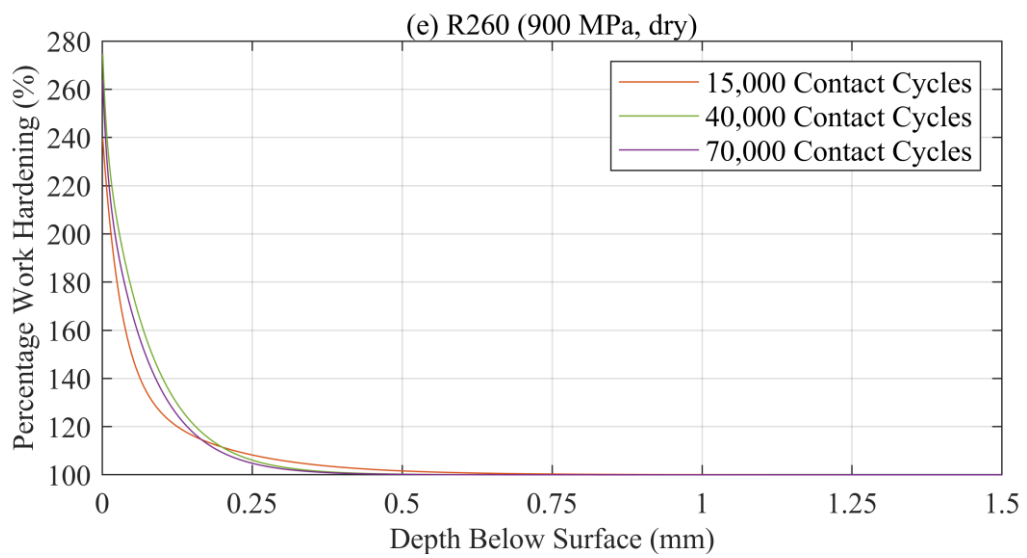
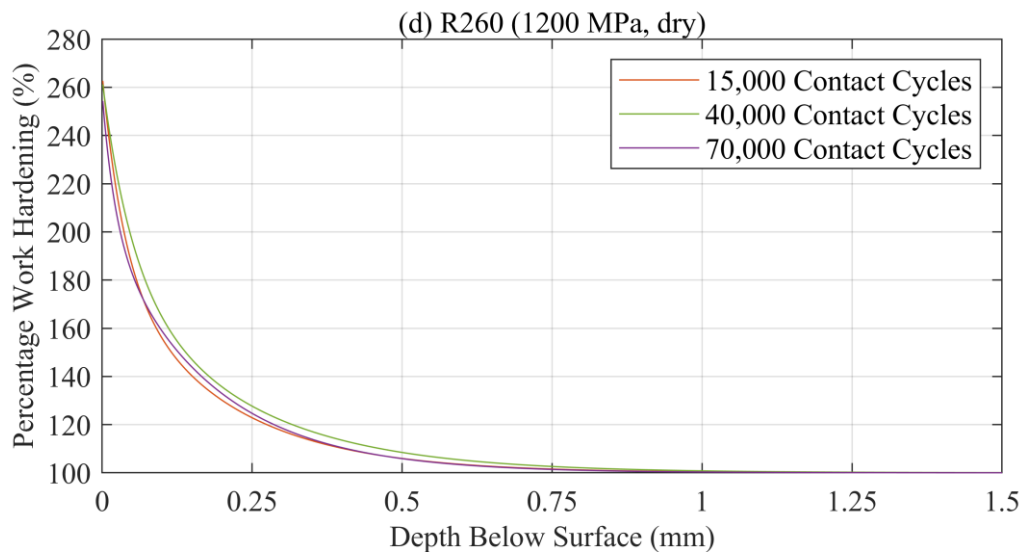


Figure A1.10: Continued.

Appendix A2: Indentation Size Error Effect for R260 Rail Steel Study

This study investigated the indentation size effect (ISE) error of measuring the hardness from R260 rail steel using a Duramin-40 microhardness tester. In this study, ten hardness measurements from the bulk undeformed region of R260 twin-disc samples were recorded using indentations loads ranging from 0.01 – 10 kg. The average bulk undeformed hardness results recorded for the different indentation load tested are tabulated in Table A2.1 and plotted in Figure A2.1.

Table A2.1: Average Vickers hardness for R260 rail steel recorded for 0.01 kg, 0.05 kg, 0.1 kg, 0.2 kg, 0.5 kg, 1.0 kg, 5.0 kg, and 10.0 kg indentation load Vickers hardness measurements.

| Vickers Hardness Setting | Indentation Load (N) | Average Vickers Hardness | |
|--------------------------|-----------------------|--------------------------|---------|
| | | HV | MPa |
| HV0.01 | 9.81×10^{-2} | 353.47 | 3467.56 |
| HV0.05 | 4.91×10^{-1} | 313.75 | 3077.93 |
| HV0.1 | 9.81×10^{-1} | 304.66 | 2988.75 |
| HV0.2 | 1.96 | 301.30 | 2955.79 |
| HV0.5 | 4.91 | 286.95 | 2815.02 |
| HV1.0 | 9.81 | 291.99 | 2864.38 |
| HV5.0 | 49.05 | 282.65 | 2772.81 |
| HV10.0 | 98.10 | 285.01 | 2795.97 |

An expression in the form of Equation A2.1 was fitted to the data to derive a relationship of Vickers hardness H against indentation loads P for measuring the bulk hardness of R260 rail steel.

$$H = \frac{A}{P + B} + H_{average} \quad \text{Equation A2.1}$$

Where A and B are coefficients found from fitting the relation to the experimental data and $HV_{average}$ is the average of the 5kg and 10kg load Vickers hardness measurements of the bulk undeformed hardness. The indentation size effect percentage error was then derived by normalising the relationship based on the average of the 5kg and 10kg indentation load measurement of the bulk undeformed hardness. The calculated ISE percentage error is plotted in Figure A2.2 and is given by Equation A2.2.

$$ISE = \frac{0.0908}{P + 0.2737} \times 100 \quad \text{Equation A2.2}$$

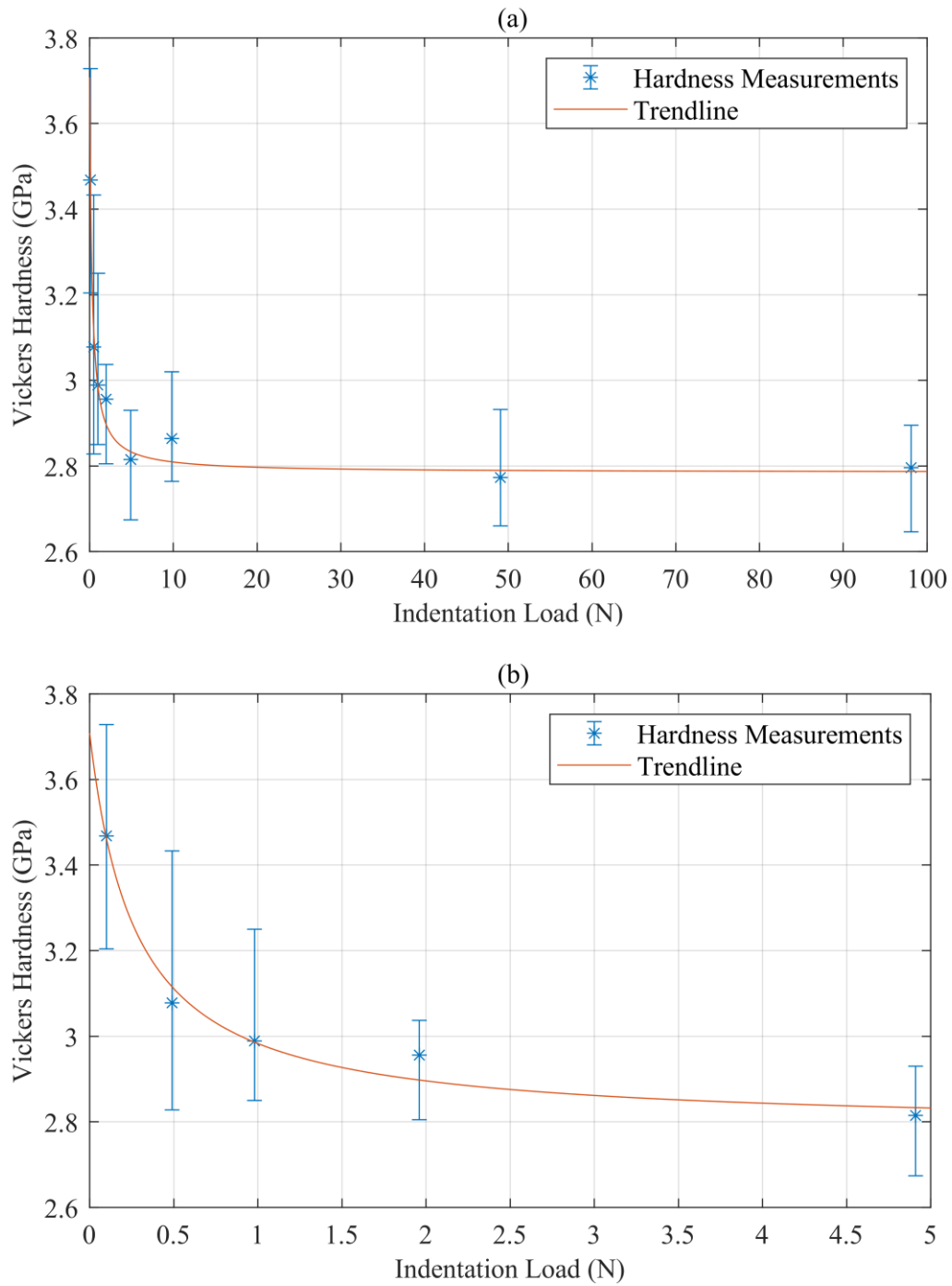


Figure A2.1: Variation of Vickers hardness measurement with indentation load ranging from (a) 0-100 N and (b) 0-5 N on the Duramin-40 microhardness indenter.

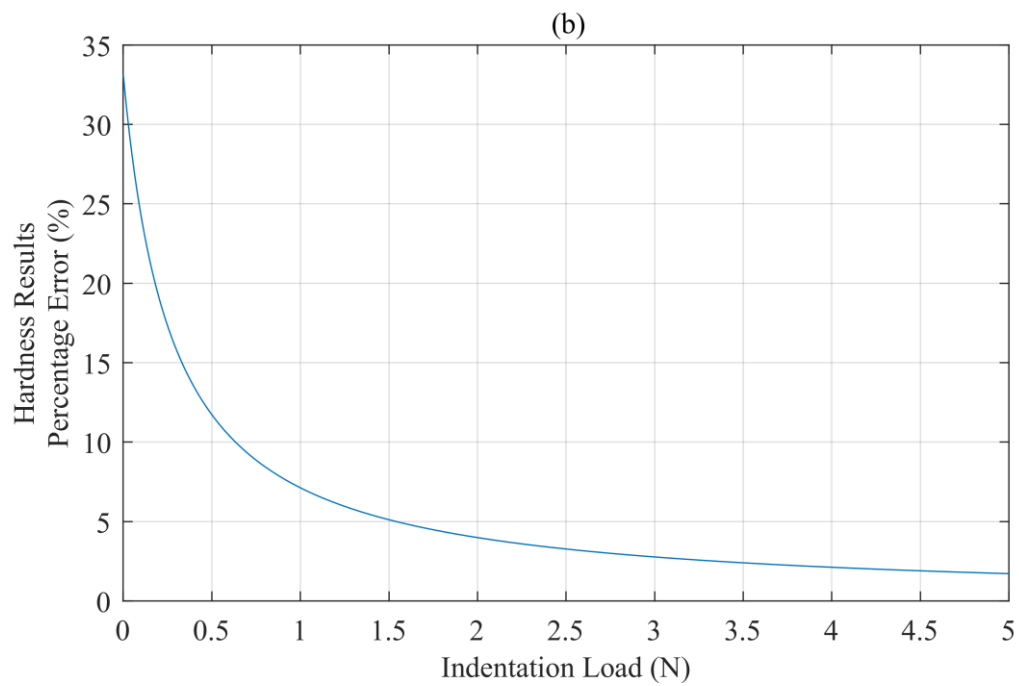
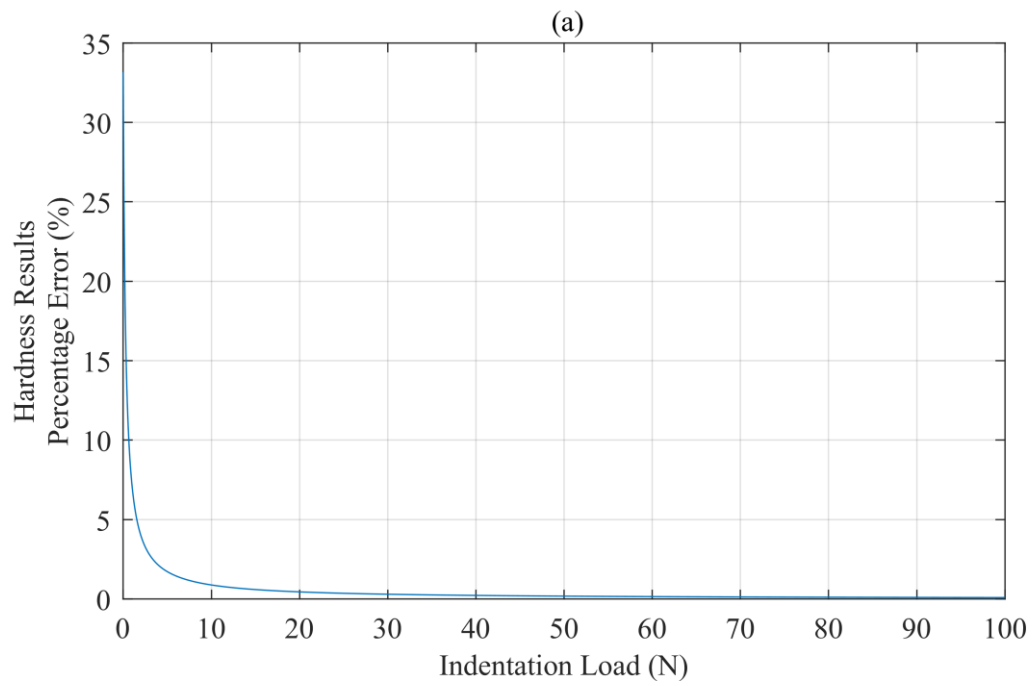


Figure A2.2: Hardness size effect error with indentation loads ranging from a) 0-100 N and b) 0-5 N for R260 rail steel on the Duramin-40 microhardness indenter.

Appendix A3: Supplementary Information for Chapter 4

Table A3.1: Plastic deformation angle and shear strain data measured at a fixed depth of 30 μm below the running surface of the R260 samples test up to 500, 15,000, 40,000, and 70,000 contact cycles uninterrupted under 1500 MPa, dry contact conditions.

| Measurement | Plastic Deformation Angle ($^{\circ}$) | | | | Shear Strain | | | |
|-------------|--|--------|--------|--------|--------------|--------|--------|--------|
| | 500 | 15,000 | 40,000 | 70,000 | 500 | 15,000 | 40,000 | 70,000 |
| 1 | 60.33 | 88.64 | 87.77 | 88.22 | 1.75 | 42.13 | 25.65 | 32.12 |
| 2 | 62.63 | 88.41 | 88.08 | 88.21 | 1.93 | 36.11 | 29.88 | 32.02 |
| 3 | 58.52 | 88.15 | 87.61 | 86.13 | 1.63 | 30.91 | 23.91 | 14.77 |
| 4 | 59.13 | 87.83 | 87.39 | 88.72 | 1.67 | 26.40 | 21.92 | 44.66 |
| 5 | 69.79 | 88.35 | 87.69 | 87.58 | 2.72 | 34.74 | 24.77 | 23.68 |
| 6 | 67.95 | 88.07 | 87.69 | 88.18 | 2.47 | 29.74 | 24.79 | 31.48 |
| 7 | 58.68 | 87.68 | 87.19 | 87.64 | 1.64 | 24.73 | 20.40 | 24.24 |
| 8 | 64.25 | 88.40 | 88.42 | 87.79 | 2.07 | 35.70 | 36.20 | 25.90 |
| 9 | 62.20 | 86.23 | 88.58 | 87.99 | 1.90 | 15.19 | 40.24 | 28.45 |
| 10 | 57.07 | 86.96 | 88.22 | 88.33 | 1.54 | 18.86 | 32.16 | 34.29 |
| 11 | 59.51 | 87.31 | 87.78 | 88.61 | 1.70 | 21.27 | 25.82 | 41.22 |
| 12 | 58.07 | 87.44 | 87.49 | 88.71 | 1.60 | 22.41 | 22.84 | 44.30 |
| 13 | 60.59 | 87.09 | 85.73 | 88.02 | 1.77 | 19.64 | 13.39 | 28.88 |
| 14 | 56.25 | 87.23 | 81.84 | 87.20 | 1.50 | 20.70 | 6.98 | 20.48 |
| 15 | 64.14 | 86.91 | 87.12 | 87.29 | 2.06 | 18.51 | 19.85 | 21.11 |
| Average | | | | | 1.86 | 26.47 | 24.59 | 29.84 |

Table A3.2: Plastic deformation angle and shear strain data measured at a fixed depth of 200 μm below the running surface of the R260 samples test up to 500, 15,000, 40,000, and 70,000 contact cycles uninterrupted under 1500 MPa, dry contact conditions.

| Measurement | Plastic Deformation Angle ($^{\circ}$) | | | | Shear Strain | | | |
|-------------|--|--------|--------|--------|--------------|--------|--------|--------|
| | 500 | 15,000 | 40,000 | 70,000 | 500 | 15,000 | 40,000 | 70,000 |
| 1 | 0 | 74.77 | 77.40 | 73.77 | 0 | 3.67 | 4.47 | 3.44 |
| 2 | 0 | 76.15 | 76.36 | 74.00 | 0 | 4.06 | 4.12 | 3.49 |
| 3 | 0 | 74.26 | 74.95 | 73.41 | 0 | 3.55 | 3.72 | 3.36 |
| 4 | 0 | 73.75 | 76.08 | 75.49 | 0 | 3.43 | 4.03 | 3.86 |
| 5 | 0 | 73.17 | 76.87 | 77.03 | 0 | 3.30 | 4.29 | 4.34 |
| 6 | 0 | 69.63 | 72.72 | 80.64 | 0 | 2.69 | 3.21 | 6.07 |
| 7 | 0 | 69.73 | 74.80 | 78.29 | 0 | 2.71 | 3.68 | 4.82 |
| 8 | 0 | 71.54 | 76.27 | 77.43 | 0 | 3.00 | 4.09 | 4.49 |
| 9 | 0 | 73.14 | 72.97 | 77.60 | 0 | 3.30 | 3.27 | 4.55 |
| 10 | 0 | 76.35 | 72.37 | 73.21 | 0 | 4.12 | 3.15 | 3.32 |
| 11 | 0 | 72.69 | 75.37 | 70.46 | 0 | 3.21 | 3.83 | 2.82 |
| 12 | 0 | 72.94 | 78.01 | 72.25 | 0 | 3.26 | 4.71 | 3.12 |
| 13 | 0 | 73.11 | 77.02 | 74.57 | 0 | 3.29 | 4.34 | 3.62 |
| 14 | 0 | 69.54 | 74.43 | 73.42 | 0 | 2.68 | 3.59 | 3.36 |
| 15 | 0 | 70.64 | 71.82 | 71.96 | 0 | 2.85 | 3.05 | 3.07 |
| Average | | | | | 0 | 3.27 | 3.84 | 3.85 |

Table A3.3: Summary of critical shear strain to failure results estimated using the RCF crack entrance angle method for the R260 twin-disc sample tested up to 500 and 70,000 contact cycles under 1500 MPa, dry contact conditions.

| Sample tested up to 500 Contact Cycles | | | Sample tested up to 70,000 Contact Cycles | | |
|--|----------------------|--------------|---|----------------------|--------------|
| Surface Inclination Angle (°) | Crack Tip Depth (µm) | Shear Strain | Surface Inclination Angle (°) | Crack Tip Depth (µm) | Shear Strain |
| 12.66 | 1.88 | 4.45 | 3.15 | 5.08 | 18.17 |
| 19.69 | 5.54 | 2.79 | 5.07 | 8.76 | 11.27 |
| 10.56 | 1.27 | 5.36 | 4.31 | 6.99 | 13.27 |
| 16.11 | 8.59 | 3.46 | 3.44 | 8.75 | 16.64 |
| 12.72 | 0.83 | 4.43 | 2.41 | 6.20 | 23.76 |
| 8.78 | 2.86 | 6.47 | 4.62 | 4.70 | 12.37 |
| 8.50 | 5.36 | 6.69 | 5.58 | 8.37 | 10.24 |
| 17.33 | 1.94 | 3.20 | 3.49 | 10.75 | 16.40 |
| 16.23 | 15.44 | 3.44 | 3.05 | 10.98 | 18.77 |
| 13.65 | 1.33 | 4.12 | 2.14 | 23.15 | 26.76 |
| 10.91 | 0.97 | 5.19 | 1.74 | 14.79 | 32.92 |
| 11.10 | 1.24 | 5.10 | 6.95 | 6.43 | 8.20 |
| 11.31 | 1.44 | 5.00 | 4.55 | 12.17 | 12.57 |
| 13.51 | 2.24 | 4.16 | 3.15 | 5.48 | 18.17 |
| 16.38 | 3.10 | 3.40 | 3.73 | 11.98 | 15.34 |
| 19.44 | 1.07 | 2.83 | 3.59 | 10.28 | 15.94 |
| 18.36 | 1.24 | 3.01 | 5.36 | 4.04 | 10.66 |
| 13.35 | 1.15 | 4.21 | 6.13 | 6.98 | 9.31 |
| 7.69 | 1.31 | 7.41 | 5.12 | 8.33 | 11.16 |
| 12.56 | 2.02 | 4.49 | 4.39 | 6.31 | 13.03 |
| 13.45 | 0.83 | 4.18 | 3.18 | 10.76 | 18.00 |
| 12.43 | 2.01 | 4.54 | 2.64 | 13.55 | 21.69 |
| 13.36 | 1.69 | 4.21 | 3.80 | 15.20 | 15.06 |
| 20.23 | 2.40 | 2.71 | 2.18 | 10.86 | 26.27 |
| 11.29 | 5.39 | 5.01 | 2.41 | 16.54 | 23.76 |
| 11.29 | 1.47 | 5.01 | 3.10 | 8.05 | 18.46 |
| 12.99 | 1.10 | 4.33 | 6.04 | 15.67 | 9.45 |
| 32.83 | 7.13 | 1.55 | 2.61 | 16.40 | 21.94 |
| 9.53 | 2.33 | 5.96 | 3.22 | 11.00 | 17.77 |
| 18.50 | 0.98 | 2.99 | 2.15 | 12.92 | 26.64 |
| 15.13 | 3.27 | 3.70 | 4.11 | 11.81 | 13.92 |
| 12.95 | 1.24 | 4.35 | 3.74 | 9.75 | 15.30 |
| 13.36 | 1.89 | 4.21 | 3.07 | 9.82 | 18.65 |
| 11.47 | 1.85 | 4.93 | 2.97 | 9.19 | 19.27 |
| Average | 2.78 | 4.32 | | 10.35 | 17.09 |

Table A3.4: Plastic deformation angle and shear strain data measured from the R260 twin-disc sample tested up to 500 and 70,000 contact cycles uninterrupted at a fixed depth of 2.78 μm and 10.35 μm , respectively, below the running surface.

| 500 Contact Cycles Sample Data | | 70,000 Contact Cycles Sample Data | |
|-------------------------------------|--------------|-------------------------------------|--------------|
| Plastic Damage Angle ($^{\circ}$) | Shear Strain | Plastic Damage Angle ($^{\circ}$) | Shear Strain |
| 67.96 | 2.47 | 88.94 | 54.09 |
| 68.87 | 2.59 | 88.15 | 31.01 |
| 70.44 | 2.81 | 87.92 | 27.58 |
| 73.57 | 3.39 | 87.27 | 20.96 |
| 76.02 | 4.02 | 87.52 | 23.13 |
| 80.01 | 5.68 | 88.32 | 34.04 |
| 78.35 | 4.85 | 86.95 | 18.78 |
| 74.88 | 3.70 | 88.24 | 32.58 |
| 82.34 | 7.44 | 87.89 | 27.09 |
| 75.97 | 4.00 | 88.82 | 48.56 |
| 71.10 | 2.92 | 87.12 | 19.84 |
| 74.34 | 3.57 | 88.26 | 32.95 |
| 72.94 | 3.26 | 88.52 | 38.76 |
| 73.02 | 3.27 | 89.06 | 60.66 |
| 82.68 | 7.79 | 87.97 | 28.23 |
| Average | 4.12 | | 33.22 |

Table A3.5: Tabulated results of the first convergence study comparing the average wear rate against the vertical brick thickness simulating the wear behaviour of R260 rail steel subjected to 1500 MPa, dry contact conditions for up to 70,000 contact cycles.

| Vertical Brick Thickness, dz (μm) | Average Wear Rate (μm / cycle) | | | |
|--|--|--------|--------|---------|
| | Run 1 | Run 2 | Run 3 | Average |
| 0.25 | 0.0273 | 0.0273 | 0.0273 | 0.0273 |
| 0.50 | 0.0272 | 0.0273 | 0.0273 | 0.0273 |
| 1.00 | 0.0271 | 0.0271 | 0.0271 | 0.0271 |
| 2.00 | 0.0266 | 0.0266 | 0.0266 | 0.0266 |
| 4.00 | 0.0254 | 0.0254 | 0.0254 | 0.0254 |
| 8.00 | 0.0238 | 0.0237 | 0.0238 | 0.0238 |
| 16.00 | 0.0206 | 0.0207 | 0.0207 | 0.0207 |
| 32.00 | 0.0158 | 0.0157 | 0.0158 | 0.0158 |

Table A3.6 Tabulated results of the second convergence study comparing the average wear rate against the number of brick columns. The simulation results generated are based on the material data of R260 rail steel subjected to 1500 MPa, dry contact conditions.

| Number of Brick Columns, Nx | Average Wear Rate ($\mu\text{m} / \text{cycle}$) | | | |
|-----------------------------|--|--------|--------|---------|
| | Run 1 | Run 2 | Run 3 | Average |
| 1 | 0.0313 | 0.0313 | 0.0312 | 0.0313 |
| 2 | 0.0292 | 0.0291 | 0.0291 | 0.0291 |
| 5 | 0.0287 | 0.0287 | 0.0287 | 0.0287 |
| 10 | 0.0284 | 0.0284 | 0.0284 | 0.0284 |
| 20 | 0.0280 | 0.0280 | 0.0280 | 0.0280 |
| 50 | 0.0276 | 0.0276 | 0.0276 | 0.0276 |
| 100 | 0.0273 | 0.0273 | 0.0274 | 0.0273 |
| 200 | 0.0271 | 0.0271 | 0.0271 | 0.0271 |
| 400 | 0.0269 | 0.0269 | 0.0269 | 0.0269 |
| 800 | 0.0267 | 0.0267 | 0.0267 | 0.0267 |
| 1600 | 0.0265 | 0.0265 | 0.0265 | 0.0265 |

Appendix A4: MATLAB Code for the SUROS2 Optical Monitoring System Wear Flake Shadow Pixel Analysis

```
%% Wear Flake Optical Image Analysis
% Quantifies the total area, area distribution, and the major and minor
% dimension of wear flake shadows on a twin-disc sample running track from
% the images obtained from the SUROS2 optical monitoring system.

clear all
close all

%% Experimental data and image directory

% Location of folder where the images that need analysing are stored and
% identifies the .tif files in that folder.
Folder = 'raw images';
FileList = dir(fullfile(Folder, '**', '*.tif'));

% SUROS2 test time and cycles data
machine_data = readmatrix('R260 Time and Cycles Data.xlsx');

% Image Capturing settings
interval = 15; % seconds

% Analysis type
Rotation_analysed = 'Full'; % Option available: Full, Half;

%% Conversion of the Image Time Stamp to Contact Cycles

[A, ia, ic] = unique(machine_data(:,3), 'first');
machine_data = machine_data(ia,3:4);

time_steps = 0:interval:interval*(length(FileList)-1);

cycles_steps = csapi(machine_data(:,1), ...
    machine_data(:,2), time_steps);

%% Image analysis

% Preallocating memory for the cell arrays and matrices that will stored
% the wear flake shadow data (total pixels, individual wear flake pixels,
% wear flake longitudinal and vertical pixel length)
total_pixels = zeros(length(FileList),1);
wear_flake_pixel = cell(length(FileList),1);
wear_flake_BoundingBox = cell(length(FileList),1);

% Set up figure to track the progress of the wear flake image analysis
% results
figure;
plot(cycles_steps(1), total_pixels(1))
xlabel('Contact Cycles');
ylabel('Total Number of Wear Flake Shadow Pixels');

for i = 1:length(FileList)
```

```

% Reads the image that needs analysing and rotate 90 degree to be
% horizontal
img = [];
Filename = [Folder '\\' FileList(i).name];
img = imread(Filename) * 16;
img = imrotate(img,-90);

% Create a locally brightened version of the image
img2 = imlocalbrighten(img);

%-----
% Detection of the twin-disc samples keyway to allow the image to be
% cropped to one full rotation of the twin-disc sample

% convert the image to grey scale
img2_grey = rgb2gray (img2);

% Binerise the image using an adaptive threshold with a sensitivity of
% 0.65
BW = imbinarize(img2_grey,'adaptive','Sensitivity',0.65);

% Clean up the image and remove any holes around the keyway
BW = ~imfill(~BW,'holes');
BW = bwareaopen(BW,80000);

% Define and located the keyways in the binerised image
SE_key = strel('rectangle',[200 500]);
BW_key = imopen(~BW,SE_key);

% Property of the keyways identified in the image
key_props = regionprops (BW_key);

% Define the horizontal position of the right hand side edge of the same
% keyway in the image and crop the image for one full rotation
if Rotation_analysed == 'Full'
    xlimit1 = floor(key_props(1).BoundingBox(1)) + ...
        floor(key_props(1).BoundingBox(3));
    xlimit2 = floor(key_props(3).BoundingBox(1)) + ...
        floor(key_props(3).BoundingBox(3));
    key_ylimit = floor(key_props(3).BoundingBox(1)) + ...
        floor(key_props(3).BoundingBox(3))
elseif Rotation_analysed == 'Half'
    xlimit1 = floor(key_props(1).BoundingBox(1)) + ...
        floor(key_props(1).BoundingBox(3));
    xlimit2 = floor(key_props(2).BoundingBox(1)) + ...
        floor(key_props(2).BoundingBox(3));
end
img2_crop = img2(:,xlimit1-200:xlimit2,:);

%-----
% Detection of the twin-disc samples running track to allow the image
% to be cropped image to be cropped again to retain information
% regarding the observable portions of the twin-disc samples running
% track

% convert the cropped image to grey scale
img2_crop_grey = rgb2gray(img2_crop);

% motion blur the cropped image in the horizontal to filter out the
% wear flake shadows on the running track but retain a clear boundary

```

```

% of the outer edge of the twin-disc sample running track and portions
% of the twin-disc samples running track that can not be observed due
% to tarnishing.
h = fspecial('motion',100,0);
img2_crop_grey_filt = imfilter(img2_crop_grey,h);

% Binerise the cropped image using an adaptive threshold with a
% sensitivity of 0.3.
BW_crop = imbinarize(img2_crop_grey_filt,'adaptive','Sensitivity',0.7);

% Remove any noise in the image that would interfere with the locating
% the twin-disc samples running track
BW_crop = imfill(BW_crop,8,'holes');
if Rotation_analysed == 'Full'

    BW_crop(1:key_props(2).BoundingBox(4),floor((1:key_props(2).BoundingBox(3)
    ) +...
        key_props(2).BoundingBox(1) - xlimit1)) =
    zeros(key_props(2).BoundingBox(4),...
        key_props(2).BoundingBox(3));

    BW_crop(1:key_props(3).BoundingBox(4),floor((1:key_props(3).BoundingBox(3)
    ) +...
        key_props(3).BoundingBox(1) - xlimit1)) =
    zeros(key_props(3).BoundingBox(4),...
        key_props(3).BoundingBox(3));
elseif Rotation_analysed == 'Half'

    BW_crop(1:key_props(2).BoundingBox(4),floor((1:key_props(2).BoundingBox(3)
    ) +...
        key_props(2).BoundingBox(1) - xlimit1)) =
    zeros(key_props(2).BoundingBox(4),...
        key_props(2).BoundingBox(3));
end

% Define and located the twin-disc samples running track in the
% binerised image
SE_track = strel('rectangle',[200 diff([xlimit1,xlimit2])-199]);
BW_crop_track = imopen(BW_crop,SE_track);

% Properties of the twin-disc samples running track identified in the
% image
track_props = regionprops(BW_crop_track);

% Define the outer edges of the observable portion of the twin-disc
% samples running and crop the image again to retain information on the
% observable portion only
ylimit1 = floor(track_props.BoundingBox(2));
ylimit2 = floor(track_props.BoundingBox(2)) + ...
    floor(track_props.BoundingBox(4));
img_crop2 = img(ylimit1:ylimit2,xlimit1-50:xlimit2-50,:);
img_crop3 = img(ylimit1:ylimit2,xlimit1-100:xlimit2,:);

%-----
% Quantification of the wear flake shadow data

% Greyscale the cropped images
img_crop2_grey = rgb2gray(img_crop2);
img_crop3_grey = rgb2gray(img_crop3);

% Calculate the local background intensity image for thresholding the

```

```

% images analysed for wear flakes
h = fspecial('motion',50,0);
background = imfilter(img_crop3_grey,h);

% Identify the wear flakes from the images analysed by pixels
% identifying pixels in the analysed that have a intensity less than
% 45% of the local background intensity image
BW_crop2 = imcomplement(img_crop2_grey >= background(:,51:end-50)*0.45);

% Update the output results
total_pixels(i) = sum(BW_crop2,'all'); % total shadow area cast by
wear_flake_pixel{i} = regionprops(BW_crop2,'Area');
wear_flake_BoundingBox{i} = regionprops(BW_crop2,'BoundingBox');

%-----

% Update the progress counter
fprintf('Image %.0f / %.0f Analysed \n', i, length(FileList));

% Update the live figure of the total wear flake shadow pixel count
subplot(3,1,1);
plot(cycles_steps(1:i),total_pixels(1:i))
xlabel('Contact Cycles');
ylabel('Total Number of Wear Flake Shadow Pixels');
subplot(3,1,2);
imshow(img_crop2)
subplot(3,1,3);
imshow(BW_crop2)
drawnow

end

%% Final Total Wear Flake Shadow Pixels Count Results Figure

close all
figure;
plot(cycles_steps,total_pixels)
xlabel('Contact Cycles');
ylabel('Total Number of Wear Flake Shadow Pixels');

```